UNIVERSITÉ DE STRASBOURG

THÈSE DE DOCTORAT

Discipline : **PHYSIQUE**

Présentée par **Julien BRIAND**

Ultrafast isomerization and vibrational coherence of biomimetic photoswitches: Experimental investigation by femtosecond transient absorption spectroscopy

Composition du jury:

RAPPORTEURS :	Irène Burghardt Josef Wachtveitl
EXAMINATEURS:	Chantal Daniel Jean-Yves Bigot
INVITÉ:	Jérémie Léonard
DIRECTEURS DE THÈSE:	Stefan Haacke Alfred Leitenstorfer

Institut de Physique et Chimie des Matériaux de Strasbourg (IPCMS)
Département d'Optique non-linéaire et de Nanophotonique (DON)

Acknowledgements

First I would like to thank the members of the jury, Irène Burghardt, Josef Wachtveitl, Chantal Daniel and Jean-Yves Bigot. It is a real honour for me that such scientists of international reputations have accepted to review and judge this work.

I thank Stefan Haacke and Alfred Leitenstorfer for their strong support, patience and appropriate advices all along these three years, and especially Stefan for to whom I owe the possibility of this Ph.D. thesis. Jérémie Léonard also had a key role in this work, always willing to help me with experimental or data analysis work, and his collaboration was important and essential for me. Together with Stefan, I think that you form an incredible team, and apart from your scientific help, I have particularly appreciated your managing skills, as you always kept an enthusiastic but also critical judgment, and never stopped helping and encouraging me during this work.

I am also thankful for the opportunity that the IPCMS institute and his director Marc Drillon gave me to achieve this work in such a tremendous scientific environment. A lot of people helped me during these three years and participated in one way or another to this work. I would like to thank Olivier Crégut, Virginie Stortz, Jean-Pierre Vola, Michèle Albrecht and Gauthier Dekyndt from the technical teams of the DON department. Their high-quality work and useful advices on experimental and technical questions related to optics, electronics and mechanics was of great importance for me and the team. I am also thankful for the help that Emilie Couzigné and Emilie Voirin, from the DMO department at IPCMS, gave me concerning sample preparations and characterizations.

The kind welcome and support from all the members of the DON department have also been important, and it was a real pleasure to work in this group. Many thanks in particular to Sébastien, Honorat and Mircea: I really enjoyed our coffee break discussions and our regular tennis trainings during my stay at IPCMS.

Last but not least, I am extremely grateful to my parents, sister, girlfriend and friends for their necessary support and for everything they did for me during this thesis.

Résumé

De nombreux systèmes présents dans la nature capturent l'énergie lumineuse et l'utilisent pour déclencher leurs fonctions biologiques. L'absorption d'un photon par un chromophore, une molécule absorbant efficacement la lumière, initie ces processus. Cela permet de promouvoir le chromophore dans un état excité, à partir duquel une photo-réaction peut démarrer. Ces réactions se déroulant à partir des états excités, convertissant l'énergie d'un photon en mouvement moléculaire et en énergie chimique, sont les initiateurs de fonctions biologiques telles que la photosynthèse, la vision ou le mouvement bactérien photo-induit (photo-taxis).

Ces réactions impliquent souvent des échelles de temps ultra-rapides, dans les domaines femtosecondes ou picosecondes, et un changement structurel du chromophore, comme une isomérisation (changement de conformation), cette dernière étant une réaction élémentaire mais d'importance générale, puisqu'elle est impliquée par exemple dans la première étape de la vision dans la rhodopsine. Cette conversion d'énergie opto-mécanique (mouvement de rotation sous l'effet de la lumière) est à l'origine du concept de photo-commutateur moléculaire. En effet, suite à l'absorption d'un photon, le chromophore de rétinal dans la protéine de rhodopsine, se trouvant dans la rétine de l'œil, isomérise avec une vitesse et une efficacité record. Grace à ce changement structurel, la photo-chimie de la rhodopsine est déclenchée.

Mais le rétinal perd ces propriétés remarquables de vitesse et d'efficacité quand il se trouve isolé en solution, ceci soulignant le rôle majeur joué par l'environnement protéique sur la photo-réaction. Compte-tenu de cette dernière remarque, l'utilisation d'autres photo-commutateurs moléculaires de faible tailles, tels que le stilbene ou l'azobenzene, s'est développée pour les études et les applications nécessitant des mouvements de large amplitudes et photo-contrôlés.

Dans ce contexte, une nouvelle famille de photo-commutateurs basés sur la structure alkylée d'Indanylidene-Pyrroline (NAIP), supposée reproduire l'isomérisation du rétinal dans la rhodopsine, a récemment été imaginée et étudiée sur ordinateur par Massimo Olivucci et al. avant d'être synthétisée. Les résultats de leurs études théoriques soulèvent de grandes espérances concernant une isomérisation ultra-rapide (sub-picoseconde) et efficace de ces chromophores en solution. Les buts de leurs travaux sont de mener une étude sur les paramètres fondamentaux contrôlant l'isomérisation, mais aussi d'introduire ces nouveaux commutateurs moléculaires, différents de ceux déjà existants (par exemple en taille, polarité ou mécanisme d'isomérisation), facilement modifiables et fonctionnalisables, dans des domaines applicatifs nécessitant des mouvements moléculaires photo-induits. En effet, ils peuvent par exemple permettre de contrôler (à la fois déclencher et inhiber) une fonction biologique grâce à la lumière.

Ce travail de doctorat rapporte l'étude expérimentale et les premiers résultats obtenus sur l'isomérisation ultra-rapide de la famille de molécules NAIP. Tout d'abord, ce sujet a nécessité la réalisation d'un montage expérimental permettant d'étudier des processus se déroulant à l'échelle de la dizaine de femtosecondes (1 fs = 10^{-15} s) qui est l'échelle des mouvements moléculaires. Une expérience de spectroscopie d'absorption résolue en temps (encore appelée spectroscopie pompe/sonde) femtoseconde a donc été réalisée. Gràce a une résolution temporelle suffisante et à une large couverture spectrale, elle permet de suivre l'évolution temporelle de telles réactions.

Brièvement cette méthode consiste à utiliser des impulsions lasers femtosecondes, provenant d'un oscillateur Ti:Saphir femtoseconde dont taux de répétition et l'énergie par implusion sont respectivement diminué et augmentée, gràce à un système amplificateur basé sur les techniques d'amplification régénérative et à dérive de fréquence (800 nm, 40 fs, 1 kHz). Le faisceau est ensuite séparé en deux et des effets non-linéaires sont utilisés. Une première impulsion très large spectralement et appelée impulsion sonde est créée par génération de continuum dans un crystal de CaF_2 (290-1000 nm). Une deuxième est obtenue par génération de seconde harmonique dans un crystal de BBO (400 nm).

Le principe de l'expérience est le suivant. Une première impulsion sonde est envoyée à travers l'échantillon et son intensité spectrale est alors mesurée. Ensuite une impulsion pompe, plus intense, va servir à déclencher un phénomène physico-chimique dans l'échantillon. Enfin, après un certain délai par rapport à l'impulsion pompe (de quelques femtosecondes à quelques nanosecondes d'écart), une deuxième impulsion sonde est envoyée. La comparaison entre les deux impulsions sondes (sans et avec le pulse d'excitation) nous donne l'effet du processus photo-déclenché dans l'échantillon à un instant $t + \tau$, τ étant le délai entre les impulsions pompe et sonde. Grace à une ligne à délai optique (motorisée et contrôlée par ordinateur), nous faisons varier le délai τ et pouvons par ce moyen échantillonner la réponse temporelle du système mesuré (voir fig. 1). Une analyse détaillée des signaux d'absorption ou d'émission de l'échantillon permet de suivre l'évolution de la photo-réaction que l'on souhaite étudier.

Les performances de sensibilité de mesure de variation d'absorption (ΔA) de l'expérience sont comparables aux meilleurs montages existants. Sa résolution temporelle est de 80 femtosecondes, suffisante pour étudier le type de réactions précédemment citées. Enfin une large couverture des régions spectrales UV, visible et proche IR est possible grâce à ce montage (290-1000 nm, 2.5 nm de résolution).

Enfin, des procédures de correction de données ont également été mises en place. Le solvant (méthanol) produit un signal pendant la coïncidence temporelle des impulsions pompe et sonde. Ce signal est utilisé pour corriger la dérive de fréquence de l'expérience, induite par la sonde (spectralement large) du fait de la dispersion de vitesse de groupe qu'elle subit. De plus, le signal du solvant est soustrait afin d'enlever ses dynamiques qui ne sont pas reliées à celles de la molécule étudiée.

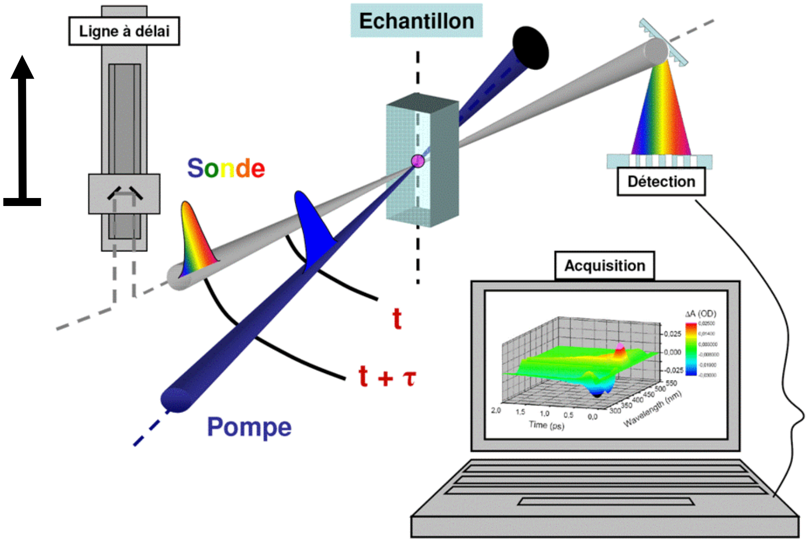

Figure 1. Principe simplifié de la technique de spectroscopie pompe/sonde.

La nouvelle famille de photo-commutateurs moléculaires inventée par M. Olivucci et al. est directement inspirée des études faites sur la protéine de rhodopsine, intervenant comme photo-récepteur pour la vision. En effet le chromophore de rétinal, inséré dans la protéine de rhodopsine, effectue une isomérisation sous l'effet de la lumière avec une vitesse (200 fs[1]) et un rendement de réaction (67%[2]) inégalés pour ce type de processus. Cette nouvelle famille est basée sur la structure alkylée d'Indanylidene-Pyrroline[3-5] (NAIP, voir fig. 2), imaginée pour reproduire, en solution, la photo-isomérisation référence du chromophore de rétinal dans la protéine de rhodopsine.

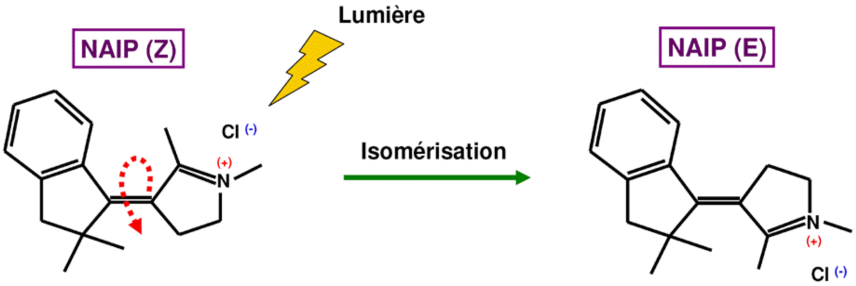

Figure 2. Représentation schématique de la réaction de photo-isomérisation de la molécule de NAIP.

La combinaison de calculs quantiques *ab initio* et de mécanique moléculaire (QM/MM) prédit, pour le photo-commutateur seul en solution (méthanol), des propriétés très similaires à celles du rétinal dans la protéine de rhodopsine. En particulier d'après ces études, la photo-isomérisation est possible autour de la double liaison centrale, sans barrière de potentiel le long du chemin réactionnel, ce dernier incluant un passage au travers d'une intersection conique. Elle prévoit aussi que la réaction peut être simplifiée et décrite en considérant seulement deux coordonnées de réactions, celle du mode de vibration de la liaison C=C et celle du mode de torsion autour de cette même liaison, cette dernière étant la coordonnée principale de réaction. Les calculs de délocalisation de la charge positive (fig. 2) dans l'état excité donnent des résultats équivalents à ceux de la rhodopsine, puisqu'environ 30 % de la charge positive est délocalisée dans cet état, provoquant une déstabilisation de la double liaison permettant la rotation. Enfin, des simulations d'évolution de population sous forme de paquet d'ondes lors de la réaction prédisent une évolution sur l'état excité d'environ 200 fs, et donc des temps d'isomérisation ultra-rapides (sub-picosecondes) et comparables à ceux du rétinal dans la rhodopsine. Cela peut notamment laisser supposer à des rendements réactionnels élevés, puisque la vitesse de la réaction d'isomérisation est supposée être un paramètre important pour y parvenir.

La figure 3 présente les propriétés statiques mesurées sur un composé représentatif, la forme zwitterionique des photo-commutateurs (ZW-NAIP). Les structures des deux isomères Z et E sont indiquées (fig. 3A), ainsi que leurs spectres d'absorption respectifs (fig. 3C) et les différences de ces deux spectres (spectres E-Z et Z-E de la fig. 3D, qui traduisent respectivement les photo-réactions Z → E et E → Z). Ceci montre que lorsqu'un isomère Z (E) de la molécule ZW-NAIP est photo-convertit en un isomère E (Z), ceci donne lieu à une différence d'absorption, le spectre E-Z (Z-E), que nous pouvons mesurer de manière statique dans l'UV-Vis comme dans la figure 3D, ou avec les mesures d'absorption femtoseconde. De plus, des mesures par RMN (fig. 3B) indiquent qu'il est possible par illumination continue (λ = 454.5 nm), de créer une solution métastable et majoritaire en isomères E (88 %) à partir d'une solution d'isomères Z (98%).

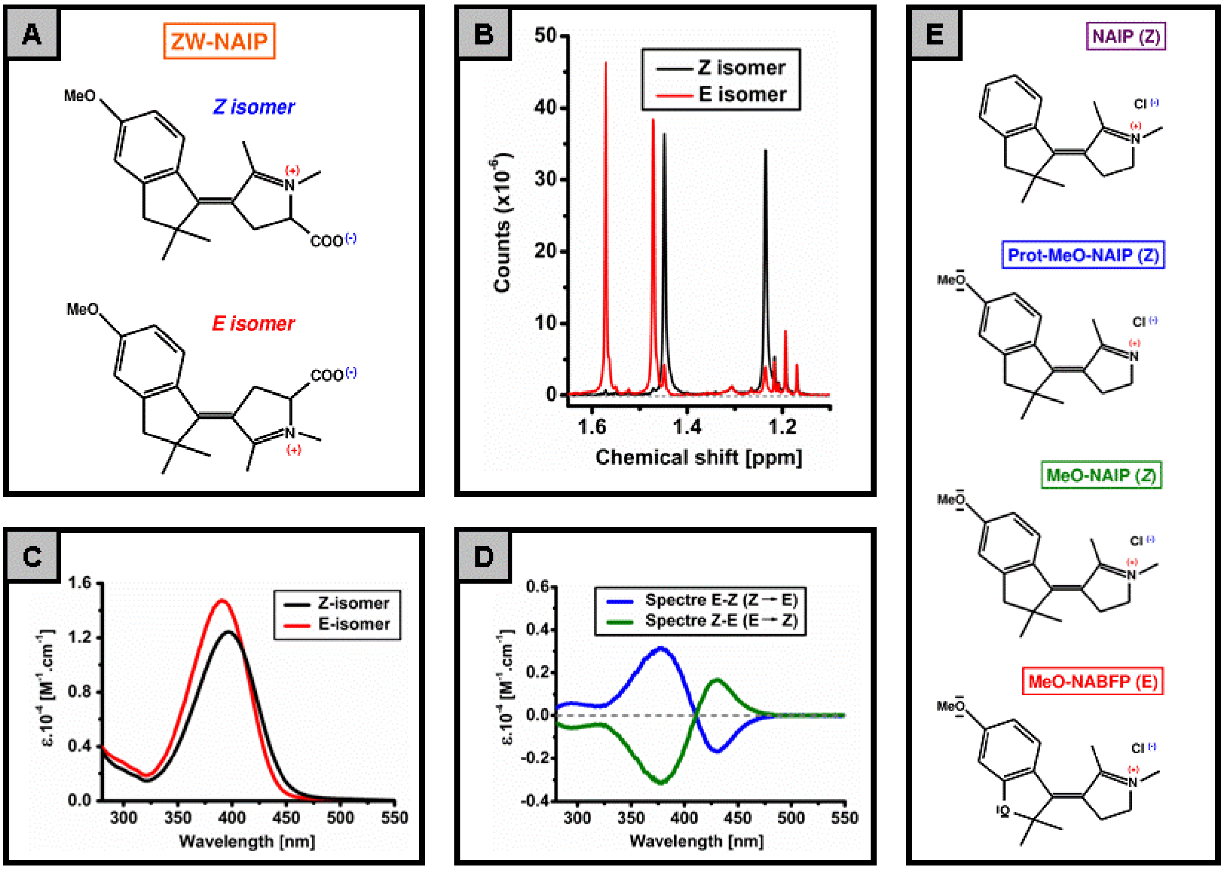

Figure 3. **A**. Structures des deux isomères Z et E de la molécule ZW-NAIP. **B**. Spectres RMN dans la région 1.1-1.65 ppm dans laquelle des signatures permettent de distinguer les deux isomères de la molécule. Ils montrent que l'obtention de majorités métastables d'isomères Z (98%) ou E (88%) est possible. **C**. Spectres d'absorption statiques des 2 isomères. **D**. Différence d'absorption des 2 spectres précédents, qui permettent de voir la différence d'absorption obtenue lors la formation d'isomères E à partir de Z et inversement. **E**. Structures des 4 autres molécules étudiées par spectroscopie ultra-rapide.

Le deuxième aspect de ce projet de doctorat a donc consisté en l'étude et l'analyse de différentes variantes de cette nouvelle famille de photo-commutateurs bio-inspirés (ou biomimétiques) de l'isomérisation de la rhodopsine, grâce au montage de spectroscopie d'absorption transitoire femtoseconde réalisé. Les structures des molécules sont présentées sur les figures 3A et 3E. Dans un premier temps, les propriétés spectro-temporelles de chaque composé ont été étudiées, dans le but de confirmer les prédictions théoriques, en apportant notamment les preuves de l'isomérisation ultra-rapide par la compréhension et la modélisation des différents signaux observés. La preuve d'isomérisation est apportée par l'observation expérimentale du spectre de différence des deux isomères (Z et E). De plus, la rapidité de la réaction prédite par la théorie a pu être confirmée. En effet, après le déclenchement de la réaction par l'impulsion d'excitation à 400 nm, des temps d'isomérisation aussi rapides que ~260 fs sont observés expérimentalement. Ensuite, la réversibilité de l'isomérisation a été investiguée avec pour objectifs de vérifier la possibilité de rotation des deux isomères (de Z → E et de E → Z), et de comparer les vitesses d'isomérisation respectives et les différences observées. Enfin les propriétés du solvant ont été variées afin d'étudier leurs influences éventuelles sur la réaction d'isomérisation.

Les cinq photo-commutateurs, présentant des substitutions différentes (NAIP, MeO-NAIP, Prot-MeO-NAIP, ZW-NAIP et MeO-NABFP, voir figures 3A et 3E) ont donc été mesurés par spectroscopie d'absorption femtoseconde[4, 6-8], révélant effectivement une isomérisation ultra-rapide. Les résultats font apparaitre deux scénarios d'isomérisation distincts. Le premier concerne la molécule MeO-NABFP qui montre un scénario d'isomérisation ultra-rapide et qui peut être majoritairement décrit par des cinétiques de réaction exponentielles ($\tau_{iso} = 600$ fs). Les quatre autres molécules (NAIP, MeO-NAIP, Prot-MeO-NAIP et ZW-NAIP) montrent des isomérisations plus rapides avec des temps d'isomérisation inférieurs à 500 fs et des indications de cohérence vibrationnelle, menant à un scénario différent du précédent, car les dynamiques ne peuvent plus être décrites uniquement par des exponentielles. En effet, les mesures de variation d'absorption effectuées montrent des signaux de paquet d'ondes, au travers de décalages spectro-temporels et d'oscillations. Avant de rentrer plus précisément dans les résultats de ce travail, il est important de préciser que le seul exemple connu d'isomérisation cohérente en solution est celui de la rhodopsine. En effet, lorsque la rhodopsine est excitée par une impulsion laser ultra-courte, un paquet d'ondes est crée dans l'état excité et persiste durant la réaction jusque dans le photo-produit. Un exemple représentatif de mesures expérimentales effectuées sur la molécule ZW-NAIP est présenté dans la figure 4.

Grâce à cette évolution de la population sous la forme d'un paquet d'ondes, la réaction peut être suivie pendant la quasi-totalité de son déroulement, grâce à l'absorption de l'état excité (vers un autre état plus haut en énergie), qui reflète une évolution de la population de l'état excité (S_1) sous forme de paquet d'ondes (voir fig. 4A et B). La superposition cohérente de plusieurs fonctions d'ondes vibrationnelles crée ce paquet d'ondes qui se déplace ensuite sur la surface de potentiel de l'état excité. L'évolution temporelle précise le long du chemin réactionnel sur l'état excité, à partir de la région de Franck-Condon, devient ainsi accessible. Cette bande d'absorption qui, selon la trajectoire du paquet d'onde, se décale à la fois spectralement et temporellement, donne un temps précis du moment où la molécule est proche de l'intersection conique (CI, région inaccessible expérimentalement), c'est-à-dire le moment où l'angle de rotation est de proche de ~90°. Ce temps se situe suivant les molécules étudiées entre 160 et 230 fs, en excellent accord avec les simulations réalisées.

Ensuite, une période temporelle sans signaux reliés à ce paquet d'onde, très probablement due au passage dans la région de l'intersection conique, a été identifiée et dure de 100 à 150 fs. Le deuxième signal spécifique est la repopulation décalée en temps et quasi-impulsive de l'état fondamental qui apparait au travers d'un signal d'absorption ($\Delta A>0$), celui-ci étant le mieux observé dans la partie rouge du spectre ($\lambda>500$ nm, voir fig. 4A et C) et arrivant après la fenêtre temporelle liée à l'intersection conique. Enfin, ce signal quasi-impulsif se transforme en oscillations de basses fréquences (60-110 cm^{-1}) et rapidement amorties ($\tau_{damping}$ = 300 fs), traduisant respectivement le mouvement et la décohérence du paquet d'onde dans les potentiels des états fondamentaux (voir fig. 4A, D et E).

Pour une analyse quantitative des dynamiques, un modèle d'ajustement « hybride » est introduit et appliqué, permettant de décrire les données de manière quantitative en tenant compte de la dualité des dynamiques, qui montrent à la fois un comportement stochastique et cohérent.

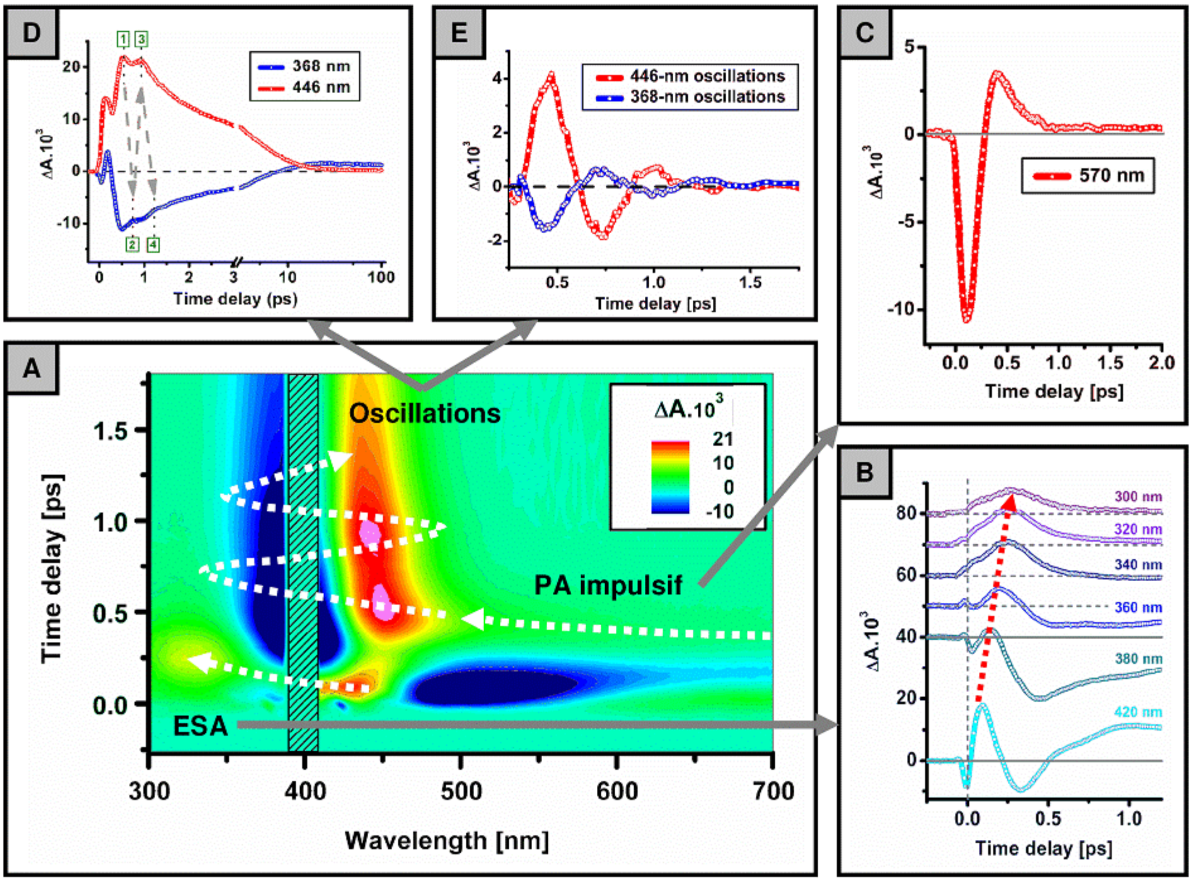

Figure 4. **A**. Représentation des données de différence d'absorption spectro-temporelles ΔA(λ,t), codées en couleur) dans la gamme 300-700 nm et dans les premières 1.8 ps. En bleu sont représentés le blanchiment (~350-420 nm) et l'émission stimulée (~520 nm), tandis que l'absorption de l'état excité (ESA, 300-450 nm) et celle du photo-produit (400-500 nm) sont représentées en rouge. Les lignes blanches en points-tillés sont un guide pour suivre l'évolution spectro-temporelle sous forme de paquet d'ondes de la population à partir de l'état excité. **B**. Traces cinétiques dans la région de l'ESA (300-420 nm) soulignant la propagation du paquet d'onde sur l'état excité pendant 230 fs. **C**. Trace cinétique à 570 nm montrant l'arrivée quasi-impulsionnelle du paquet d'ondes dans l'état fondamental après ~400 fs. **D**. Traces cinétiques de part et d'autre (368 et 446 nm) du maximum du spectre d'absorption de ZW-NAIP (397 nm) dans lesquelles des d'oscillations amorties et anti-phasées sont observées. Elles sont extraites par une procédure spécifique et représentées en **E**.

Toutes ces mesures expérimentales et leurs analyses mènent à une modélisation et à un scénario réactionnel résumé sur la figure 5. L'isomérisation de ces quatre commutateurs peut être décrite en impliquant deux modes réactionnels, un mode d'étirement intervenant dans les premières ~50 fs, suggéré par l'activité Raman limitée par la résolution temporelle de l'expérience dans la gamme de fréquences autour de 1600 cm^{-1}, et un mouvement de torsion pouvant être presque entièrement suivi durant la réaction d'isomérisation. Ensuite, après ce passage à travers la région de l'intersection conique et sa fenêtre temporelle associée, un signal d'absorption de l'état fondamental (S_0) nous permet de continuer à suivre la réaction. En effet, le paquet d'onde initialement créé dans l'état excité, conserve sa cohérence et est observé après 260 à 380 fs suivant les échantillons considérés. Cela donne donc un timing très précis du temps d'isomérisation des différentes molécules, qui est donc du même ordre de grandeur que celui du rétinal dans la rhodopsine. Enfin, dans la continuité de ce dernier signal, des oscillations cohérentes sont observées dans l'état fondamental, traduisant l'oscillation du paquet d'ondes dans le potentiel de l'état fondamental suivant la coordonnée de réaction (torsion).

Ces résultats suggèrent donc un chemin réactionnel sans barrière de potentiel, corroborant expérimentalement les calculs théoriques et les simulations réalisées sur ces composés. De plus, les signatures cohérentes de type paquet d'ondes observées permettent de donner un timing précis de la réaction d'isomérisation, c'est à dire du mouvement moléculaire de torsion.

Ce phénomène de cohérence vibrationnelle, depuis l'état excité et conservée jusque dans l'état fondamental, est observé pour la première fois sur un photo-commutateur en solution, rendant le travail sur cette nouvelle famille très prometteur. De plus, la comparaison avec l'isomérisation référence du rétinal dans la rhodopsine souligne l'aspect biomimétique visé car les signaux spectro-temporels, et par conséquent, la topologie des surfaces d'énergie potentielle, sont reproduits. Enfin la relaxation vibrationnelle et le refroidissement des molécules dans l'état fondamental sont achevés au bout de ~30 ps.

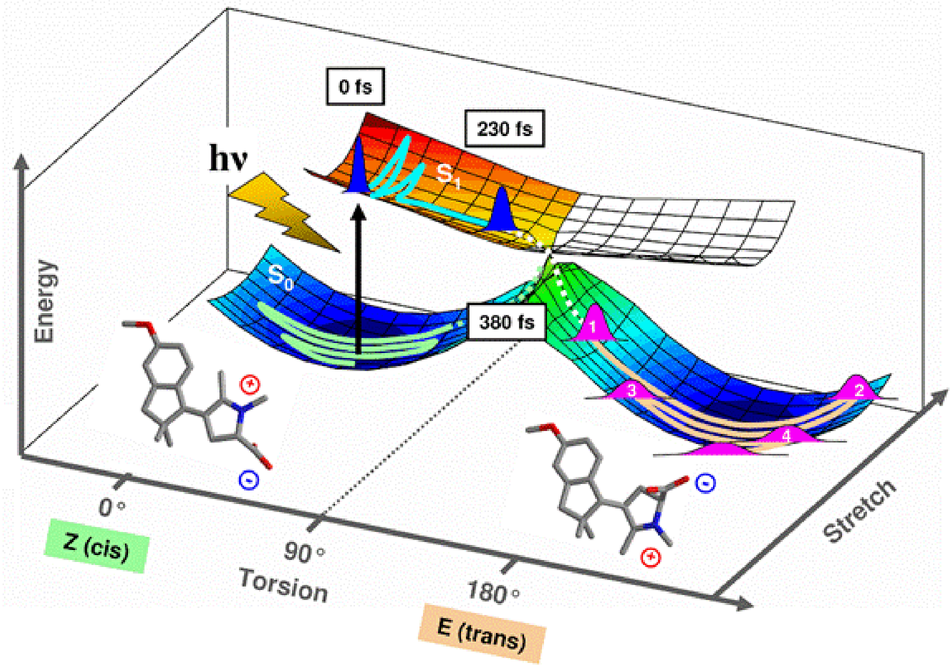

Figure 5. Exemple du scénario de la réaction d'isomérisation du photo-commutateur ZW-NAIP.

Enfin, des effets de substitution modifiant les dynamiques de la réaction d'isomérisation ont pu être observés expérimentalement, les molécules étudiées ne différant seulement que par le changement d'un ou de quelques atomes dans la structure NAIP. Celles affectant la partie rotative pyrroline influencent principalement la fréquence intrinsèque du mode de torsion, comme cela a été vu avec les différents périodes d'oscillation mesurées sur les quatre photo-commutateurs montrant une isomérisation dans un régime de cohérence vibrationnelle (de 300 à 560 fs). Les substitutions les plus importantes concernent l'autre moitié indanone de la molécule. Le fait d'ajouter un atome d'oxygène, placé comme dans la MeO-NABFP entre le groupe pyrroline et le groupement phényle, mène sûrement à une surface de potentiel de l'état excité moins favorable. En effet, sa réaction d'isomérisation se révèle être beaucoup plus lente (temps de formation exponentiel de 600 fs), et se déroule de manière non cohérente (pas d'observation du paquet d'onde dans l'état fondamental). Toutes ces mesures expérimentales donnent des valeurs concrètes qui vont être utilisées par les théoriciens pour mieux comprendre l'influence de ces substitutions sur la réaction d'isomérisation.

De manière à étudier plus précisément les propriétés de photo-commutation de ces composés, l'étude de la bi-directionnalité de la réaction (Z → E et E → Z) de deux molécules (ZW-NAIP et MeO-NAIP) a été réalisée. La première conclusion importante est que l'isomérisation se déroule sur la même échelle de temps dans les deux directions (écart ≤ 50 fs), indiquant des surfaces d'énergie potentielles et des chemins réactionnels très similaires pour les deux isomères, comme cela a été prédit par la théorie. De plus, dans le cas de la molécule ZW-NAIP, grâce à une simple soustraction des données mesurées dans les deux directions et qui permet de s'affranchir des signaux de relaxation vibrationnelle dans l'état fondamental, la signature de formation des isomères devient visible à une échelle sub-picoseconde, corroborant l'interprétation du scénario d'isomérisation ultra-rapide en régime cohérent décrit précédemment.

L'influence de l'environnement de la molécule a également été étudiée par des mesures réalisées sur un photo-commutateur (ZW-NAIP) dans trois solvants aux propriétés différentes (méthanol, butanol, décanol). Les expériences montrent des dynamiques de la molécule extrêmement similaires dans les trois solvants. En effet, ni la viscosité ni les changements de constante diélectrique n'influencent la vitesse d'isomérisation (~380 fs). Seule la thermalisation de l'état fondamental est faiblement affectée (augmentation de ~30% du méthanol au décanol), et est probablement reliée aux paramètres de conductivité thermique des solvants. De la même manière, ce ralentissement de la relaxation de l'état fondamental est en accord avec une relaxation diélectrique plus lente dans les solvants moins polaires. La réaction d'isomérisation dans le décanol est aussi rapide, mais cependant le rendement quantique de la réaction se trouve être plus faible, montrant que le solvant peut sûrement intervenir dans ce cas sur la région d'énergie potentielle ou se décide le rendement, probablement la région de l'intersection conique. Cette étude démontre que les dynamiques de l'isomérisation de ces photo-commutateurs sont principalement régies par des paramètres intra-moléculaires, et que les paramètres inter-moléculaires peuvent avoir un rôle en influençant le rendement de la réaction. Comme des mouvements moléculaires de large amplitude sont concernés, cette quasi-invariance à l'environnement se trouve être surprenante. Une étude à la fois théorique et expérimentale plus approfondie se révèle nécessaire afin de confirmer et mieux comprendre ces premières observations expérimentales.

La photo-isomérisation est donc un processus clé impliqué dans de nombreuses fonctions biologiques, et sur lequel des questions fondamentales restent à élucider, comme les paramètres gouvernant la vitesse de réaction, l'efficacité ou les propriétés de cohérence parfois observées.

Cette nouvelle famille de photo-commutateurs basés sur la structure NAIP apparait donc comme un excellent modèle pour étudier précisément le déroulement de réactions d'isomérisation cohérentes, et donc de changements structurels moléculaires, en combinant à la fois des études théoriques et expérimentales. Comme leurs structures sont facilement modifiables, des substitutions influençant la vitesse d'isomérisation et la fréquence du mode de torsion ont pu être observées expérimentalement. Néanmoins, le rendement réactionnel maximum est de 0.25-0.3, significativement plus faible que celui de la rhodopsine (0.67). Des paramètres intra-moléculaires, contrôlant la vitesse d'isomérisation, semblent être inclus dans la structure NAIP et presque insensibles à l'environnement, ce qui peut être une très bonne propriété pour les applications futures de ces composés. Mais d'autres paramètres de l'environnement semblent être capables d'influencer le rendement d'isomérisation, et manquent encore dans la structure NAIP. Si la vitesse peut se révéler être une condition nécessaire pour de bons rendements quantiques, ce travail montre qu'elle n'apparaît cependant pas être suffisante.

D'autres études expérimentales se présentent désormais pour continuer ce travail et mieux comprendre la photo-physique de la famille NAIP. Tout d'abord, des expériences de contrôle cohérent, basées sur la même technique de spectroscopie d'absorption en incluant des techniques de mise en forme d'impulsions sur le faisceau pompe, peuvent être une direction intéressante, visant à contrôler les propriétés cohérentes[9] ou à améliorer le rendement de la réaction[10]. Lorsque des solutions d'énantiomères pures des formes chirales de molécules NAIP seront disponibles, nous pensons à réaliser des mesures de dichroïsme circulaire résolues en temps, pour étudier l'éventuelle uni-directionalité de la rotation. De plus, nous pensons également à une expérience à trois impulsions, comprenant une impulsion excitatrice à 400 nm, une impulsion sonde (continuum de lumière blanche UV-Vis), et une troisième impulsion infrarouge, non-résonnante avec une transition, qui serait envoyée durant la période du passage au travers de l'intersection conique identifiée grâce à ce travail (entre 230 et 380 fs pour ZW-NAIP par exemple). Cette impulsion courte et de forte intensité pourrait modifier localement la surface d'énergie potentielle et ainsi influer sur le résultat de la réaction[11].

La collaboration entre la théorie (Pisa), la synthèse (Ferrara, Perugia) et la spectroscopie expérimentale (Strasbourg, Lausanne, Zurich) a bien fonctionné et ouvre de nouvelles directions de recherche ou d'application. En effet, les chimistes essaient actuellement d'incorporer les commutateurs NAIP dans des peptides, également de créer une molécule qui s'auto-assemble, et enfin synthétisent une version chirale de la structure. Les théoriciens calculent en ce moment les chemins réactionnels des molécules restantes (NAIP et MeO-NABFP), développent aussi un modèle simplifié de la structure NAIP pour diminuer le temps des calculs, et enfin pensent à inclure un troisième mode pour décrire plus précisément les surfaces d'énergie potentielle.

De plus, les résultats apportés par ce travail et d'autres techniques de spectroscopie (fluorescence femtoseconde et spectroscopie dans l'IR-moyen) nous font penser que ces photo-commutateurs peuvent devenir un nouveau système modèle pour l'étude conjointe à la fois théorique et expérimentale des réactions d'isomérisation en régime cohérent, de la dynamique de paquet d'ondes lors de ce type de réaction, et aussi en particulier de la dynamique moléculaire au voisinage des intersections coniques. Cela pourrait donner de nouvelles indications pour la compréhension des paramètres les gouvernant ainsi que sur les effets de cohérence. De plus, certaines fonctionnalisations de ces photo-commutateurs comme le déclenchement de fonctions biologiques par contraintes stériques (repliement d'une protéine par l'isomérisation du commutateur par exemple) ou électrostatique (une des molécules possède un moment dipolaire permanent sur la partie rotative) sont en cours de développement afin d'apporter des retombées applicatives à ce projet.

Références :

1. Schoenlein, R. W.; Peteanu, L. A.; Mathies, R. A.; Shank, C. V., The first step in vision: femtosecond isomerization of rhodopsin. *Science* **1991,** 254, (5030), 412-415.

2. Dartnall, H. J. A., *Vision Res.* **1967,** 8, 339-358.

3. Lumento, F.; Zanirato, V.; Fusi, S.; Busi, E.; Latterini, L.; Elisei, F.; Sinicropi, A.; Andruniów, T.; Ferré, N.; Basosi, R.; Olivucci, M., Quantum Chemical Modeling and Preparation of a Biomimetic Photochemical Switch. *Angew. Chem. Int. Ed.* **2007,** 46, (3), 414-420.

4. Sinicropi, A.; Martin, E.; Ryazantsev, M.; Helbing, J.; Briand, J.; Sharma, D.; Léonard, J.; Haacke, S.; Cannizzo, A.; Chergui, M.; Zanirato, V.; Fusi, S.; Santoro, F.; Basosi, R.; Ferré, N.; Olivucci, M., An artificial molecular switch that mimics the visual pigment and completes its photocycle in picoseconds. *Proc. Nat. Acad. Sc. USA* **2008,** 105, (46), 17642-17647.

5. Melloni, A.; Paccani, R. R.; Donati, D.; Zanirato, V.; Sinicropi, A.; Parisi, M. L.; Martin, E.; Basosi, R.; Fusi, S.; Latterini, L.; Ferré, N.; Olivucci, M., Modeling, Preparation and Characterization of a Dipole Moment Switch Driven by Z/E Photoisomerization. *submitted* **2009**.

6. Briand, J.; Bräm, O.; Léonard, J.; Cannizo, A.; Zanirato, V.; Chergui, M.; Olivucci, M.; Haacke, S., Coherent Ultrafast Torsional Motion and Isomerisation of a Biomimetic Dipolar Photoswitch. *Submitted* **2009**.

7. Briand, J.; Helbing, J.; Cannizzo, A.; Chergui, M.; Zanirato, V.; Haacke, S.; Olivucci, M., Ultrafast Isomerization Dynamics of Biomimetic Photoswitches. *Proceedings of the XVIth international conference on Ultrafast Phenomena (UP), Springer Series in Chemical Physics* **2009**.

8. Briand, J.; Léonard, J.; Olivucci, M.; Haacke, S., Manuscript in preparation. **2009**.

9. Branderhorst, M. P. A.; Londero, P.; Wasylczyk, P.; Brif, C.; Kosut, R. L.; Rabitz, H.; Walmsley, I. A., Coherent Control of Decoherence. *Science* **2008,** 320, (5876), 638-643.

10. Prokhorenko, V. I.; Nagy, A. M.; Waschuk, S. A.; Brown, L. S.; Birge, R. R.; Miller, R. J. D., Coherent Control of Retinal Isomerization in Bacteriorhodopsin. *Science* **2006,** 313, (5791), 1257-1261.

11. Sussman, B. J.; Townsend, D.; Ivanov, M. Y.; Stolow, A., Dynamic Stark Control of Photochemical Processes. *Science* **2006,** 314, (5797), 278-281.

Contents

General Introduction

Several systems found in nature can capture light energy and utilize it as a source to drive their biological functions. The absorption of a photon by a chromophore, an efficient light-absorbing molecule, initiates the process. It promotes the chromophore into an excited state, from where a reaction can start. Excited-state reactions, converting photon energy into motion and chemical energy, are the initiators of important biological processes such as photosynthesis, phototaxis or vision.

They often involve ultrafast time scales, in the femtosecond to picosecond domain, and a structural change of the chromophore, such as isomerization (change of conformation), which is an elementary reaction of general importance, involved for instance in the first step of vision in rhodopsin. This opto-mechanical energy conversion is at the origin of the concept of molecular photoswitches. Upon absorption of a photon, the retinal chromophore, in the membrane protein rhodopsin located in the rods in the eye retina, isomerizes with record speed and efficiency. Thanks to this prior structural change, its photochemistry is efficiently triggered, ultimately leading to a nerve impulse. It is also the only example of coherent isomerization in solution. Indeed, when excited with an ultrashort laser pulse, a wave packet is created in the excited state and persists into the photoproduct.

Interestingly, the retinal chromophore looses his outstanding speed and efficiency properties when taken outside of rhodopsin, thus highlighting the optimization role played by the protein environment on the photo-reaction. Thus, the use of other molecular switches, such as azobenzene or stilbene, has widely spread for studies and applications requiring photo-controlled, large amplitude motions.

In this context, a new family of photoswitches based on the N-alkylated indanylidene-pyrroline (NAIP) framework, expected to mimick the isomerization of retinal in rhodopsin, has been recently computer-designed and synthesized by Massimo Olivucci and coworkers[1, 2]. The results of their theoretical investigations have raised great expectations for possible ultrafast (sub-picosecond) and efficient isomerization of these chromophores in solution. The aims of their work consist of a deeper investigation of the fundamental parameters controlling isomerization reactions, and also of possible applicative use of the new molecular switch.

This Ph.D work reports the first results obtained by an experimental investigation of the ultrafast isomerization of the NAIP molecule family. First, a measurement tool had to be built to study processes occurring on the femtosecond (1 fs = 10^{-15} s) time scale, the one of molecular motions. The experimental setup is based on the transient absorption spectroscopy technique. With suitable time resolution and a broadband spectral coverage, it allows to follow in time the evolution of such reactions. Several variants of the NAIP switches were studied by this technique, revealing their ultrafast dynamics. Investigation of the possible bi-directional isomerization and the influence of the solvent environment were also carried out, in order to further investigate the switching properties of these molecules.

In an introductory section, the basics of the isomerization reaction, the energy levels and transitions involved are presented (Chapter 1). The ultrafast and efficient isomerizations of the retinal-containing membrane protein family are introduced as reference examples, together with the important results from the literature about their spectroscopy. The theoretical and computational modelling of such reactions is also briefly introduced. Finally, specific coherent, wave packet-like signatures, sometimes observed with ultrafast spectroscopy, are presented and illustrated.

Chapter 2 introduces the experimental techniques required, such as femtosecond lasers and non-linear processes. The setup and its characteristics are presented in details, together with the data that are acquired and the information that they contain. In particular, the data include signals which are not related to the dynamics of the molecular system under study (solvent signal for instance) and which can be corrected for. The data processings are detailed as they are important in the analysis and discussions of the next chapters. Finally, data analysis and fitting are briefly introduced.

The NAIP photoswitch properties are then detailed in Chapter 3. Its structure, computational modelling and theoretical calculations are introduced. The different NAIP variants studied in this work and their steady-state properties are finally presented.

Chapter 4 gathers the results obtained by transient absorption spectroscopy on five NAIP-based molecules. Four of these structures show a common coherent isomerization scenario and are compared. The coherent, wave packet-like signatures observed are giving a precise clocking of the reaction evolution, i.e. the molecular motion involved. A specific fitting function is introduced in order to quantitatively describe the data. The last molecule, featuring a specific substitution, shows a slower and quasi-incoherent reaction, and is analyzed separately. Interpretations and discussions on the isomerization scenarios and substitution effects are proposed, and the biomimetic aspect of the NAIP switches is also put into perspectives.

Chapter 5 presents a study of the forward and backward photo-isomerization reactions. Both the time scale and the quantum yield of the reverse reaction are important questions to be answered.

Finally, the possible effects of environmental parameters, studied by varying the solvent properties, are investigated (Chapter 6). This is also an interesting point to be studied as large amplitude torsional motions are involved.

Chapter 1

Introduction to ultrafast photo-isomerization

This chapter begins with an introduction to the processes, the electronic transitions involved and the mechanism of photo-induced isomerization. It is followed by a description of experimental observations on a particular family of biological photo-switches, the retinal-containing protein family, and their isomerization reaction modelling is also presented. Finally, the concepts of wave packet and vibrational coherence are explained. Examples of their experimental observations are given to highlight the possibility they offer to follow, with a good temporal accuracy, structural changes at a molecular scale.

A. Introduction

1. Spectroscopy of molecules in the condensed phase

Upon absorption of a photon, a molecule may be promoted into its first excited state S_1. From this state, various intra-molecular processes may occur which are represented in figure 1.1. Fluorescence is the radiative process occurring between the first excited state S_1 and the ground state S_0. When it is measured with time resolution, the lifetime of the excited-state becomes accessible. When no other decay channel is possible, the excited-state lifetime (radiative lifetime) is typically in the nanosecond time range. However, non-radiative energy relaxation processes may also occur, and compete with radiative channels. The former may proceed on a much shorter time scale. They are responsible for ultrafast energy relaxation or S_1 quenching. Intra-molecular non-radiative processes are vibrational relaxation and internal conversion (IC). Isomerization reactions correspond to the second type of process.

After excitation, the system is out of equilibrium in the excited state, and evolves back to, or towards a new, equilibrium ground state. The excited-state evolutions that we will consider along this Chapter, and study in the rest of the thesis, are occurring on a sub-picosecond to picosecond time scale.

Indeed, they can be followed thanks to the radiative fluorescence signal for example, or through stimulated signals, that are presented in figure 1.1 (green arrows). Specific techniques (transient absorption spectroscopy, see Chapter 2) are capable of accessing, and spectro-temporally resolve, transitions such as excited-state absorption (ESA) and stimulated emission (SE), characterizing, like time-resolved fluorescence, the excited-state evolution. Similarly, ground state bleach* (GSB) or photoproduct absorption (PA) characterize the dynamics in the electronic ground state. For instance, vibrationally-excited population in the ground state is one aspect of the dynamics which can be investigated. Indeed, the corresponding spectrum is close to that of the vibrationally relaxed (equilibrium) spectrum, except it is spectrally larger due to the excess energy that could not be dissipated before.

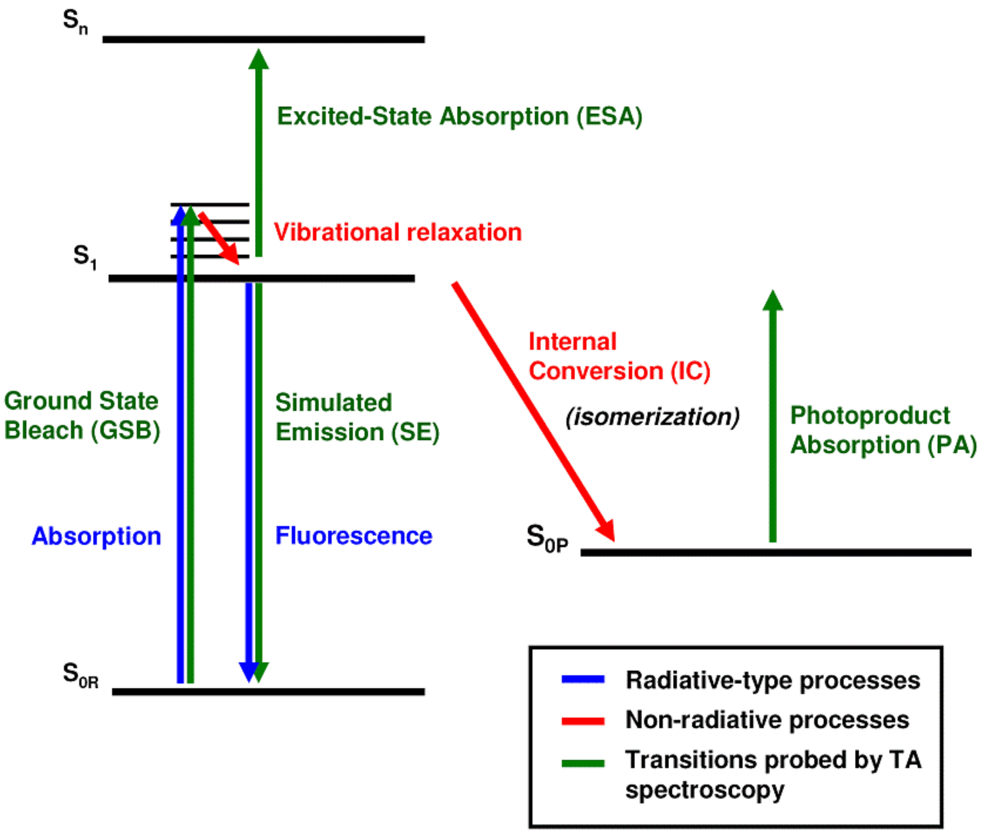

Figure 1.1. Schematic illustration of intra-molecular energy relaxation processes initiated by light absorption. The radiative-type processes (absorption, fluorescence) are represented by blue arrows, and non-radiative ones (vibrational relaxation and internal conversion) by red arrows. In this simplified Jablonski diagram (intersystem crossing and triplet states have not been considered), the vertical axis correspond to energy, while the horizontal one has no physical meaning. S_{0R} and S_{0P} designates the reactant and photoproduct ground states, respectively, while S_1 and S_n correspond to the first and the n^{-th} excited states. The green arrows correspond to the transitions that can be probed by absorption spectroscopy (see Chapter 2).

Analysing these signals can lead to the precise timing of the process involved, such as an internal conversion as presented below. In this case, only intra-molecular processes were considered, but inter-molecular processes, such as energy or charge transfers, and heat dissipation to the surrounding (e.g. solvent molecules or a protein) can also come into play.

---

* The ground state bleach transition designates the loss of electrons in the ground state of the system because they have been promoted into the excited state by the excitation.

2. Photo-isomerization

The conformational change of a molecular structure from one isomer configuration into another is a chemical process which can be initiated by light (absorption of a photon). The photo-induced rotation about a C=C bond, referred to as photo-isomerization, is a simple mechanism to convert light into mechanical motion on a molecular scale. It is also involved in many photo-biological systems, often triggering a biological function, the most famous example probably being the retinal isomerization in rhodopsin, the first step in vision[3].

The molecule involved in a photo-isomerization is a chromophore, usually named a photoswitch. The molecular isomers are referred to as *cis* and *trans* (or *Z* and *E*) isomers, according to their isomerical structures.

An example of such a photo-chemical reaction is the *trans* → *cis* photoisomerization of stilbene. As shown in figure 1.2, the stilbene molecule, initially being in a *trans* configuration, and upon absorption of a photon of appropriate energy, is photo-converted into the *cis* form, the process being reversible.

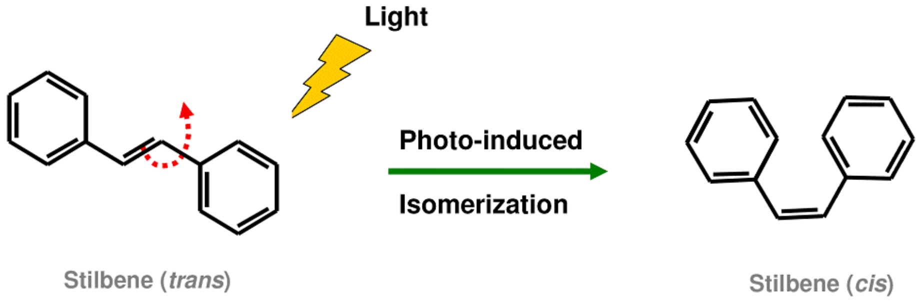

Figure 1.2. Principle of photo-isomerization. A molecule (here stilbene), is in a given structural conformation (*trans* in the present case). Upon light irradiation, it absorbs a photon and undergoes a large structural change towards another isomerical structure (*cis*).

The photo-physics of ultrafast isomerization reactions can be explained by the non-radiative processes that have been introduced above. Thus mainly vibrational relaxation, internal conversion and energy redistribution to the surrounding environment are concerned.

Photo-isomerization reactions are currently described by two (ground- and excited-state) electronic potential energy surfaces (PES, see § 1.B.3), both joining in a region called the conical intersection (CI). The PESs are describing the electronic states energies as a function of reaction coordinates, being molecular vibrational modes in the case considered here. This differs from the representation of figure 1.1, where no reaction coordinates were coupled to the electronic states. The torsional coordinate around a C=C bond is always included in these descriptions as the motion of interest is a rotation. The reaction path followed by the excited-state population then defines the reaction scenario. Indeed, according to the Franck-Condon principle, light absorption may be described by a “vertical” arrow, indicating that the transition between two electronic states is always much faster than nuclear motions. Consequently, immediately after (brief) excitation, the geometry of the system is identical to that just before excitation. But the molecular motions are suddenly governed by a new potential energy surface (the one of the first excited-state), and the geometry of the system starts evolving. Ultrafast spectroscopy allows an experimental tracking of the reaction path and isomerization timing, using the signals presented above.

When the isomerization has been initiated, the excited-state population then follows the reaction path, which is either leading back to the reactant isomer or to the formation of the photoproduct isomer. As these two usually have separate absorptions, they can be spectrally distinguished, and the amount of new isomers formed compared to that of starting reactant isomers defines the isomerization reaction quantum yield.

In the next section, examples of ultrafast and efficient photo-isomerizations, taken from the retinal protein family, are presented. The photo-physics of their reactions, derived from ultrafast spectroscopy measurements, is also detailed.

B. The retinal-containing protein family

The retinal protein family constitutes the best-known example of systems in which ultrafast light-induced conformational changes take place[4, 5]. Two reference bacterial and animal retinal proteins are rhodopsin, the photo-sensitive protein in vision, and bacteriorhodopsin, a protein which uses light to generate a proton gradient, thus driving photosynthesis in *Halobacteria*. In both cases, the primary process is the isomerization of a retinal chromophore bound to the protein.

1. Bacteriorhodopsin

a. Role, structure and photocycle of bacteriorhodopsin (bR)

Photosynthetic activity in halobacteria (*Halobacterium salinarum*), a biological energy-conversion device, is based on the membrane protein bacteriorhodopsin (bR), which acts as a light-driven proton pump[5]. The retinal-protein bR consists of a retinal chromophore embedded into 7 α-helices made of 248 amino acids. The retinal molecule is covalently bound to the lysine Lys216 amino acid of one α-helix *via* the protonated Schiff base[6-8]. In the light-adapted ground state of bR, the retinal chromophore is in the *all-trans* configuration.

Upon absorption of a photon, it undergoes a photocycle, during which a proton is pumped across the membrane, converting photo-energy into an electrochemical gradient, used for ATP synthesis. This photocycle, spanning time scales for fs/ps to ms, can be followed by analysing the dynamics of the spectrally-shifted photocycle intermediates[9]. Its photocycle overview is depicted in figure 1.3.A.

The process triggering this photocycle is the *all-trans* → *13-cis* isomerization of the retinal chromophore (see figure 1.3.B). This primary step is a very efficient (~0.6 reaction quantum yield[10]) and ultrafast (500-fs photoproduct formation time[11, 12]) isomerization reaction.

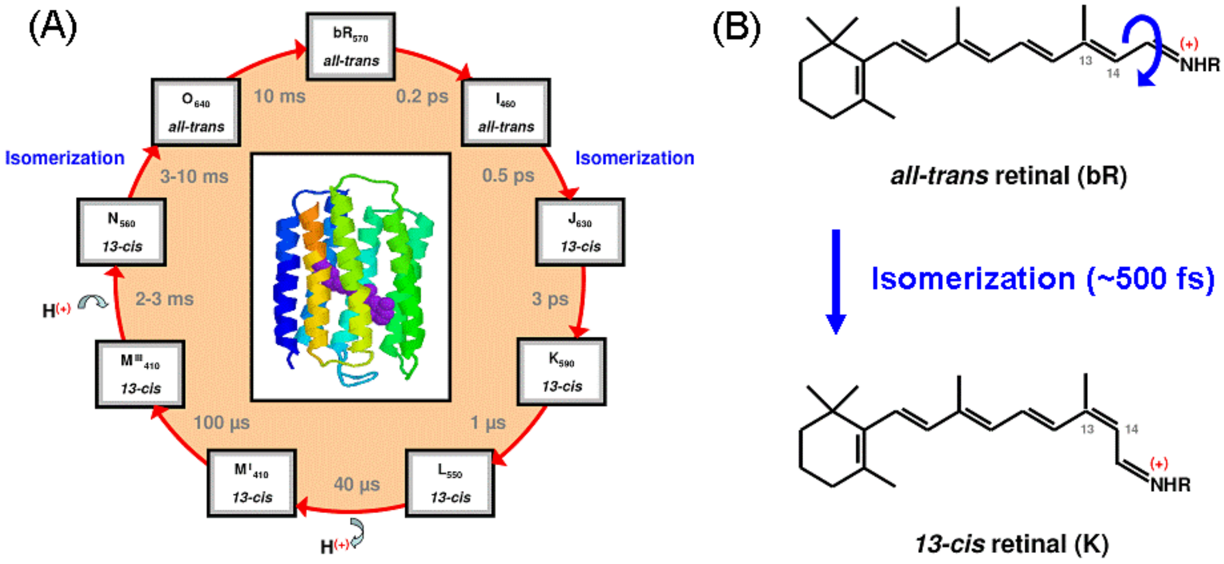

Figure 1.3. **A**. bR's photocycle. The different intermediates names, corresponding time scales and absorption maxima from the literature are indicated, as well as the retinal conformation. The simplified structure is of bacteriorhodopsin is indicated (inset, retinal in purple). **B**. *All-trans* → *13-cis* isomerization scheme of retinal, initiating the bR photocycle.

b. Ultrafast isomerization revealed by femtosecond spectroscopy

Several groups[11-14] have shown, using ultrafast (fs/ps) transient absorption spectroscopy, that the ground state photo-isomerized product (called J_{630} and hereafter photoproduct) is formed in ~500 fs (concerning the debate on J_{630} being a ground or excited state intermediate see reference[15]), relaxing into a second intermediate (K_{590}) on a 3-ps timescale[*]. They also found indications of a 150 to 200-fs evolution on the excited-state potential energy surface (PES), assigned to vibrational relaxation in that particular state.

The various numbers of studies performed on bacteriorhodopsin fluorescence or stimulated emission all agree on the fact that the fluorescence decay is not mono-exponential[16-19]. In the recent high-quality results obtained by Schmidt et al.[20], dominating time constants of 0.15 and 0.45 ps were found, respectively assigned to vibrational relaxation in the excited-state and internal conversion *via* isomerization.

Figure 1.4 shows a summary of the previous results in a schematic picture, which was first introduced in the 80's[11, 12]. The potential energy profiles of the ground (S_0) and first excited (S_1) states are

---

[*] See also Chapter 2, where data on bR measured with our setup are briefly introduced together with transient absorption spectroscopy.

represented as a function of the most reaction-connected coordinate, which was identified to be the torsional mode[11-13, 21, 22]. As explained in § 1.B.3, recent experiments and theoretical modelling have revised this model and improved it, considering a second reaction coordinate (stretching), as indicated in the figure (see § 1.B.3 for details).

As shown in figure 1.4, bacteriorhodopsin (bR_{570}, S_0) is promoted with light excitation into its first excited state S_1. The population then moves on the excited-state potential energy surface (PES) along stretching coordinates on a ~150-fs time scale. Then it continues to evolve on the PES along the torsion coordinate, going through a spectroscopically-dark region where excited and ground states potentials cross each other. 40% of the population goes back to the bR_{570} reactant state, while 60% forms the photoproduct precursor on a 500-fs timescale (J_{630}). Then ground state vibrational cooling occurs with a ~3-ps time constant leading to the K_{590} intermediate.

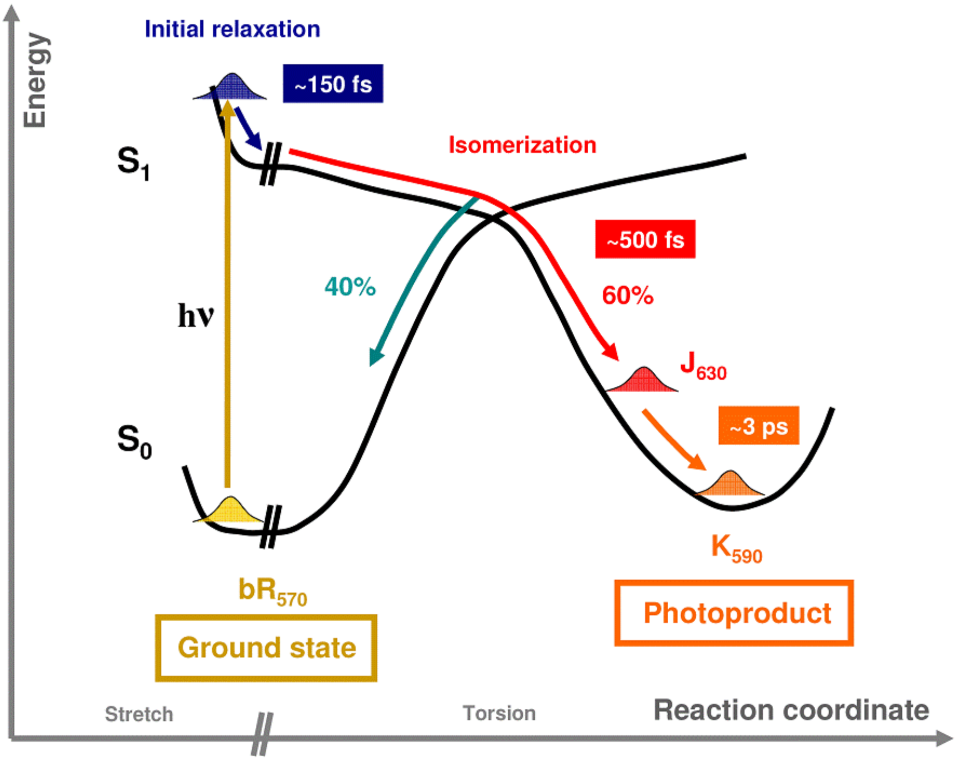

Figure 1.4. Simplified model summarizing the bR dynamics. See text for details.

2. The visual pigment rhodopsin

a. Photochemistry of rhodopsin

Rhodopsin is a pigment protein spanning the membrane of rod cells. It is the photoreceptor in almost all known visual systems[3]. It is constituted of a retinal chromophore embedded in 7 α-helices made of 348 (in bovine rhodopsin) amino acids (see inset of fig. 1.5.A). The retinal molecule is covalently linked to one of the helices to the amino acid Lys296 *via* the protonated Schiff base[23].

The rhodopsin photochemistry, mediating the light transduction and ultimately leading to a nerve impulse, is also initiated by the absorption of a photon by the retinal chromophore[3-5, 24-26]. The primary process is a *cis* → *trans* isomerization of the retinal, again followed by the appearance of different reaction intermediates (see fig. 1.5.A).

The selective *11-cis* → *all-trans* isomerization of retinal in rhodopsin occurs around the $C_{11}=C_{12}$ double bond, and is achieved with the record value of ~200 fs[3, 21, 27] (see fig. 1.5.B). It is the most efficient isomerization known, with a reaction quantum yield of ~0.67[28].

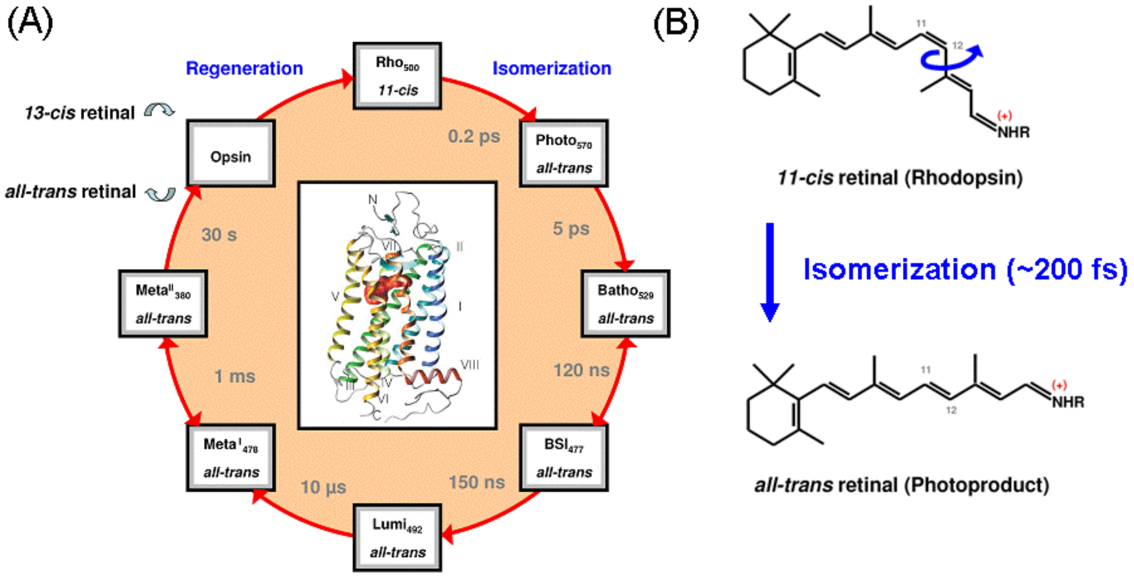

Figure 1.5. **A**. Rhodopsin's photochemistry. The different intermediates names, their corresponding time scales and absorption maxima are indicated, as well as the retinal conformation for each intermediate. The simplified structure is of rhodopsin (inset, retinal in red) is taken from reference[29]. **B**. *11-cis* → *all-trans* isomerization of retinal initiating the rhodopsin photochemistry.

b. Ultrafast and coherent isomerization of rhodopsin

The first measurement of the isomerization reaction speed of rhodopsin was brought by Schoenlein and coworkers[27] who performed a femtosecond transient absorption measurement (see Chapter 2) in the visible spectral range. Thanks to their high time resolution, they could follow the evolution of the early dynamics of rhodopsin, reporting that the photoproduct formation is completed on a ~200-fs time scale (Rho_{500} → $Photo_{570}$, see figure 1.5.A) and followed by vibrational relaxation/cooling in the photoproduct on a ~5-ps time scale ($Photo_{570}$ → $Batho_{529}$).

These results were confirmed and deeper investigated by the same research team[30, 31] and others[32]. In particular, they could better resolve strong oscillatory features suggested by the previous experiment[27], thus confirming that rhodopsin isomerization reaction occur on a regime of vibrational coherence (see § 1.C).

Femtosecond fluorescence up-conversion experiments were performed on rhodopsin[33, 34], finding that its fluorescence is mainly composed of an ultrafast (0.12-0.33 ps) and dominant (~70%) component, and of a slower one (1-2 ps, ~30%). The first decay was suggested to be responsible for the photoproduct formation while the second one was assigned to the unreactive part of the rhodopsin photoreaction (0.33). As no rise time or Stokes shift was found in these fluorescence experiments (210-fs time resolution), it was suggested, combining transient absorption and fluorescence results, that the motion on the S_1 excited state potential energy surface is faster than ~0.1 ps.

Figure 1.6 presents a summary of these results in a simplified picture. The potential energy profiles of the ground (S_0) and first excited (S_1) states are schematically represented, like for bR, as a function of two reaction coordinates (stretching and torsion[3, 5, 21, 27, 35], see § 1.B.3 for details). The scenario depicted in figure 1.6 can be summarized as follows. Rhodopsin (Rho_{500}, S_0) is promoted with light excitation into its first excited state S_1 (Rho*). Then the created wavepacket moves on the excited-state potential energy surface (PES, see part 2-c below) along the torsion coordinate on a sub-100-fs time scale. 30% of the population goes back to the Rho_{500} reactant state, while 70% forms the photoproduct on a 200-fs timescale. This formation is followed by damped oscillations (see dashed red line in fig.1.6), initiated by the wave packet created in the excited state and which has survived into the photoproduct state (see § 1.C for details). Then vibrational cooling occurs with a ~5-ps time constant.

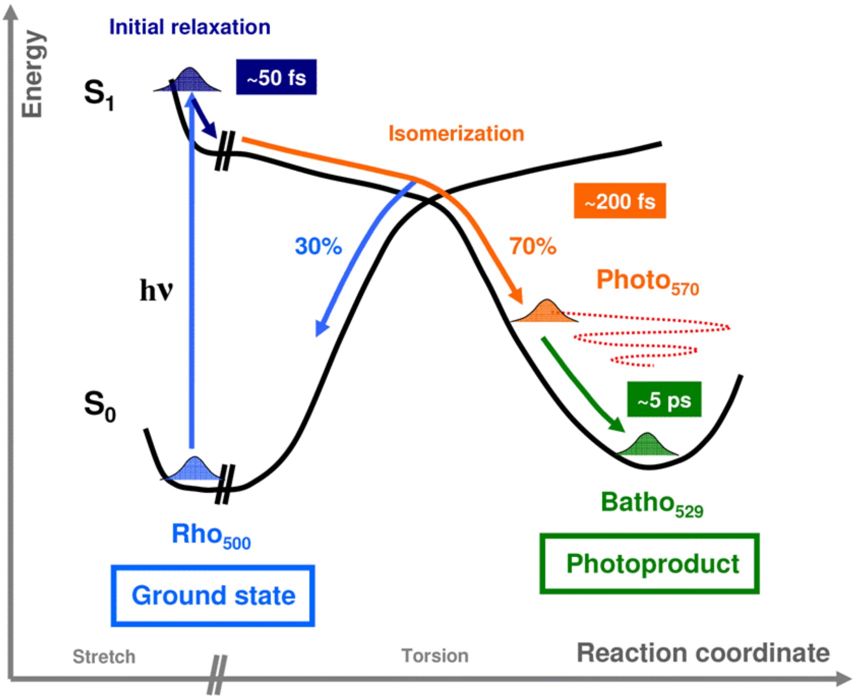

Figure 1.6. Schematic picture of rhodopsin's isomerization dynamics. See text for details.

.

Other bacterial rhodopsins (halorhodopsin[5, 36, 37], proteorhodopsin[38-40], or sensory rhodopsins[41]) and rhodopsin analogues (isorhodopsin[42], 13-demethylrhodopsin[43]) have been studied by the same spectroscopy techniques. They all show similar protein structures, the same photo-physics and isomerization scenario, leading to efficient photoproduct formation on a sub-ps time scale. The reported values are gathered in table 1.1 and compared to rhodopsin and bR.

Protein	τ_{iso}	Φ_{iso}	coherence
Rhodopsin	**200 fs**	**0.67**	**+**
Isorhodopsin	**400 fs**	**0.47**	**-**
13-demethylrhodopsin	**600 fs**	**0.22**	**-**
Bacteriorhodopsin	**500 fs**	**0.6**	**-**
Sensory rhodopsin I	**~400 fs**	**~0.6**	**-**
Proteorhodopsin	**~300 fs**	**~0.5**	**-**
Halorhodopsin	**1 ps**	**0.3**	**-**

Table 1.1. Summary of isomerization times, quantum yields and observation of coherence in the photoproduct state for rhodopsin and analogues (blue) and bacterial rhodopsins (green).

Several observations can be made by comparing these retinal proteins. First, they are all improving the retinal isomerization speed and efficiency compared to when the latter is in solution[44], highlighting the major role played by the protein scaffold. Moreover, the general trend is that the fastest reactions ensure the highest quantum yields, suggesting that isomerization speed and quantum efficiency are closely linked. Finally, isomerization in a regime of vibrational coherence, persisting into the photoproduct state (see § 1.C), is only occurring in rhodopsin, where the extreme speed may play a role as well.

3. Modelling of ultrafast isomerization of rhodopsins

A simple 2-state model with a unique reaction coordinate was suggested already in the mid-1980s'[11, 12, 27] to interpret the results for both photo-isomerizations presented before, restricting the description exclusively to the torsional coordinate.

According to this model, after optical excitation, the excited-state population, located in the Franck-Condon (FC) region, is on a repulsive part of the S_1 potential. Population motion/evolution occurs along this torsional coordinate to an avoided-crossing region between ground and excited-state electronic potentials. From this position, the population falls down into the ground state *via* radiationless $S_1 \rightarrow S_0$ internal conversion. The speed of the ground-state photoproduct formation is determined by the speed of motion along the reaction coordinate, the torsional mode. The photoproduct formation proceeds on the same time scale (~200 fs for rhodopsin) as the torsional motion involved in the isomerization process. Only half a torsional vibration time is needed to form the photoproduct, suggesting a reaction at the maximum speed limit and a ballistic reaction scenario. This hypothesis was strongly supported by the observation of vibrational coherences in the photoproduct of rhodopsin[27, 30, 31].

But more detailed measurements and deeper analysis[15, 17, 18, 45] led to the inconsistency of part of this model. It was first suggested to include a third state into play (the so-called 3-state model[15, 17]), but further experiments[46-48] and *ab initio* calculations on both rhodopsin and bR protonated Schiff base chromophores[35, 49-52] lead to another and now commonly accepted description, the 2-mode/2-state model.

The C=C bond, around which the isomerization takes place, initially has a double bond character. However, the torsion occurs around a single bond. By a concerted vibrational single-bond compression and double-bond stretching (referred to as skeletal stretching), the characters of single and double bonds are inverted and the rotation around the C=C bond becomes possible. It thus led to a more complete modelling of the reaction, now involving two modes.

The excited-state (ES) properties of chemically different chromophores embedded in diverse protein environments or in solution can be accurately evaluated by means of hybrid quantum mechanics/molecular mechanics (QM/MM) computational strategy based on multiconfigurational perturbation theory and complete-active-space-self-consistent-field geometry optimization[53] (see Chapter 3 for details on QM/MM strategy). *Ab initio* multi-configurational second-order perturbation theory was used to establish the photoisomerization path model of retinal chromophores[35] (rhodopsin and bR). It is indeed a suitable approach in photochemistry and photobiology to compute photochemical reaction paths. Once a molecule is excited, it starts to evolve on the potential energy surface (PES), reaches a point of conical intersection[54, 55] (CI) and decays (see fig. 1.7). The CIs provide key mechanistic entities for the description of photochemical reactions and they correspond to theoretical molecular structures only living for a few femtoseconds and located at a ~90° bond twist angle, where excited- and ground-state PES energy difference is minimum. They play a fundamental role in the understanding of reactive processes involving at least two potential energy surfaces (PES), and thus in the description of photochemical events, as they correspond to photochemical funnels for an efficient decay to the ground state. One of the best examples of a photochemical process where a CI plays a key role is the rhodopsin protein. The PES topologies around the CI location may have a fundamental influence on the *cis*/*trans* branching, and thus one the reaction quantum yield, but are unfortunately not accessible by spectroscopy.

Excited-state reaction can be described by computing a minimum energy path (MEP) starting at the Franck Condon (FC) point and ending at the CI. In particular, calculations[35, 50] showed that the initial (sub-50 fs) excited-state motion is dominated by C=C stretching modes (compression and elongation), followed by torsion motion around the C_{11}=C_{12} (or C_{13}=C_{14} for bR), leading to isomerization. Calculations also brought arguments against the 3-state model, as the S_1 and S_2 PESs are calculated to be well-separated, and thus no avoided crossing between them is observed.

This results in a reaction scenario shown in figures 1.7.A and B. The rapid C=C stretching relaxation from the Franck-Condon (FC) geometry on the S_1 PES leads to an almost flat region of the surface, referred to as the stationary point (SP), from which the conical intersection (CI) is reached *via* C=C bond torsion, and from where decay to the ground state occur.

Moreover, recent quantum chemistry calculations on rhodopsin[56] (wave packet propagation on PES methods, see Chapter 3 also) showed that, after an initial ~60 fs stretching motion, the CI is reached in ~110 fs in rhodopsin *via* a bicycle-pedal[21] motion scheme, described by two concerted torsions, resulting in an approximately volume-conserving structural change.

This 2-mode/2state isomerization model presented for rhodopsin can be transposed and applied to the other ultrafast photo-isomerization reactions, and in particular to the other retinal proteins presented above.

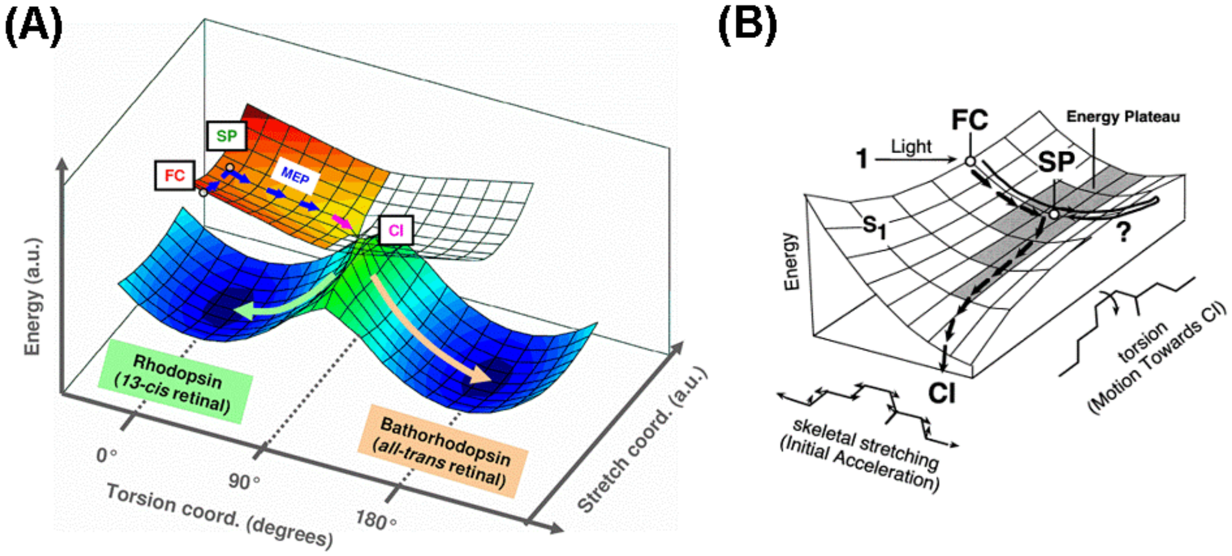

Figure 1.7. **A**. Isomerization reaction model. Light excitation promotes the molecule in the Franck-Condon region (FC), where ultrafast skeletal stretching takes place, leading to a stationary point (SP), followed by evolution along the torsional coordinate towards the conical intersection (CI). The minimum energy path (MEP) of the reaction is indicated. **B**. Zoom into the excited-state PES showing evolution according to the 2-mode model. Picture from Cembran et al.[52].

C. Coherences in isomerization reactions

1. Wave packet theoretical description

The use of coherent laser light can modulate the amplitudes and phases of wave functions $\psi_n(r,t)$. Figure 1.8 shows a schematic representation of a diatomic molecule, which is electronically-excited with an ultrashort laser pulse. If the pulse bandwidth is broad enough, i.e. if the pulse duration is short compared to the vibrational period of the molecule, the pulse can spectrally cover, and thus coherently excite, multiple vibrational eigenstates. The latter superimpose to create a coherent superposition of eigenstates wave functions, which can be written as:

$$\psi(r,t) = \sum_n c_n \psi_n(r) e^{-i(\omega_n t - \varphi_n)} \qquad (1.1),$$

where $\psi_n(r)$ and ω_n are the eigenfunctions and transition frequency of the n^{th} vibrational level, c_n and φ_n represent the amplitude and phase of the latter, with r being a nuclear coordinate.

This superposition of eigenstates wave functions produces a spatially localized and moving coherent superposition state, which is referred to as a wave packet[57-59]. The interferences of the eigenstates wave functions, being alternatively constructive and destructive at a particular r value, are at the origin of the spatial localization. When created with appropriate initial conditions, the wave packet oscillates back and forth along the r reaction coordinate, with the period of the vibrational motion of the molecule. The wave packet is now analogous to a moving classical particle, but at atomic/molecular resolution.

The vibrational coherence refers to a collective behaviour among an ensemble of molecules, the vibrational levels being coherent because of specific phases and amplitude relations between them. It reflects the nonstationary wave packet dynamics of individual molecules, describing the nuclear motion. This can lead to a better understanding of a reaction, as the wave packet evolves from the initial state, through transition states, and towards final products.

Given the coherent properties of laser light, and the spectral bandwidth achievable with a femtosecond laser, it has become the ideal initiator for studying molecular wave packet motions.

The reported vibrational coherences measured during the dissociation of the ICN molecule[60] demonstrated the first experimental observation of wave packets in molecular systems. In addition, as the spreading of the wave packet was minimal up to a few ps, it established that the molecules ensemble coherence can be induced, even though the reaction starts with a random and noncoherent ensemble.

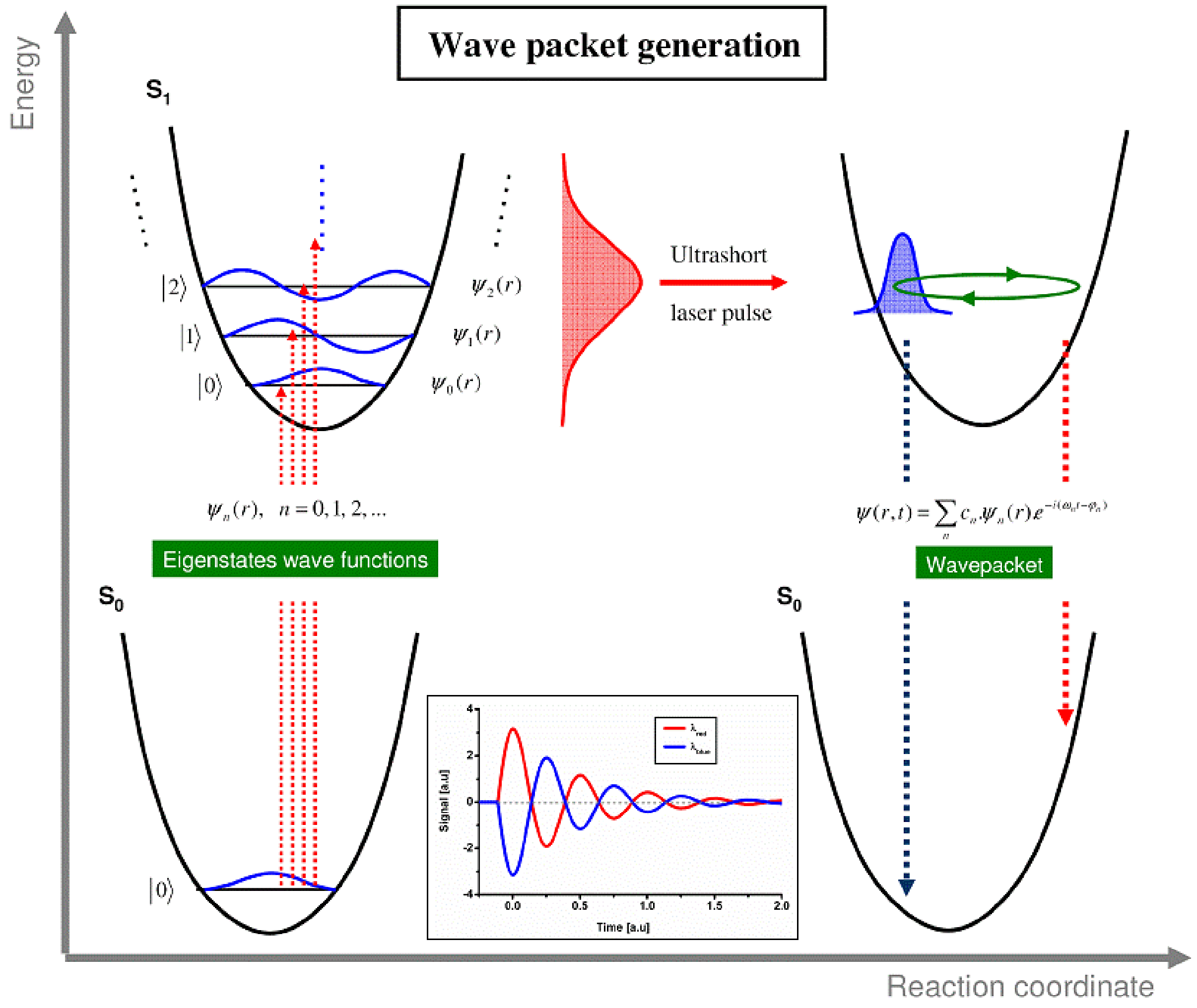

Figure 1.8. Wave packet generation principle. A laser pulse coherently excites multiple vibrational wave packets in a molecule. The superposed eigenstates wave functions interfere to create a spatially localized wave function, referred to as a wave packet. Anti-phased oscillatory features, reflecting wave packet evolution and motion back and forth on the PES, may appear in the signals (inset graph). Scheme adapted from references[4, 58].

In the stochastic regime, the created wave packet relaxes very rapidly to a quasi-static distribution, and subsequent kinetics can be described by rate equations (see Chapter 2). On the contrary, when non-stationary vibrational states are created by femtosecond pulses and vibrational coherence appears, oscillations modulating the underlying measured signal (see inset graph in fig.1.8) or dynamically-shifting bands may be observed. This coherent oscillations can result from three main processes[31, 61] which are briefly introduced in the next three sections using examples closely related to this thesis. The vibrational coherence can be produced in the excited state and modulate ES transition signals (§ 1.C.2). It can also persist along the reaction path and be observed in the photoproduct ground state (§ 1.C.3). Finally it may also be initiated by Resonant Impulsive Stimulated Raman Scattering (RISRS), which creates coherent vibrational motion on the reactant ground state potential energy surface (§ 1.C.4).

2. Observation of wave packets on excited-state PES

Wave packets dynamics can be observed in the excited state through excited-state absorption (ESA), stimulated emission (SE) or fluorescence signals. For example, ultrafast motion on the ES potential surface can be followed by a dynamic band shift of the ESA signal, either blue- or red-shifting as a function of time.

ESA blue-shifts have been suggested for rhodopsin[27, 30, 31] (~50 fs), 13-demethylrhodopsin[43], and is more clearly highlighted in isorhodopsin, where a ~100 fs delay was observed[42] between the most red-shifted and blue-shifted wavelengths containing the ESA signal (see fig. 1.9.A). This was attributed to the initially created wavepacket, leaving the Franck-Condon region in ~100 fs.

Excited-state (ES) low-frequency vibrations have also been reported in several molecules through their excited-state signals, revealing the torsion frequency of a particular bond in the ES [e.g. in stilbene ESA[62], bR and retinal SE[63, 64], in PYP SE[65] or in bacterial reaction centers[66, 67]). In particular Zgrablic et al.[68] reported weak modulations of the fluorescence up-converted signal of the protonated Schiff base of retinal diluted in various solvents. The oscillations are reflecting the creation and evolution of vibrational wavepackets along the torsional mode of the retinal. They yield, irrespectively of the solvent properties (dielectric constant or viscosity), a ~280-fs period (~120cm^{-1}) and a dephasing/decoherence decay time of 300 to 400 fs. The extracted oscillatory features are presented in figure 1.9.B.

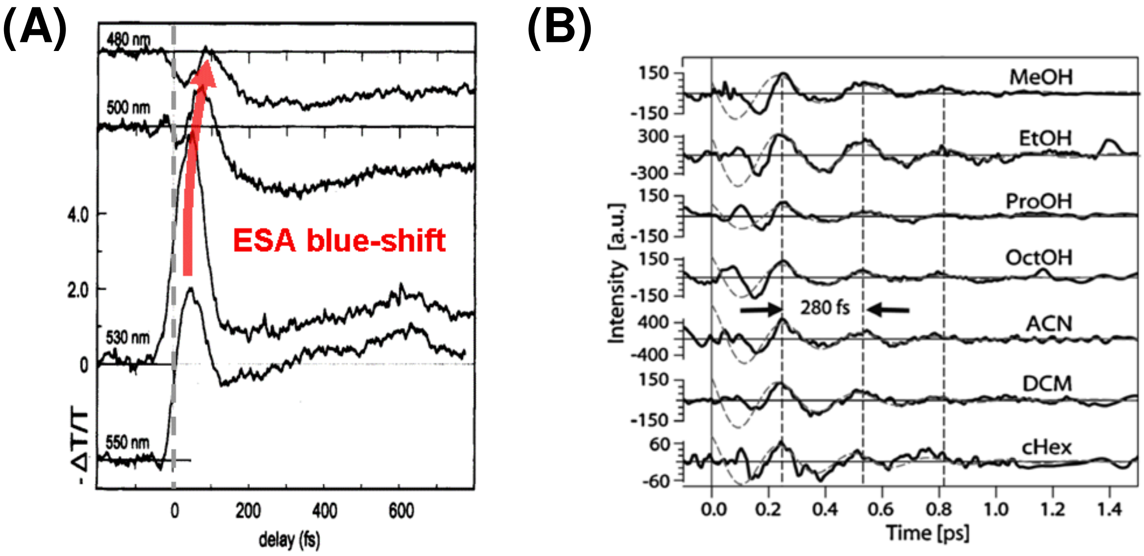

Figure 1.9. **A**. Isorhodopsin transients at 550, 530, 500 and 480 nm showing a blue-shift of the excited state absorption (ESA) on a 100-fs time scale. Picture taken and adapted from Schoenlein et al.[42]. **B**. Oscillatory residuals from exponential fits of fluorescence up-conversion measurements of the *all-trans* PSBR chromophore in various solvents. Picture taken from Zgrablic et al.[68].

3. Coherent isomerization of rhodopsin: wave packet oscillations in the photoproduct state

Low-frequency oscillations (550-fs period, ~60 cm^{-1}) were first observed in rhodopsin by the group of C.V. Shank[27, 30, 31], and were assigned to coherent oscillations in the photoproduct ground state, the wave packet being initially produced in the excited state and preserved through the coherent isomerization process. They were indeed showing larger amplitudes and a 180° phase reversal on both blue and red sides of the photoproduct absorption spectrum. Figure 1.10 displays transient absorption data measured on rhodopsin by Haran et al.[32] where these low-frequency (assigned to a torsional mode) oscillations are observed in the red side of the photoproduct absorption (see traces at 600 and 620 nm). The isomerization in a regime of vibrational coherence is probably achieved by a barrierless reaction from the Franck-Condon (FC) excited state to the primary product, and it has been emphasized that the ultrafast coherent process from the excited FC state will lead to the very efficient photoproduct formation. This remains the only example of coherent photo-isomerization of a molecule in solution.

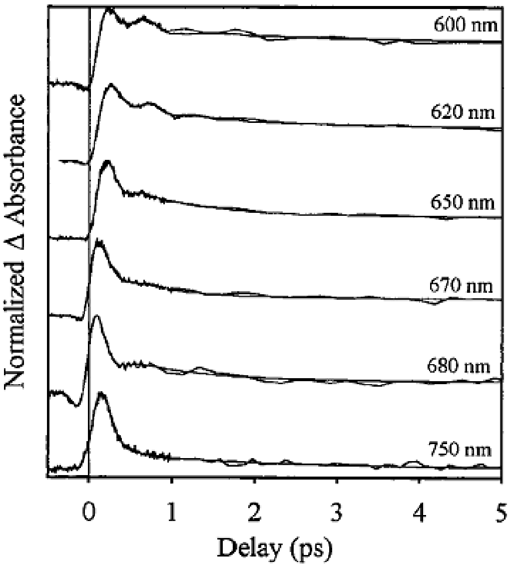

Figure 1.10. Rhodopsin selected kinetic traces from transient absorption measurements. Low frequency (~60 cm^{-1}) and rapidly damped oscillations in the photoproduct ground state can be distinguished. Picture taken from Haran et al.[32]

4. Vibrational ground-state coherences produced by RISRS

Ground state high-frequency oscillations, commonly believed to be produced by Resonant Impulsive Stimulated Raman Scattering (RISRS), have been observed in various samples (e.g. in bR[47, 64, 69] or light-harvesting (LH) antennas reaction centers[70]). RISRS is a process where the pump excitation impulsively populates Raman-active vibrational modes in the ground state, provided its pulse duration is appropriate[71, 72]. Indeed, the amplitude of oscillations, observed in the probe signals, depends on the short stay of the wave packet onto the excited-state PES, and thus too short or too long pulses, compared to a considered vibrational period, would lead to an inefficient process.

For retinal proteins and similar isomerizing molecules, Raman-active ground-state vibrational modes in the range 800 – 1600 cm^{-1} were observed, as shown in figure 1.11 (data from Kahan et al.[64]).

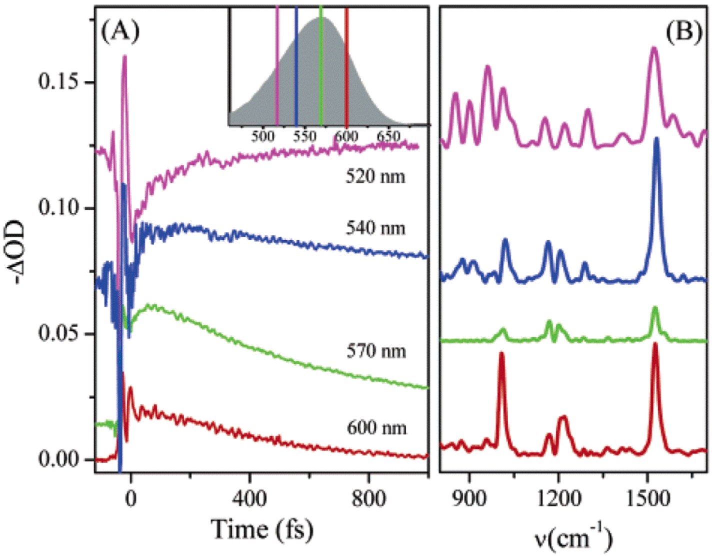

Figure 1.11. **A**. bR transient absorption kinetic traces at 520, 540, 570 and 600 nm (bR bleach region) obtained using 7-fs pulses. **B**. Fourier transform of oscillatory features showing vibrational modes in the 800-1600 cm^{-1} region. Note that vibrational modes are best observed on the blue and red sides of bR absorption spectrum (maximum at ~570 nm). Picture taken from Kahan et al.[64].

Chapter 2

The transient absorption experiment, data processing and analysis

This Chapter consists of an introduction to femtosecond pump/probe spectroscopy principles. The setup that has been built is described, as well as the data acquisition, processing and analysis. With this spectroscopy technique[59], the process to be studied is clocked from the precise moment that the sample under investigation absorbs a photon from the pump pulse. Passage of a probe pulse through the sample after a controlled delay time provides a snapshot of the status of the system at that particular time. Indeed, as the pump and probe pulses are synchronously produced, the difference in optical path lengths translates into a delay time between the two pulses at the sample location, thanks to the finite speed of light (300 $nm.fs^{-1}$). The complete spectrally-resolved time evolution of the system is reconstructed from the individual snapshots.

This transient absorption technique requires ultrafast pulses generated by a Ti:Sapphire ultrafast laser, which is presented in § 2.A.1. Wavelengths conversion processes, such as Second Harmonic generation (SHG) and White-Light Generation (WLG), are needed for sample excitation at the appropriate wavelength, and for broadband absorption detection measurements, respectively. The relevant non-linear optical processes are detailed and illustrated in § 2.A.2.

The pump/probe principle and setup are then explained in § 2.B, with a qualitative illustration of the spectro-temporal absorption changes ($\Delta A(\lambda,t)$) measured on bacteriorhodopsin, which has been introduced in Chapter 1. Before the advent of broadband spectroscopy, single-wavelength measurements at selected wavelengths were performed. The broadband detection allows for a faster and full coverage (hundreds of nanometers measured at the same time) of the signals. This gives a better overview of the full spectro-temporal dynamics of the sample under study, and thus a better understanding of wavelength-dependent phenomena (e.g. band shifts or delayed signals).

The coherent signal of the solvent is described in details in § 2.C.1. It is observed on a ~200 fs window around time zero and over the entire probed wavelength range. We use this signal to determine and correct for the Group Velocity Dispersion (GVD, see § 2.C.2), which is an issue due to the broadband spectral coverage and the ultrafast dynamics we want to investigate. But this solvent signal, often referred to as the coherent "artifact", is also overlapping with the molecule contributions at short times. Molecular signal can be efficiently disentangled from the solvent signal by simple subtraction of the solvent signal (§ 2.C.3).

Finally after GVD and solvent corrections, the signals can be analyzed using fitting techniques which are briefly presented and illustrated in § 2.D.

A. Femtosecond laser and non-linear optics basics

1. Femtosecond Ti:Sapphire laser

a. Ti :Sapphire oscillator

Titanium-doped sapphire[73] (Ti:Sapphire) gain medium-based lasers are widely used in the field of optics and especially in ultrafast (femtosecond) spectroscopy.

The Ti^{3+} titanium ion is responsible for the laser action of Ti:Sapphire, which is a crystalline material composed of Sapphire (Al_2O_3) where a small percentage of Al^{3+} ions are substituted by Ti^{3+} ions, combining advantages of both Ti^{3+} ions and Sapphire. Indeed, Sapphire has a good thermal conductivity, allowing high powers and intensities, and Ti^{3+} has a very large gain bandwidth, with maximal gain and lasing efficiency around 800 nm. Another advantage is that optical pumping has to be done in the green region of the spectrum (broad absorption spectrum centered at ~500 nm), where high-power diode-pumped solid-state lasers are available. In figure 2.1.A the absorption and emission bands of Ti:Sapphire are presented.

Optical pumping creates a population inversion in the 4-level scheme of Ti:Sapphire (see fig. 2.1.B), and subsequent lasing in the broad emission band centered around 800 nm proceeds.

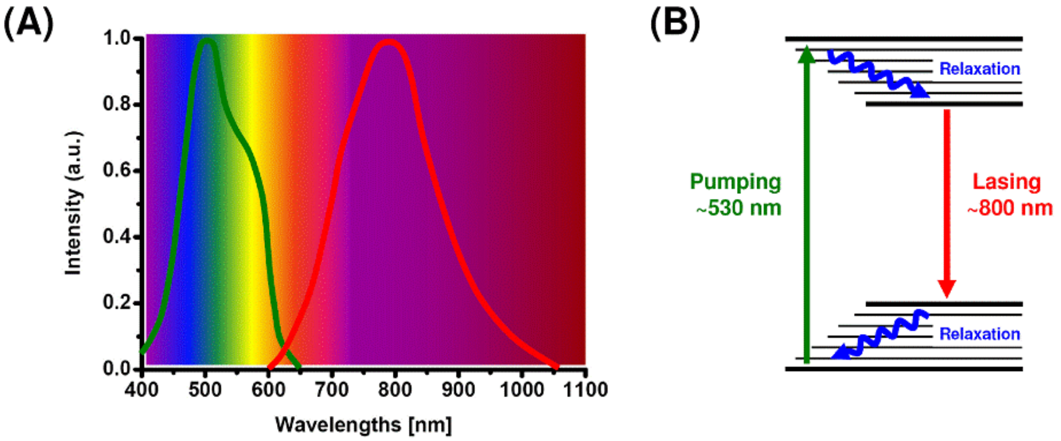

Figure 2.1. **A**. Absorption (green curve, maximum at ~500 nm) and emission (red curve, maximum at ~800 nm) bands of Ti:Sapphire. **B**. Laser operation represented by a 4-level scheme.

Due to its very broad gain bandwidth, Ti-Sapphire allows to generate ultrashort (femtosecond regime) pulses, using the mode-locking technique (see e.g. references[74-76]). It consists in locking the relative phase of the modes so that femtosecond regime can be initiated. Mode-locking can be achieved by self-focusing (Kerr lens mode-locking[77], KLM) in the gain medium, and initiated by introducing a small perturbation in the cavity length. The KLM effect self-stabilizes the pulses.

Typically Ti:Sapphire oscillators at ~80 MHz repetition rate with pulse duration below 40 fs are very stable and commercially available. Ti:Sapphire oscillators even producing sub-5fs pulses (single-cycle limit is 2.7 fs at 800 nm) have been achieved in laboratories since the late 90s'[78].

b. Amplified Ti :Sapphire systems

Using the femtosecond pulse train from the oscillator, it is possible to generate more intense pulses at lower repetition rates using the Chirp Pulse Amplification[79] (CPA) and Regenerative Amplification[80] (RA) techniques. Increasing the peak power is of great importance to be able to access non-linear processes, which require high intensities. Two of them will be presented in the next section.

Briefly, the technique of CPA involves temporally stretching an ultrashort pulse (from an oscillator), then safely amplifying it in a solid-state material at reduced peak power, and finally recompressing the amplified pulse as close as possible to its original duration. This technique, discovered in the mid-80s by Strickland and Mourou[79] and which is schematically presented in figure 2.2, allows to significantly increase the pulse peak power[81, 82], while operating at low optical damage (for the crystal) and minimizing non-linear effects (like self-focusing).

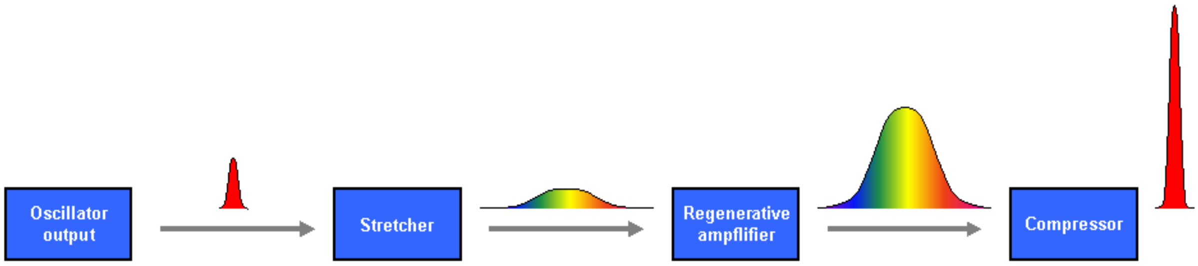

Figure 2.2. Diagram showing the principle of Chirp Pulse Amplification (CPA). The oscillator output is stretched such that the red frequencies travel ahead of the blue ones. The peak intensity is reduced in the process but the pulse is then amplified in the Regenerative Amplifier (RA) and finally recompressed in a grating-pair compressor.

The stretcher (or compressor) is a device usually based on wavelength dispersive systems such as gratings or prisms[83-86]. They can be arranged in such a way to create different optical paths for each wavelength of the spectrum, so that for example bluer wavelengths take more time to travel through the system than redder ones. Hence, the output is stretched and looks like a temporal rainbow (red in the leading edge and blue in the tailing edge). The pulse can in such a way be stretched over nanoseconds, and can further be recompressed in the compressor using the reversed process.

In between the stretcher and the compressor, the pulse is amplified using the regenerative amplification (RA) technique. The principle of RA is to confine, by polarization using Pockels' cells, a single pulse selected from a mode-locked train, amplify it to an appropriate energy level, and then "dumps" it outside the cavity. The amplification takes place as the pulse passes through the laser rod, which has been optically excited by a pulse from a pump laser (such as Nd:YLF). Typically an input pulse in the nanoJoule range at a ~MHz repetition rate can be amplified to the milliJoule range at a ~kHz repetition rate.

After amplification the pulse must be compressed back to its original duration. A compressor device based on a wavelength dispersion system similar to the stretcher is commonly used.

c. Experimental Ti :Sapphire system

The experimental transient absorption (pump/probe) setup is based on a Ti:Sapphire regenerative amplifier laser system[87] (*Pulsar*, Amplitude Technologies), delivering 800-nm, 40-fs pulses at a repetition rate of 5 kHz. Figure 2.3 gathers the system global design and its main characteristics.

Briefly the ultrashort pulses entering the amplified system are delivered by a Ti:Sapphire femtosecond oscillator (*Femtosource Synergy 20*, FEMTOLASERS) producing 800-nm, ~20-fs pulses at a repetition rate of 63 MHz. This oscillator is pumped at 532 nm by the second harmonic of the fundamental mode (TEM00) from a diode-pumped solid-state (DPSS) Nd:YAG laser (*Opus 2W*, Laser Quantum Ltd). The amplified system pump laser (output power 27 W) is a DPSS Nd:YLF laser (*DM20*, Photonics Industries, Inc.) producing 527-nm, 200-ns pulses at a repetition rate of 5 kHz.

The amplifier system is a Ti:Sapphire laser based on the so-called chirped pulse amplification (CPA) scheme that has been described above. The system amplifies pulses from the Ti:Sapphire oscillator and consists of a stretcher, a regenerative amplifier (coupled with a single pass amplifier) and a compressor (see boxes labelled 1, 2 and 3 on figure 2.3, respectively).

The amplification stage consists of a Ti:Sapphire regenerative amplifier which produces around 0.5 mJ stretched pulses at 5 kHz. The regenerative cavity includes two Pockels cells in order to optimize the contrast ratio out of the amplifier. One is used to seed the stretched pulse into the regenerative cavity and the other dumps out the pulse at the maximum energy level. The high power delivered by the system is ensured by a single-pass amplifier after the regenerative cavity. The DPSS Nd:YLF laser is used to produce the gain in both Ti:Sapphire crystals of the regenerative and single-pass amplifiers.

The amplified pulses are compressed back to short duration using a classical compressor design. Two gratings with an optimized number of lines transmit the very broad spectrum bandwidth with excellent efficiency.

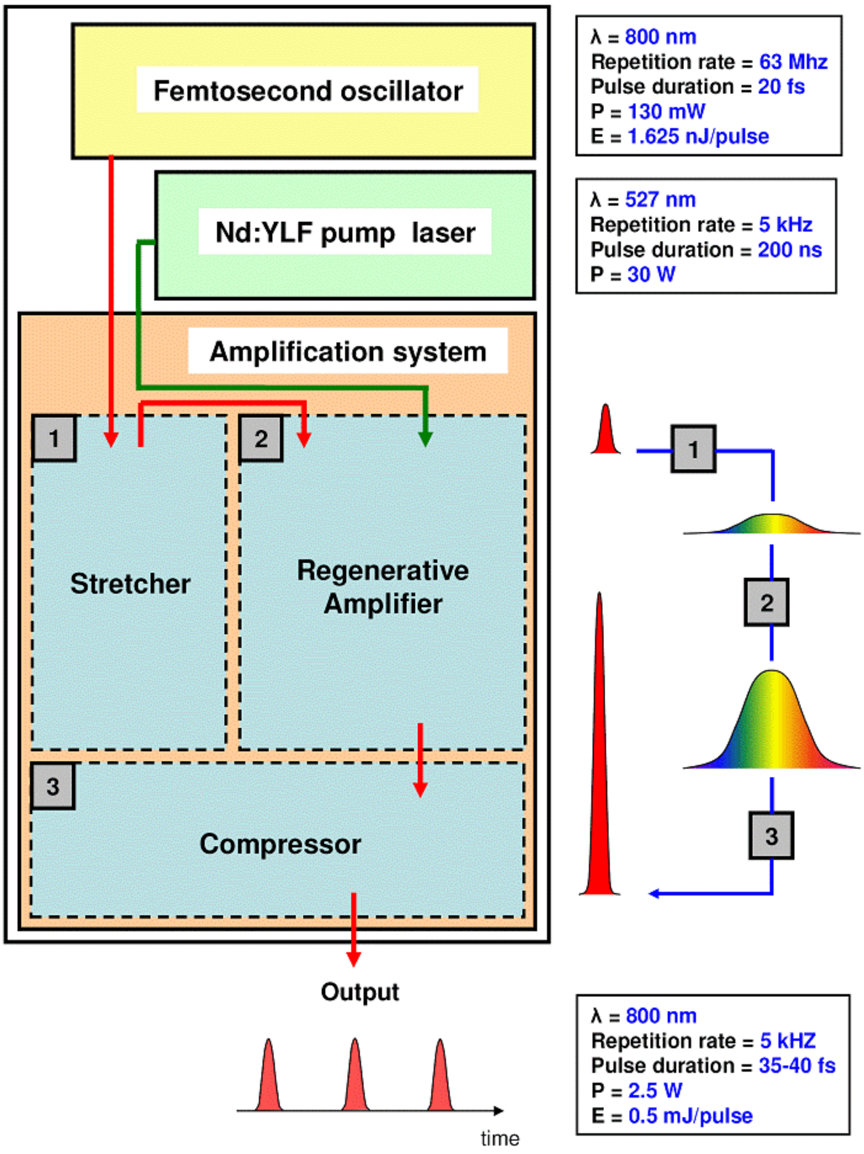

Figure 2.3. Simplified design of the amplified laser system and its main characteristics.

At the amplified system output, a part of it can be used to optimize the compression amplifier system using air filamentation. The principle is presented in figure 2.4 where a short focal-length (typically 50 mm) lens is used to create a filament whose pattern projection is observed on a piece of paper. Improving the filament brightness and colors yield efficiently compressed pulses[88]. This optimization is important as short pulses allow for a better UV-extension of the continuum generated in the CaF_2 crystal (see below).

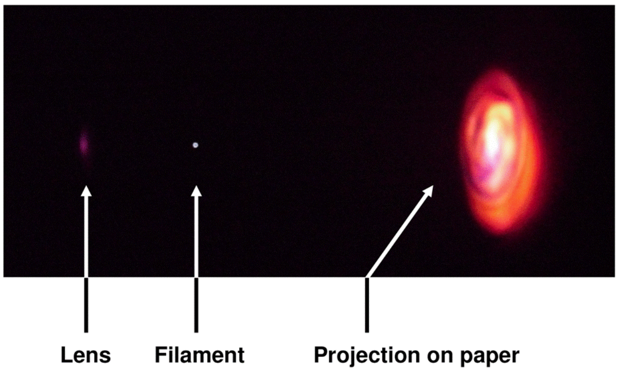

Figure 2.4. Compression optimization principle. A filament is generated in air by focusing (50-mm focal length) a part of the amplifier output beam. The filament pattern is observed on a piece of paper and compression gratings are set to optimize the appearance of orange, yellow and green colors.

2. Non-linear optical processes for femtosecond spectroscopy

The previously-described laser system produces pulses usually centered at ~800 nm. Depending on the absorption of the sample under investigation and on the spectral coverage required in the experiments, one may need to convert this wavelength into others in order to be able to access different regions of the spectrum. Two useful non-linear wavelength-conversion processes are presented and illustrated in the next paragraphs.

a. Second Harmonic Generation (SHG)

Second Harmonic Generation[89, 90] (SHG) consists in frequency-doubling an incoming beam with the help of a specific medium, as presented in Figure 2.5. This is only possible at high optical intensities where a medium response can become highly non-linear, as explained by a Taylor expansion of a medium polarization in powers of the electric field (scalar version) :

$$P = \varepsilon_0 (\chi^{(1)} E + \chi^{(2)} E^2 + \chi^{(3)} E^3 + ...) \, , \qquad (2.1)$$

where $\chi^{(1)}$ is the well-known linear susceptibility, whereas $\chi^{(n)}$ is the coefficient for the n$^{\text{th}}$ order non-linear process. When the electric field becomes very large, terms of index > 2 can become important. Several conditions have to be achieved to generate this process. First the incoming beam has to be intense, because SHG is a non-linear process involving the of 2$^{\text{nd}}$-order susceptibility $\chi^{(2)}$, which is orders of magnitudes smaller than $\chi^{(1)}$. This is easily achieved by focusing femtosecond pulses into the medium. Second, non-linear, birefringent and non centro-symmetric crystals are required, to have $\chi^{(2)} \neq 0$. Crystals such as BBO[91] (β-barium borate, β-BaBO$_4$) are commonly used for frequency-doubling because they are transparent in the visible, have no inversion symmetry and a relatively large susceptibility $\chi^{(2)}$. A critical parameter to maximize the efficiency is the phase-matching angle conditions[92] between the incoming beam and the non-linear crystal. Another important parameter is the thickness of the crystal. Indeed, depending on the pulse duration and the wavelength used for SHG, there is a constraint on the non-linear crystal so as to have limited effects of Group Velocity Mismatch (GVM). This thickness for a quasi-static interaction length is, for example, 0.2 mm for 40-fs, 800-nm pulses. It should also be mentioned that this frequency-doubling operation rotates the 400-nm polarization by 90° compared the original 800-nm one.

400-nm and 800-nm beam spectral shapes, measured with a fiber spectrometer (*USB2EPP*, StellarNet, Inc), are given in figure 2.5. Their spectral widths are 10 and 32 nm, respectively. The Fourier transform of these bandwidths for supposed Gaussian shaped and Fourier transform limited pulses gives FWHM pulse durations of ~20 fs for both beams.

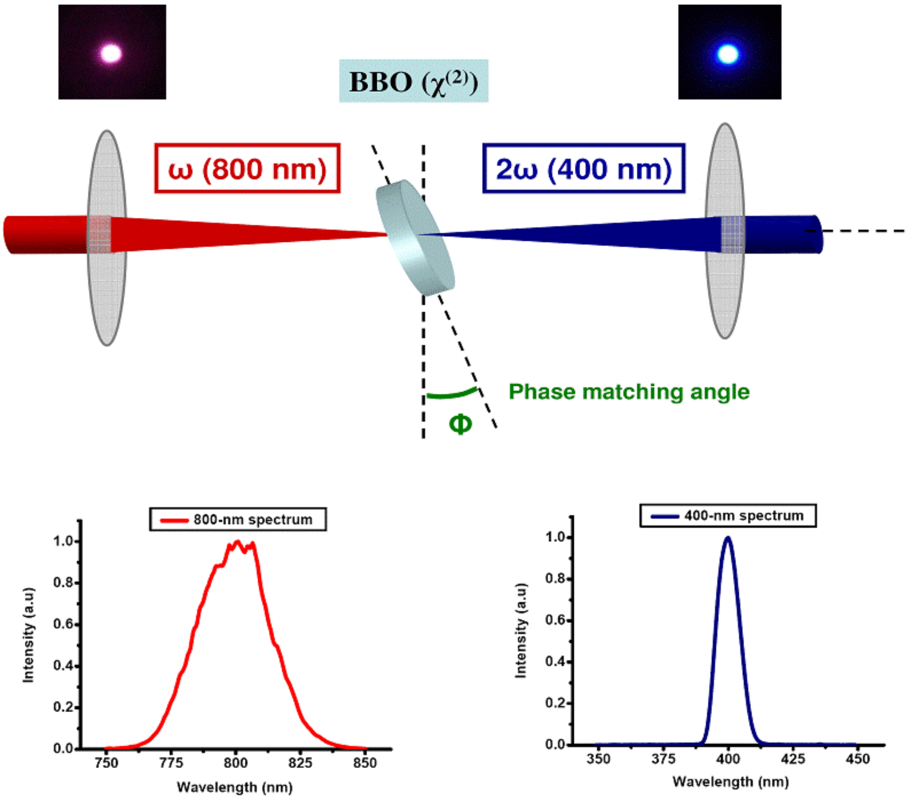

Figure 2.5. Second harmonic generation principle. An intense pulse train (here at 800 nm) is focused into a birefringent material (such as BBO) and under proper phase-matching angle conditions the incoming beam can be efficiently frequency-doubled (400 nm). Both pictures were taken in the laboratory with 40-fs 800-nm pulses frequency-doubled in a 0.2-mm thick BBO crystal. The 800 and 400-nm beam spectra are also indicated.

b. White Light Continuum (WLC) generation

In order to be able to produce a broad spectral range in a single pulse, one can generate a wavelengths continuum in a transparent medium. As explained for Second Harmonic Generation, intense laser pulses can induce a non-linear response of a medium. Continuum or white-light generation[93, 94] is a third order non-linear process involving $\chi^{(3)}$. The non-linear refractive index induces a frequency chirp of the incoming beam (mainly by self-phase modulation, SPM), which simply means that the pulse spectrum broadens due to non-linear interactions.

Continuum generation involves complex phenomena and is most likely a result of the interplay between several dynamical processes. SPM[94-96] associated with self-focusing is considered to be the dominant and triggering process which leads to spectral broadening. But the latter cannot explain completely the continuum spectral characteristics, and the reasons still remain unclear. Other processes such as four-wave mixing, self-steepening, anti-Stokes Raman spectral broadening, Group Velocity Dispersion or filament fusion and break-up may play a role as well[97-100].

Crystals such as sapphire (Al_2O_3) or calcium fluoride (CaF_2) are commonly used. They are transparent in the visible, have inversion symmetry and a relatively large non-linear susceptibility[101] $\chi^{(3)}$. When pumped at 800 nm, they can produce broadband continua extending from UV up to near-IR.

Figure 2.6 shows the principle of supercontinuum generation in the 2-mm CaF_2 plate used in the experimental setup, and a set of portions of the white-light continuum, defining the spectral regions experimentally accessible with our setup. The 290-950 nm range is easily obtained by using different color filters to appropriately isolate wavelength ranges, and adjusting the focus and intensity of the 800-nm beam into the CaF_2 crystal. The combination of the spectrometer and CCD camera settings allows measuring ~320-nm-broad spectra in a single experiment, with a ~2.5 nm spectral resolution.

Optimization of the continuum generation and characteristics has been achieved. For the purpose of experiments performed in the case of this Ph.D. and for other studies also, we aimed at extending the continuum as far as possible into the UV region. Tests using different non-linear crystals (CaF_2, BaF_2, MgF_2, LiF and sapphire) with different thicknesses (0.8, 1, 2, 3, 4 mm) and varying the focusing conditions (with 50-, 100-, 150- and 200-mm focal-length lenses) have been realized. The best compromise between continuum stability, crystal safety, UV-extension of the white light and its intensity was achieved with a 2-mm CaF_2 crystal and a 100-mm focal-length lens, in good agreement with reference[100].

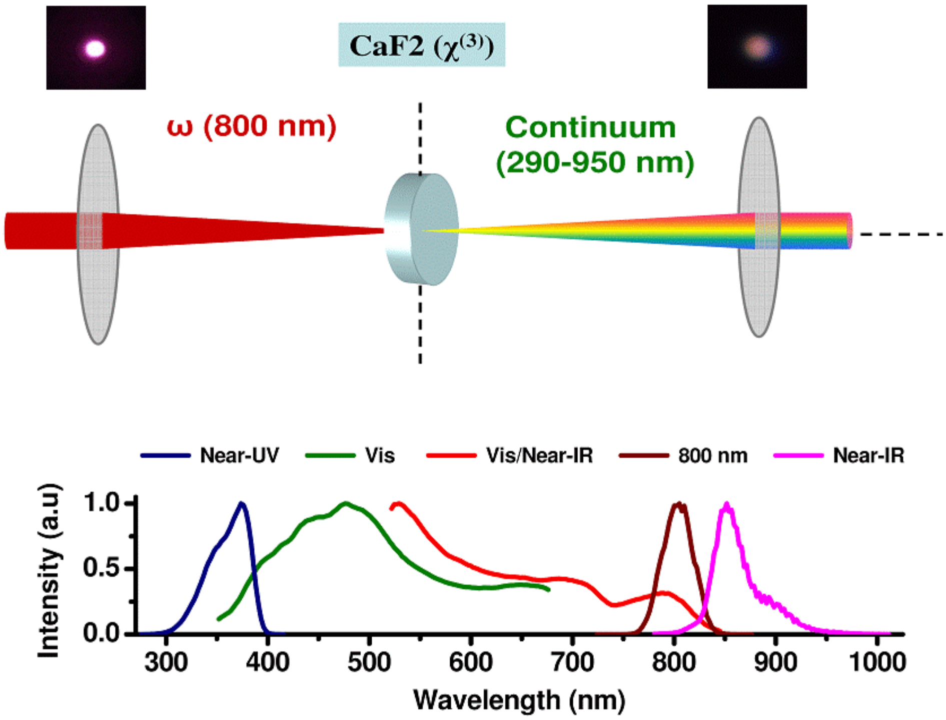

Figure 2.6. White-light generation principle. A femtosecond pulse train (in this example at 800 nm) is focused into a $\chi^{(3)}$ material which creates a broadband continuum. Both pictures were taken in the laboratory with 40-fs 800-nm pulses focused into a 2-mm CaF_2 crystal. Examples of white-light continua recorded with the CCD camera are also plotted. The accessible spectral range for transient absorption experiments is extending from UV (~300 nm) to the near-IR (~950 nm).

Figure 2.7 shows an example of 2-photon absorption (1 from the pump, 1 from the probe) measured with the pump/probe setup (see § 2.B) in a Zinc Sulfide (ZnS) plate. This response occurs only during the temporal overlap of pump and probe, thus characterizing the group velocity dispersion (GVD) and temporal width of the continuum. We can observe on this picture the effect of GVD introduced by the transmittive optics on the probe path, the redder wavelengths (~700 nm) being shifted in this example by ~120 fs compared to the bluer ones (~410 nm).

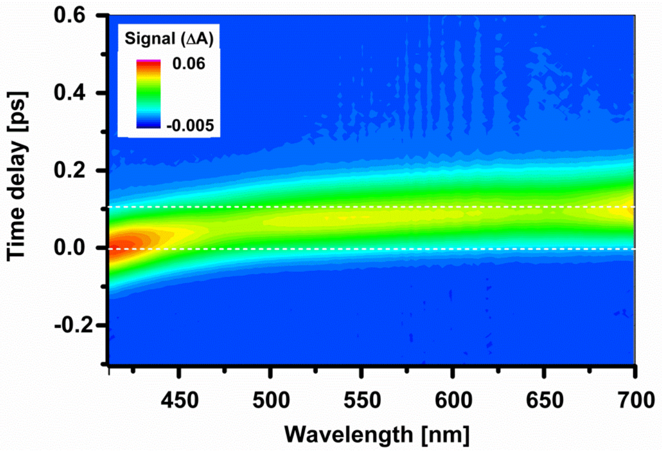

Figure 2.7. Pump/broadband-probe measurement in the visible range of a ZnS plate (40 µm) The two-photon absorption signal (ΔA>0), peaking at larger time delays with increasing wavelengths, highlights the chirp of the continuum.

B. Femtosecond transient absorption spectroscopy and experimental setup

1. Transient absorption (TA) spectroscopy

a. Static (steady-state) absorption spectroscopy

The wavelength-dependent steady-state absorbance A (or Optical Density, OD) of a sample is given by the following equation:

$$A(\lambda) = -\log\left(\frac{I(\lambda)}{I_0(\lambda)}\right) \qquad (2.2)$$

where I is the light intensity transmitted through the sample and I_0 is the incident intensity.

The measurement of the absorbance requires a spectrophotometer and the obtained steady-state spectrum is used to characterize the sample. Basically, a static absorption spectrum in the UV-Vis range gives information about the electronic states. It measures the energy differences for transitions from the thermal equilibrium state, referred as the ground state (S_0), to states higher in energy, named excited states (S_n). It also gives information about the dipole moment and oscillator strength of the probed $S_0 \rightarrow S_n$ transitions.

The concentration C (M) and wavelength-dependent molar extinction coefficient $\varepsilon(\lambda)$ ($M^{-1}.cm^{-1}$) are related to the absorbance, according to the Beer-Lambert- law:

$$A(\lambda) = \varepsilon(\lambda) L C \qquad (2.3),$$

where L is the thickness (cm) of the measured sample.

b. Ultrafast transient absorption (TA) spectroscopy

An ultrafast transient absorption experiment consists in sending a broadband, weak and ultrafast pulse (continuum or white-light pulse, hereafter referred as a probe pulse) through the sample and to record its transmitted spectrum ($I_{p\,off}$). Then a second, stronger pulse, resonant with an electronic transition, brings the sample into an excited state, and possibly triggers a photo-chemical process in the sample. After an adjustable delay time, another probe pulse is sent through the sample and its spectrum is again recorded ($I_{p\,on}$). The pump-induced absorption change ΔA is given by:

$$\Delta A(\lambda,t) = A(\lambda,t)_{P_{on}} - A(\lambda,t)_{P_{off}} = -\log\left(\frac{I(\lambda,t)_{P_{on}}}{I(\lambda,t)_{P_{off}}}\right) \quad (2.4)$$

where P_{on} and P_{off} indicate when the pump is on or off.

Using the Beer-Lambert law, which is only valid for weak (< few %) absorption changes and incoherent (stochastic) processes, one can write:

$$\Delta A(\lambda,t) = \sum_{i,j} \varepsilon_{S_i \to S_j}(\lambda)\, \Delta C_{S_i}(t)\, L \quad (2.5),$$

where $\varepsilon_{i \to j}$ represents the molar extinction coefficient of the considered i→j transition, and ΔC_i the difference of concentration (population) of molecules present in the S_i state when the pump beam is applied or not. This equation is only valid if the molar extinction coefficient is time-independent, which means that no relaxation or coherent processes are occurring, and thus the time and wavelength variables can be separated in this particular case. This simply tells whether the S_i state is more ($\Delta C_i > 0$) or less ($\Delta C_i < 0$) occupied when the pump is applied.

Let us consider the case in which the pump promotes part of the population into the first excited state S_1. The same part is now lacking in the S_0 ground state. This gives a contribution called the ground state bleaching (GSB). The corresponding ΔA signal is:

$$\Delta A_{GSB}(\lambda,t) = \varepsilon_{S_0 \to S_1}(\lambda)\, \Delta C_{S_0}(t)\, L \; < 0 \quad (2.6)$$

This quantity is negative because the concentration in S_0 is larger when the pump is not applied, thus leading to a negative value for ΔC_{S0}, while L and $\varepsilon_{0 \to 1}$ are >0. The ground state has lost population due to the excitation by the pump pulse.

Based on the same idea, stimulated emission (SE), that is a transition from S_1 back to S_0 concerning the population of molecules that have been promoted to S_1 by the pump, is also a negative signal because ΔC_{S1} is >0 in this case but $\varepsilon_{1 \to 0}$ is <0.

Induced absorptions can also appear. They concern transitions between new (excited or photoproduct) states and a higher state S_n. They are called excited state absorption (ESA) or photoproduct absorption (PA). These ΔA signals are positive because populations are increased by the pump pulse and their respective ε coefficients are positive.

The population of these states will then evolve back to the equilibrium and thus the four discussed signals will then decay (except PA) along with the population changes. This technique thus allows to follow the population evolution as a function of time.

The ratio between both recorded intensities gives the absorption change ΔA induced by the excitation pulse according to eq. (2.4). A positive ΔA corresponds to an induced absorption, while negative ΔA represents emission or photo bleaching[*] (see above). The delay between both pump and probe pulses is precisely controlled so as to record these absorption changes (or difference absorption spectra) over a large number of time delays between pump and probe pulses. Figure 2.8 displays a schematic representation of the pump/probe experiment.

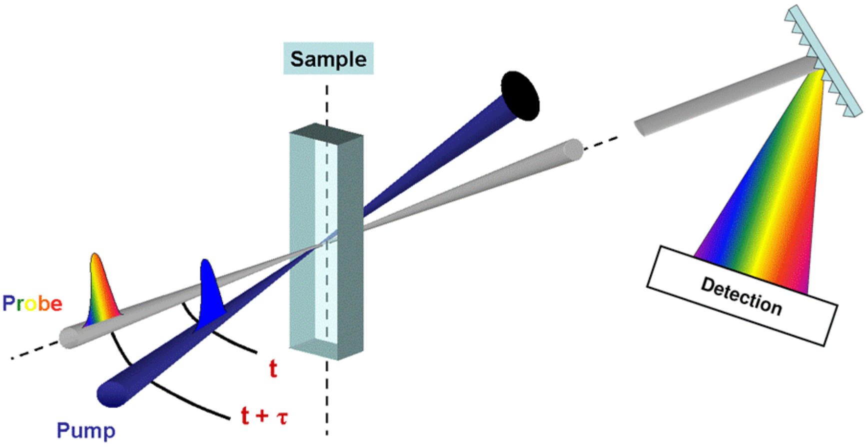

Figure 2.8. Scheme representing the pump /probe technique. A broadband pulse (probe) is first sent through the sample and its transmittance spectrum is recorded. Then a strong, resonant excitation pulse triggers dynamical process in the sample. After an adjustable delay time τ, another probe pulse is sent through the sample and its spectrum is again recorded. Comparison between both probe pulses gives the pump-induced absorption changes at a given delay time τ.

Ultrashort laser pulses are needed to have the best possible time resolution, in order to capture effects on the shortest possible timescale. In the experiments described below the TA experiments are performed in the near-UV to visible range (290-700 nm), and the signals correspond to transitions between electronic states. These transitions between electronic states are, in molecules for example, broad bands extending over tens or hundreds of nanometers.

2. Experimental setup and characteristics

a. Experimental pump/probe setup

The experimental pump/probe setup is based on the Ti:Sapphire regenerative amplifier laser system described above. Figure 2.9 depicts the important components of the setup.

The amplified laser system output is separated using a fused silica beam splitter (CVI Melles Griot).

---

[*] We can mention here that these signal assignments are valid in the considered situation of stochastic, incoherent processes. As it is presented below, the example of the coherent solvent signal analysis does not follow this interpretation.

The first part is used to generate by Second Harmonic Generation (SHG) the pump beam at 400 nm, using a 0.2-mm thick BBO crystal (29°, Crystech). The beam then goes through a Berek compensator (Laser 2000), so as to adjust its relative polarization to the one of the probe beam. The 400-nm beam is then focused onto the sample with a 200-mm focal length UV fused silica lens (CVI Melles Griot).

The second part of the output is sent through a computer-controlled motorized delay line (*ESP300*, Newport) to be able to finely adjust the time delay between the pump and the probe beams. A home-built 4-passage arrangement of the delay line has been developed to be able to access time delays up to 6 ns. The 800-nm beam is then focused using a 100-mm focal length lens (CVI Melles Griot) into a 2-mm thick CaF_2 crystal, mounted on a loud speaker slowly oscillating (0.5-1 Hz) orthogonally to the input beam. The 800-nm pulses generate a white-light continuum which can be used in our experiments from 290 to 950 nm. The generated supercontinuum is recollimated using a 50-mm focal length parabolic mirror (Edmund Optics). Then the white-light beam is separated into probe and reference beams by a beam splitter. The probe beam is then focused at the sample location using a 100-mm focal length second parabolic mirror (Edmund Optics). After the sample, the continuum is recollimated using a 100-mm UV fused silica lens (CVI Melles Griot). Both beams are finally sent through the monochromator.

It should be mentioned that all mirrors on the 400-nm and 800-nm paths are high-quality dielectric mirrors (CVI Melles Griot). Metallic mirrors on the probe and reference paths are UV enhanced mirrors (CVI Melles Griot), suitable for the reflecting the broad continuum (290-950 nm) with a good efficiency. All transmitting components have a thickness as small as possible to minimize the chirp.

The relative pump and probe polarization is set to magic angle (54.7°). Adjusting the pump polarization relatively to the linear probe one is done either using a Berek compensator (Laser 2000) or a $\lambda/2$ plate (CVI Melles Griot).

Both beams are focused into a 0.5-mm path length quartz capillary (Polymicro Technologies LLC) with a spot diameter between ~120 and 300 µm (FWHM) and ~60 µm (FWHM), respectively. The diameters FWHMs were derived from power measurements, using a razor blade mounted on a micrometric displacement stage, the beam being gradually blocked and the power being measured.

Only part of the total amplified pulses energy is used for the TA experiment presented here. The complete setup also includes a third harmonic generation (266 nm), an optical parametric amplifier in a non-collinear geometry (NOPA) and finally a femtosecond fluorescence down-conversion experiment still under development.

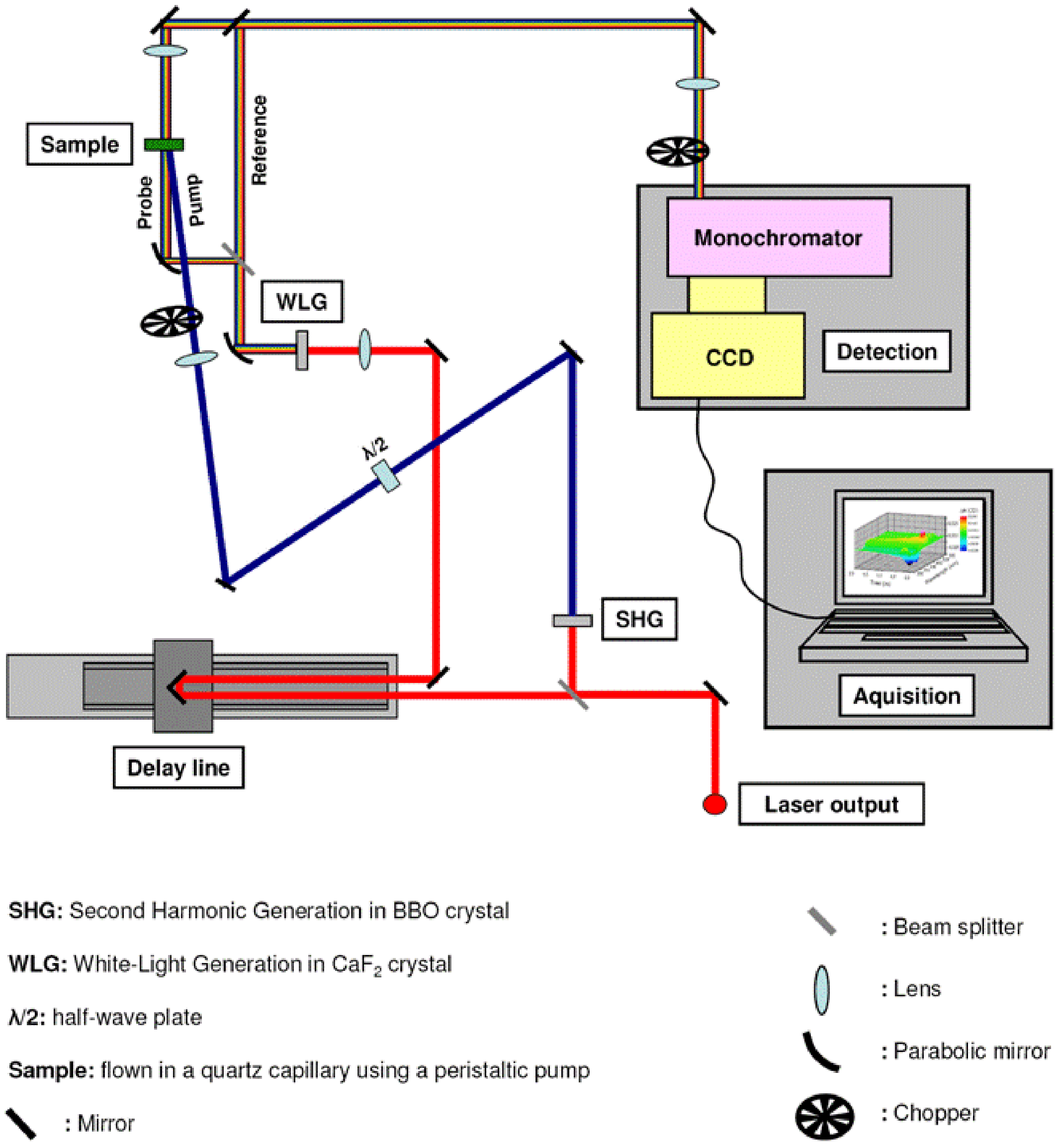

SHG: Second Harmonic Generation in BBO crystal

WLG: White-Light Generation in CaF_2 crystal

λ/2: half-wave plate

Sample: flown in a quartz capillary using a peristaltic pump

Figure 2.9. Simplified design of the transient absorption (pump/probe) setup. See text for details.

b. Acquisition system

The pump beam is chopped at 113.63 Hz (5 kHz divided by 44) and a second chopper 227.27 Hz (5 kHz divided by 22) is used as the camera shutter, using controllers (*MC1000A*, Thorlabs). Probe and reference signals are recorded using a spectrograph (H25 *monochomator*, Jobin-Yvon) and a CCD camera (*SPEC-10:400B*, Princeton Instrument) at a 227.27 Hz acquisition rate (acquisition speed constraints are imposed by the CCD camera). While the pump is OFF, the CCD camera accumulates probe and reference signals while they are ON, and reads when they are OFF. When the pump is then ON, the same operation is repeated.

Figure 2.10 displays a typical image of both probe and reference beams dispersed onto the CCD camera. Absorption changes at a specific delay can be derived from both (with and without pump) recorded probe signals, while reference signals are used to correct for the continuum fluctuations, improving the data signal-to-noise ratio. Data can be recorded from 290 to ~1000 nm with this experiment, with 2.5 nm resolution, and up to time delays of 6 ns. Data are acquired using a home-implemented Visual Basic (Microsoft) acquisition program.

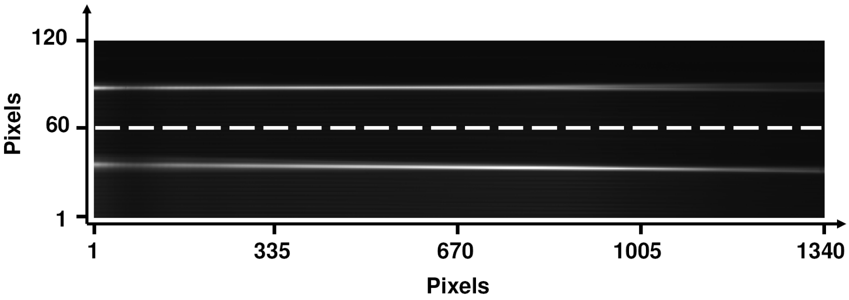

Figure 2.10. Image recorded with the CCD camera of the probe and reference white light beams intensities after dispersion into the monochromator. The y-axis pixels are separated (white dashed line) into 2 equal parts of 60 pixels each, one for the probe and the other one for the reference. The x-axis pixels are converted with proper calibration into wavelengths (here from 400 nm to 720 nm).

Background drift effects are avoided thanks to a home-made routine which was implemented into the acquisition program and a computer-controlled shutter arrangement placed in the experimental setup. Before each delay line scan, meaning every ~2 min, a new background is taken and only after that the following scan is started. All individual scans are saved in a specific folder and before any scan averaging (usually 10 to 30 scans are recorded), the stability of the measured signal throughout the experiment is checked.

c. Characteristics and settings of the experiment

The typical time resolution of the experiment is ~80 fs. This is obtained by measuring the temporal width of the Raman signal of methanol (~357 and ~450 nm for a 400-nm pump). As it can be observed in transient absorption data shown in figure 2.17 in the next section, the chirp of the pulses can also be observed in these Raman signals (weak blue-shift with time). The Instrument Response Function (IRF) of the experiment is approximated by a Gaussian function of ~80 fs FWHM (full-width at half-maximum) as presented in figure 2.11. Further checks with the solvent response (see next section) and a 40-µm thick Zinc Sulfide (ZnS) plate indicate that the IRF stays ~80 fs on the 320-

750 nm spectral range. Due to group velocity mismatch (GVM), it becomes slightly larger below 320 nm. The IRF is for example ~100fs at 300 nm.

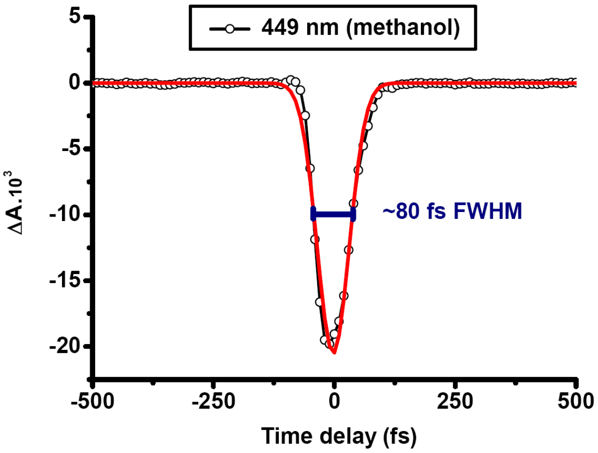

Figure 2.11. Gaussian fit of the Raman signal of methanol at 449 nm. The fit yields a FWHM of 80 fs.

The white-light continuum probe and reference experimental alignment is optimized using a home-made procedure. A routine implemented in the acquisition program allows for a live fine adjustment of the reference alignment with respect to the probe, so that the continuum fluctuations are efficiently corrected by the reference beam. As shown in figure 2.12.A, we monitor both signals on the CCD camera and improve the values of the RMS and peak to peak RMS values of the ratio between probe and reference signals (see figure 2.12.B).

The reference beam helps to correct for the white-light continuum fluctuations. It is however not going through the sample, so it does not take into account noise which may be generated in the capillary by the sample flow for example. The obtained typical data root-mean-square (RMS) noise is 3.10^{-5}, after a 35-minutes measurement (15 delay line scans) on a spectral window of 320 nm with ~250 time points.

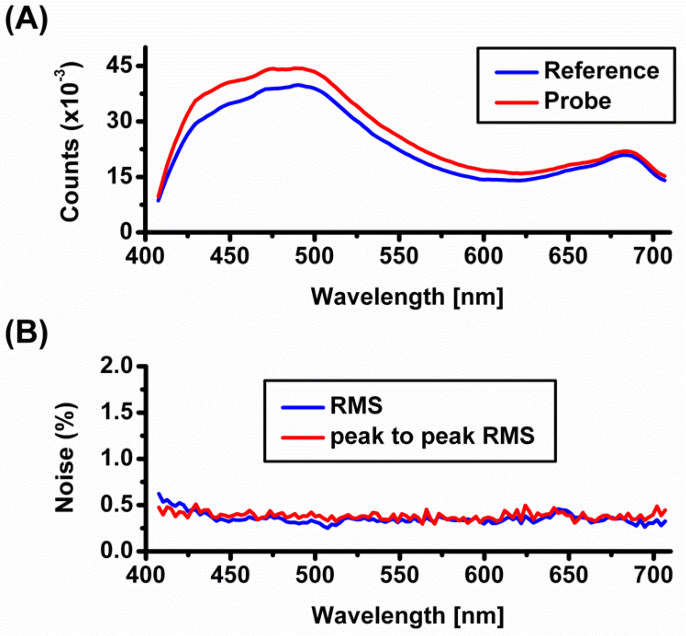

Figure 2.12. **A**. Probe and reference live spectra observed with the acquisition program. This is recorded using CG420, KG1 and KG5 filters on the continuum path. **B**. Live-calculation of the RMS and peak-to-peak RMS of the ratio between probe and reference spectra. With a correct alignment the noise level is low and constant over the spectral range.

The Group Velocity Dispersion (GVD) and its compensation are shown in a separate section in detail, as it is a very important point for the data analysis and the interpretation of this work.

Throughout this Ph.D. work, the measurements are performed using a square capillary cell (Polymicro Technologies LLC) of 500-µm path-length with 250-µm thick fused silica walls. The sample solution is circulated through the capillary using a peristaltic pump (*L/S pump drive*, Masterflex) and appropriate tubings (*Viton tubings L/S*, Masterflex), at a sufficient speed so as to refresh the excitation volume between two successive pump pulses.

Sample absorptions are always adjusted to a convenient optical density (OD) which is always a trade-off between the absorbance of the sample at the pump wavelength and absorption of the white-light continuum by the sample. A typical range of values used in the experiments presented below is $0.7 < OD_{sample} < 1.4\ mm^{-1}$.

The excitation energy density is always set in the linear regime of excitation, which is, in the case of the photoswitches data presented later on (Chapters 4, 5 and 6), below ~1.5mJ/cm^2 per pump pulse.

3. Data and information obtained from ultrafast TA experiments

A transient absorption experiment is introduced below to show the type of data that are acquired and the qualitative information that they contain. In the last section (see § 2.D), quantitative treatments of the data will be introduced as well.

A TA experiment outcome is presented in figure 2.13A, showing a representation of the absorption changes (ΔA, measured quantity) of bacteriorhodopsin* (bR), taken as an example here (see Chapter 1 also for details). ΔA is plotted as a function of two variables, time and wavelength, extending from -0.5 to 5ps, and 410 to 720 nm, respectively. Positive ΔA, coded in red, represent absorption processes such as excited-state or ground-state photo-induced absorptions (e.g. ESA, PA), while negative, blue-coded signals correspond to stimulated emission (SE) or photo-bleaching (GSB) of the sample. Figure 2.13B shows a slice of the data (a spectrum) at a particular delay time (0.5 ps), where these positive and negative contributions are clearly observed. Figure 2.13C shows a schematic representation of the four electronic transitions that are considered.

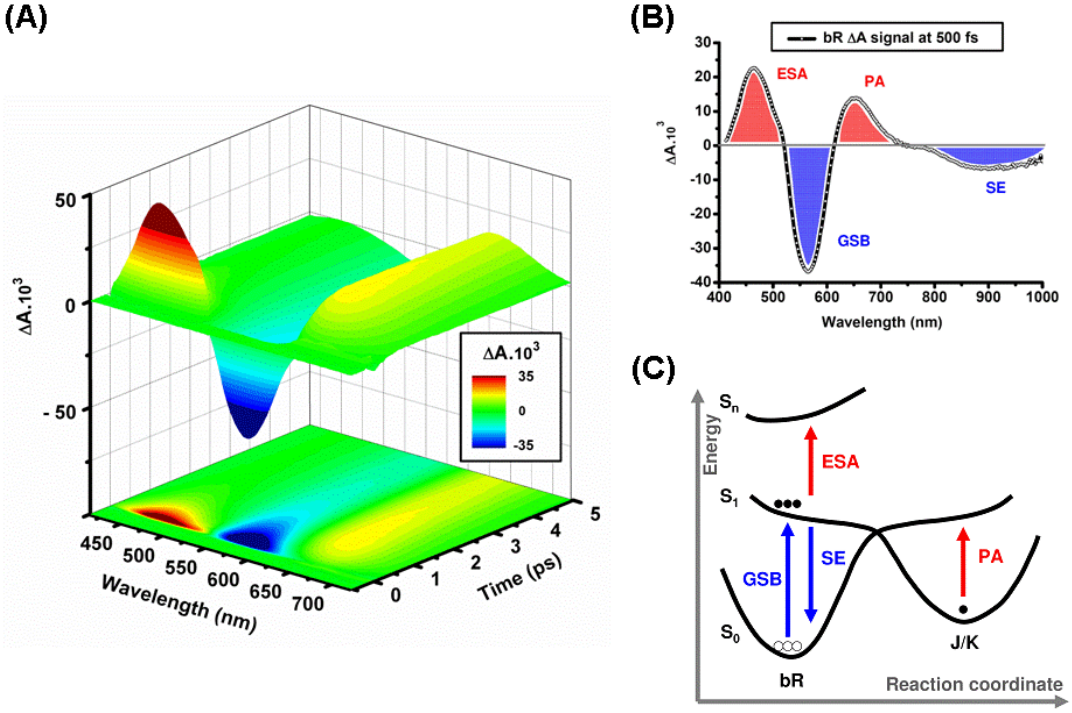

Figure 2.13. **A**. Example of 3D data set obtained with our TA experiment setup. In this case the sample is bR pumped at 400 nm and probed in the visible range. **B**. Spectrum of bR at 500 fs in the 400 -1000 nm range. The observed signals (red = absorption, blue = bleach or emission) at this delay are excited state absorption (ESA), stimulated emission (SE), photoproduct absorption (PA) and ground state bleach (GSB). **C**. Assignments of the different measured signals according to the bR energy levels (see Chapter 1 and below for details).

---

* The light-adapted bR proteins were diluted in a buffer solution (pH=7.4) to an OD of 0.7 mm^{-1} at 568 nm and were pumped at 400 nm. The experiment was performed in the linear regime of excitation.

Figures 2.14A and B show spectra and transients at selected time delays and wavelengths, respectively. Immediately after the excitation pulse, which populates the excited-state and thus bleaches the ground state, we observed excited-state absorption (ESA), observed in the 400-520 nm region, stimulated emission (SE, not shown) and ground state bleaching (GSB), between 520 and 620 nm. At 0.5 ps (see fig. 2.14A), while ESA, SE and GSB amplitudes are decreasing, a positive band appears around 640 nm, assigned to the absorption of the photoproduct (PA). The ESA and SE decays, the GSB recovery, and the simultaneous appearance of the PA can be also observed in the transients of figure 2.14B. After ~3ps (fig. 2.14A and B), excited state signatures have vanished, and only ground state thermalization processes are occurring, leading to the quasi-static difference spectrum observed at 30 ps in figure 2.14A. It corresponds to the difference spectrum between bR and its twisted photoproduct K, showing that bR isomerization has occurred on this time scale.

So thanks to the TA technique and to a careful interpretation of the data, a reaction initiated by the pump pulse, being in the case of bR a photo-induced molecular structural change, can be followed in time, through the spectral signatures of the probed (electronic) transitions.

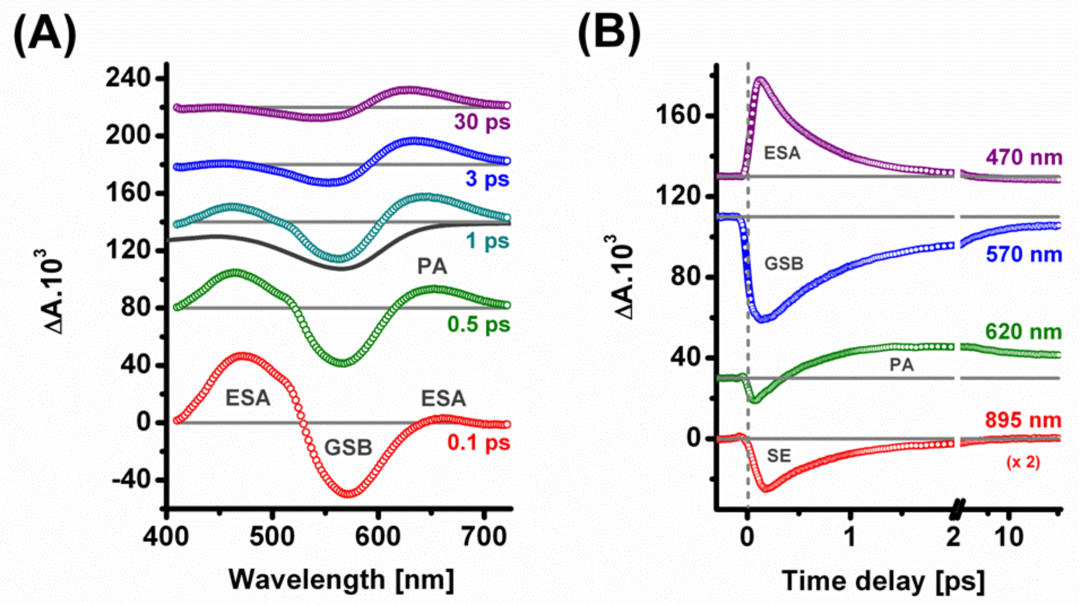

Figure 2.14. **A**. bR spectra at selected time delays (0.1, 0.5, 1, 3 and 30 ps). Along with the 1-ps spectrum, the inverted scaled ground state absorbance is shown (solid line). **B**. bR transients at selected wavelengths (470, 570, 620 and 895 nm). The observed signals (positive = absorption, negative = bleach or emission) are indicated on the figures (excited state absorption (ESA), stimulated emission (SE), photoproduct absorption (PA) and ground state bleach (GSB)).

C. Data processing and corrections

1. The solvent response

Within a time-window of ~200 fs around time zero, non-linear, coherent wave mixing of pump and probe occurs in the solvent and quartz capillary, producing an apparent pump-induced ΔA. This signal, called hereafter "solvent response", is mostly due to cross-phase modulation (XPM) and two-photon absorption (TPA), possibly appearing on the whole wavelength range, and to Raman contributions, giving signals at solvent-dependent specific wavelengths[102-104]. This coherent ultrafast signal, sometimes referred to as the coherent "artifact", is presented in figure 2.15.A in the case of methanol.

The solvent response is only occurring during the during the pump/probe temporal overlap, and determines time zero at all wavelengths. As clearly observed in figure 2.15.A and 2.15.B, time zero, i.e. the pump/probe overlap in time, is wavelength-dependent. This is due to group velocity dispersion (GVD) which affects the white-light continuum, and thus the pump/probe measurements. It is introduced by the transmitting optics in the probe path. Although the GVD has been minimized by thin optics, the leftover GVD introduces a substantial time-zero shift over the studied spectral window (~500 fs over the considered 290-720 nm range). The circles and solid line define the wavelength-dependent time zero, resulting from GVD. At each individual probe wavelength, time zero is defined within ± 10 fs as being the time-axis mid-point of the coherent solvent signal, in agreement with XPM simulations[102-104]. In order to characterize the GVD, a third-order polynome is used to fit the location of the wavelength-dependent time zero. Given the ultrafast dynamics at stake in the following Chapters, accurate GVD compensation is mandatory and is detailed below (see § 2.C.2).

Figure 2.15 B and C show two selected transients at 320 and 500 nm, where TPA and XPM processes are dominating, respectively. It highlights the second important data correction which concerns the solvent signal itself. Indeed, it is overlapping in the first ~200 fs with that of the molecule under investigation. In order to unravel its short-time dynamics, the sample response has to be disentangled from the solvent contribution. This is done by subtraction of the pure solvent measurement from the sample data, according to a procedure detailed in § 2.C.3.

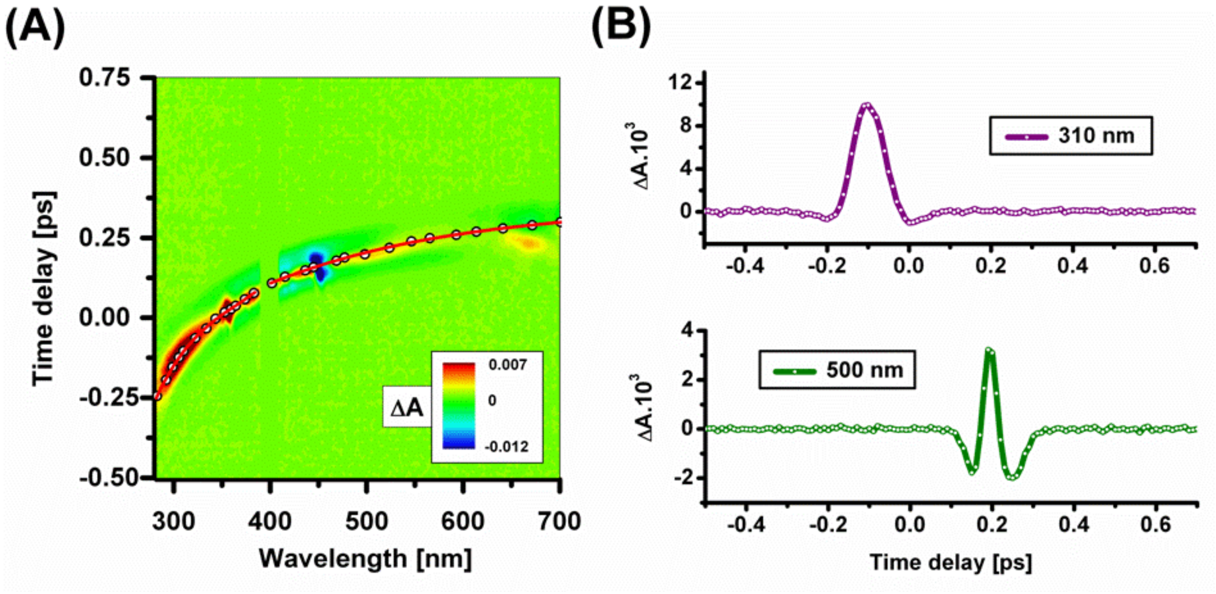

Figure 2.15. **A**. Time-resolved UV-Vis transient absorption change (ΔA) data of methanol solvent. Positive ΔA is coded in red and negative in blue. Data points (circles) chosen for GVD correction are also indicated together with the polynomial fit (red line) defining the GVD curve. The experimental data points correspond to the time-axis mid-point of the solvent signal. **B**. Transients at 310 and 500 nm, showing prominent TPA and XPM processes, respectively.

2. Group Velocity Dispersion (GVD) correction

In the following a representative example is introduced to illustrate the GVD compensation mentioned above. It consists of a measurement of a photoswitch response (ZW-NAIP, see Chapter 3 and 4 for details) in methanol, and of the exact same experiment repeated with the pure solvent only.

A home-implemented Matlab (The Mathworks, Inc.) routine time-shifts the data for the different wavelengths according to the determined GVD polynome presented above. Figure 2.16 shows the signal of the pure solvent (methanol) and ZW-NAIP photoswitch sample in methanol solution before (figures 2.16.A and C, respectively) and after (figures 2.16.B and D, respectively) the GVD correction in the UV region, where the chirp is the most pronounced. The same procedure is applied to the data measured in the visible spectral range.

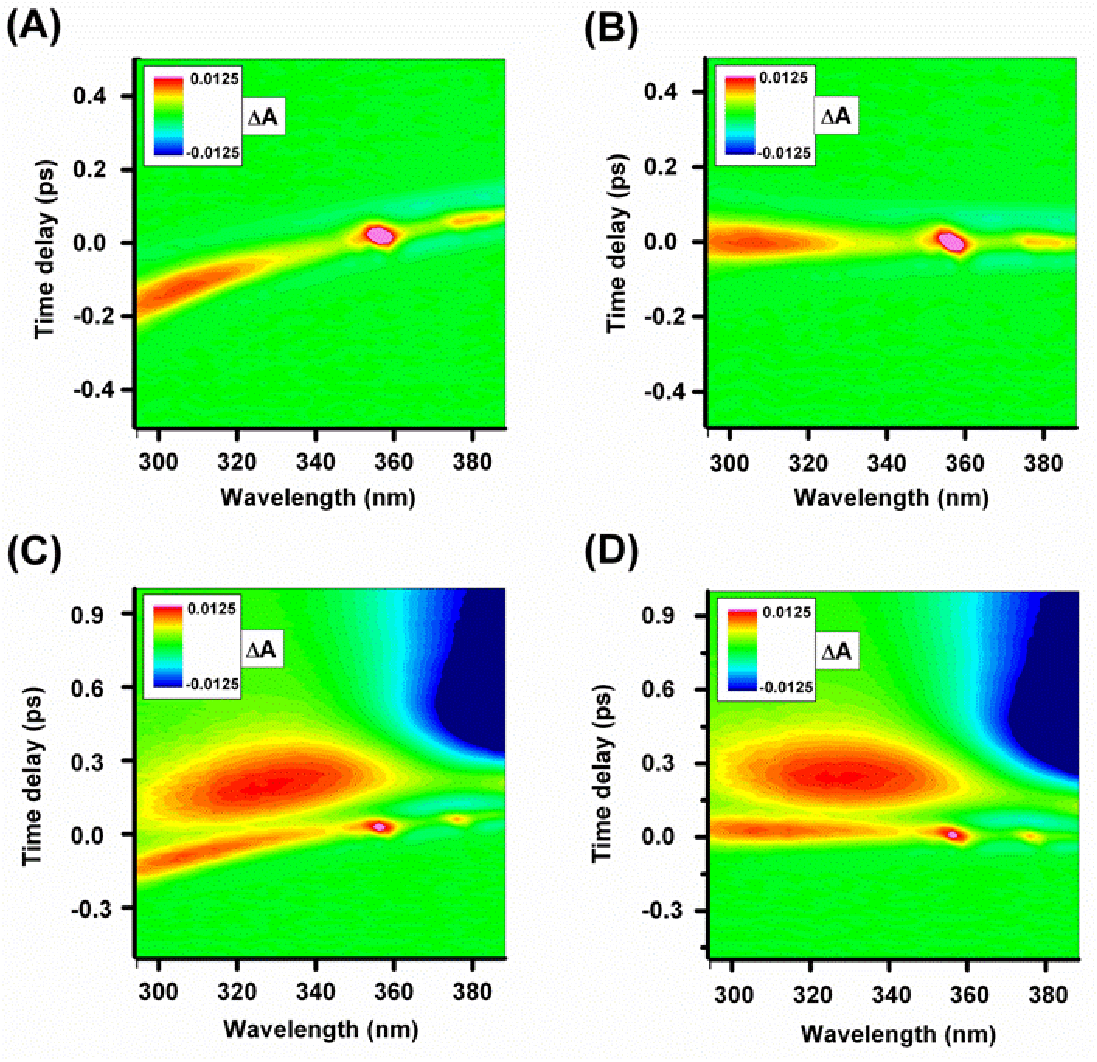

Figure 2.16. **A**. Spectro-temporal transient absorption raw data of methanol in the quartz capillary in the UV region for time delays between -0.5 and 0.5 ps. **B**. Same as A after GVD compensation. **C**. Spectro-temporal transient absorption raw data of ZW-NAIP in methanol in the -0.5 to 1 ps time range. **D**. Same as C after GVD compensation. In figures C and D, the solvent signals overlap with the ESA and GSB of the ZW-NAIP photoswitch.

3. Solvent contribution subtraction

In all the transient absorption experiments which are considered in the next Chapters, the combined response of pure solvent and quartz capillary is always measured, in the exact same experimental conditions as for the sample we want to investigate. This solvent response overlaps with the one of the sample in a ~200-fs time window around time zero. This ultrafast contribution can be neglected if the dynamics at stake are slow compared to its duration. But as it will be presented the excited-state contributions are too short (as fast as 100 fs) to neglect this solvent correction[2, 104, 105].

Figures 2.17C and F present the result of the subtraction of the solvent data (figures 2.17B and E) from the raw data (figures 2.17A and D) in the UV and Vis regions, respectively. The subtraction is performed in the time window of interest that is between -0.5 and 0.5 ps. A multiplication factor (always <1, wavelength-independent) is used to take into account the sample absorption at the excitation wavelength, which indeed reduces the amplitude of the solvent contribution in the sample data. More than 90% of the solvent contribution can be removed with this subtraction.

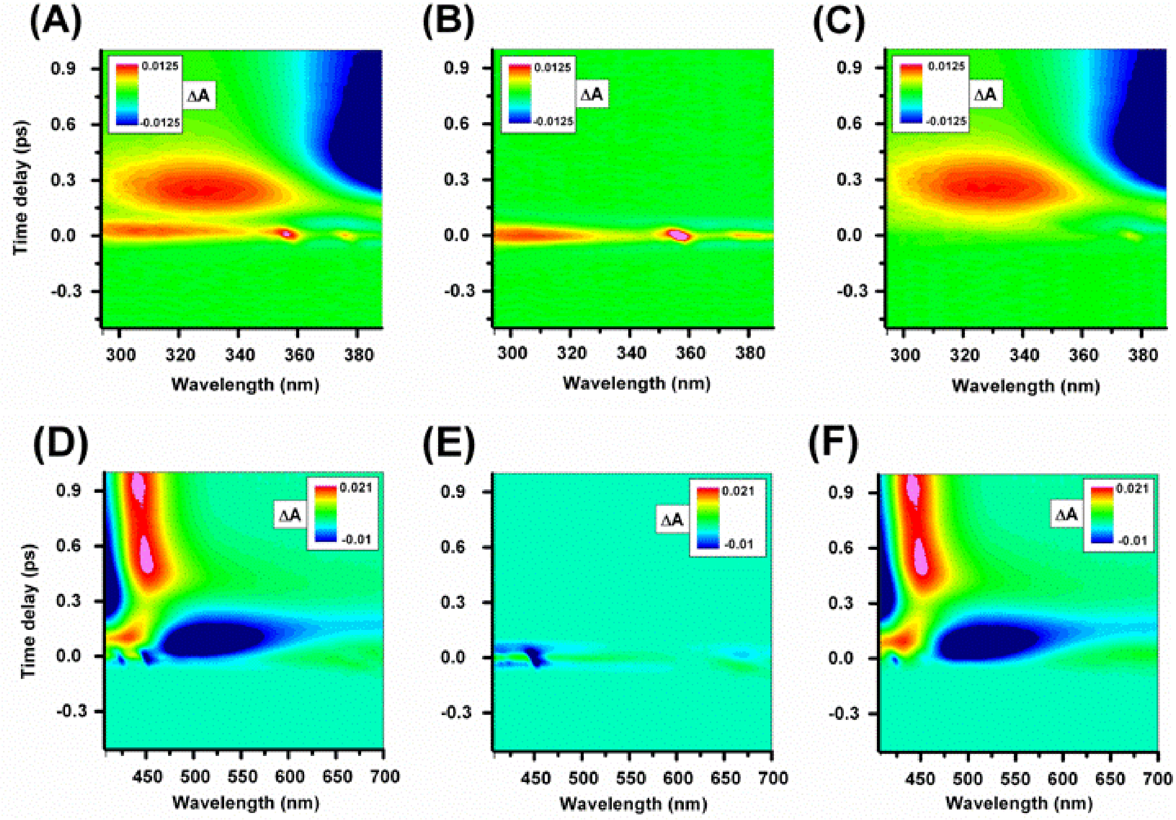

Figure 2.17. **A**. Time-resolved UV transient absorption change ΔA data of ZW-NAIP, containing the solvent (methanol) signal around time zero. Positive ΔA is coded in red and negative in blue. Note that the color scale is the same in B and C. **B**. Time-resolved visible transient absorption data of the solvent signal measured separately under the same experimental conditions. **C**. Result of the substraction of the solvent signal from the raw data. **D**, **E** and **F**. Same as A, B and C, respectively, but in the visible region of the spectrum.

A procedure for this type of "artifacts'" subtraction is explained in detail in reference[104]. In the present case their theoretical factor was taken as a reference starting value and the subtraction factor was then improved by closely looking at the subtracted data, and notably checking the results at wavelengths where methanol Raman signals are observed.

Other solvents than methanol have also been used. Deuterated methanol-d4 is used in Chapter 5 and a sample is diluted in two other alcohols (butanol and decanol) in Chapter 6. Their responses under 400-nm pump excitation are all similar to what has been presented for methanol.

Figure 2.18 shows the solvent subtraction result at selected wavelengths. In each plot the kinetic traces of the pure solvent response, the photoswitch and solvent solution transient and the trace resulting from the subtraction are plotted. The effect of the solvent contribution can be removed, yielding a more reliable analysis of the sample ultrafast dynamics.

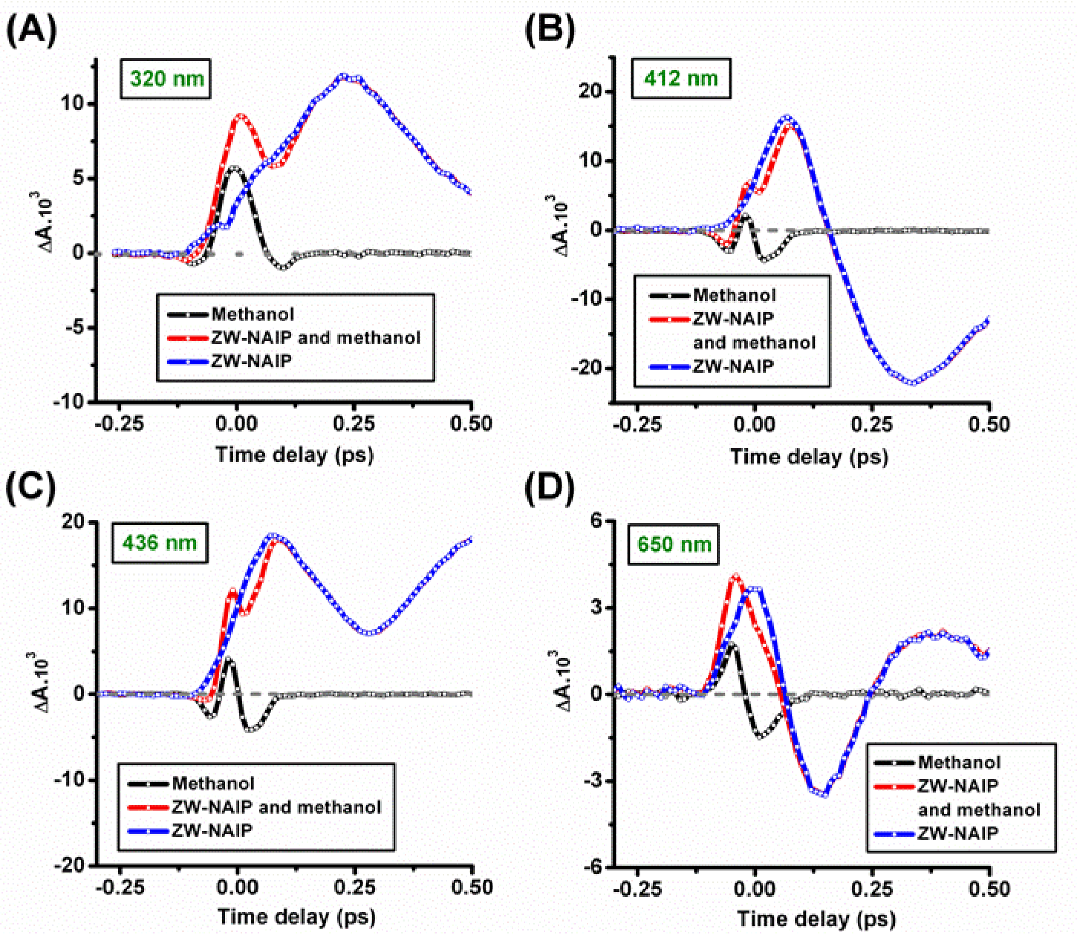

Figure 2.18. Kinetic trace of ZW-NAIP containing the solvent response (red curve), kinetic trace of the pure solvent (black curve), and result of the subtraction (blue curve) at 320 nm (**A**), 412 nm (**B**), 436 nm (**C**), and 650 nm (**D**).

D. Introduction to data analysis

1. Exponential kinetics

Transient absorption data very often involve contributions from different transitions that are spectro-temporally overlapping. The corresponding processes possibly occur on different time scales. For a quantitative analysis of the population dynamics, the data have to be fitted according to a model.

A common model to describe the transient response of multi-level systems is presented below. It assumes that the kinetics of the system can be fully described by rate constants (or decay constants) corresponding to transitions between energy levels. This stochastic description implies that coherent optical effects are not occurring, or that they occur on time scales orders of magnitude smaller than the one we expect to model. This means that the initially-created wavepacket rapidly relaxes towards a quasi-stationary distribution, and that coherence effects (see Chapter 1) or vibrational relaxations are not present in (or faster than) the considered dynamics. Within the validity limits of such a model, one can solve the linear system of rate equations (for a general example on 3-level systems see reference[106]), that are first-order differential equations. It yields a sum of decaying exponential functions multiplied by the Heavyside step function $H(t-t_0)$ centered on the signal onset time t_0:

$$H(t-t_0)\times\sum_i A_i e^{-\frac{t-t_0}{\tau_i}} \qquad (2.7),$$

where A_i is the amplitude of the $i^{\text{-th}}$ decay constant τ_i. The decay time constants are thus describing the population dynamics (statistical kinetic evolution) of the system under study, from its out-of-equilibrium position induced by the excitation, back to the ground state equilibrium.

According to this model, the experimental kinetic traces (transients) may be analysed using a sum of exponential functions (eq. (2.7)) convoluted with the instrument response function (IRF) of the experimental setup:

$$Fit(t) = H(t-t_0)\times\sum_i A_i e^{-\frac{t-t_0}{\tau_i}} \otimes IRF \qquad (2.8)$$

Assuming a Gaussian shape of the IRF (see fig. 2.11), the analytical expression of eq. (2.8) is:

$$Fit(t) = \sum_i \frac{A_i}{2}.e^{-\frac{\sigma^2}{2\tau_i^2}}.e^{-\frac{t-t_0}{\tau_i}}.\left[(1+erf\left(\frac{t-t_0-\sigma^2/\tau_i}{\sigma\sqrt{2}}\right)\right] \qquad (2.9),$$

where *erf* designates the error function and σ is the standard deviation of the Gaussian IRF. Hence, the Full-Width-at-Half-Maximum (FWHM) of the IRF is:

$$FWHM = \sigma \times 2\sqrt{2\ln(2)} \qquad (2.10)$$

The function is implemented in Origin (OriginLab, inc.) and is used to fit the experimental data, the residuals being minimized using a least-square method (χ^2 value) implemented into an iterative algorithm.

An example of fit using this function on a bR transient in the ground state bleach region (568 nm) is given in figure 2.19. Four time constants are sufficient to fit the data, as highlighted by the residuals flatness. The values are in good agreement with previous work[11, 12, 14]. Another important outcome of the procedure is the amplitudes (A_i) associated to the different time constants (τ_i) of the fit, and we will refer to them in the next Chapters.

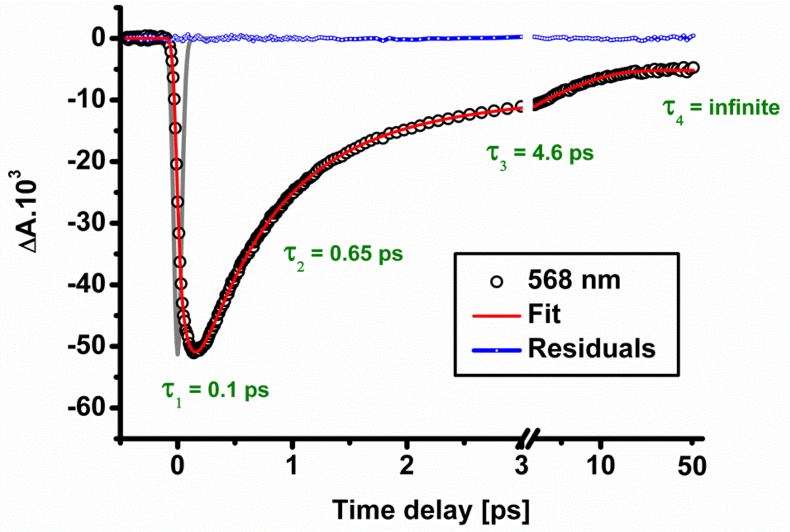

Figure 2.19. Example of fit (red line) on bR data at 568 nm (black circles) together with the fit residuals (blue line). The Gaussian IRF (grey line) is also plotted.

2. Singular Values Decomposition and Global Analysis

Singular Value Decomposition[107-109] (SVD) is a linear algebra matrix factorization method which can be used as a noise filtering or data reduction procedure. The SVD theorem stands that any matrix of dimension *(m x n)*, and in particular the **ΔA(λ,t)** matrix acquired by TA spectroscopy, can be decomposed into the following product of three matrices:

$$\Delta A(\lambda, t) = U.S.^{t}V \qquad (2.11)$$

where $^t\mathbf{V}$ corresponds to the transpose of matrix **V**. Matrices **U** and $^t\mathbf{V}$ are orthogonal, unitary and of dimension *(m x m)* and *(n x n)*, respectively. The *(m x n)* **S** matrix is only containing diagonal elements, sorted in decreasing order and referred to as the singular values (SV).
When the dynamics are purely stochastic (see discussion above), then eq. (2.11) can thus be written:

$$\Delta A(\lambda,t) = U(\lambda).S.^tV(t) \qquad (2.12),$$

where wavelength and time variables are separated. Hence the columns of **U** correspond to basis set of spectra (referred as singular spectra in the following) and the columns of **V** to basis set of transients (singular transients). It should be mentioned that these singular spectra and transients do not correspond to real data, and that only a linear combination given by equation (2.12) permits to retrieve meaningful data.

Discrimination between singular vectors carrying dynamical information on the system under study and those associated to noise can be made. The number of significant components is the number of singular values (diagonal elements of **S**) which sufficiently differs from the noise level.

An experimental dataset has been presented in figures 2.13 and 2.14. It is a bR transient absorption measurement in the 410-720 nm region. As already mentioned, in bR, spectro-temporal relaxation takes place in the excited state on a short time scale. Moreover, we observe 2 to 3 weak, anti-phased and low- frequency (~180 cm^{-1}) oscillations in the transients around 520 nm and 700 nm. These types of processes break the separability of time and wavelength variables, as they are wavelength-dependent time evolutions. This is why the SVD procedure (and further global analysis, see below) is applied on the subset of data corresponding to time delays >0.5 ps.

A typical outcome of this procedure is presented in figure 2.20.A, where singular values are plotted. One may identify the first 3 or 4 SV as being distinct from the others. Their associated singular spectra and transients are carrying the spectral and dynamical information about the bR system, and the others do not contain any information, and are thus corresponding to noise. In fact, a careful selection of the most significant singular values (SV) always has to be made. A practical way of choosing the number of SV kept for analysis is obtained by subtracting the raw data set with the reconstructed matrix using the pre-selected SV. When featureless residuals are obtained by this subtraction, the SV selection is stopped, the vectors associated to SV of higher index only consisting of noise. In figure 2.20.B featureless residuals are obtained by subtracting the reconstructed matrix (considering the first 4 SV) from the raw data.

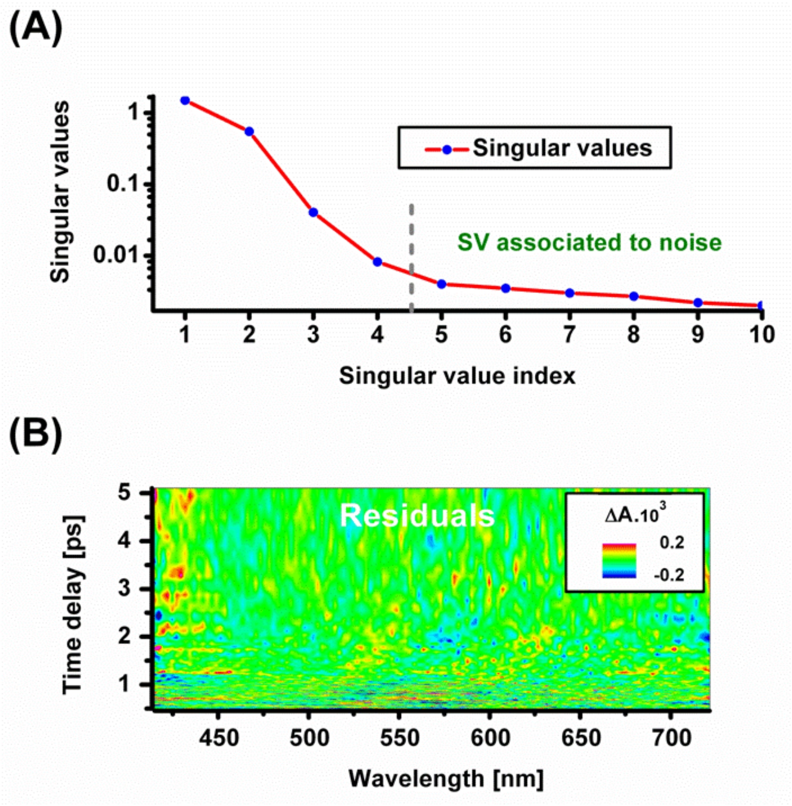

Figure 2.20. **A**. First ten Singular Values (blue dots) from the data SVD decomposition. **B**. Featureless residuals obtained by subtracting the reconstructed matrix with the first 4 SV from the raw data set.

The selected singular transients, weighted by their associated SV, are then used for analysis. Their fitting is performed using a sum of exponential functions such as the one described in eq. (2.9). A global analysis, i.e a simultaneous fit of these time vectors is made, setting parameters such as exponential decays (τ_i) and experimental-dependent parameters (t_0, σ) as global parameters, while leaving the amplitudes (A_i) as local ones. With this procedure, the data dimensionality is greatly reduced, and the global fitting of these weighted SV transients enables to catch global time constants describing the system dynamics while saving computational time. Figure 2.21.A shows the fit of the weighted first 4 singular transients of the bR data. Residuals in the experimental noise level are obtained using 4 time constants of 0.53, 0.93, 6.2 ps and one of infinite time. They are shown in figure 2.21.B.

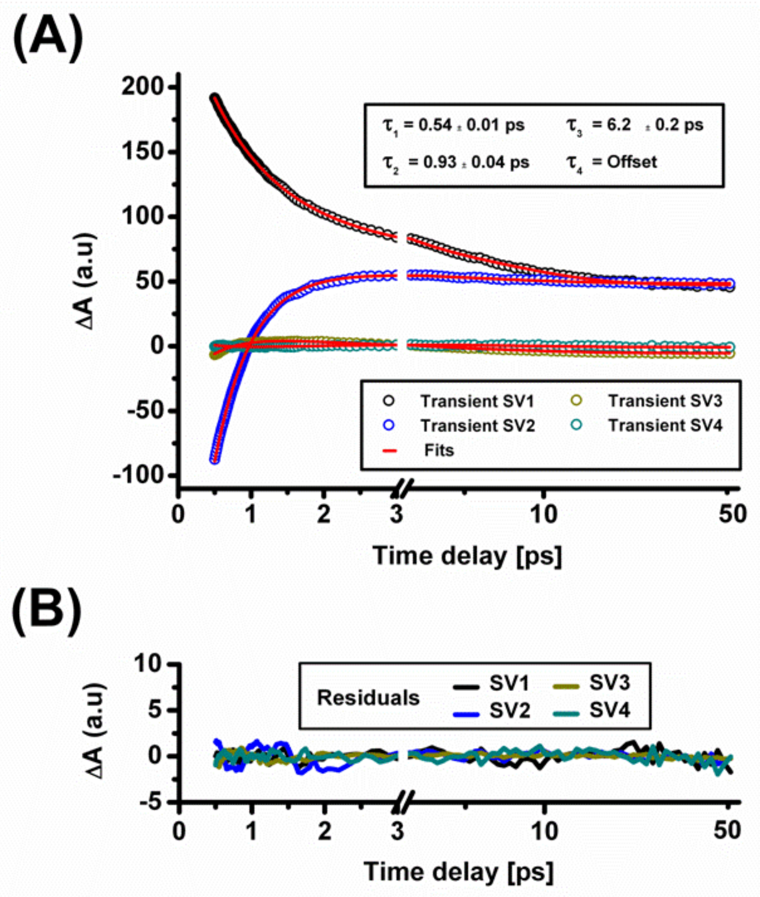

Figure 2.21. **A**. Global fitting of the four prominent (weighted) singular transients (black, blue, gold and cyan circles, respectively) for the full transient absorption spectral dataset analysed at time delays > 0.5 ps, and their corresponding fits (red lines). **B**. Residuals of the global fit for the singular transients.

The final step is the reconstruction of the Decay Associated Difference Spectra (DADS) of the decay time constants obtained by the global fitting[107-109]. A linear combination of the decay-associated amplitudes and the singular spectra yields DADS:

$$DADS_i(\lambda) = \sum_{j=1}^{N} A_{j,i}.U_j(\lambda) \qquad (2.12)$$

where $A_{j,i}$ are the different amplitudes associated to the time constant τ_i of the j^{-th} singular transient, N being the total number of singular values kept for analysis. Each $DADS_i$ represents the spectral dependence of the amplitude associated to a given decay time constant τ_i. A DADS spectral shape is a sum of amplitudes of different processes (e.g. ESA, SE, GSB, PA) evolving on the same time scale.

The DADS obtained for the bR example are presented in figure 2.22. The first DADS which decays in 0.53 ps contains contributions from SE (negative amplitude for λ >550 nm) and ESA (positive amplitude for λ <520 nm, see figure 2.22.A). The GSB recovery and PA rise are also present but hidden by the first two stronger contributions. The quasi-static DADS (blue line, infinite on the measurement time scale), corresponding to the difference spectrum of bR and its photoproduct K, showing that bR isomerization has occurred, is plotted in figure 2.22.B. The 0.93 and 6.2-ps DADS mainly show ground state contributions (GSB and PA). These time constants are not perfectly matching the “reference” time scale (~3 ps) introduced in Chapter 1, especially the 0.93-ps one. The difference is likely due to the 400-nm pump beam which excites the retinal in S_3 (rather than S_1 with the usual 570 nm pump), as pointed out in reference[14], where the J photoproduct seems to appear with two separate time constants in that case.

Even though SVD and global analysis have to be used and interpreted with care, it is able to give information on large spectral ranges that we will use in the next Chapters.

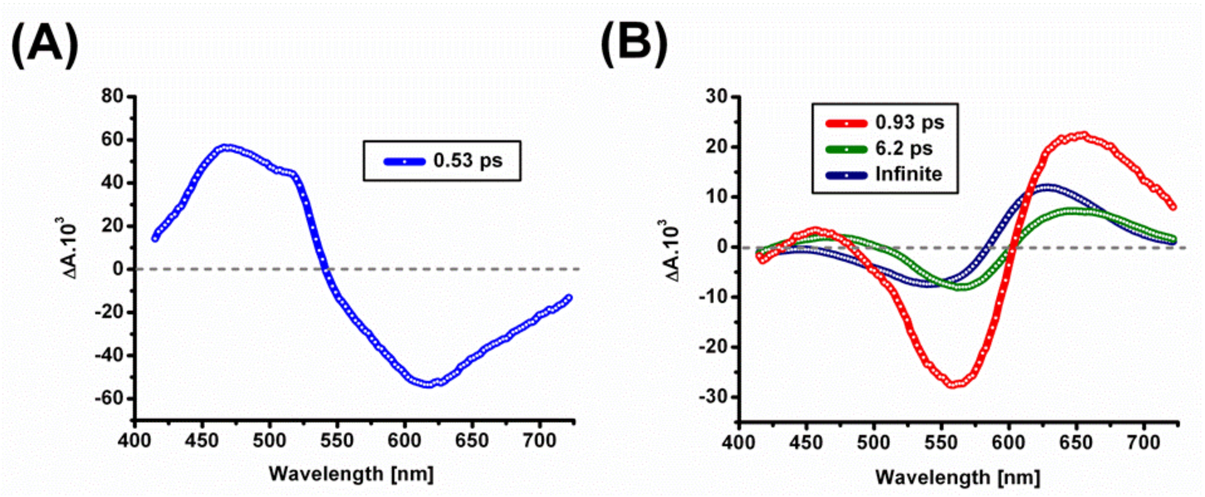

Figure 2.22. **A**. 0.53-ps DADS obtained by SVD and global analysis on bR data. **B**. 0.93, 6.2 and infinite DADS of bR.

Chapter 3

Introduction to IP-based photoswitches

A. Motivation for new biomimetic molecular switches

The design and preparation of new molecular photoswitches is a research area of interest, as providing novel materials, with alternative (or better) properties than already existing photoswitches can be an attractive target towards applications. Creating new molecular switches, differing in size, polarity, photoisomerization mechanism, and possibly providing a higher quantum yield, can offer new possibilities for example in the fields of molecular motors, or light-control of biological functions.

The strategy employed in the present case consists of combining two different approaches[53]. The first one is to be inspired by the locked skeleton of Diarylidenes' structure (see fig. 3.1). These are molecules capable of rotation around a single photo-isomerizable bond. A structure based on this framework already avoids the issue of bond selectivity, i.e. competing isomerization channels, as in retinal.

The second and novel approach is to include the electronic structure and photoisomerization mechanism of the best existing photoswitch, rhodopsin, the visual pigment of higher organisms (see Chapter 1). The retinal protonated Schiff base chromophore (see fig. 3.1) of rhodopsin is to date the fastest known and the most efficient *E/Z* (*cis/trans*) photoswitch. The isomerization selectivity, directionality and efficiency of retinal chromophores are lost when they are irradiated in solution[44]. In other words, the efficiency of the reaction is greatly enhanced by the protein environment. These unique and attractive properties thus make this system a reference and inspiring model for the design of this new class of biomimetic molecular switches. The design and synthesis challenges are to incorporate into the synthetic photoswitch structural features that confer photo-physical properties similar to the ones of retinal embedded in a protein.

As far as reaction speed is concerned, a barrierless excited-state potential is a minimum requirement. To this end, it is obvious that destabilizing the central isomerizing double bond will help in making it single-bond like. The dipole moment change or charge translocation character of the first excited state is a key ingredient in the retinal protonated Schiff base of rhodospsin[35, 110] and we will show in § 3.B.2.b that it is very similar in IP-based switches. Indeed, calculated barrierless reaction minimum energy path (§ 3.B.2.c) and ultrafast evolution on the excited-state potential energy surface (§ 3.B.2.d) show that molecular switches based on the Indanone-Pyrroline (IP) framework (see fig.3.1) is one way of replicating photophysical properties of the protein-embedded retinal chromophore[1, 2, 53].

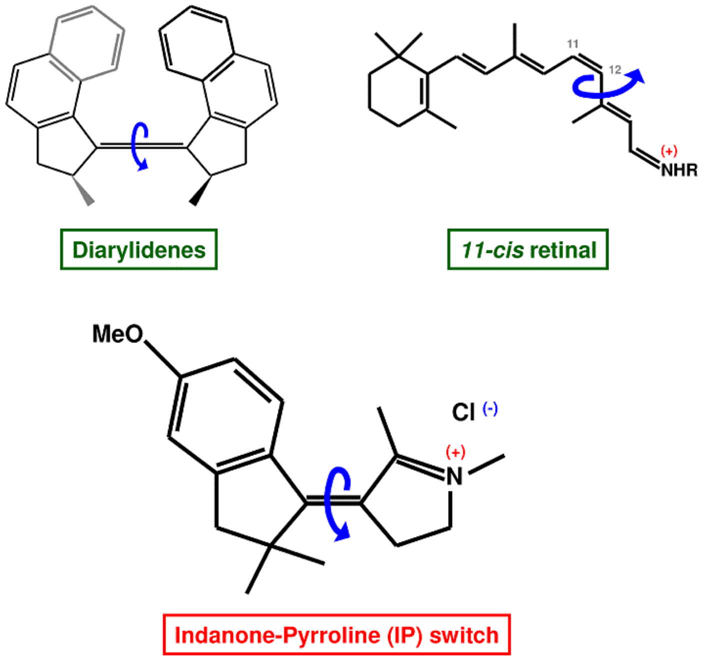

Figure 3.1. Molecular structures of diarylidenes molecules and *11-cis* retinal inspiring the Indanone-Pyrroline(IP)-based photoswitch family.

The IP-based photoswitches are also synthetically flexible. This allows the preparation of switches with tunable maximum absorption wavelengths (see fig. 3.7.B for example, 360nm < λ_{max} < 430 nm). Substitutions or incorporation of several groups are accessible (methoxy group, alkylation …) in order to modify the π-orbitals system, or for example incorporate a permanent dipole moment on the rotating part (see ZW-NAIP structure in fig. 3.7.A). Work is also in progress towards functionalization and incorporation of such switches into peptides. In addition, these molecules are also soluble in polar solvents and their isomerization efficiencies are already comparable to azobenzene.

The molecule synthetic procedures are described in detail elsewhere[1, 111, 112] and are out of the scope of the present work. One may add though that, as the synthesis requires several steps, and thus time, efforts are currently made to achieve a self-assembling IP-based photoswitch.

B. Calculated properties of IP-based photoswitches

1. Quantum Mechanics / Molecular Mechanics (QM/MM) methods

The *ab initio* (first-principles) complete-active-space self-consistent-field (CASSCF) quantum chemical method[113] is a multiconfigurational procedure for a description of the electronic and equilibrium structure of a molecule.

These CASSCF wave functions can be used for multiconfigurational 2nd-order perturbation theory computations[114, 115] (CASPT2) of the dynamic correlation energy of each electronic state, which leads to quantitative evaluations of the excitation energies (S_0-S_1) and, although with less precision, excited-state energy differences S_1-S_n.

An *ab initio* CASSCF//CASPT2 protocol in a quantum mechanics/ molecular mechanics (QM/MM) scheme has been recently implemented by M. Olivucci and co-workers[50]. Equilibrium geometries and electronic energies of the system under study are determined at the CASSCF and CASPT2 levels, respectively.

This allows for the evaluation of the excitation energy of chromophores (treated quantum mechanically) embedded in protein and solution environments (described by molecular mechanics (MM) AMBER force fields). The errors obtained with this protocol compared to experimental data (examples are rhodopsin and retinal in solution[49, 50, 53, 116, 117] or GFP[53, 118]) are of only a few kcal.mol^{-1} (~15 nm, < 5% error on S_1-S_0 energy), indicating the accuracy of this approach.

As these methods, at the cost of calculation time, allows for realistic modelling of the excited states of solution-phase (methanol) protonated and N-alkylated Schiff bases such as the IP-based switch presented in figure 3.1, they were used to describe in details the excited state and photochemical reaction paths of the IP-based photoswitches[1, 2, 111]. This *ab initio* CASSCF//CASPT2 method is thus considered to be a good compromise between computational cost and accuracy, the latter being important for comparison with experimental data.

2. Predicted properties of IP-based photoswitches

a. Ground state structures and absorption spectra

The schematic structures of both isomers of the methoxylated MeO-NAIP (see § 3.C.1 also) photoswitch are indicated in figure 3.2A. The 3D structures and details about the QM/MM geometry optimization can be found in reference[2]. An important remark is that the molecule is not completely planar. As the structure is already twisted around the central C=C double bond (by ~11°) in the ground state equilibrium conformation (Z), it is, in a geometrical point of view, a “ready-to-isomerize” structure.

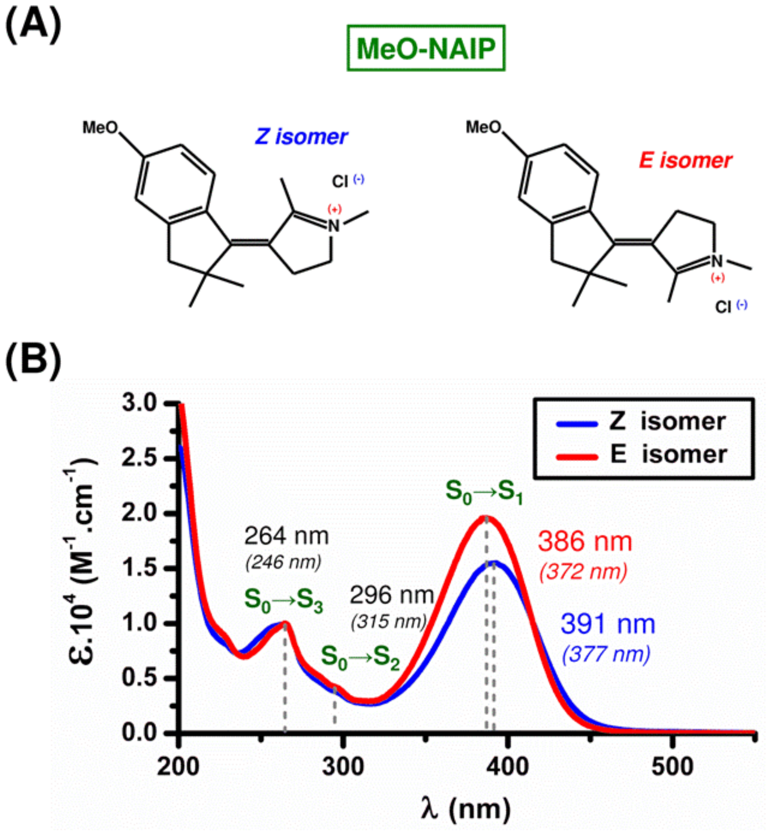

Figure 3.2. **A**. Structure of both Z (*cis*) and E (*trans*) isomers of the MeO-NAIP photoswitch. **B**. Absorption spectra of both Z (blue line) and E (red line) isomers[2] together with absorption bands maxima from absorption measurement and calculations (values in parenthesis), showing the accuracy of the predictions for the first three excited-state transitions from the ground state.

The QM/MM results allow for the assignment of the absorption bands found in experimental absorption spectra. Figure 3.2.B shows the experimental absorption spectra of both Z and E isomers of MeO-NAIP. The more intense band at 391 nm is assigned to the $S_0 \rightarrow S_1$ transition, while the shoulder at 296 nm and the band at 264 nm correspond to $S_0 \rightarrow S_2$ and $S_0 \rightarrow S_3$ transitions, respectively. The values of the calculated absorption maxima of these three bands are accurately predicted (see values in parenthesis) and the calculated oscillator strengths of the transitions are also consistent with experimental data (MeO-NAIP: f = 0.55, 0.06 and 0.07 for $S_0 \rightarrow S_1$, $S_0 \rightarrow S_2$ and $S_0 \rightarrow S_3$, respectively). Moreover, the calculated dipole moment changes upon $S_0 \rightarrow S_1$ excitation are 8.3 and 10.5 Debyes for Z and E isomers, respectively, very close to the value found for rhodopsin[50] (11D).

b. Charge translocation in the excited state

As mentioned in § 3.A, the photo-induced charge transfer is a key parameter[35, 110]. The retinal chromophore has an extended conjugated π-system along the retinal polyene backbone to the β-ionone ring, which paves the way for an efficient excited-state charge translocation of the positive charge located on the $N{=}C_{15}$ moiety.

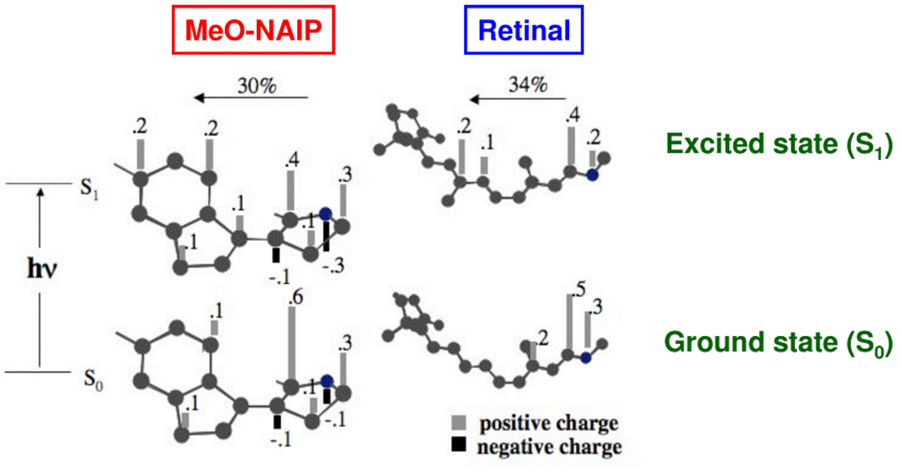

Figure 3.3. Computed ground state charge distributions for MeO-NAIP switch and retinal, together with the excited state charge distributions upon vertical excitation. The charge translocation values are similar in both cases (30 and 34%, respectively). Partial charges are given in atomic units. Figure adapted from references[2, 53].

The similarity between the IP-based photoswitch models and the electronic structure of the retinal molecule is evident when the computed charge distribution[1, 2, 53] is plotted (see fig. 3.3). Briefly, the data indicate that, upon excitation, the molecule undergoes a 30% charge transfer through its reactive central double bond. This value is very close in magnitude compared to the 34% charge transfer observed for rhodopsin. This means that ~30% of the positive charge located on the pyrroline ring in the ground state is shifted onto the indanone ring thanks to its ability to stabilize it in the excited state.

Figures 3.4.A, B and C show simplified pictures of the conjugation mechanism, the translocation route and the charge distribution in the ES, respectively. They show the conjugation of the π-orbitals which allows delocalizing (in the excited state) the positive charge over the entire molecule. The central isomerizable bond is then weakened and reveals a single bond character in the excited state allowing the pyrroline group to rotate, as highlighted in figure 3.4C.

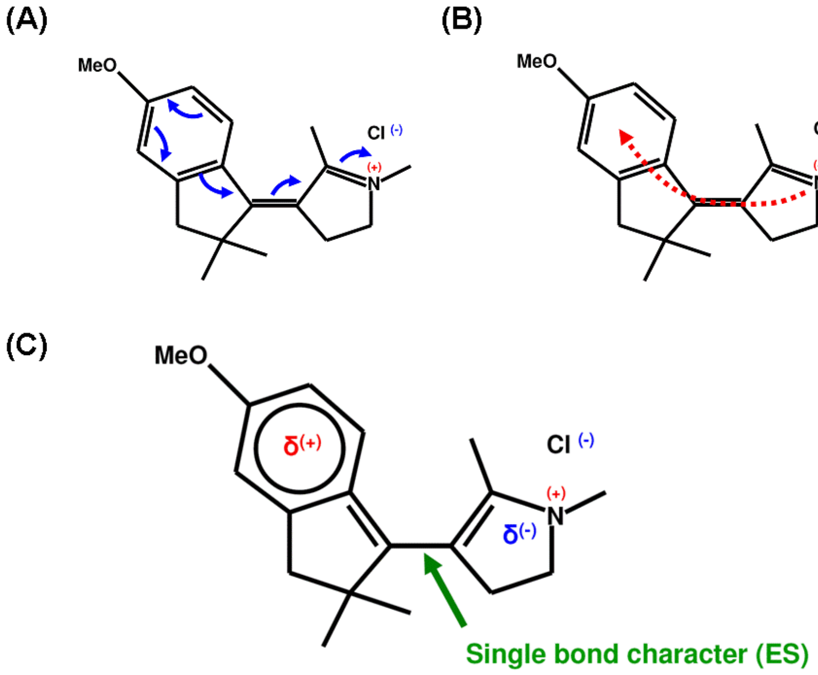

Figure 3.4. **A**. General conjugation mechanism of the π electronic orbitals in IP-based molecule. **B**. Arrow showing the translocation route of the positive charge from the pyrroline moiety to the phenyl ring after optical excitation. **C**. In the excited state, the positive charge translocation brings a single bond character to the initial central double bond, allowing isomerization to proceed.

c. Potential energy surface (PES) and reaction path calculations

Using the QM/MM computational methods, the CASSCF//CASPT2/AMBER photoisomerization path, the so-called minimum energy path (MEP), has been computed for both *Z*→*E* and *E*→*Z* reactions in methanol solution. The results show that both reaction mechanisms primarily involve only 2 modes, the stretching and twisting of the central double bond (see Chapter 1 also). The stretching is related to the bond order change and subsequent C=C bond length relaxation and acts on a very short time scale (<50 fs). The torsional mode, corresponding to the twisting of the C=C bond, occurs with a period of a few hundreds of femtoseconds.

Figure 3.5, adapted from reference[2], presents the calculated energy differences between the ground state (S_0) and the first excited state (S_1) along of the reaction coordinate, the torsional mode. Both

Z→*E* and *E*→*Z* reaction mechanisms feature barrierless reaction paths. It suggests that this IP-based photoswitch family has an ultrashort excited-state lifetime, and thus a very weak fluorescence, whose maximum is computed to be located at ~520-530 nm. The fluorescence (or stimulated emission) window should be associated to small torsion angles, as indicated by the computed oscillator strength of the S_0→S_1 transition[2]. A conical intersection (CI) is accessed at a ~90° twisted structure, and then the E isomer ground state is reached, giving a structure ~180° twisted around the central bond. A non-reactive path leads back to the Z isomer, as observed for other switches (Chapter 1), and the quantum efficiency is thus the ratio of the E isomers formed over the total number of excited Z isomers.

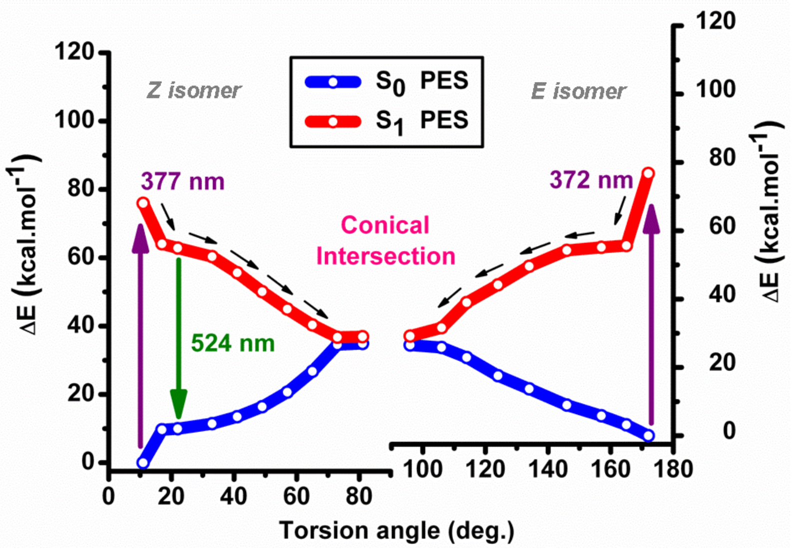

Figure 3.5. Computed minimum energy paths (MEP) of the potential energy surfaces (PES) of the ground state (S_0) and first excited state (S_1) for Z→E and E→Z photochemical reaction along the isomerization coordinate (torsion). This shows the barrierless path for both reactions. Vertical arrows indicate calculated electronic transitions (absorption in purple, emission in green). Figure adapted from Sinicropi et al.[2].

d. Population dynamics simulations

The *Z*→*E* reaction path presented above can be used by a quasi-classical wave packet trajectory to estimate the excited-state lifetime. The photoisomerization of IP-based switches have been reduced to a 2-mode / 2-state model, as indicated above. The two modes driving the reaction are the stretching mode (corresponding to the expansion of the double bond and contraction of the single bonds) and the reactive torsional mode (describing the twisting of the central double bond). This is the simplest possible parameterization of the bond-order inversion that has been previously described (see §2.B.2.b). Thus, assuming this simplification, a suitable function is fitted to the *Z*→*E* energy differences calculations. The resulting effective potential energy surface (PES) simulates the previously described S_1 *Z*→*E* energy profile (CASPT2//CASSCF/AMBER), as presented in fig. 3.5.

The S_1 excited-state population motion is then simulated by generating a classical wave packet of 1,000 trajectories defined by constructing a Wigner distribution. The results of the simulation, adapted from reference[2] and presented in figure 3.6.A, indicate that the population oscillates across -and broadens along- the reaction-path valley of the excited state without splitting. The wave packets population maxima, reflecting the average trajectory, reach the energy minimum associated to the conical intersection (CI) on a ~200 fs timescale. The model also predicts that the stretching mode is instantaneously excited, moves from the Franck-Condon (FC) out of equilibrium position towards the equilibrium on a ~20-fs timescale, and oscillates across the latter during the motion on the S_1 PES. On the contrary, the torsional mode slowly accelerates until ~100 fs, but then quickly acquires kinetic energy, most probably from the steepness of the S_1 PES slope. It thus drives the population faster from there to the CI decay point (see fig. 3.6.A and B). The 2D minimum energy path (MEP) is indicated on figure 3.6.A (white dashed line) and summarizes the simulated dynamics: the population first moves away from the FC region along the stretching coordinate on a ~20fs time scale, and then evolves along the torsional coordinate on a ~200-fs time scale.

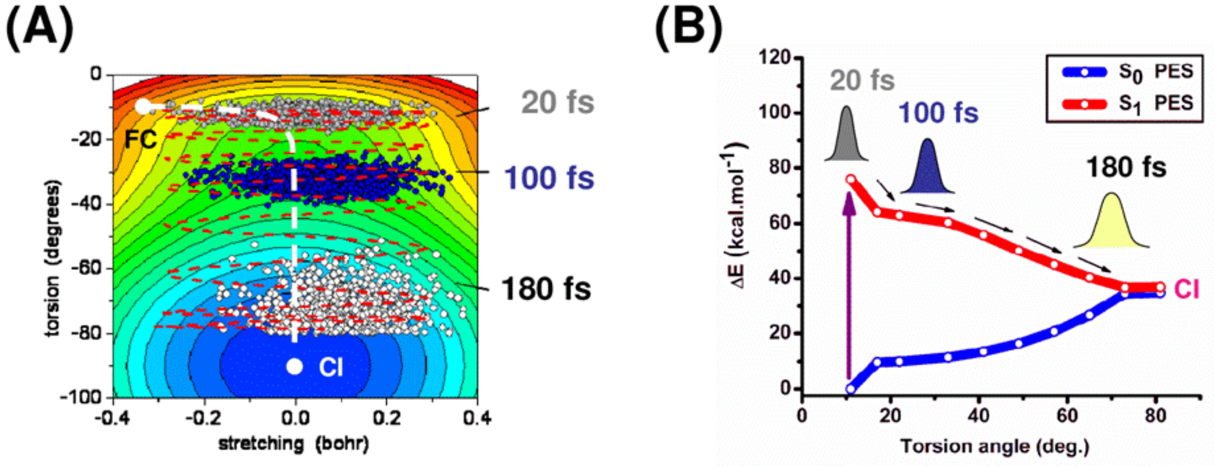

Figure 3.6. **A**. Simulation of the population dynamics using a 2D-model of the S_1 potential energy surface. The average position of the wave packet as a function of time (red dashed curve), and three snapshots of the wave packet at 20 fs (gray spots), 100 fs (blue spots) and 180 fs (white spots) are shown. In background the color contour plot of the 2D potential is included. The minimum energy path (MEP) from the Franck-Condon (FC) region to the conical intersection (CI) is indicated (white dashed line). **B**. Wave packet snapshots (at 20, 100 and 180 fs) positions along the torsion coordinate of the PES. Figures adapted from Sinicropi et al.[2]

These results (charge translocation in the excited state, barrierless reaction path including a conical intersection, and population dynamics simulation) are all very similar to what has been found for rhodopsin and point towards great expectations for a sub-picosecond excited-state (S_1) lifetime, a 2-mode (stretch and torsion) model isomerization scenario and thus an ultrafast isomerization reaction for these IP-based molecular switches.

C. Structures and static properties of the investigated IP-based photoswitches

1. Structures and absorption spectra

Different IP-based photoswitches have been synthesized[1, 111, 112] and five of them have been studied in this work by transient absorption spectroscopy.

Their structures and absorption spectra in methanol solution are presented in figures 3.7.A and B, respectively. The structure on the top left of figure 3.7.A is the parent compound, the N-alkylated Indanylidene Pyrroline (NAIP) switch, which is a chloride-alkylated Schiff base ion-pair.

The 4 other photoswitches are derived from this structure. They all feature a methoxy group linked to the phenyl ring on the indanone moiety. The MeO-NAIP switch is the NAIP one with only this methoxy group (MeO) added. The Prot-MeO-NAIP (protonated MeO-NAIP) molecule has the MeO-NAIP structure where an alkyl group on the pyrroline moiety has been protonated. The ZW-NAIP (zwitterionic NAIP) molecule possesses the same structure as MeO-NAIP except that a carboxylate acid group is added to the pyrroline ring, and thus it features a permanent dipole moment on the rotating part. Finally, the MeO-NABFP (MeO-NA BenzoFurano Pyrroline) molecule compares with MeO-NAIP except for an oxygen atom replacing a carbon on the five-membered ring of the indanone moiety.

The respective absorption spectra of the stable isomers of NAIP, Prot-MeO-NAIP, MeO-NAIP, ZW-NAIP and MeO-NABFP are presented in figure 3.7.B and have absorption maximum wavelengths ($S_0 \rightarrow S_1$ transition) at 359, 390, 391, 397 and 429 nm, respectively. Thus, adding electron-donating groups have a bathochromic effect (red-shift) on the absorption wavelength. We can already mention that, with the present structure, an efficient excited-state charge delocalization may be related with a blue-shift of the S_0-S_1 absorption maximum. Indeed, the more the excited-state structure is destabilized, the higher is the energy difference between the ground and the first excited state.

A cuvette containing ZW-NAIP molecules is presented in figure 3.7.B. These photoswitches have a more or less pronounced yellowish color depending on their absorption wavelength.

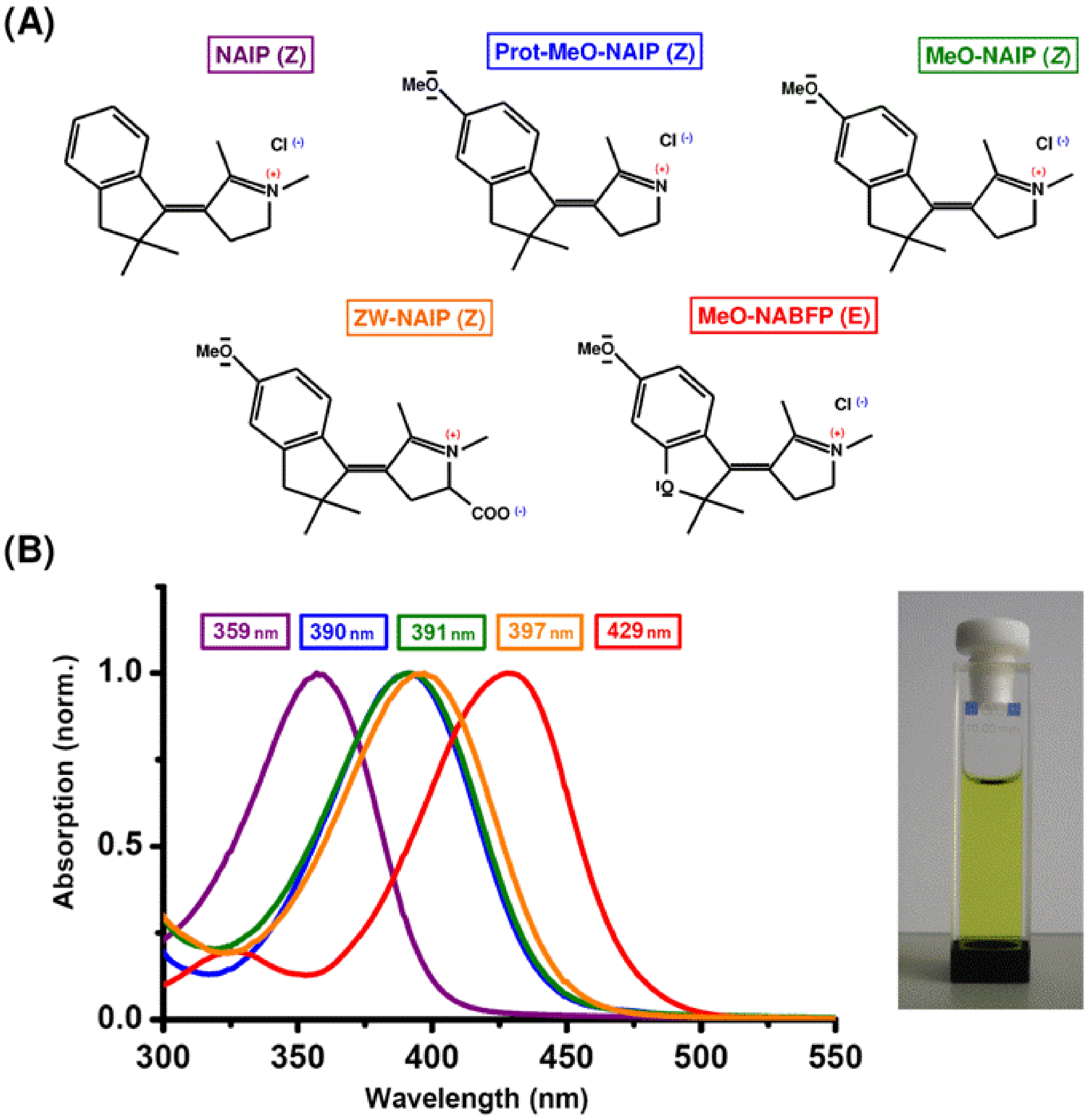

Figure 3.7. **A.** IP-based structures of the 5 photoswitches investigated. Note the change of name (E) according to CIP rules for MeO-NABFP. **B.** Corresponding normalized absorption spectra.

2. Isomer static differentiation

When freshly prepared and kept in the dark, at room temperature, 4 of these switches (MeO-NAIP, Prot-MeO-NAIP, ZW-NAIP and NAIP) present a >90 % Z-isomer ratio. Upon light excitation at a chosen wavelength at which the E isomer absorbs more than the Z one, it is possible to reverse this ratio. It has been shown that after proper illumination, the E form is stable for hours. If the sample is kept in the dark for ~24h, at room temperature, the >90% Z-isomer stationary state is recovered spontaneously[1, 2, 111, 119].

The pure E- and Z-isomer UV-Vis spectra have been determined[2], using photospectrometry techniques and High Pressure Liquid Chromatography (HPLC). We used ^{1}H-NMR spectroscopy to measure the isomer ratios, as discussed in Chapters 4 and 5. As an example, the MeO-NAIP's Z- and E-isomers molar extinction coefficients and their differences are plotted in figure 3.8.A and B. They have very similar absorption spectra in shape, but the E-isomer spectrum is blue-shifted and has a larger molar extinction coefficient compared to the Z-isomer form. Their $S_0 \rightarrow S_1$ absorption peak positions are $\lambda_{max}(E) = 386$ nm and $\lambda_{max}(Z) = 391$ nm, with extinction coefficients of 19,560 cm^{-1} and 15,480 cm^{-1}, respectively[1]. The E-Z difference spectrum shown in figure 3.8.B has a maximum at 374 nm (+ 4 630 M^{-1}cm^{-1}) and a minimum at 424 nm (- 2 060 M^{-1}cm^{-1}). The difference is relatively small, $\Delta\varepsilon/\varepsilon$ being ~35% at maximum (374 nm). The isosbestic point is located at 407 nm.

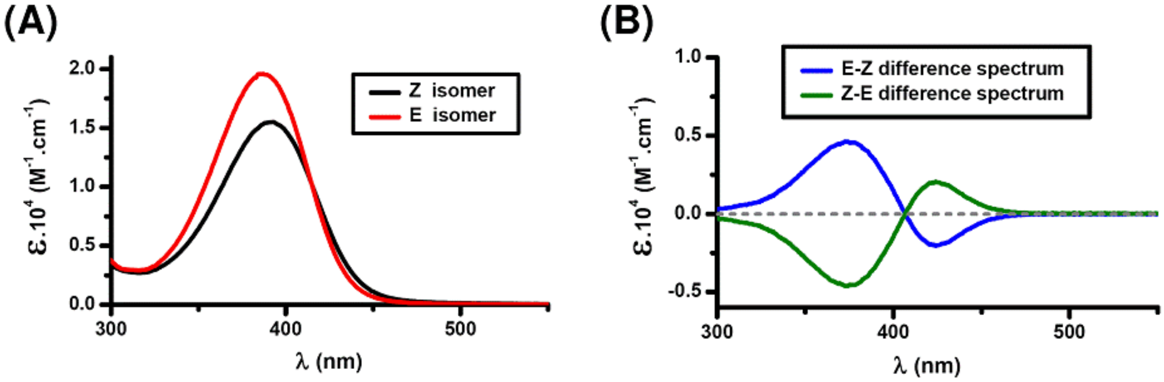

Figure 3.8. **A**. Absorption spectra of MeO-NAIP's pure E- and Z-isomers (Data from L. Latterini et al from reference[2]). **B**. E-Z and Z-E difference spectra of MeO-NAIP. The corresponding wavelengths for the extrema are 374 nm (± 4 630 M^{-1}cm^{-1}) and 424 nm (± 2 060 M^{-1}cm^{-1}).

Based on the same idea as UV-Vis absorption spectra, the pure E- and Z-isomer steady-state Fourier transform infrared (FTIR) spectra in the mid-IR spectral region (1400-1700 cm^{-1}) can also be determined. The MeO-NAIP E- and Z-isomer FTIR spectra are shown in figure 3.9.A. The main absorption band is the C=C stretch mode absorbing at 1560 and 1575 cm^{-1} for the E and Z forms, respectively. The E-Z difference spectrum is presented in figure 3.9.B (Data from Helbing et al. from reference[2]).

Much like UV-Vis ultrafast spectroscopy, ultrafast Vis pump / mid-IR probe transient absorption spectroscopy can also be used to measure and characterize the isomerization of these photoswitches through the C=C bond stretch dynamics. This study was performed in parallel by our colleagues Julien Réhault and Jan Helbing at ETH Zurich, Switzerland.

Together with to the transient absorption experiments performed in Strasbourg and Zurich, fluorescence up-conversion experiments on the photoswitches were carried out at EPFL Lausanne by

O. Bräm, A. Cannizzo and M. Chergui, in order to bring complementary and accurate excited-state lifetime measurements, as only one excited-state signal is measured (fluorescence), without any other overlapping contributions.

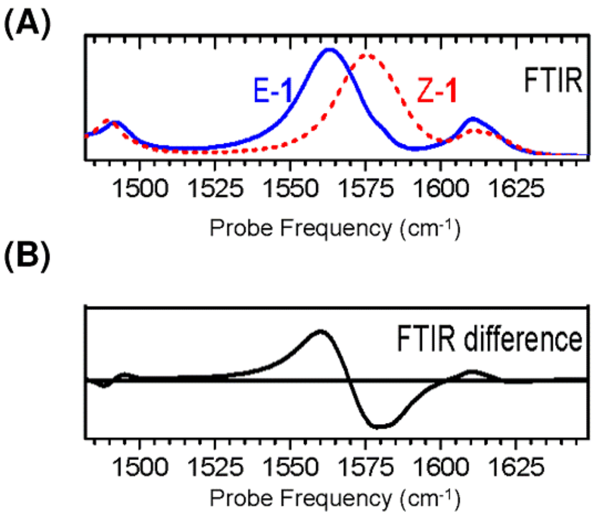

Figure 3.9. **A**. Mid-IR FTIR spectra of MeO-NAIP's E- and Z-isomers in the 1480-1650 cm^{-1} region (picture taken from Helbing et al. from reference[2]). **B**. E-Z FTIR difference spectrum of MeO-NAIP.

D. Experimental work plan

Given the calculated properties of the IP family cited above (large charge translocation in the ES, favorable calculated reaction path and population simulations), a rhodopsin-like isomerization reaction is expected. Experimental work is thus required to provide accurate experimental time scales concerning the ground- and excited-state signals, and thus the isomerization timing.

The first experimental question that is raised is whether isomerization is occurring and if it is accurately detectable (through a E-Z isomers difference spectrum). The isomerization quantum yields determined by other techniques may also be retrieved.

The second, central question is the time scale on which the different signal contributions and structural dynamics associated with isomerization are occurring. Our theoretician colleagues are expecting a sub-ps timescale of excited-state signals and isomerization reaction.

As these first questions were positively answered (see the following Chapter 4), other experimental opportunities appeared. The explanation of the dynamics at stake, the comparison between different IP-based compounds (the 5 switches shown in figure 3.7) and the effect of these substitutions were the first steps of this deeper investigation. In addition, the study of the bi-directionality of the rotation mechanism, meaning *Z*→*E* and *E*→*Z* reactions, and the investigation of the reaction dependence on the solvent properties were also suggested and performed. Finally, as it is shown in the next Chapter, 4 of the 5 studied molecules show pronounced wave packet-like signatures during isomerization, as the ones introduced in Chapter 1 (dynamic band shifts, coherent oscillations). Detailed investigations of these dynamics and a comparison between the coherent properties of the photoswitches have been achieved.

E. Sample preparation, characterization and experimental settings

1. Sample preparation

The different photoswitch samples, received as powders, are diluted to the proper optical density in commercial solvents. The most utilized solvent is methanol, as theoretical calculations are performed with this solvent environment. Deuterated methanol is also used when NMR spectroscopy is coupled to the transient absorption experiments. Dilution is performed with two other alcohols (butanol, decanol) concerning the solvent properties investigation of Chapter 6.

The optical density (OD) is set in the 0.7-1.4 mm^{-1} range at 400 nm (the excitation wavelength), except for the NAIP molecule, which absorption is the most blue-shifted and was set to an OD of 0.3 mm^{-1} at this wavelength. The OD value for a particular sample is always a trade-off between the amount of sample available, a large sample volume (large reservoir), a sufficient OD at the pump wavelength, and the fact that the probe continuum is transmitted through the sample on the whole measurement wavelength range. The fused silica capillary used for transient absorption experiments is 0.5mm-thick.

2. Experimental settings

The sample is circulated using a peristaltic pump so as to refresh the sample in between two excitation laser shots. The different sample containers are carefully kept in the dark throughout the transient absorption experiments, the steady state absorption or NMR measurements. The relative polarizations of pump and probe beams are always set to the magic angle (54.7°). The different experiments have been carried out in the UV-Vis region from 300 nm to 700 nm and in time ranges from -0.5 ps up to 100 ps. The number of time points is comprised between 250 and 300, with 10 to 15-fs steps as far as early dynamics are concerned.

The excitation of the sample by the pump pulse at 400 nm is always set in the linear regime. Figure 3.10 shows the results of the excitation density dependence of ZW-NAIP. Figure 3.10.A represents ΔA spectra in the visible at 0.4 ps for different excitation densities. The 400-nm excitation pulse Full-Width at Half-Maximum (FWHM) diameter is set to 150 µm. The energy per pulse is varied from 28 to 1000 nJ per pulse (0.16 to 5.64 mJ.cm^{-2}). Figure 3.10.C shows the ΔA values of the signal at 0.4ps at 446 nm for the different excitation conditions. The sample response is linear below 300 nJ per pulse, which corresponds to a threshold of 1.7 mJ.cm^{-2}. As shown in figure 3.10.B, the kinetic traces (example at 446 nm, but valid on the whole wavelength range) overlay well for values below this threshold.

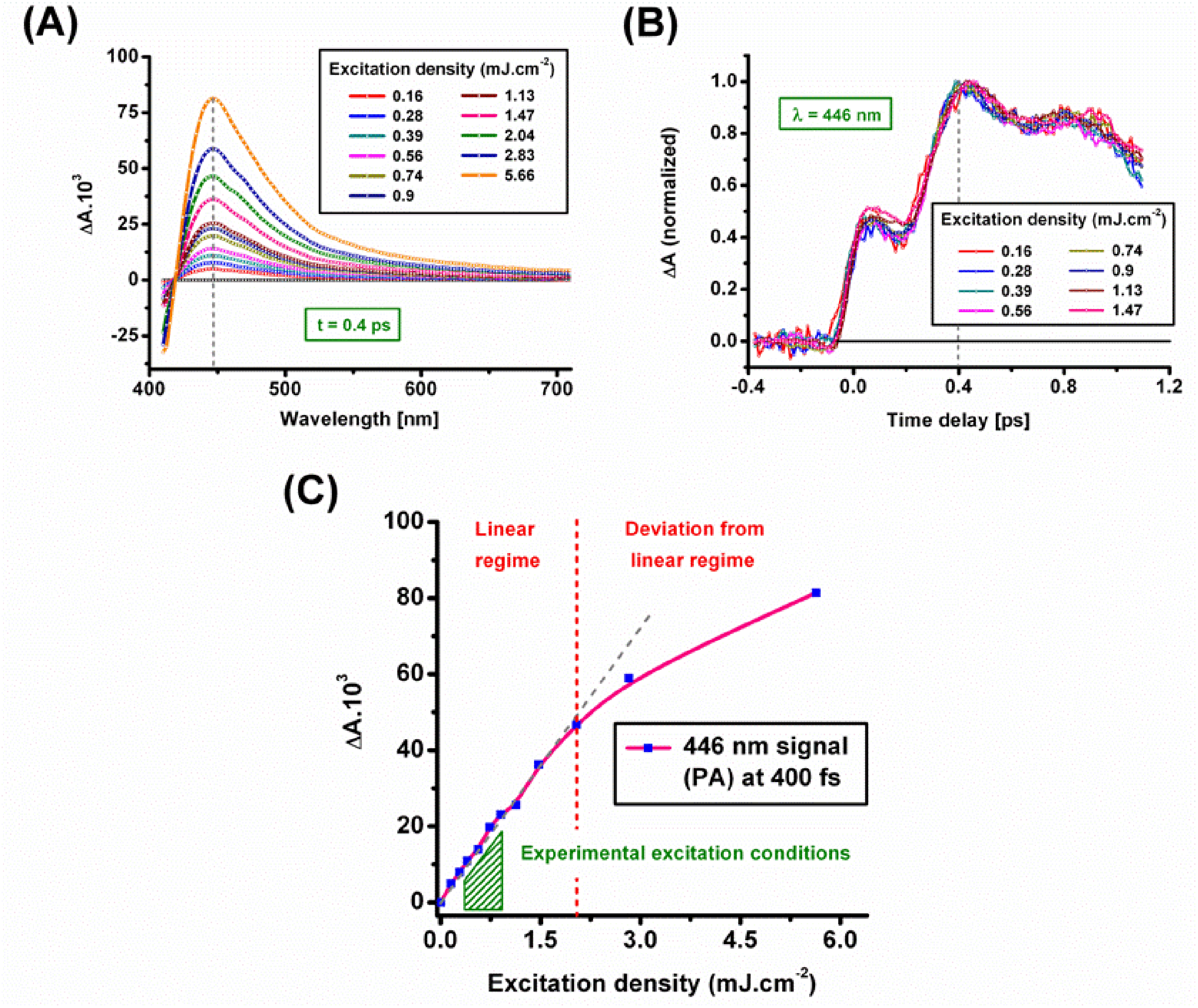

Figure 3.10. **A**. ΔA Spectra of ZW-NAIP in the visible at 0.4 ps for different excitation densities. **B**. Kinetic traces at 446 nm (from -0.4 to 1.1 ps) for different excitation densities showing the overlaying responses. **C**. ΔA signal value at 446 nm and at 0.4 ps for different excitation densities. The sample signal response is linear below a threshold value (~1.7 mJ.cm^{-2}), after which it deviates from this linear regime. The behaviour is the same on the whole measured wavelength range.

In the different experiments further presented, the values of the diameter and pump energy per pulse have been sometimes varied. Diameters from 120 to 250 µm (FWHM) and pump energies from 30 to 200 nJ per pulse have been used, corresponding to excitation densities between 0.3 and 0.8 mJ/cm^{-2}, i.e. at least twice below the linearity regime threshold. This corresponds to a ratio of excited molecules compared to the total amount of molecules always in the order of a few %.

An easy way of verifying that these different experimental conditions do not depart from the linear regime is the ΔA signal given by the molecules. The example of the hot ground state signal shown in figure 3.10 is linear up to ΔA ≤ 4-5% for this specific sample, wavelength and time delay. The hot ground state feature is common to all molecules, and unlike the bleach its maximum value is always separated from the 400-nm excitation wavelength. In addition, its dynamics seems to depend only on the solvent, not on the solute (see Chapter 4). These properties make this signal a good reference figure, and in all datasets presented in this thesis, this signal is always lower (maximum of $\Delta A=2.4\%$) than this threshold value.

This consideration is valid for MeO-NAIP, Prot-MeO-NAIP, ZW-NAIP and MeO-NABFP, whose linearities were anyway separately checked. The NAIP case is a little different, as it is weakly absorbing at 400 nm, and thus larger excitation densities were used. The linearity of the sample response with respect to the excitation density was also checked, and excitation densities values again kept at least twice below the linear regime threshold.

3. Sample characterization

Steady state absorption spectra are always measured before and after TA experiment. They are recorded using a UV-Vis spectrometer (U-3000 spectrophotometer, Hitachi). Information about possible sample degradation and isomer photoconversion are derived from these spectra. Figure 3.11.A displays two spectra of ZW-NAIP in methanol, measured right before and after transient absorption experiment. A small difference is observed. Plotting the difference of the latter spectra shows the E-Z difference spectrum (fig. 3.11.B), showing that only Z→E photoconversion has occurred during this experiment. Thus no sign of sample degradation is observed, as this change is only due to isomer photoconversion.

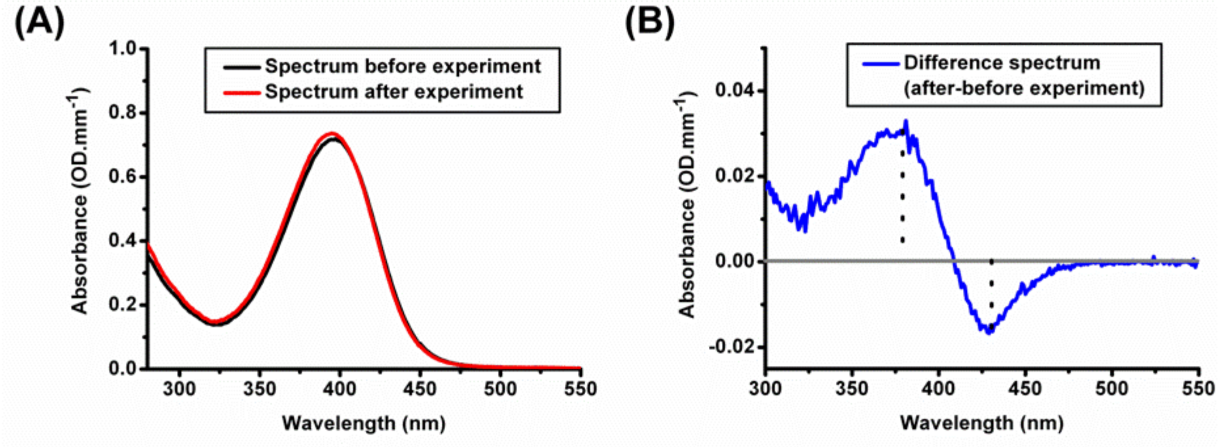

Figure 11. **A**. Steady-state absorption spectrum of ZW-NAIP before (black line) and after (red line) transient absorption experiment. **B**. Difference spectrum of the latter spectra corresponding to the E-Z difference spectrum, thus demonstrating a Z→E photoconversion during the experiment.

Nuclear Magnetic Resonance (NMR) is an important complementary technique to characterize the isomer ratio (see also Chapter 5) of the prepared samples and becomes mandatory when it needs to be precisely determined. ^{1}H-NMR spectra are acquired using a 300-MHz ^{1}H-NMR spectrometer (Avance 300 MHz, Bruker). Figure 3.12 shows an example of NMR peak-shifts measurements on ZW-NAIP ([C]=3.10^{-2} M in 1mL of CD_3OD). Two specific H-signatures, highlighted in figure 3.12.A, are displayed in figure 3.12.B and C. When the molecule is in Z or E conformation, the local environments of these two groups are changed, probably because of the effect of the methyl group located on the switchable pyrroline moiety. This produces different chemical shifts for these specific signatures depending on whether the molecule is in a Z or E conformation. Thus NMR becomes a quantitative isomer-sensitive technique, as the signals areas are proportional to the number of protons involved in the Z or E conformation. The computation of the respective areas of the signals thus gives the isomer ratio. In one case (Z isomer black curves), the sample was carefully kept in the dark. The Z isomer form represents more than 98.5 % of the molecules. The other signal (E isomer, red curves) shows the NMR spectra after a 24-h irradiation with an Argon laser at 454.5 nm. The isomer ratio is then 88.5% E : 11.5 % Z.

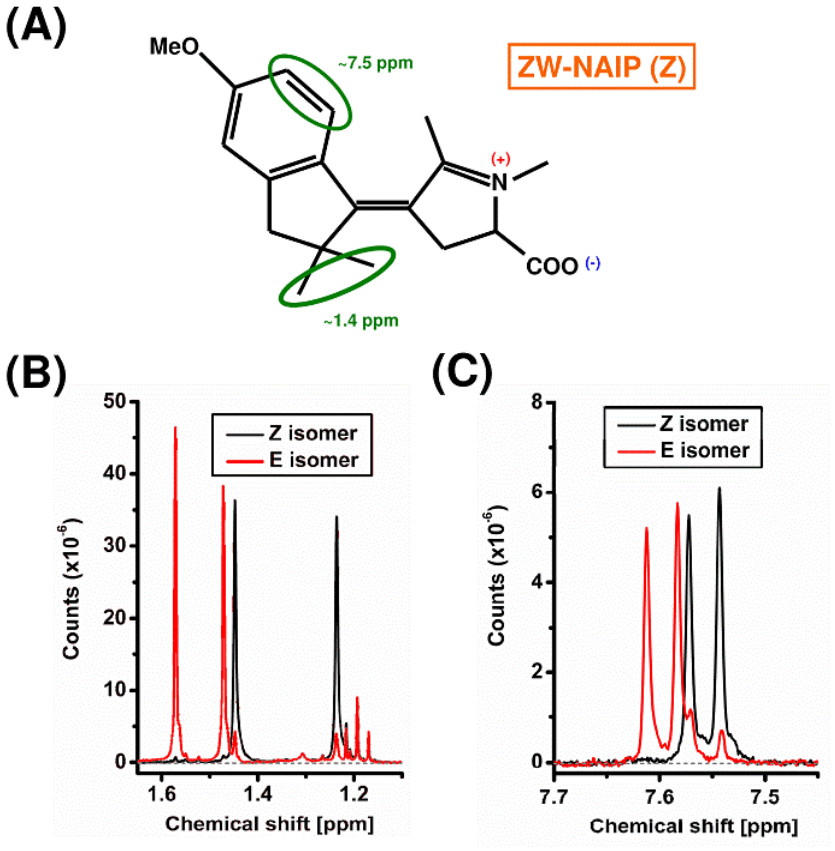

Figure 12. **A**. Structure of ZW-NAIP molecule. Protons giving ^{1}H-NMR signals used to differentiate Z and E isomers are encircled. **B**. NMR spectrum given by the 2 methyl groups in the 1.1 to 1.65 ppm region. **C**. NMR spectrum of the 2 adjacent protons of the phenyl group in the 7.45-7.7 ppm region. The area below these signals helps to determine the Z:E isomer ratio.

Chapter 4

Transient absorption measurements on IP-based photoswitches

This chapter is dedicated to the qualitative presentation and quantitative analysis of experimental data acquired with the TA setup (described in Chapter 2) on five IP-based photoswitches presented in Chapter 3 and diluted in methanol.

A. The zwitterionic switch ZW-NAIP

The structure of ZW-NAIP has been presented in Chapter 3 and is recalled here in figure 4.1C. The specificity of this molecule compared to the others is that a permanent dipole moment of ~15D[111] is located on the rotating pyrroline head. It also features the methoxy group attached to the phenyl ring as in MeO-NAIP.

1. Steady-state absorption and experimental conditions

The zwitterionic compound ZW-NAIP[111] is diluted to an OD of 0.7 mm^{-1} in methanol solution. The pure E and Z isomer spectra[111], obtained after HPLC and spectrometry are shown in figure 4.1A. As already mentioned, when the sample is kept in the dark at room temperature, more than 95% of the molecules are in the Z-isomer form, as it has been observed using NMR spectroscopy by our colleagues[111, 119] and also confirmed in our laboratory (see Chapter 3 and 5).

Steady-state absorption spectra were taken before and immediately after the transient absorption experiment and are plotted in figure 4.1.B. Figure 4.1.C displays the difference spectrum of the static spectra (after experiment – before experiment). The E-Z difference spectrum, determined from figure 4.1A, is overlaid as a reference. The isosbestic point is located at 410 nm. Both spectra compare well, showing that the $Z \rightarrow E$ reaction observed in the TA experiments (see § 4.A.2) creates long-lived E species, in agreement with their ~6h relaxation time constant measured by Réhault et al.[119]. No sign of sample degradation is found after the ~2h measurement time.

From the UV-Vis steady-state spectrum measured after the experiment, we can conclude that the Z/E ratio has changed from 95/5 to ~85/15. This gives an average ~10 % E isomer content, and given that $\varepsilon_Z/\varepsilon_E$ at 400nm is 0.9, the E isomer signature should not have more than ~11% relative value. Thus the signals observed in this experiment are mainly assigned to the *Z*→*E* photo-reaction. In the following, the minority *E*→*Z* reaction is neglected.

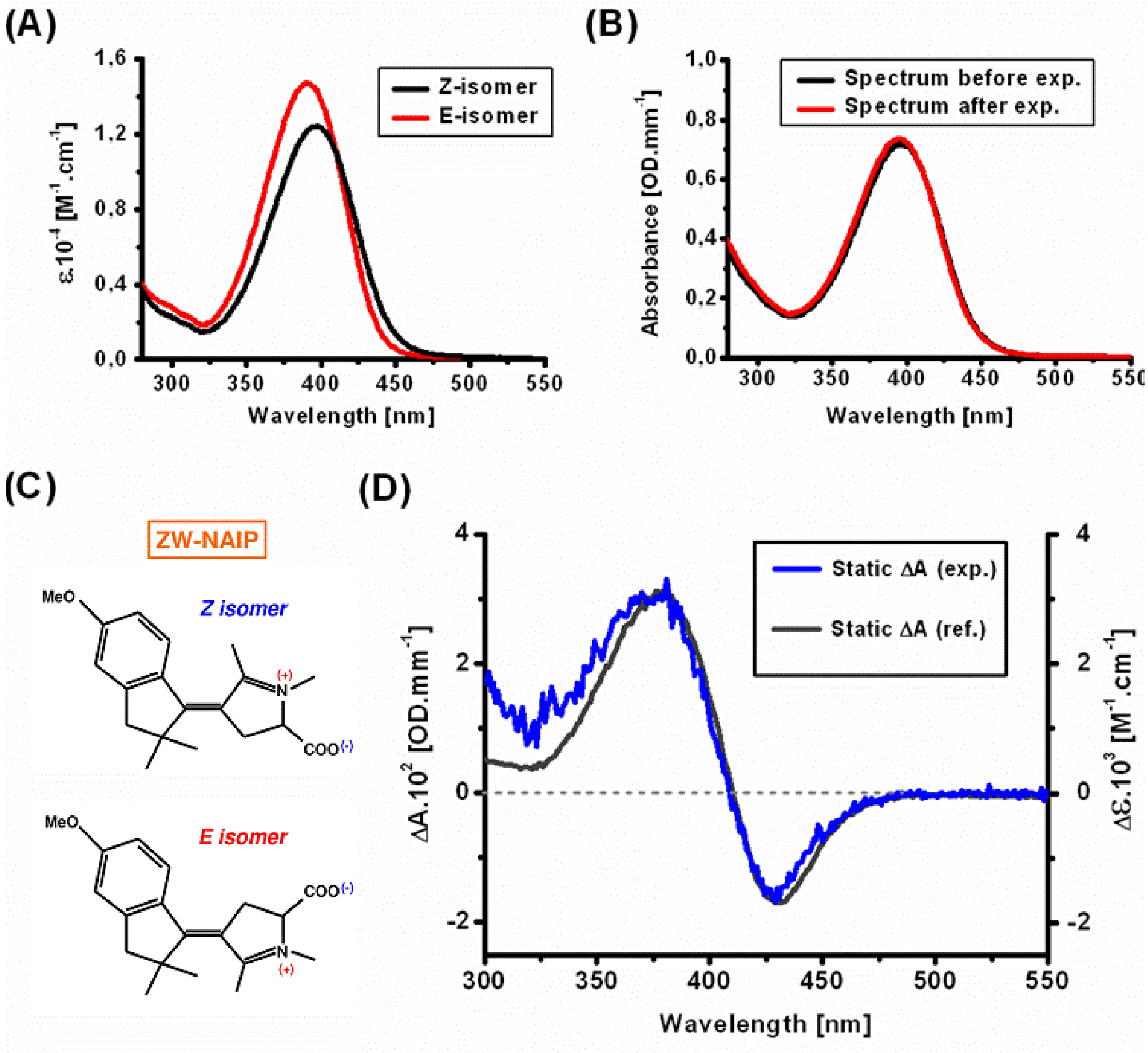

Figure 4.1. **A**. Absorption spectra of pure ZW-NAIP E and Z isomers (Data from L. Latterini et al.[111]). **B**. Sample absorption spectra measured before and after transient absorption experiments. No sample degradation is observed, except a small difference plotted in D. **C**. Structures of ZW-NAIP Z and E isomers. **D**. E-Z difference spectra. The latter overlays with the reference E-Z difference spectrum, therefore showing the *Z* → *E* photoconversion.

2. Photo-induced isomerization followed by TA spectroscopy

Figure 4.2.A displays the wavelength and time-resolved pump-induced absorption changes (ΔA) of ZW-NAIP molecules in methanol. The ΔA 2D-map is presented in the range of 300 – 700 nm as a function of time-delay between pump and probe pulses up to 100-ps. Negative ΔA, coded in blue, is due to ground state bleach (GSB) or stimulated emission (SE), while positive, red-coded ΔA represents excited-state absorption (ESA) or photoproduct absorption (PA) bands.

Excited-state (S_1) dynamics are observed during the first ~0.3 ps, followed by internal conversion ($S_1 \rightarrow S_0$), oscillations (see in particular pink areas around 450 nm in fig. 4.2.A, and fig. 4.3) and thermalization in the ground state beyond 0.3 ps until ~20 ps. After, a quasi-static spectrum is observed up to 100 ps. Figures 4.2.B and 4.2.C present selected spectra and kinetic traces from the same data set.

The time-zero transient spectrum (see fig. 4.2.B) shows two narrow positive and negative structures at ~376 nm and ~425 nm, respectively. They constitute instantaneous Stimulated Raman signals due to a ~1600-cm^{-1} ZW-NAIP vibrational mode, which is sufficiently coupled to the optical excitation to be clearly observed in our experiment. They are ~1600 +-150 cm^{-1} blue and red-shifted from the excitation wavelength, and can thus be assigned to C=C, C=N or C=O stretching modes of the ZW-NAIP molecule in agreement with references[111, 119]. Remarkably, the blue-shifted signature shows up as a positive ΔA, whereas the red-shifted one appears negative. We suggest that in both cases we observe a Stokes stimulated Raman signal in which the absorbed photon has an energy larger than that of the produced by stimulated emission. Hence, the red-shifted negative peak can be understood in a scheme where the pump is absorbed and Raman emission is stimulated by the probe. On the contrary, the blue-shifted positive peak may be associated to the absorption of a probe photon and the stimulation of Raman Stokes emission by the pump.

Stimulated emission (SE, ΔA<0) is observed from ~450 nm to the red-most part of the spectrum. At t=0.15 ps, this SE signal is largest around 510-520 nm. The apparent spectral evolution of SE from 0 to 0.15 ps is due to the presence of a fast decaying excited-state absorption (ESA1), most clearly seen in the 0-ps spectrum (fig. 4.2.B) from 600 to 700 nm. Note that, fluorescence up-conversion measurements[105], characterizing the same transition as SE, showed i) λmax = 520 nm, ii) 140 fs fluorescence lifetime and iii) no fluorescence spectral shift. The red-wavelength short-lived ESA1 rises and decays within the IRF and dominates the SE in the first ~100 fs (see kinetic trace at 650 nm, figure 4.2C). It is most probably a signature of molecules located in or close to the Franck-Condon region.

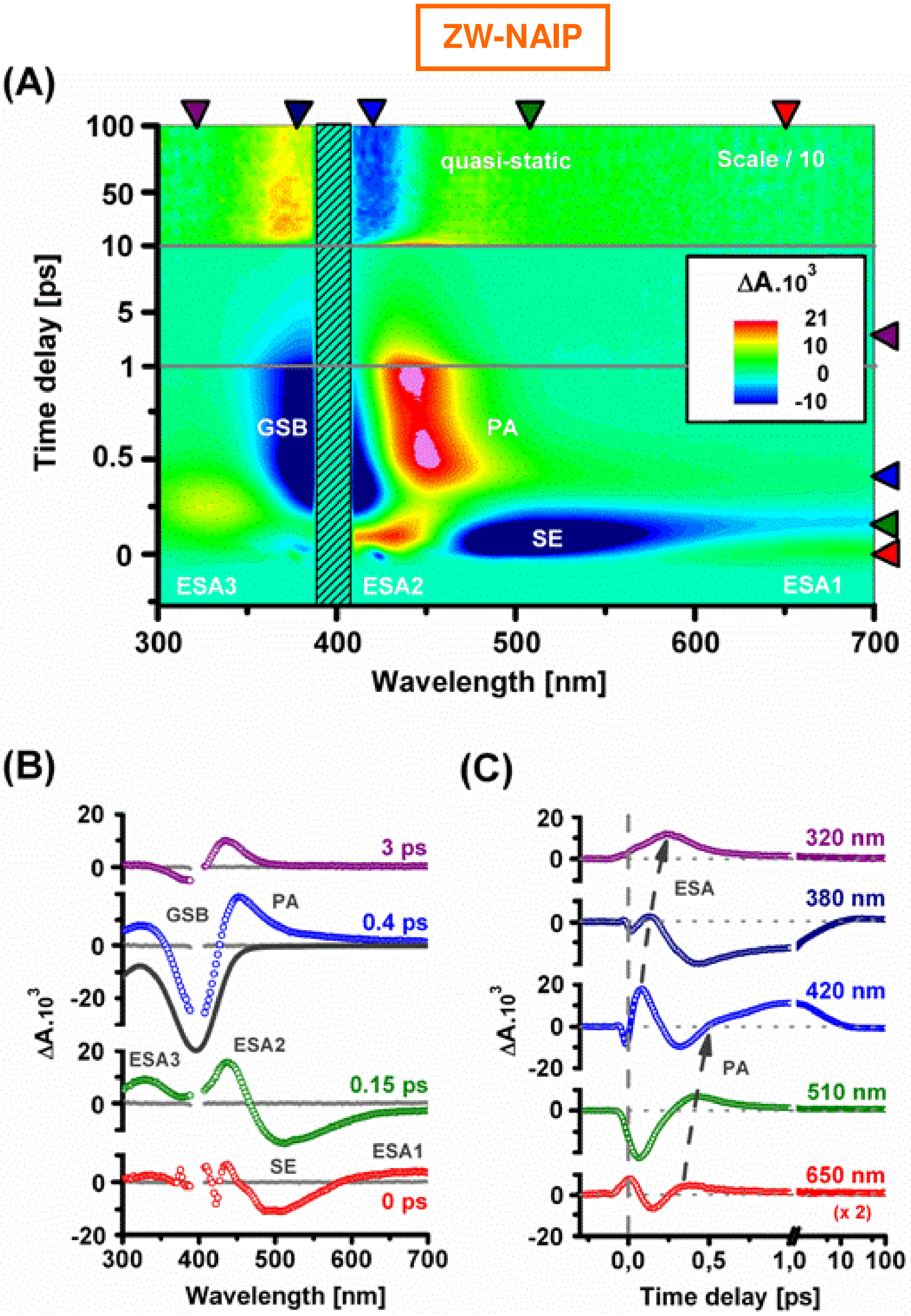

Figure 4.2. **A.** 2D map of the UV–Vis transient absorption change ΔA of ZW-NAIP in methanol as a function of wavelength and time delay. The time scale is separated into 3 linear sections, from -0.25 to 1 ps, 1 to 10 ps and 10 to 100 ps. The color scale is chosen to highlight specific, lower-amplitude features discussed in the text. Hence, pink and dark blue represent larger amplitude, out-of-scale data. Because of noise due to pump light scattering around 400 nm, the crossed-out portion is disregarded. **B.** Transient spectra (open circles) at delays indicated by the cursors on the right handside of figure 4.2A. The zero signal level is defined by negative-delay (-0.2 ps) spectrum (gray lines). Along with the 0.4-ps spectrum, the opposite of the ground state absorbance is shown (solid line). **C.** Kinetic traces selected at wavelengths indicated by the cursors on the top of figure 4.2A. Curved arrows highlight the spectral shift of excited-state absorption (ESA) and photoproduct absorption (PA). Both spectra and transients are vertically shifted for clarity.

At shorter wavelengths, two positive absorption bands labeled ESA2 and ESA3 are observed, which are best seen at 0.15 ps (see fig. 4.2.B) with their maxima at 420 nm and 320 nm, respectively. While ESA2 appears shortly after an initial negative signal (ground state bleach, GSB), ESA3 is clearly delayed in time (see fig 4.2.A and 4.2.C), and reaches its maximum at t=0.23 ps only, showing non-exponential rise kinetics. In addition, a close inspection of the transient signal at 380 nm (fig. 4.2.C) shows a small positive contribution peaking at ~0.12 ps, which is attributed to an ESA overcoming the GSB. Therefore we conclude that ESA2 and ESA3 are not due to transitions between different states, but most probably a single ESA band associated to the same $S_1 \rightarrow S_n$ transition, which spreads over the GSB contribution and spectrally shifts (see dashed arrow on fig. 4.2.C) from ~440 nm at time zero, to 320 nm at t=0.23 ps. This pronounced dynamic spectral shift point to a wave packet-like behavior in the excited state.

Another indication for non-exponential dynamics is found in the 510-nm kinetic trace (fig. 4.2.C) which shows a break in its slope at t~0.2 ps. It is caused by a delayed, short-lived absorption signal (see fitting and interpretation below), which follows the initial SE signal and peaks at 380 fs in the 650-nm transient, and at 420 fs in the 510-nm trace. These time delays are significantly larger than the average fluorescence lifetime[105] and are occurring about 150 fs after the maximum of ESA3. Hence we assign the delayed absorption to ground state photoproduct absorption (PA). Photoproduct designates hereafter the ground state species resulting from the $S_1 \rightarrow S_0$ internal conversion, regardless of them being either in Z or E isomer.

The time-delayed PA signal (see 650, 510 and 420-nm transients in fig. 4.2.C) is initially very broad (420-700 nm, see fig. 4.2.A and the 0.4-ps spectrum in fig. 4.2.B), but narrows very rapidly within ~50 fs to form the first peak (pink region around 0.5 ps in fig. 4.2.A) of a series of rapidly-damped oscillations. The latter alternatively modulate two bands: the negative band between 350 and 420 nm associated to GSB (cf. comparison of the 0.4-ps spectrum and steady-state transmission in fig. 4.2.B), and a positive band between 420 and 470nm associated to the PA of an incoherent, vibrationally hot population in the ground state. As shown in figures 4.3.A and B, the oscillations are best seen in the blue (368-nm transient) and red edges (446-nm transient) of the ground state absorption spectra of both isomers, corresponding to the wave packet turning points. They can be isolated from the underlying incoherent kinetics (see fig. 4.3.C and data analysis below), and appear anti-phased, as expected for a wave packet oscillating around the ground-state equilibrium position. Subsequent swinging and damping give rise to a series of 2 to 3 oscillation maxima, persisting for almost 1.5 ps.

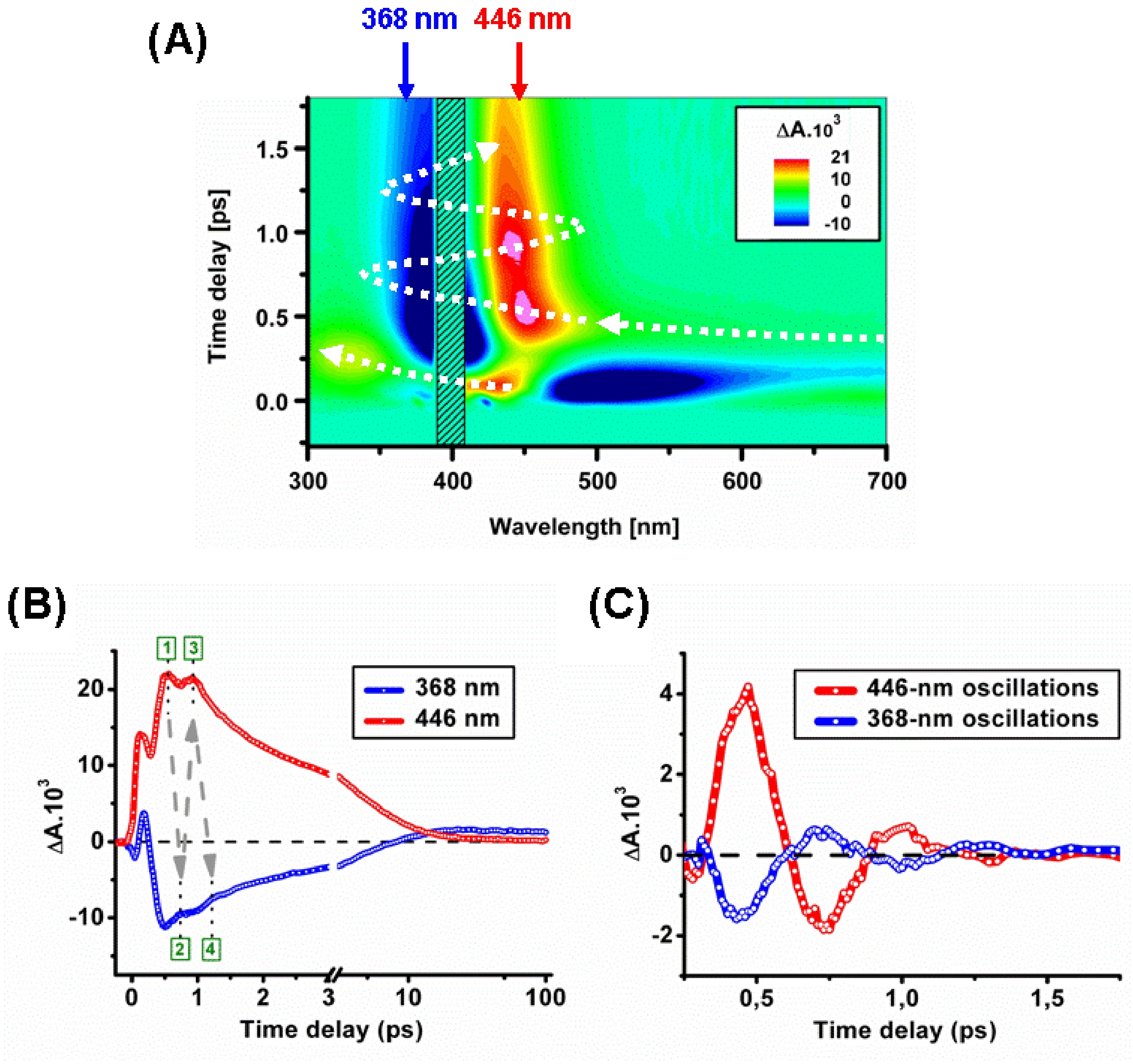

Figure 4.3. **A**. 2D-map of the UV–Vis transient absorption change ΔA of ZW-NAIP in the first 1.8 ps. Coherent spectro-temporal signatures are highlighted by the dashed arrows **B**. Selected kinetic traces on the blue (368 nm, blue curve) and red (446 nm, red curve) sides of the $S_0 \rightarrow S_1$ ZW-NAIP absorption, as indicated by the arrows in A. Anti-phased oscillations (numbered 1 to 4) are associated to coherent vibrational motion in the ground state. Dashed arrows are guides to the eye. The first positive peak, however, is due to ESA. **C**. Oscillatory part of the signals at 368 (blue curve) and 446 nm (red curve) obtained by subtracting the incoherent kinetics contributions from the raw data (see data analysis below).

As seen in figure 4.3.A or in the transients of figure 4.3.B, damping of the ground state coherence goes along with ground-state thermalization processes (reduction of PA and GSB contributions). This shifts the PA maximum down to 420 nm, and leads to partial GSB recovery in the 3-ps spectrum (see fig. 4.2.B).

Further evolution, most probably inter-molecular vibrational relaxation reduces both negative and positive ΔA, as shown in figure 4.4. For t≥~20 ps, a quasi-static difference spectrum is observed (see fig 4.2.A), mostly corresponding to the E-Z difference spectrum, showing that isomerization is completed.

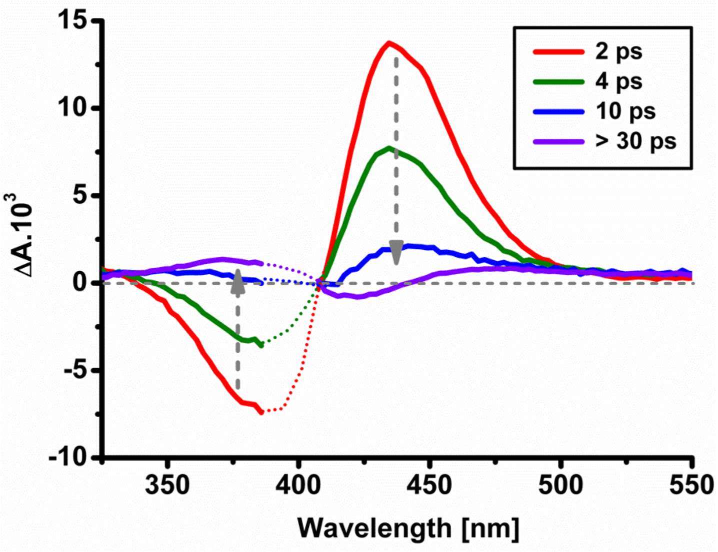

Figure 4.4. Selected spectra of ZW-NAIP (325-550 nm) at time delays of 2, 4, 10 and >30 ps, showing vibrational relaxation of Z and E hot isomers and the appearance of the quasi-static spectrum.

Here we emphasize that the $S_1 \rightarrow S_0$ relaxation occurs at ~0.38 ps according to the maximum of the PA, whereas a fully relaxed E/Z difference spectrum is observed after ~20 ps only, since it is masked, at earlier times, by a stronger signature of vibrationally hot Z and E isomers. However, we will argue in § 4.A.4.b (another experimental indication will also be given in Chapter 5) that isomerization occurs on the 0.38 ps time scale and is responsible for the $S_1 \rightarrow S_0$ internal conversion.

After excited and ground-state contributions have relaxed, further evolution beyond ~30 ps leads to a quasi-static difference spectrum. It is displayed in figure 4.5 together with the E-Z difference spectrum obtained independently[111]. Both spectra are in good agreement at wavelengths shorter than 420 nm, with a positive band corresponding to the signature of the 6-nm-blue-shifted E isomer. This clearly indicates that isomerisation is accomplished before 30 ps. This positive contribution from the E-isomer can already be seen after ~8 ps in the 368-nm transient (figure 4.3B), where the signal crosses the 0-offset line and stays positive. This is in excellent agreement with femtosecond mid-IR data performed by Réhault et al.[119].

Note that in contrast to the reference E-Z difference spectra, the quasi-static spectrum shows a broad positive absorption for $\lambda > 450$ nm. It is no longer observed in a second experimental run performed on freshly-synthesized molecules (see Chapter 5). Hence we attribute it to the long-lived signature of a by-product of partial degradation of the ZW-NAIP molecules.

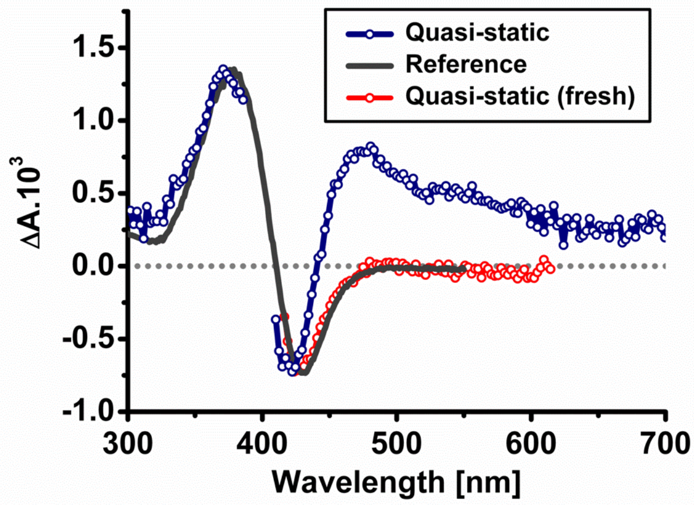

Figure 4.5. ZW-NAIP normalized quasi-static spectrum (blue line with open circles) measured for long time delays (averaged between 50 and 100 ps). The pure E-Z difference spectrum determined by HPLC and photospectrometry (solid grey) as well as the quasi-static spectrum from Chapter 5 (red line with open circles) are overlaid for comparison.

3. Fitting model and quantitative analysis

a. Failure of exponential fitting

Fitting the transient absorption data using only exponential functions, as the one defined in eq. (2.9) (see Chapter 2), leads to unsatisfactory results.

For instance, a sum of IRF-limited exponential rise and decay is unable to fit the peak-like character of the PA signal for $t \geq 0.25$ ps, and also at 510 nm (fig. 4.6.A), the above-mentioned slope change around 200 fs is missed. The residuals between 0 and 1 ps are much larger than the experimental noise, and thus unsatisfactory.

Moreover, fitting with exponential functions yields unrealistically large amplitudes (and large error bars on decay time constants, see figure caption), for example at wavelengths around 650 nm. As a matter of fact (see fig. 4.6.B), a fit with four exponential decays (one infinite) yields a maximum amplitude of $\Delta A = -0.115$ for the SE contribution, which is about 10 times larger than expected at this wavelength, assuming equal oscillator strength for absorption and emission*.

---

* The extrapolated maximum GSB value at t_0 is <4%, in agreement with the ratio of excited molecules. Assuming equal oscillator strength for GSB and SE, it would lead to a maximum SE amplitude also below 4% at 520 nm. Based on time-resolved fluorescence data, we expect the SE at 650 nm to be several times smaller than at 520 nm, yielding an expected SE amplitude of about 1%, which is significantly lower than the 11.5% value obtained by this inadequate fit.

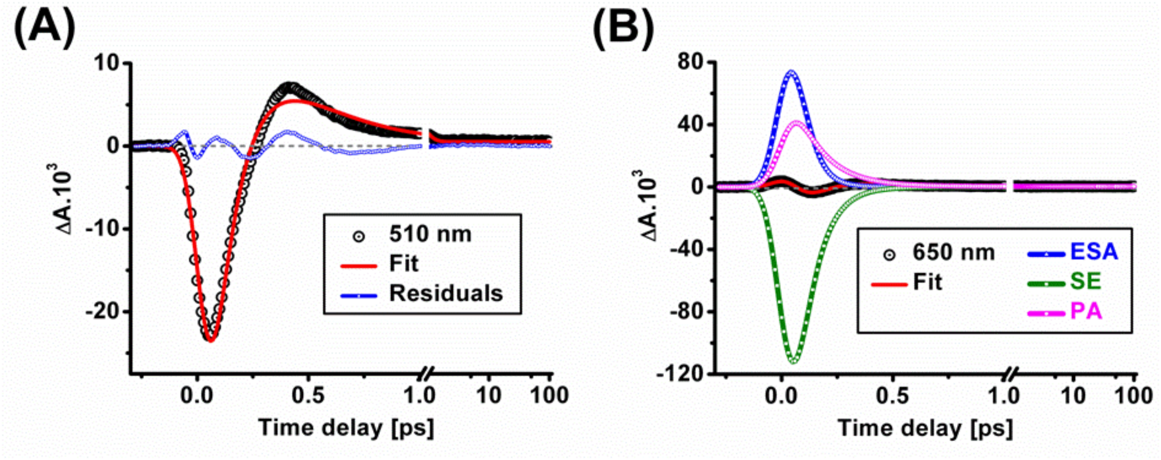

Figure 4.6. **A**. Kinetic trace (black circles), fit (red line) and residuals (blue line) at 510 nm using eq. (2.9). The peak-like character of the positive PA band is poorly fitted. 3 time constants are used (0.17 ± 0.06 ps, 0.21 ± 0.07 ps and infinite). **B**. Kinetic trace at 650 nm (black circles) and fit (red line) using eq. (2.9) as a fitting function. In this case the fit quality is satisfactory but the amplitudes of the different contributions (ESA in blue, SE in green and PA in pink) are out of realistic ranges. 4 time constants are used (0.06 ± 0.04 ps, 0.08 ± 0.09 ps, 0.12 ± 0.06 ps and infinite).

Finally, figure 4.7 presents the 320-nm experimental transient together with a simulation including ESA decay time constants (which are detailed later, see § 4.2.4.b), but including a convolution with a fixed 80-fs IRF value (time resolution of the experiment, see Chapter 2). This unambiguously shows the need for a larger Gaussian convolution function FWHM value as well as a time-shift with respect to time zero, possibly reflecting the wavepacket time-spreading and shifting as the reaction proceeds.

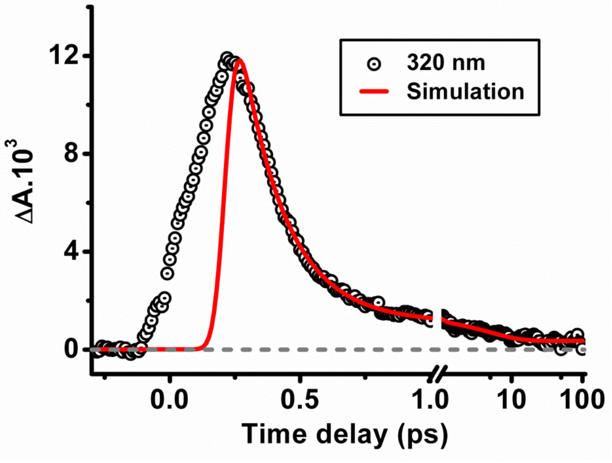

Figure 4.7. Kinetic trace at 320 nm (black circles) together with a simulation (red line) using the 80-fs IRF value for the convolution, showing the obvious need for a larger Gaussian rise and a time-shift with respect to time zero.

b. New fitting model

As suggested by the data presented above, the signals are neither fully coherent nor stochastic, but rather a mixture of both, leading to the failure of the exponential model. To overcome this problem, the fitting functions are modified so as to take into account the coherent-like features, with the aim of creating a “hybrid” model, which can account for the duality of the ZW-NAIP molecular dynamics.

To this end, a specific fitting function is associated to each assigned molecular transitions (i.e. ESA, SE, PA and GSB) observed in the transient absorption experiments. For specific signals, a clear improvement in the fits is obtained (see examples in § 4.A.3.c) using wavelength-dependent and time-delayed signals, and Gaussian standard deviation (σ) values larger than that of the IRF.

First, the SE, ESA1 and ESA2 signals can be adjusted by eq. (2.9) because they are instantaneous and do not show any spectral shift.

But as highlighted in figure 4.7 above, ESA3 clearly shows the need for a larger Gaussian standard deviation than that of the IRF and a time-shift. Its associated fitting function is an adapted form of eq. (2.9), using a free value for σ_{ESA3} and a time-shift t_{ESA3} with respect to t_0. The latter parameters are found to be wavelength-dependent. This adaptation is consistent with the wave packet time evolution and spreading as the reaction proceeds.

$$ESA3(t,\lambda) = H(t - t_0 - t_{ESA3}(\lambda)) \times \sum_i A_{ESA3_i}(\lambda)\, e^{-\frac{t-t_0-t_{ESA3}(\lambda)}{\tau_{ESA3_i}}} \otimes e^{-0.5\left(\frac{t}{\sigma_{ESA3}(\lambda)}\right)^2} \qquad (4.1)$$

The same idea is applied to model the PA ground-state contribution. The time shift t_{PA} originates from the fact that the photoproduct is formed only after excited-state evolution has occurred, and the larger σ_{PA} value is derived from the wave packet behaviour and its subsequent spreading as the reaction proceeds. So this function reflects a quasi-impulsive and delayed arrival of a wave packet-like population in the ground state after excited-state evolution. As already mentioned above, wavelength-dependency is introduced in the appropriate parameters. The fitting function reads:

$$PA(t,\lambda) = H(t - t_0 - t_{PA}(\lambda)) \times \sum_i A_{PA_i}(\lambda)\, e^{-\frac{t-t_0-t_{PA}(\lambda)}{\tau_{PA_i}}} \otimes e^{-0.5\left(\frac{t}{\sigma_{PA}(\lambda)}\right)^2} \qquad (4.2)$$

According to a model with a delayed PA formation, the ground state bleach (GSB) does not recover during the first hundreds of femtoseconds, and then suddenly does. To account for this we assume that the GSB signal is constant during the first hundreds of femtoseconds ($t_{GSB}(\lambda)$). Bleach recovery starts only after this time shift, when the wave packet reaches the ground state. Eq. (4.3) presents the function modelling this constant bleach signal $A_{GSB}(\lambda)$ before $t_{GSB}(\lambda)$, the latter being a fit parameter.

$$GSB(t,\lambda) = \left\{ \sum_i A_{GSB\,i}(\lambda) \times \left(H(t-t_0) - \left(H(t-t_0-t_{GSB}(\lambda)) \times (1-e^{-\frac{t-t_0-t_{GSB}(\lambda)}{\tau_{GSB_i}}}) \right) \right) \right\} \otimes e^{-0.5\left(\frac{t}{\sigma}\right)^2} \qquad (4.3)$$

As an illustration, eq. (4.3) is plotted as a function of time with arbitrary values of the parameters.

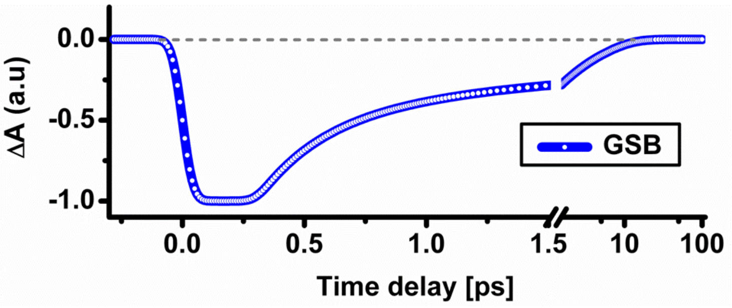

Figure 4.8. Illustration of the GSB fitting function with arbitrary values of the parameters. The GSB is constant at early time and, after a time-delay, starts to recover.

c. Results of the fits

A quantitative analysis of the data is now presented using the model functions described above. The quantitative timing associated to the spectrally-shifting UV ESA (ESA3) and the delayed onset of the PA can be obtained by fitting a selection of kinetic traces. Four representative examples of transients fits are presented in this paragraph and show the relevance of the fitting model. All fit parameter values are summarized in table 4.1.

Figure 4.9 displays the results of such fits and their decomposition into the different overlapping contributions (SE, ESA1-2-3, GSB and PA). At 650 and 510 nm (fig. 4.9.A and B), the instantaneous contributions (IRF-limited rise time) are assigned to SE (green) and ESA1 (blue). The delayed contribution is due to PA (pink), according to the above discussion. In particular, the fit at 510 nm is more accurate than that of figure 4.6.A (χ^2 reduced by a factor 7) and all features of the PA are well reproduced. In both fits the ESA1, SE and PA amplitudes are reduced to realistic values. In particular, the SE amplitude falls in the expected range. The fits yield PA maxima at 320 fs and 370 fs at 650 nm and 510 nm, respectively, which are slightly earlier than those obtained by data pointing.

At 410 nm (see fig. 4.9.C), instantaneous contributions are associated with GSB and ESA2. Note that GSB has to start with maximum amplitude at t=0. Exponentially decaying GSB would lead to unrealistically large amplitudes for GSB and ESA2. The plateau-like early-portion of GSB cannot be proven to exist, but it is assumed here *a priori*, in full consistency with the delayed onset on the PA. In that particular kinetic trace, GSB and PA almost perfectly cancel each other after ~1ps, the GS recovery starting after the delay corresponding to the GSB plateau and the delayed PA arrival. The time constant for the ground state recovery is found to be 270 fs.

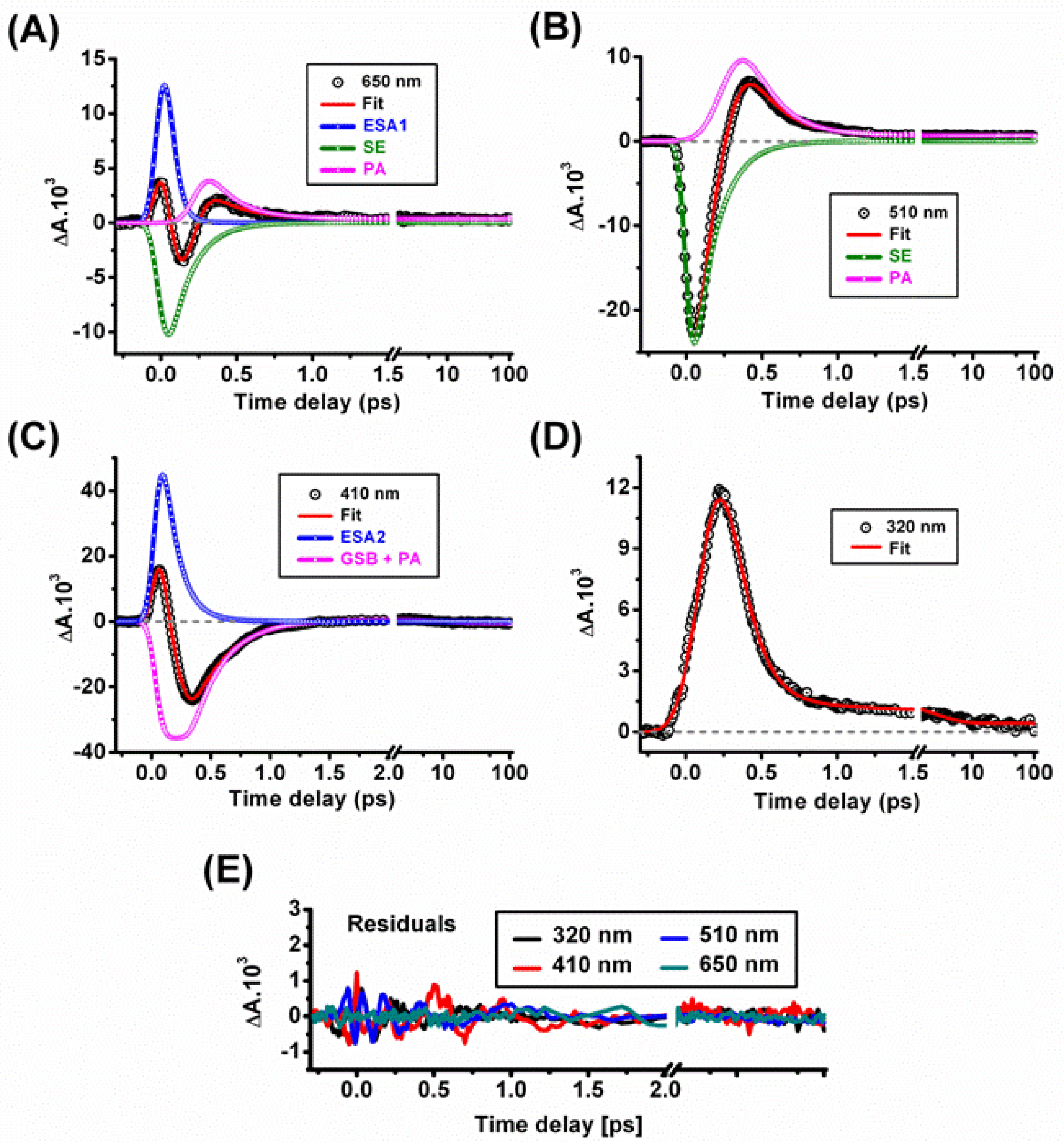

Figure 4.9. Selected kinetic traces (black dots) and corresponding fits (red lines) at **A**. 650 nm, **B**. 510 nm, **C**. 410 nm and **D**. 320 nm. The different contributions to the fitting functions are identified as ESA (blue), SE (green) and ground state signals, GSB or PA (pink). See text and table 4.1 for details. **E.** Residuals of the 4 fits, falling into the experimental noise level except for those at 410 nm, in which weak oscillatory features are observed (see next section).

At 320 nm the steady-state absorption is minimum (see fig. 4.1), and so is the GSB. Consequently, ESA3 is observed almost pure in fig 4.9.D. The rise of the signal is significantly slower than the IRF and is fitted with a Gaussian FWHM of 280 fs and a time shift of 130 fs with respect to time zero. In line with the above data presentation, this underscores ESA3 being the result of a gradual spectral shift of the ESA band, in contrast to the ~IRF-limited rise of ESA2 at 410 nm. The 230-fs time scale of the ESA3 shift suggests that the excited-state wave packet progresses along a low-frequency mode. Then, the fitting of single transients from 650 to 410 nm (Fig. 4.8.A, B and C) yields the time-shift of the delayed PA component, that is the onset time of the ground-state population after $S_1 \rightarrow S_0$ conversion. Its value continuously evolves from 240 fs at 650 nm to 300 fs at 410 nm (see pink values in table 4.1 below).

	ESA	SE	GSB	PA
650 nm	A_{ESA1} = 0.041 τ_{ESA1} = 0.05 ps	A_{SE} = -0.018 τ_{SE} = 0.15 ps	---	t_{PA} = 240 fs, σ_{PA} = 175 fs A_{PA1} = 7.10^{-3}, τ_{PA1} = 0.19 ps A_{PA2} = 4.10^{-4}, τ_{PA2} = Offset
509 nm	---	A_{SE} = -0.039 τ_{SE} = 0.15 ps	---	t_{PA} = 260 fs, σ_{PA} = 270 fs A_{PA1} = 0.021, τ_{PA1} = 0.19 ps A_{PA2} = 7.10^{-4}, τ_{PA2} = Offset
410 nm	A_{ESA2} = 0.085 τ_{ESA2} = 0.13 ps	---	t_{GS} = 300 fs A_{GS1} = -0.035, τ_{GS1} = 0.27 ps A_{GS2} = 10^{-3}, τ_{GS2} = 11 ps A_{GS3} = 5.10^{-4}, τ_{GS3} = Offset	
320 nm	t_{ESA3} = 130 fs, σ_{ESA3} = 280 fs $A_{ESA3(1)}$ = 0.031 $\tau_{ESA3(1)}$ = 0.13 ps $A_{ESA3(2)}$ = 10^{-3} $\tau_{ESA3(2)}$ = 2.7 ps	---	---	---

Table 4.1. Table summarizing the fitting parameter values from the four different fits at 650, 509, 410 and 320 nm presented in Figure 4.9. For each fit, t_0 is ~0 ps and $\sigma = \sigma_{IRF}$ = ~80fs, unless another value is specified.

d. Fitting of oscillatory features

Similar delayed fitting functions are also used to extract the kinetics underlying the oscillatory part of the transients, for example at 368 and 446 nm (see fig. 4.10). The observed oscillatory signals are analyzed by a delayed, exponentially-damped sine function *Oscill(t,λ)*. It is added to the above PA(t,λ) and GSB(t,λ) functions used to describe incoherent dynamics. The fitting function thus writes $F(t,\lambda) = PA(t,\lambda) + GSB(t,\lambda) + Oscill\,(t,\lambda)$ with:

$$Oscill(t,\lambda) = H(t - t_0 - t_{start}(\lambda)) \times A_{osc}(\lambda) \times \cos(2\pi(\frac{t - t_0 - t_{start}(\lambda)}{T_{osc}}) + \Phi_{osc}(\lambda)).e^{-\frac{t - t_0 - t_{start}(\lambda)}{\tau_{dec}}} \quad (4.4),$$

where A_{osc} is the amplitude, T_{osc} the period and Φ_{osc} the phase of the oscillations. τ_{dec} is the decoherence (dephasing) decay time. A time-shift t_{start} is used to account for the fact that oscillations only start. after a time delay with respect to t_0.

A simultaneous fit of a blue-sided (368nm) and a red-sided (446 nm) absorption wavelength is done, using the same decay times for the incoherent part *PA(t) + GSB(t)*, and a common oscillation period and decoherence time. The kinetic traces and their corresponding fits are presented in figure 4.10 together with the residuals. Note that the first peaks in the kinetic traces are attributed to ESA.

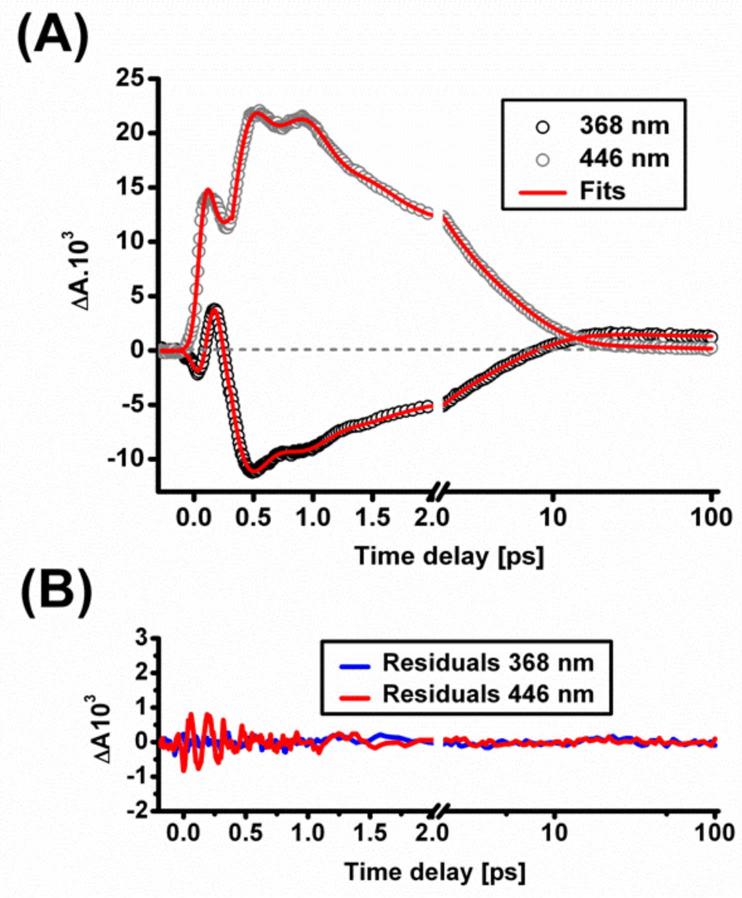

Figure 4.10. **A**. Kinetic trace at 368 nm (black circles) and 446 nm (grey circles) and their fits (red lines) obtained with eq. (4.4). **B**. Fit residuals at 368 nm (blue line) and 446 nm (red line).

Figure 4.11A compares the incoherent contribution *PA(t) + GSB(t)* obtained by the fit to the raw kinetic traces for both 368 and 446-nm wavelengths. The decay constants of the incoherent part resulting from this procedure are in good agreement with the more precise SVD and global fitting analysis performed to obtained ground state thermalization decays, which are detailed below (0.85 and 4.55 ps compared to 1.1 and 4.85 ps found with SVD and global fitting).

The oscillatory residuals, obtained by subtracting the fits of fig. 4.11.A from the 368 and 446-nm transients, are presented in figure 4.11.B, together with the corresponding *Oscill(t)* resulting from the fit of the raw data by F(t). The oscillating part has a period T_{osc} = 560 ± 10 fs (~60 cm^{-1}) and a dephasing time τ_{dec} = 320 ± 20 fs. They characterize the oscillatory behaviour of the vibrational wave packet in the ground state. This fitting procedure developed throughout § 4.A.3, suggested by the data observation and by the fit quality and relevance, also supports the picture of a vibrational wave packet evolving rapidly on the ES potential energy surface, arriving impulsively in the ground state, and evolving rapidly towards the potential energy minimum of the latter. The wave packet arrival time is also in very good agreement with the C=C double bond re-formation time scale found in femtosecond mid-IR spectroscopy[119].

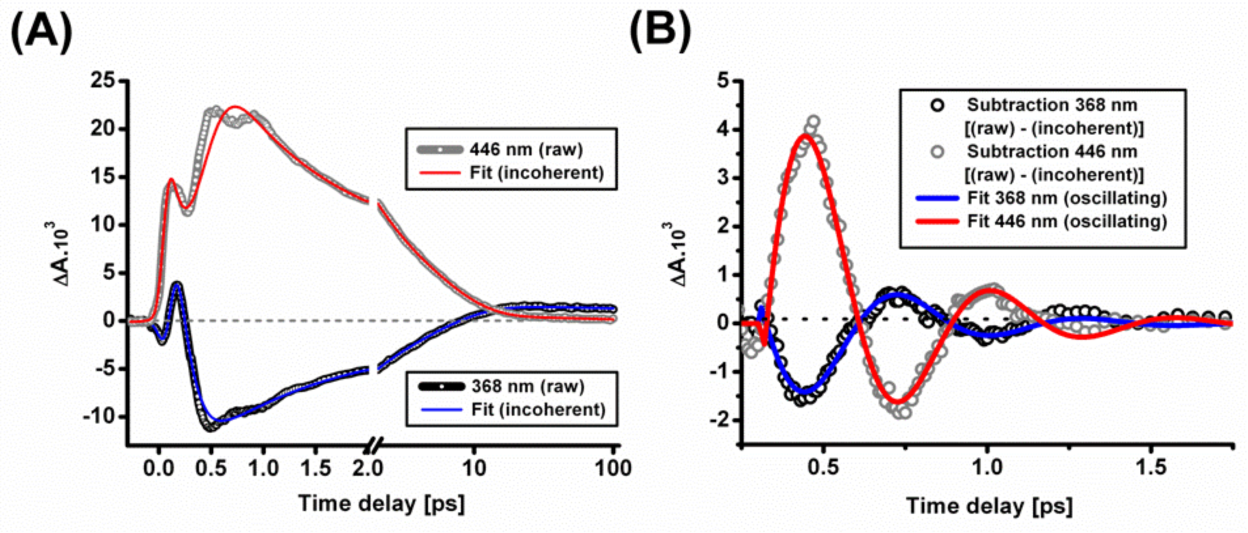

Figure 4.11. **A**. Kinetic traces at 368 and 446 nm together with the incoherent part (*PA(t)* and *GSB(t)*) of each fitting function. **B**. Oscillatory residuals (obtained by subtraction of the incoherent part of the fit from the raw data) at 368 and 446 nm together with their respective oscillatory part from the fit.

4. Further analysis and discussion

a. Formation of E isomer

As it has already been emphasized with the presence of the E-Z difference spectrum, the isomerization is unambiguously accomplished before 20 to 30 ps. Looking closer into specific kinetic traces, as for example around 370 nm, where the E isomer photoproduct absorption is maximum, the E isomer signature can be distinguished after ~8 ps, as the signal crosses the 0-offset line and from then stays positive. But we believe the isomerization time to be faster than this value. Indeed, the first signal attributed to a ground state signature is already observed at 380 fs. The different coherent signatures (ESA dynamic shift, impulsive arrival in the ground state, followed by oscillations) observed in the data support a scenario of coherent isomerization. The analogy with rhodopsin isomerization (see part § 4.E.2 of this Chapter) on the different signatures, time scales and reaction scenario also comes into play, as these photoswitches were created so as to mimick the rhodopsin dynamics. Moreover, as it will be highlighted in Chapter 5, another series of experiment, studying forward and backward photo-reactions (Z → E and E → Z) of this compound, and a simple analysis based on a data subtraction, supports this model, as the isomer signature can already be distinguished on a sub-ps time scale.

The isomerization quantum yield for the Z → E reaction can be derived from the transient absorption experiments[*]. The Z isomer leftover bleach value (from the molecules that have been converted into E and have thus not come back to the Z reactant state) derived from the quasi-static difference spectrum is $\Delta A = -4{,}4.10^{-3}$ at 375 nm for example. The maximum bleach value at this wavelength is $\Delta A = -17.10^{-3}$. But as ESA is also present during the early times of the signal, this value may just be useful to set the maximum reaction quantum yield, which would then be ~0.26. In fact, the signal is also modulated by oscillations, and the bleach value may appear larger than what is really is. A more precise value can be obtained from a fit with the previously described model at that wavelength, which gives $\Delta A = -15.10^{-3}$, and thus a quantum yield for the Z → E of ~0.29. This approximate value is good agreement with the more reliable ones obtained independently by Réhault et al.[119] using NMR and mid-IR spectroscopy.

---

[*] It is however not very accurate, given that the quantum yield is about 0.25 and that the isomers have very similar absorption spectra (both in molar extinction coefficients and absorption maxima), yielding a very small difference spectrum which is difficult to measure precisely because it is close to the noise level.

b. Thermalization in the ground state

As presented in figures 4.2 and 4.3, after ~1.2 ps, oscillations and dynamical spectral shifts become negligible or have almost vanished. Therefore global fitting, with conventional sums of exponential functions, becomes appropriate. Prior to this, we process the data by singular value decomposition (SVD, see Chapter 2) which reduces the full 2-dimensional data map (fig. 4.2.A) into a linear combination of a few dominant kinetic traces (four in the present case, see fig. 4.12.A) and their associated spectral amplitudes.

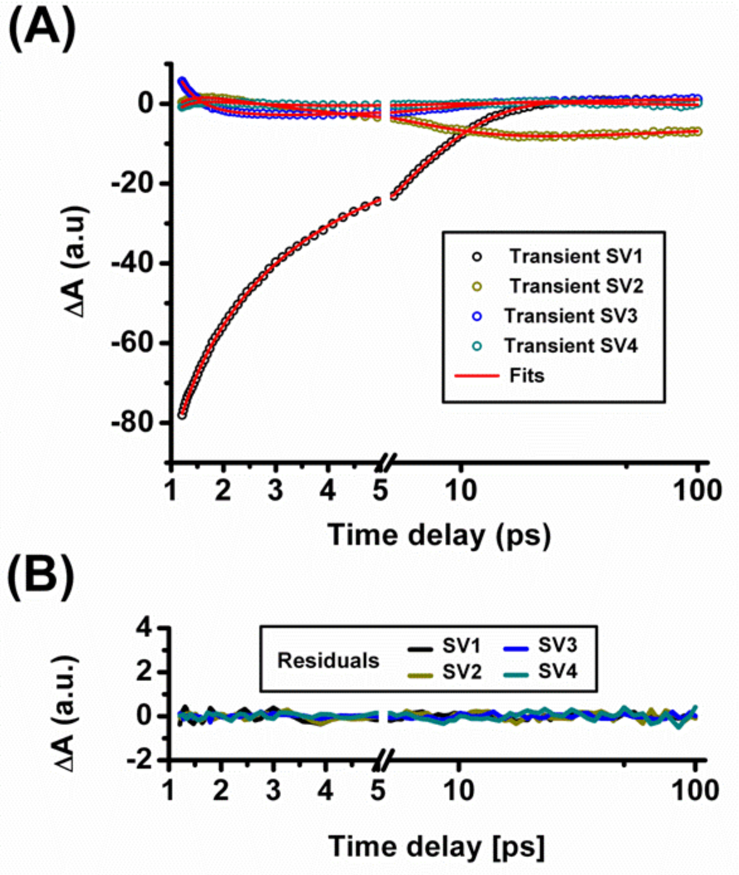

Figure 4.12. **A**. Global fitting of the four prominent (weighted) time vectors (black, gold, blue and cyan circles, respectively) for the full transient absorption spectral dataset analysed at time delays > 1.2 ps, and their corresponding fits (red lines). **B**. Residuals of the global fit of the SVs' transients.

Five time constants are sufficient to fit simultaneously the singular transients with featureless residuals. The fitting functions given by eq.(2.9) were used with the time origin t_0 set to 300 fs, as the GS signals only start to decay after this approximate time shift (see § 4.A.3.c). The resulting fits are plotted together with the SV transients in figure 4.12A and the residuals are given in figure 4.12B. The dominant time constants are 1.09 ± 0.02 ps and 4.85 ± 0.03 ps, and an infinite time constant (offset function). A sub-ps component (not shown), to account for the fast leftover signals, and a very weak

(DADS amplitude of ΔA = 2.10^{-4}) and spectrally unstructured component of 78.5 ± 15 ps are also needed for optimal flattering of the residuals. The latter contribution is most probably due to imperfect magic angle conditions and is thus neglected in the data analysis and discussion.

The three dominant DADS (see § 2.D.2 in Chapter 2) are shown in figure 4.13. The infinite-time DADS overlays very well with the quasi-static spectrum shown in figure 4.5. In the range 400-500 nm the longer-lived 4.8-ps DADS is ~10 to 20 nm blue-shifted with respect to the shorter-lived, 1.1-ps one. These time scales are consistent with dielectric solvation of the transient ground state structure or Intra-molecular Vibrational Relaxation (IVR), and subsequent cooling due to heat dissipation into the solvent[120]. The blue-shift underscores the idea of progressive loss of excess energy. These results and time scales are in line with time-resolved mid-IR data[119].

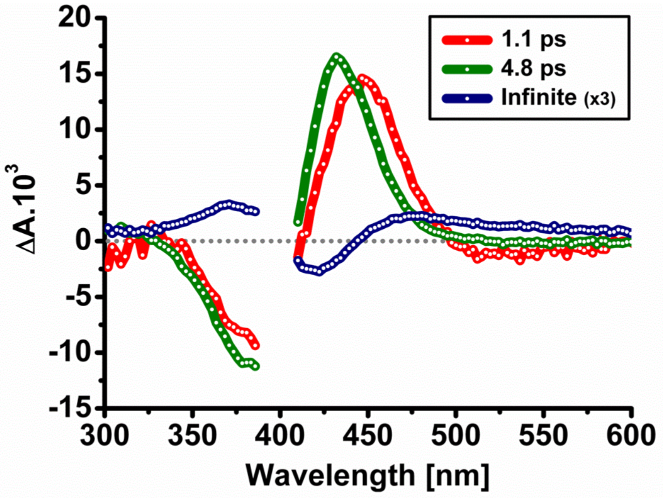

Figure 4.13. Decay Associated Difference Spectra (DADS) of the slowest components of the transient absorption data of ZW-NAIP. The two major decay components of 1.1 ps and 4.8 ps are related to solvation/IVR and cooling.

The shape of the DADS of both 1.1 and 4.8 ps are distinct from the E-Z difference spectrum which shows ΔA>0 for λ<407 nm (see fig. 4.1D). Note that since E and Z forms have very similar absorbances, their difference spectrum will easily be masked by the larger-amplitude one generated from “hot ground-state molecules”. As a matter of fact, the E-Z difference spectrum starts to be distinguishable for t>8 ps only, when the concentration of vibrationally hot molecules has sufficiently decayed.

It remains therefore unclear, at this point, whether the internal $S_1 \rightarrow S_0$ conversion occurring at 0.38 ps populates both E and Z ground state conformers or if Z is populated alone and the Z → E reaction being accomplished with the vibrational excess energy. We defer this discussion to § 4.C.4, focusing on the reaction scenario.

The same type of analysis has been performed on the 300-330 nm spectral range of the TA data for times larger than 0.35 ps. In this spectral range, the ground state bleach is minimum and the ESA is observed almost pure. The analysis (see Complementary Information) reveals a dominant (~90%) component of 0.15 ps assigned to the residence time of the wave packet in the spectral range of the observation. A slower and weaker component of 0.85 ps (~10%) is found similarly as in the fluorescence analysis[105].

c. Coherent properties

The **ZW-NAIP** data presented above show three distinct coherent signatures:

a- The ***dynamic shift*** of the ***excited-state*** absorption band from ~420 nm to ~300 nm on a ***230-fs*** time scale, most probably reflecting wave packet-like motion on the excited-state potential energy surface. The blue shift originates from the energy difference between the S_1 and S_n potential energy surfaces, which increases along the torsional coordinate as the reaction proceeds on the excited state, in good agreement with PES calculations for the S_1-S_2 and S_1-S_3 energy differences[2].

b- The ***delayed and quasi-impulsive arrival*** of the wave packet-like population in the ***ground state*** observed with the photoproduct absorption band peaking at ***380 fs*** on the red-most edge of the spectrum, and the consecutive time-shift of the this value as we consider bluer wavelengths (120-fs time-shift from 650 to 440 nm).

c- The ***oscillations*** in the ***ground state***, following this delayed impulsive re-population, with a period of ***560 fs*** and a ***320-fs*** damping time constant. This low-frequency mode (60 cm^{-1} vibrational energy) of can be attributed to a torsional mode, while the dephasing time constant of ~320 fs reflects the fast intra-molecular coupling, leading to the loss of the molecules ensemble coherence. This point will be further discussed in Chapter 6.

Figure 4.14 shows an overview of ΔA signals observed at early time delays, which highlights the three specific coherent signatures. Note that no signal other than the temporal spreading of ESA and PA is observed in the time window between 0.23 and 0.38 ps.

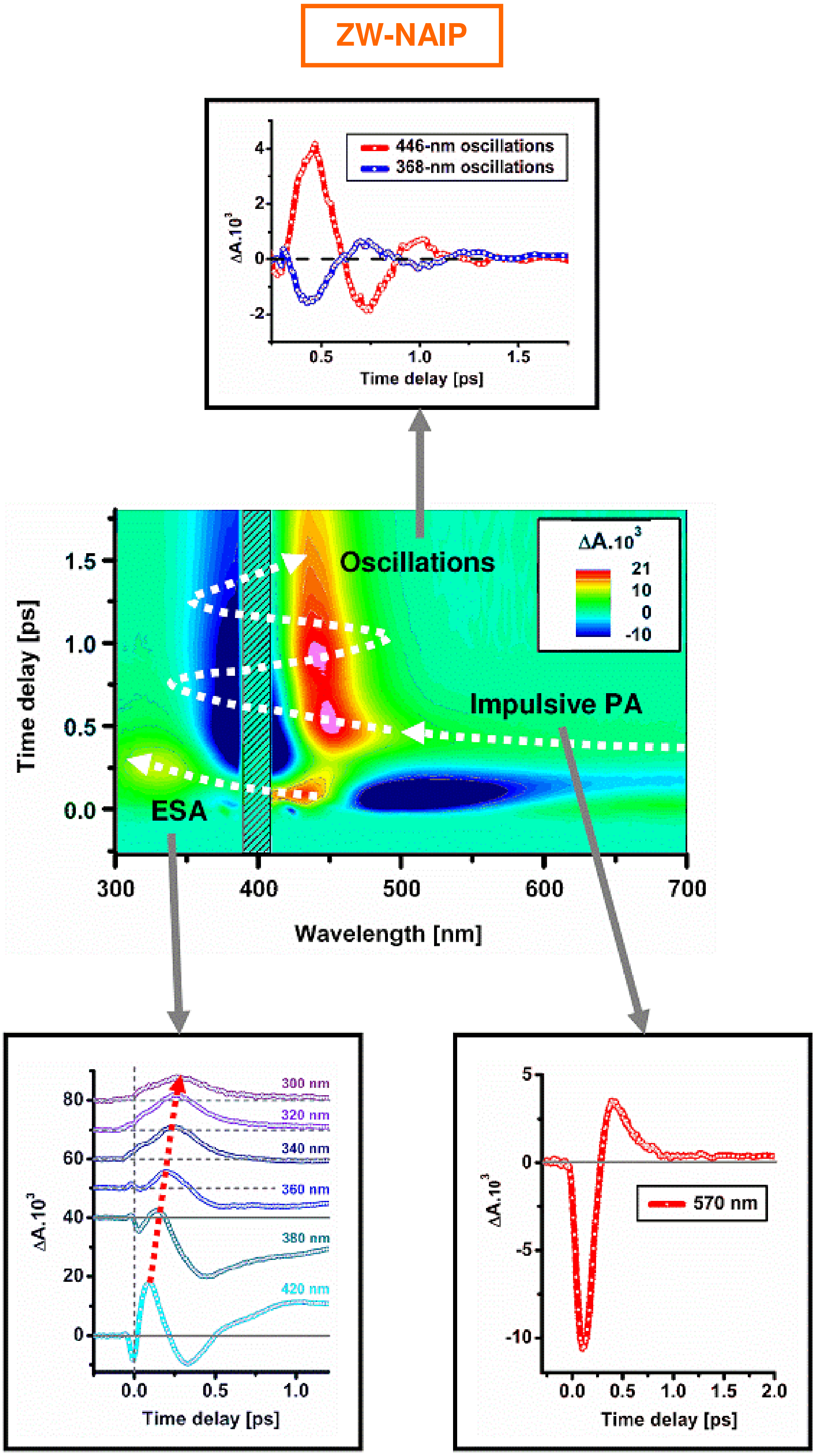

Figure 4.14. Summary panel showing the coherent signatures in the ΔA data of ZW-NAIP in methanol. The dynamic ESA shift, the impulsive arrival of the wave packet and the subsequent oscillations in the ground state are highlighted and linked to the ΔA 2D-map.

B. The MeO-NAIP, protonated-MeO-NAIP and NAIP switches

As the data and the analysis of the three other NAIP-based switches (MeO-NAIP, Prot-MeO-NAIP and NAIP) are very similar to those of ZW-NAIP, they are presented simultaneously with a special focus on the most important features and differences. Complementary information can be found at the end of the manuscript.

1. Steady-state absorption and experimental conditions

The MeO-NAIP, Prot-MeO-NAIP and NAIP compounds were diluted in methanol to an OD of 1.1, 1.4 and 0.3 mm^{-1} at 400 nm, respectively. As shown by NMR spectroscopy, the sample solutions contain more than 90% of Z isomers (see Chapter 5).

Steady-state absorption spectra were measured before and immediately after the transient absorption experiments and their differences (as well as quasi-static spectra from TA experiments) reveals the Z-E isomer difference spectrum showing that $Z \rightarrow E$ photo-conversion has occurred (see Chapter 5 for MeO-NAIP and NAIP and Complementary Information for Prot-MeO-NAIP).

2. Isomerizations revealed by TA spectroscopy

The panels displaying the complete wavelength and time-resolved absorption changes (ΔA) of MeO-NAIP, Prot-MeO-NAIP and NAIP molecules in methanol can be found in the Complementary Information section. All data can be described the same way as what has been done with ZW-NAIP. Similarly, excited-state (S_1) dynamics are observed during the first ~0.3 ps (MeO-NAIP and Prot-MeO-NAIP) or ~0.2 ps (NAIP), followed by internal conversion ($S_1 \rightarrow S_0$), oscillations (see also fig. 4.15, 4.16 and 4.17) and thermalization in the ground state beyond 0.2-0.3 ps until 30 ps. After this delay, a quasi-static spectrum is observed up to 100 ps. As it has been highlighted for ZW-NAIP, dynamic spectral shifts and coherent oscillations pointing to a wave packet-like population in both excited and ground states are observed.

As shown in the panels of figures 4.15, 4.16 and 4.17, stimulated emission (SE) is observed from ~450 nm to 700 nm. At t=0.1 ps, the SE signal is largest around 510-520 nm for MeO-NAIP and Prot-MeO-NAIP. One difference concerning the NAIP sample is that the fluorescence has lower amplitude and is shorter-lived compared to the other molecules. Again the apparent spectral evolution of SE from 0 to 0.1 ps is due to a short-lived excited-state absorption (ESA1) in the 600-700 nm region.

At shorter wavelengths, the two positive absorption bands ESA2 and ESA3 are observed with their maxima at 410-420 nm and 300-320 nm, respectively. ESA2 again appears within the time resolution of the experiment, while ESA3 is time-delayed, and is maximum at t=0.2 ps for MeO-NAIP and Prot-MeO-NAIP and at 0.16 ps for NAIP. Again we conclude that these ESA signals most probably belong to a single ESA band associated to the same $S_1 \rightarrow S_n$ transition, which competes with the GSB contribution at short delays, and spectrally shifts from ~410-420 nm at time zero, to 320 nm at 0.2 ps (or ~0.16 ps for NAIP), as a result of excited-state wave packet evolution.

The 510-nm transients (see data panels in the Complementary Information section) show a break in their slopes around t~0.1-0.2 ps. It is due to a delayed, short-lived absorption signal following the SE signal and peaking at 320, 290 and 260 fs for MeO-NAIP, Prot-MeO-NAIP and NAIP at 650 nm, respectively (see also fig. 4.19). These time delays are also significantly larger than the average fluorescence lifetimes of the molecules. Indeed, for MeO-NAIP fluorescence[2] is slightly shorter-lived than that of ZW-NAIP and has thus largely decayed after 320 fs. Prot-MeO-NAIP has not been studied by femtosecond fluorescence up-conversion, but excited-state dynamics in the TA experiments appear to be on the same time scale as that of MeO-NAIP. For NAIP, the fluorescence up-conversion signal is limited by the time resolution of the experiment (~100 fs[121]). Moreover, these PA maxima are also appearing ~100 fs after the maximum of the ESA3 signal in each case. They are thus assigned, as discussed for ZW-NAIP, to ground state photoproduct absorption (PA).

Series of rapidly damped oscillations are observed in the three data sets, modulating alternatively GSB and PA bands. Figures 4.15, 4.16 and 4.17 show oscillating kinetic traces at two wavelengths on the blue and red edges of the ground state absorption band of each compound. 2 to 3 oscillations can be observed for each molecule, up to a delay of 1.2 ps. They can be isolated from the incoherent kinetics using the same procedure as described in § 4.A.3.d, as shown in the panels of figures 4.15, 4.16 and 4.17 for MeO-NAIP, Prot-MeO-NAIP and NAIP, respectively. The fits of these transients (see Complementary Information) yield anti-phased oscillations with periods of 425, 305 and 415 fs (±10fs) and damping time constants of 280, 300 and 180 fs (±20fs) for MeO-NAIP, Prot-MeO-NAIP and NAIP, respectively.

After the disappearance of oscillations and dynamical spectral shifts (~1.2 ps), SVD and global analysis are applied as previously described in § 4.A.4.b. This leads to the ground-state thermalization time scales and their corresponding DADS. They are given in the Complementary Information section. As found for ZW-NAIP, two DADSs associated to ground state relaxation processes are obtained for all molecules. The values of two time constants involved are in the same range (1-1.5 ps and 4.8-9ps) and the DADSs associated to the fast and to the slower decays present the same spectral characteristics as what has been found for ZW-NAIP (10 to 20-nm blue-shift of the positive band from the shorter-lived to longer-lived DADS), suggesting that the ground-state thermalization is very similar in all the NAIP molecules. These time scales are also confirmed by femtosecond mid-IR spectroscopy[2].

Further evolution leads to a quasi-static difference spectrum for t≥~30 ps for each molecule (see Chapter 5 and Complementary Information). They are all in agreement with the E–Z difference spectra, showing that isomerization is completed within this time scale.

3. Summary of coherent properties

The **MeO-NAIP**, **Prot-MeO-NAIP** and **NAIP** data presented above show, with slightly different time scales, the three distinct coherent signatures discussed for ZW-NAIP:

a- The ***dynamic shift*** of the ***excited-state*** absorption band from ~420 nm to 320-300 nm on a ***200-fs*** (MeO-NAIP and Prot-MeO-NAIP) and ***160-fs*** (NAIP) time scale, reflecting wave packet-like motion on the excited-state potential energy surface.

b- The ***delayed and quasi-impulsive arrival*** of the wave packet-like population in the ***ground state*** observed with the photoproduct absorption band peaking at ***320 fs***, ***290 fs***, and ***260 fs*** on the red-most edge of the spectrum for MeO-NAIP, Prot-MeO-NAIP and NAIP, respectively.

c- The consecutive ***oscillations*** in the ***ground state***, following this delayed impulsive re-population, with a period of ***425 fs***, ***305 fs*** and ***415 fs*** and ***280-fs***, ***300-fs*** and ***180-fs*** damping time constant for MeO-NAIP, Prot-MeO-NAIP and NAIP, respectively. These low-frequency modes of vibrational period 78, 109 and 80 cm^{-1} are in the range of torsional modes, with short dephasing (decoherence) time constants of 200-300 fs.

The data corresponding to these three signatures are summarized in figures 4.15, 4.16 and 4.17 for MeO-NAIP, Prot-MeO-NAIP and NAIP, respectively. Note that no signal other than temporal spreading of ESA and PA is observed in the time windows between 0.2 and 0.32 ps (MeO-NAIP), 0.2 and 0.29 (Prot-MeO-NAIP) and 0.16 and 0.26 ps (NAIP). These coherent properties will be further discussed in § 4.C, followed by a detailed interpretation and discussion for the NAIPs (ZW-NAIP, MeO-NAIP, Prot-MeO-NAIP and NAIP) reactions.

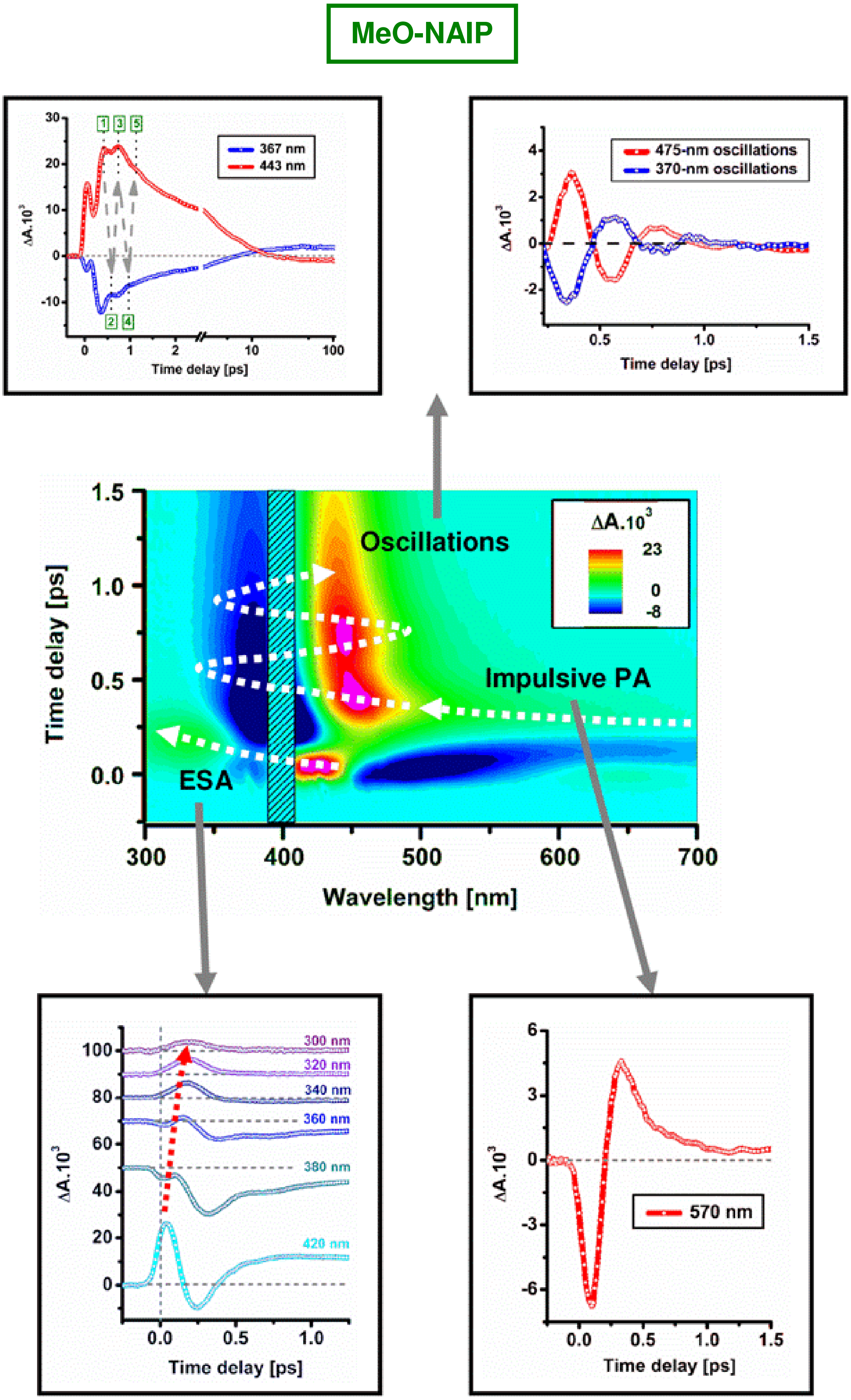

Figure 4.15. Summary panel showing the coherent signatures in the ΔA data of MeO-NAIP in methanol. The dynamic ESA shift, the impulsive arrival of the wave packet and the subsequent oscillations in the ground state are highlighted and linked to the ΔA 2D-map.

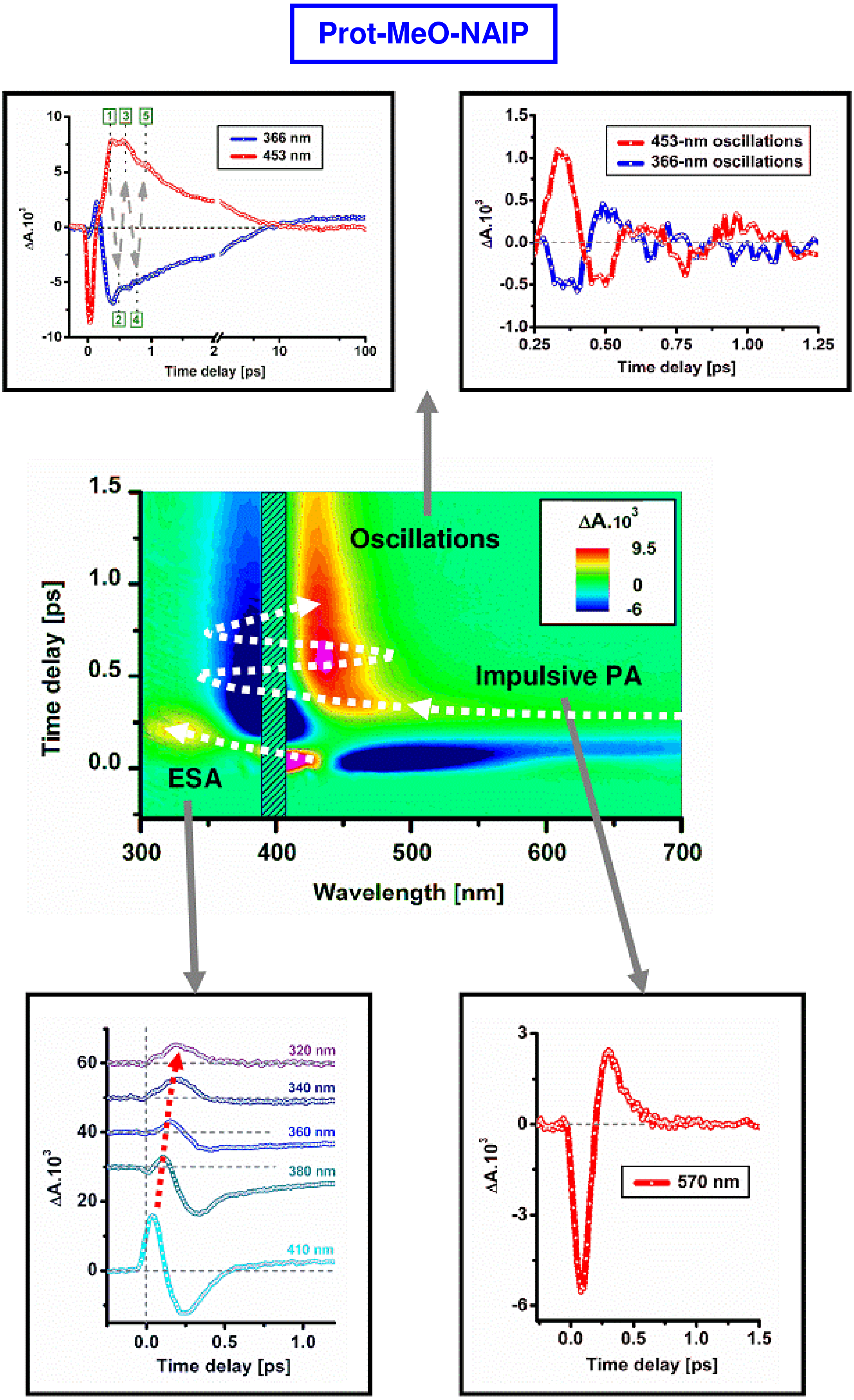

Figure 4.16. Same summary panel as in fig. 4.15 but for the ΔA data of Prot-MeO-NAIP in methanol.

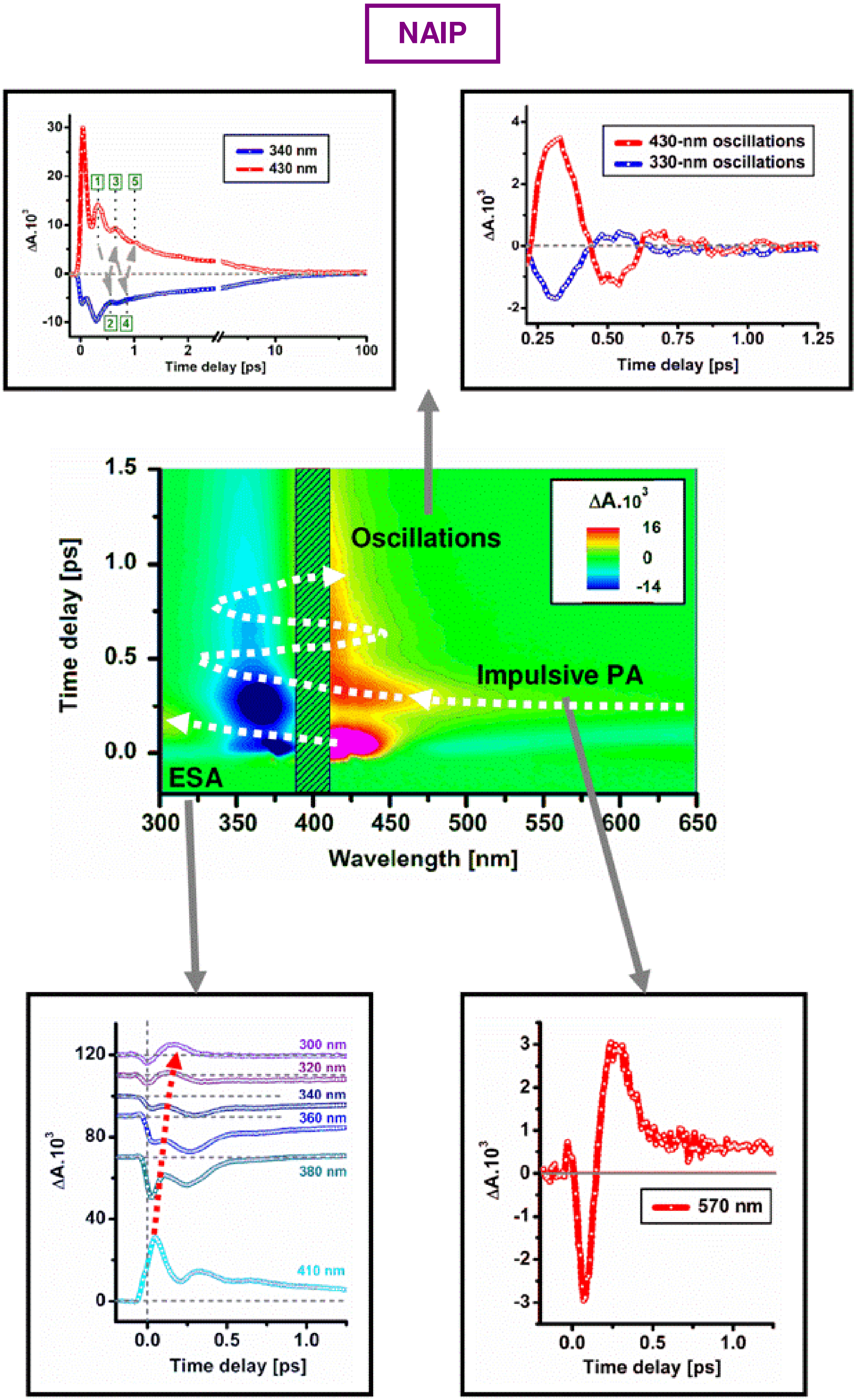

Figure 4.17. Same summary panel as fig. 4.15 but for the ΔA data of NAIP in methanol.

C. Comparison of coherent properties and reaction scenario

1. Dynamic shift of the excited-state absorption

Figure 4.18.A presents the transients of the ESA3 band in the UV region for the four NAIP molecules (ZW-NAIP, MeO-NAIP, Prot-MeO-NAIP and NAIP). As previously mentioned, this is the region where the time shift and spreading of ESA3 is the most pronounced. By comparing the four transients, we find a gradual time shift from NAIP (160 fs), to Prot-MeO-NAIP and MeO-NAIP (200 fs), and finally to the ZW-NAIP molecule (230 fs), these values being summarized in the table of figure 4.18.B.

Another remark is that, by looking at the temporal width of the ESA3 signal, and eventhough it is partially overlaid with the GSB signal for NAIP, the spreading of the wave packet-like shape of ESA3 seems to follow the same trend as the time shift increases.

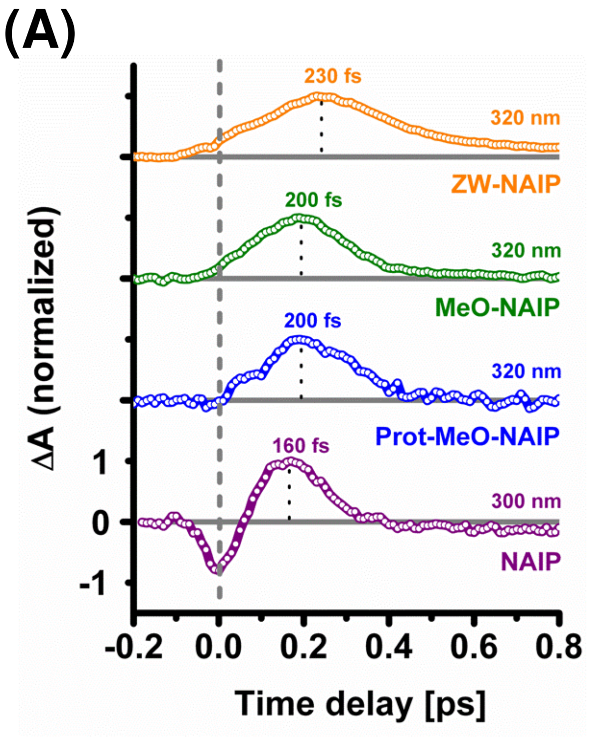

(B)

Molecule	ESA shift
ZW-NAIP	230 fs
MeO-NAIP	200 fs
Prot-MeO-NAIP	200 fs
NAIP	160 fs

Figure 4.18. **A**. Transients in the UV region for ZW-NAIP, MeO-NAIP, Prot-MeO-NAIP (320 nm) and NAIP (300 nm). The transients have been normalized to the respective ESA maxima and vertically displaced for clarity. **B.** Table summarizing the reported ESA maxima for the different NAIP molecules.

2. Delayed and impulsive wave packet arrival in the ground state

Figure 4.19.A shows the transients (normalized to their respective SE maxima) at 650 nm of the four NAIP molecules on the same time axis from -0.2 to 0.8 ps, highlighting the arrival of the delayed, quasi-impulsive PA signature. The PA signals peak at 380, 320, 290 and 260 fs at 650 nm for ZW-NAIP, MeO-NAIP, Prot-MeO-NAIP and NAIP, respectively. These values are summarized in the table of figure 4.19.C. As for the ESA shift, NAIP is the fastest and ZW-NAIP is the slowest molecule. NAIP wave packet temporal width appears clearly smaller than that of ZW-NAIP.

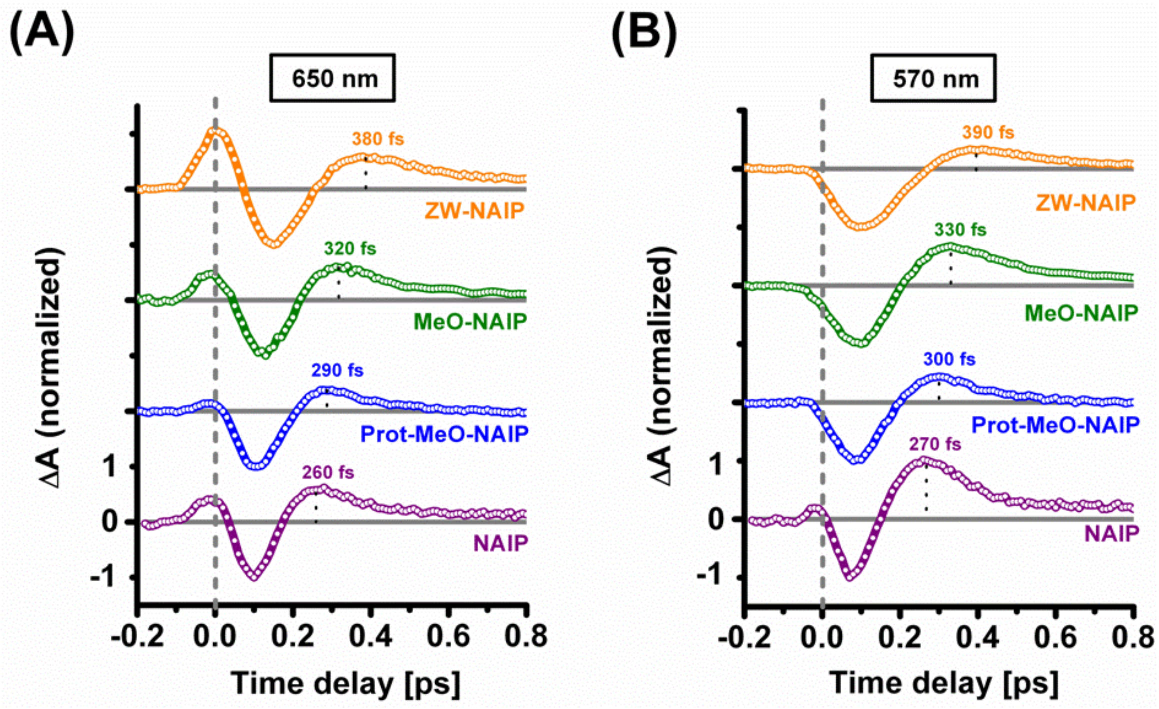

(C)

Molecule	Arrival time
ZW-NAIP	380 fs
MeO-NAIP	320 fs
Prot-MeO-NAIP	290 fs
NAIP	260 fs

Figure 4.19. **A.** Transients at 650 nm for ZW-NAIP, MeO-NAIP, Prot-MeO-NAIP and NAIP, showing the delayed PA arrival times. **B**. Same as A at 570 nm. **C**. Reported values for PA maximum at 650 nm for the 4 coherently-isomerizing photoswitches. The maxima given by the raw data (peak time of PA) are indicated for each molecule.

In figure 4.19.B, the transients are plotted for the same molecules but at 570 nm, 80-nm blue-shifted compared to the previous transients (650 nm). Remarkably, the wave packets only weakly shift and spread at these wavelengths, meaning that it is quickly evolving on the barrierless ground state PES.

3. Coherent oscillations in the ground state

Oscillations are the last coherent signatures observed in the 4 NAIP molecules. They were extracted at two specific wavelengths (using the procedure described in § 4.A.3.d) blue- and red-shifted from the ground state absorption maxima. They all appear anti-phased at both wavelengths, as expected (see fig. 4.14, 4.15, 4.16 and 4.17 for ZW-NAIP, MeO-NAIP, Prot-MeO-NAIP and NAIP, respectively). The oscillations are assigned to modulation of ground state contributions (i.e. GSB and PA), and reflect the motion, on the S_0 PES, of a vibrationally coherent wave packet, which has been initially created in the excited state and has kept its phase information throughout the isomerization process.

Figure 4.20.A gathers the oscillations extracted from the red edge of the absorption maxima of the 4 data sets. This figure clearly shows that Prot-MeO-NAIP oscillation frequency is the shortest, followed by NAIP and MeO-NAIP having apparently similar periods, while ZW-NAIP shows the lowest frequency. The table of figure 4.20.B gathers the oscillations periods (and frequencies) and damping time constants values determined for the different molecules

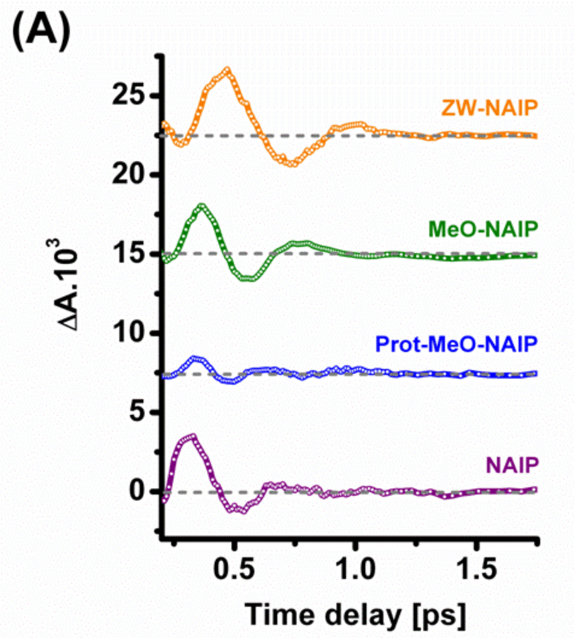

(B)

Molecule	Period	Frequency	Damping time
ZW-NAIP	565 fs	59 cm^{-1}	320 fs
MeO-NAIP	425 fs	78 cm^{-1}	280 fs
Prot-MeO-NAIP	305 fs	109 cm^{-1}	300 fs
NAIP	415 fs	80 cm^{-1}	180 fs

Figure 4.20. **A**. Extracted oscillations (see procedure in § 4.A.3.d) for the 4 NAIP switches. The traces are vertically shifted for clarity. **B**. Reported values for oscillations period (the conversion into frequency is also indicated) and damping decay time constant for the 4 coherently-isomerizing photoswitches. The oscillations

periods (frequencies) have error bars of ±20 fs (±2 cm^{-1}) and the damping times of ±20 fs. Fits at other wavelengths further confirmed these values.

All molecules show low-frequency oscillations in the range 60–110 cm^{-1}. More interestingly, they seem to follow a trend which could be related to the changes of moment of inertia, in agreement with the different substitutions brought to the pyrroline moiety. Indeed, both MeO-NAIP and NAIP molecules feature the same pyrroline part, and their oscillations frequencies are found to be very close, around 80 cm^{-1}. The Prot-MeO-NAIP molecule, where a methyl group is replaced by a proton on the pyrroline ring reveals a higher frequency (~110 cm^{-1}), while, on the other hand, the ZW-NAIP compound, which features an additional COO- group, shows a lower frequency of ~60 cm^{-1}.

These torsion frequencies from repeated (see Chapter 5 and 6 also) experimental data may be used as input values for possible improvements of theoretical models. In fact, in reference[2] a value of ~120 cm^{-1} (~280 fs) was calculated for the frequency associated to the reactive torsion of the MeO-NAIP compound. It was obtained assuming a rigid rotation around the central bond of both left (indanone) and right (pyrroline) moieties of the molecule and computing its reduced moment of inertia. But this calculated value differs from the experimental one by ~35% (~140 fs). This point will be further investigated in close collaboration with theoretical work.

4. Coherent isomerization scenario

As introduced in Chapter 1, in photo-isomerizing systems periodic oscillatory signals, commonly assigned to vibrational coherences, have been observed for various molecules in solution, both in the excited[62-65, 68] as well as in the ground state[31, 47, 69]. In most cases, ground-state coherent vibrational dynamics result from Resonant Impulsive Raman Scattering (RIRS). For protein-bound retinal and similar isomerizing molecules, Raman-active ground-state vibrational modes in the range 1000-1500 cm^{-1} were observed[47, 64, 69]. However, in these systems, low-frequency RIRS in the range 60-100 cm^{-1} has not been reported, even in experiments performed with favourable pump pulse durations[63]. Only in the case of rhodopsin was a 60 cm^{-1} mode observed *in the photoproduct all-trans state,* associated with torsion around retinal's isomerizing double bond[27, 31]. Similarly here, we argue that NAIPs' (standing for ZW-NAIP, MeO-NAIP, Prot-MeO-NAIP and NAIP) ground-state oscillations are not produced by RIRS, but are the signature of a wave packet initially created in the excited state, which survives in the photoproduct after crossing the conical intersection. In addition, we can compare these molecules to the similar one MeO-NABFP, which differs in that an oxygen atom substitutes a carbon in the indanylidene moiety. Besides a negligible effect on the ground state torsional frequency, the substitution should not affect the possibility of a low-frequency RIRS signal, and yet oscillations are absent in the MeO-NABFP data (see § 4.D).

The data reported above for the NAIPs photoswitches show that the molecules isomerize in a vibrationally-coherent regime, thus evolving in concert according to a coherent motion first on the excited state, then in the ground state while dispersing into an incoherent vibrationally unrelaxed population. Remarkably, this relatively well-focussed population can be tracked in time, leading to the following scenario and precise clocking of the different steps of the reaction (see fig. 4.21).

At t=0, optical excitation is coupled to a vibrational mode around 1600 cm^{-1}, as highlighted by the stimulated Raman signal in the t=0 spectra, which most likely is a C=C stretch. This experimental observation supports the existence of a π-π* transition with bond order change, which weakens the isomerizing double bond[1, 2, 53], and which was directly evidenced by the mid-IR bleach bands[2, 119].

For the 4 NAIP switches, fluorescence[2, 105, 121, 122], stimulated emission as well as ESA 1 and 2 bands are then observed to occur within the IRF and to decay with times of 0.1 to 0.14 ps (~90 % amplitude) and ~1 ps (~10%), as found by fluorescence up-conversion measurements and confirmed by this work.

Coherent low-frequency vibrational motion on the excited state causes the blue-shift of ESA2 into ESA3 that rises on a time scale slower than the IRF and is maximal at 0.16 to 0.23 ps. Since fluorescence has already largely decayed at that moment, the time-delayed ESA3 band is associated with excited-state molecules in a non-fluorescent geometry, most probably with a large degree of torsional angle. As a matter of fact, according to theoretical predictions[1, 2, 111], the S_1-S_0 transition dipole moment significantly drops as the isomerizing bond is twisted. Unlike fluorescence, the ESA allows us to follow the wave packet along a low-frequency motion, towards the region where internal conversion to the ground state occurs.

Then the spectrally-broad visible PA band emerges suddenly and reaches its maximum at t=260 to 380 fs, that is approximately 100 to 150 fs after the maximum of ESA3. In the present situation of coherent reaction dynamics, this means that during a ~100-150-fs time window the vibrational wave packet created in S_1 produces no signature other than that related to its temporal spreading. Therefore, we attribute this 100-150-fs time window to the passage through the “spectroscopically dark” region of a conical intersection. Consequently, this early PA signature should be attributed to molecules arriving impulsively in the ground state *after* internal conversion.

Once in the ground state, the wave packet undergoes strongly damped vibrational oscillations, whose frequencies of 60 cm^{-1} to 110 cm^{-1} is consistent with torsional motion around the central C=C bond for the differently substituted NAIPs pyrroline groups. Rapid damping (180 to 320 fs damping time) of these oscillations, most probably by intra-molecular coupling of the torsional mode with other ground state vibrational modes (see Chapter 6 also), goes along with formation of an incoherent, vibrationally-excited population.

Finally, the first spectroscopic evidence of the E isomer as a positive ΔA emerges only after vibrational relaxation has sufficiently progressed to narrow the Z bleach and E photoproduct bands, much like in the transient mid-IR spectra[2, 119]. For all molecules, after ~20-30 ps, a quasi-static Z/E difference spectrum is reached. This scenario of wave packet-like photo-isomerization of NAIP photoswitches is depicted in figure 4.21.

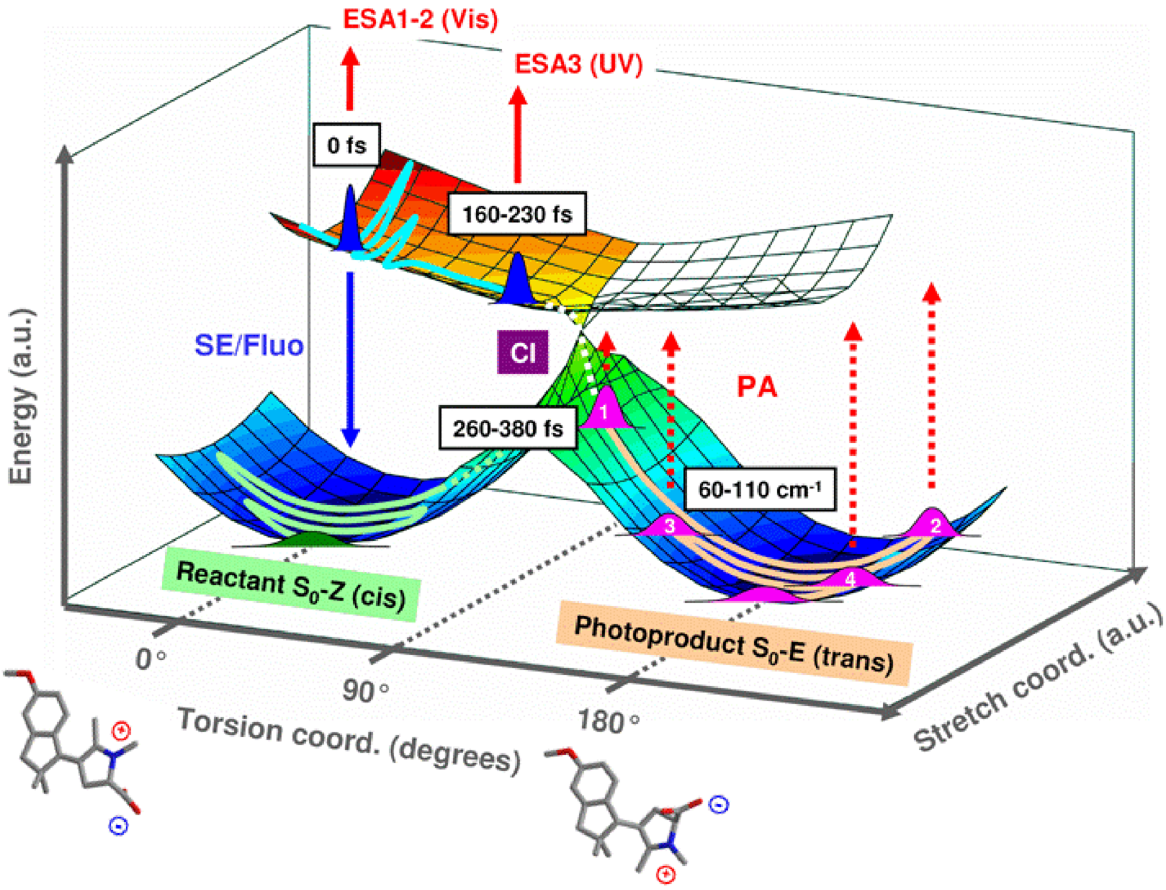

Figure 4.21. Proposed scenario and timing for NAIPs photo-reaction. Immediately after photoexcitation, ESA and emission (SE/Fluo) are observed. While the molecules leave the fluorescent window, the ESA band spectrally and temporally shifts (160 to 230 fs), reflecting motion along the torsional coordinate. After a spectroscopically dark period of ~100-150 fs, associated with the passage through the conical intersection, the molecules populate the ground state in both isomer conformations in form of an oscillating, rapidly damped wavepacket with a ~300 to 560-fs period (60-110cm^{-1}) depending on the molecule. This is schematically indicated by turning points 1 to 4, along the reaction coordinate. As explained in the text, both ground state Z and E potentials are populated in parallel. The ZW-NAIP E and Z isomer structures are also indicated as examples.

In the present case, due to the small differences of Z and E absorption spectra in the UV-VIS range, it is difficult to assign the ground-state torsional wave packet and the "vibrationally hot" PA to one of the two isomers. Actually, in the light of the ~20-25% isomerisation yields, these signals are most probably dominated by the majority Z-like conformers. However, the branching into Z or E ground states occurs at the conical intersection, that is during the “dark time window”. Therefore, both conformers are (re-)formed on the same time scale (see references[2, 119] and also Chapter 5). The 0.25-0.38-ps occurrence time of maximum PA signal should thus be considered as the isomerisation time.

In line with that, femtosecond mid-IR spectroscopy[2, 119] clearly shows that reformation of C=C double bond characteristic of the ground state happens with time constants of ~0.3 ps.

The alternative scenario of ground state Z → E isomerization, i.e. after passing the conical intersection, can be ruled out as the ground state barrier is computed to be as high as ~30 kcal.mol^{-1} in MeO-NAIP for example (1.3 eV) and the PA transition wavelength of 500 nm indicates that the molecular S_0 wavepacket has only 14 kcal.mol^{-1} (0.6 eV) excess energy at $t \leq 0.4$ ps. This can be deduced from the computed S_0-S_1 energy difference along the reaction coordinate (see Chapter 3). The subsequent vibrational relaxation further reduces the excess energy and thus alleviates the possibility of ground-state isomerization. In other words, E isomers have to be formed earlier than 0.4 ps, i.e. at the crossing of S_1-Z and S_0-E potential energy surfaces at the conical intersection.

Tied together, these observations give strong support to previous theoretical investigations of similar molecules, including retinal in rhodopsin, which do predict that optical excitation initially triggers C=C stretch relaxation which in turn funnels energy into a low-frequency, torsional mode[2, 35, 50]. This reactive mode drives the system towards the conical intersection into the (photoproduct) ground state and the internal conversion is associated with isomerisation. The full range of excited-state propagation times observed (0.16-0.23-ps) is in good agreement with the predicted ~200-fs evolution along the torsional mode for the MeO-NAIP[2] (see Chapter 3). Here we emphasize, that in the present limit of coherent reaction dynamics, the ability to track the wave packet dynamics clearly shows that the fluorescence lifetime is significantly shorter than the formation of the ground state photoproduct. This is in contrast to more "slowly" isomerizing systems, for which the fluorescence lifetime and photoproduct formation time are equal (see MeO-NABFP discussion below).

D. The MeO-NABFP photoswitch

1. Steady-state absorption and experimental conditions

The MeO-NABFP photoswitch exists in solution at room temperature only in a mixture of E and Z isomer always close to a 50%-E / 50%-Z isomer ratio[123]. Thus, in terms of almost selective Z → E isomerization and observation of the difference spectrum of E and Z as an isomerization proof, this photoswitch is not a good candidate.

Nevertheless, and eventhough the experiment will always reveal a mixture of both Z → E and E → Z isomerization reactions (which appear though to be on the same time scale for the NAIP samples, see Chapter 5), the transient absorption experiment was performed in the same measurement conditions as for the other photo-switches. Indeed, the MeO-NABFP molecule is important to us because it features a substitution of a carbon atom by an oxygen atom on the indanone moiety, making it the most red-absorbing one. Some conclusions on the influence of that particular substitution may be obtained from this experiment.

The MeO-NABFP compound is diluted in methanol to an OD of 1.3 mm^{-1} at 400 nm. No pure isomer spectra could be obtained by photospectrometry and HPLC[124]. Steady-state absorption spectra were taken before and immediately after the transient experiment and are displayed in figure 4.22.A.

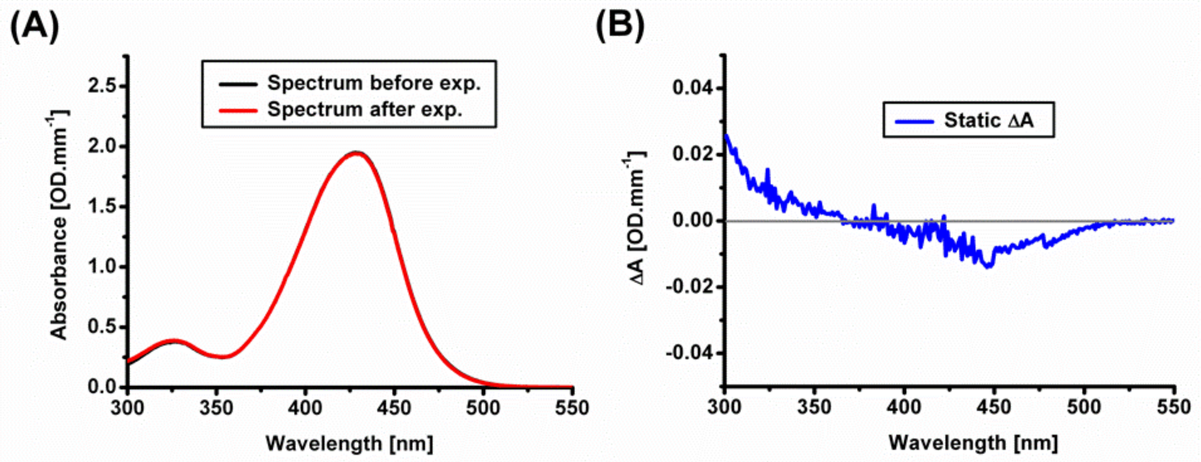

Figure 4.22. **A.** MeO-NABFP absorption spectra taken before and after the transient absorption experiment. **B.** Difference of the absorption spectra of fig. 4.22.A. It does not show any obvious indication of isomer photoconversion

From the good agreement between both spectra, we can conclude that no sample degradation has been caused by laser exposure. As shown by the difference plotted in figure 4.22.B, no detectable isomer ratio change of the mixture could be measured. As the starting solution is not pure (~50%-E-

50%-Z), both photo-reactions ($Z \rightarrow E$ and $E \rightarrow Z$) are taking place. Hence, an isomer difference spectrum would have a very small amplitude if both $Z \rightarrow E$ and $E \rightarrow Z$ isomerizations cancel each other, especially if E and Z isomers have comparable small shifts and extinction coefficients as for the other compounds. The isomers may also be unstable and not live more than a few minutes, the time needed to measure the static spectrum after the experiment.

2. Isomerization revealed by TA spectroscopy

Figure 4.23.A displays the wavelength (300-650 nm) and time-resolved (up to 100ps) absorption changes (ΔA) of MeO-NABFP molecules in methanol. As indicated on figures 4.23.A and B, ESA, SE, GSB and PA contributions are also observed in this compound, ESA and SE being centered around 390-400 and 500 nm, respectively, similarly to what was observed for the previous molecules. The GSB and PA bands are red-shifted (peaking at 430 and 460 nm, respectively), as expected from the absorption spectrum of MeO-NABFP compared to those of NAIPs molecules.

Excited-state signals (ESA and SE) and GSB, the latter being counterbalanced at early times by the ESA signal, are observed immediately after excitation (see 0-ps, 0.15-ps and 0.3-ps spectra in fig. 4.23.B). Being already suggested in the 0.3-ps spectrum, the PA and the GSB contributions (centered at 460 and 430 nm, respectively) appear more clearly in the 0.6-ps, while ESA and SE are still decaying. Further ground state relaxation leads to a quasi-static spectrum after ~30 ps. We mention also that, as seen on figure 4.23.A around 330 nm, a small part of the ESA seems to shift in time, as reported for the other photoswitches.

The first qualitative difference in the data of MeO-NABFP is that ground state anti-phased coherent oscillations modulating the signals are absent. Moreover, the wave-packet-induced spectral shifts extending into the red, like the ones identified before, seem to have vanished, as there is no positive signature identified previously as a delayed and quasi-impulsive PA following the SE. However, a closer inspection of the data shows that a contribution from the PA is observed as a break in the slope of the transients (see guide-to-the-eye in fig. 4.23.C). But it is weak compared to the SE signal, and thus the signal remains negative, as it is still largely dominated by SE. Remarkably, the time scale on which SE and ESA are evolving clearly appears to be longer compared to the other molecules, as seen on the transients of figure 4.23.C. Finally, the GSB recovery and the PA rise seem to evolve on the same time scale as the ESA and SE decay (see fig. 4.23.B and C). As we will show below, exponential functions with a common time origin at t=0 can describe the kinetics sufficiently well, indicating that, as observed qualitatively here, the dynamics are primarily incoherent, unlike the NAIPs photo-isomerizations that were presented before.

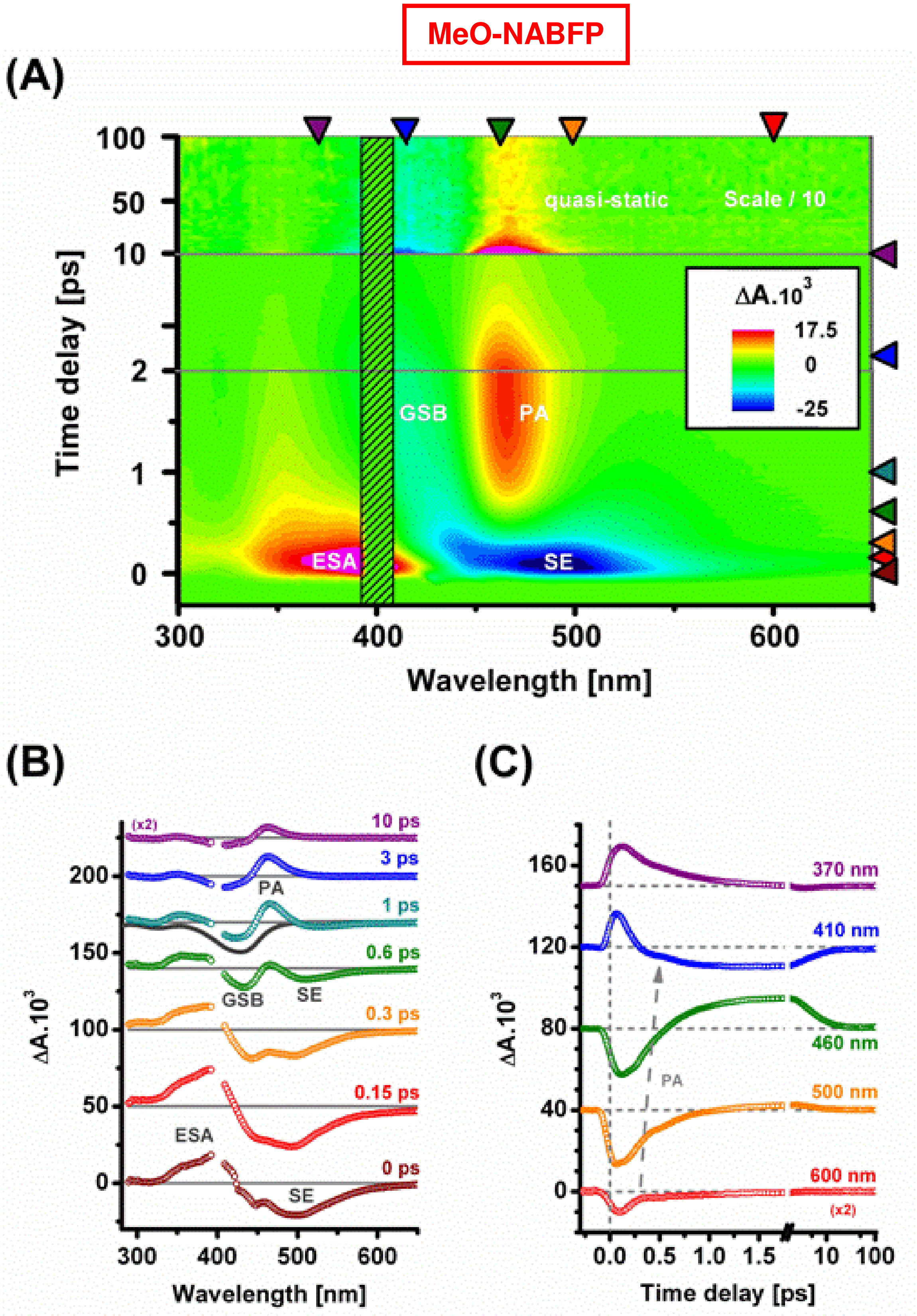

Figure 4.23. **A**. 2D map of the UV–Vis transient absorption change ΔA of MeO-NABFP in methanol as a function of wavelength and time delay. **B.** Spectra (open circles) at delays indicated by the cursors on the right of figure 4.23.A. Together with the 1-ps spectrum, the inverted ground state absorption is shown (solid line). **C.** Transients at wavelengths indicated by the cursors on the top of figure 4.23.A. Both spectra and transients are vertically shifted for clarity.

The quasi-static spectrum observed for MeO-NABFP is displayed in figure 4.24 which shows that it is a long-lived (>100-ps, the time window of the measurement) ground state (as seen by comparison with the scaled transmission spectrum of the sample in figure 4.22.A) transient (this structure is not seen in the absorption spectrum measured a few minutes after the experiment) contribution. It could thus be attributed either to a long-lived ground-state relaxation component, or also to the isomer difference spectrum, in the case in which the isomers are not stable for more than a few minutes.

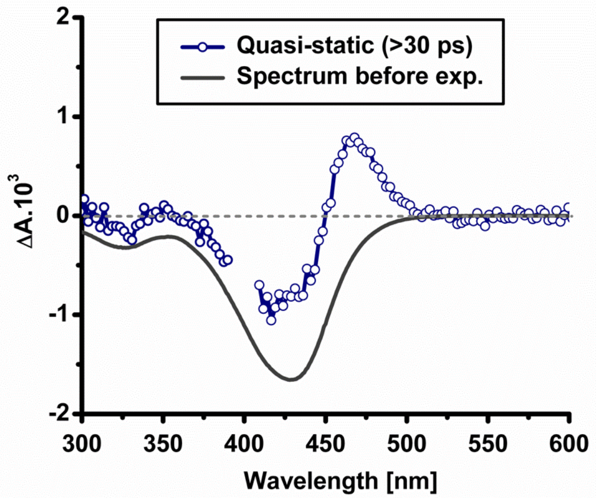

Figure 4.24. MeO-NABFP quasi-static spectrum (blue line and circles) observed at long time delays (>30 ps, averaged between 50 and 100 ps). The steady-state transmission spectrum (grey line) of MeO-NABFP is overlaid for comparison.

MeO-NABFP data fitting with time-zero-referenced exponential functions such as eq. (2.9) is possible, unlike for the NAIP molecules where time-shifts were needed. Figure 4.25 shows a fit at 465 nm, in the maximum of the PA band, using four time constants and an offset. The signal at 465 nm is composed of SE and PA contributions. The fit yields a SE rise time of 0.1 ± 0.01 ps and a decay time constant, which also corresponds to the rise of the PA, of 0.43 ± 0.02 ps. These values are in line with the results of fluorescence up-conversion measurements on MeO-NABFP[121] (0.1 ps rise time and 0.6 ps decay time constant). The two longer decays of 2.2 and 5.8 ± 0.5 ps are associated with ground state relaxation. The residuals are flat after ~0.5 ps, but before, a structure is observed. This is due to the small PA contribution that the exponential functions are unable to fit. Nevertheless, the dynamics of MeO-NABFP are largely dominated by rate-equation-like dynamics.

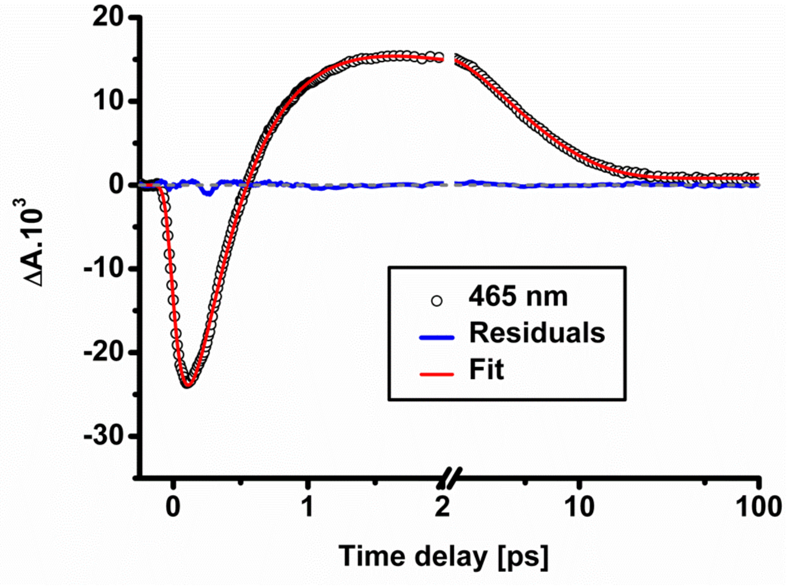

Figure 4.25. MeO-NABFP transients at 465 nm, in the maximum of the PA band. A fit with a function such as Eq. (2.9) is shown, using 4 time constants of 0.1 ps (vibrational relaxation in the excited-state), 0.45 ps (isomerization time constant), 2.2 and 5.8 ps (ground state relaxation) and an offset (quasi-static spectrum). The residuals are plotted. They are flat after ~0.6 ps, while before a small structure is observed, induced by a very weak PA signature in the 465 data. Nevertheless, the rate-equation-like function fits well the MeO-NABFP excited-state (SE) decay and photoproduct formation, unlike for the NAIP molecules.

SVD is applied to the dataset only after 0.8 ps, when the weak PA signature has completely disappeared, and the prominent singular transients are analyzed with global analysis (see Complementary Information). 4 time constants are sufficient to fit the singular transients and the DADSs presented in figure 4.26A and B are obtained. The shorter-lived DADS of 0.65-ps decay constant (fig. 4.26.A) is the sum of GSB, SE and ESA contributions, and is in very good agreement with the 0.6-ps decay found by fluorescence up-conversion measurements[121]. Figure 4.26.B shows the thermalization DADSs (1.3 and 5.6 ps) related to vibrational relaxation/solvation and cooling in the ground state and the DADS (infinite time constant) associated to the quasi-static spectrum observed at long delays.

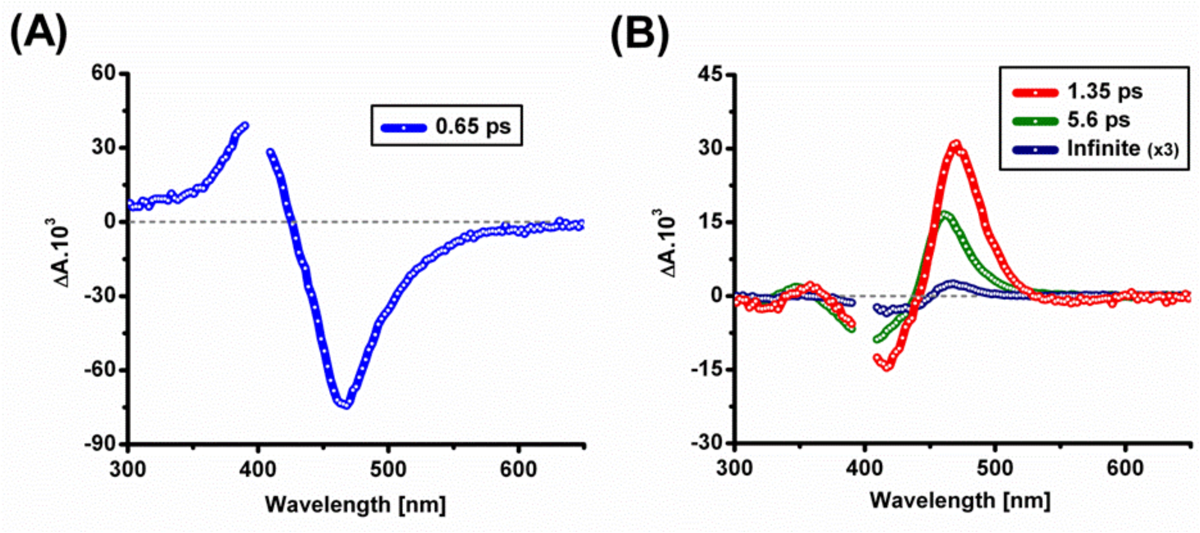

Figure 4.26. **A**. MeO-NABFP Decay Associated Difference Spectra (DADS) of the fastest component (0.65 ps) obtained by SVD and global analysis, associated to excited-state dynamics. **B**. DADS related to ground state dynamics (1.3 and 5.6 ps, red and green lines with circles) and DADS (infinite, blue line with circles) corresponding to the quasi-static spectrum observed at long time delays.

3. MeO-NABFP: ultrafast incoherent isomerization

It has been highlighted above that MeO-NABFP dynamics are different than that of the NAIP-based molecules. The ground state relaxation dynamics are proceeding on the same time scale, but it does not show prominent ground-state coherences and the excited-state evolution clearly occur with a longer decay time of 0.6 ps. No oscillations are observed, but a weak PA signature is nevertheless distinguishable, as well as a weak-amplitude ESA portion shifting in the UV range.

Analysis of fluorescence up-conversion measurements performed on MeO-NABFP indicates that the fluorescence can be globally fitted on the full fluorescence wavelength range (430-650 nm) using an exponential rise of 0.1 ps and a decay of 0.6 ps[121], in very good agreement with the analysis results presented above. Thus the dynamics may be explained as follows. Intra-molecular vibrational relaxation takes place in the excited-state during ~100 fs as suggested by the rise times obtained from fluorescence and SE signals. Then, the population decays to the ground state with a 0.6-ps time constant, which also corresponds to the rise of the photoproduct absorption. Comparison with the other molecules suggests that the excited state PES has a smaller slope providing less acceleration along the torsional coordinate. One cannot exclude the existence of a small energy barrier, slowing down the torsional motion in these molecules.

But weak wave packet-like PA and ESA signals are also observable, which means that a small part of the molecules also isomerize with the same coherent scenario than the one presented before.

Hence, two interpretations can be given. First, as the sample solution contains both isomers, the dynamics could be very different for one isomer compared to the other. One would isomerize in the coherent regime and the other one through an incoherent isomerization process, the coherence being lost to a large extent in the excited state. A second possibility is that the excited-state dynamics of both isomers are equal, but that two decay channels to the ground state are possible with this molecule. A first one, dominant, would lead to an incoherent isomerization in 0.6 ps, and a second faster one would occur with the same scenario that has been presented in detail in part 4.C.4.

E. Interpretation and conclusion

1. Coherent ultrafast isomerization and substitution effects

As highlighted in § 4.C.3, the different substitutions performed on the NAIP pyrroline moiety mainly influence the torsional frequency, and could be explained by the change of moment of inertia. It is thus an interesting experimental finding but it is not critical as far as the parameters controlling isomerization in these molecules are concerned.

On the contrary, substitutions located on the indanone moiety reveal much more information. First, the steady-state absorption spectra are red-shifted when electron-donating group are added to the structure. The MeO-NAIP, Prot-MeO-NAIP and ZW-NAIP (391 to 397 nm) are ~35 nm red-shifted from that of NAIP (~360 nm). Adding an oxygen atom into the structure further red-shifts the absorption maximum by 30 nm (429 nm). This red-shift suggests that the conjugation length of the π-orbitals is increased. Alternatively, and assuming that the energy of S_0 is fixed by the Schiff base cation – counter ion interaction, a red-shift indicates an increasing dipole moment change, i.e. charge translocation in S_1.

The design of the switches followed the idea that an increased charge translocation would destabilize the C=C double bond and thus facilitate, i.e. speed up isomerization. We observe experimentally that the excited-state dynamics and the isomerization timing are slower when we add electron-donating groups on the indanone moiety: the excited-state lifetime is multiplied by a factor of ~4-5 for MeO-NABFP compared to NAIPs. Our experimental measurements of isomerization speeds correlate with a blue-shift of the absorption wavelength, from NAIP (360 nm) to MeO-NABFP (430 nm). This poses two questions: a) is the design idea of a charge translocation induced C=C destabilization correct ? and b) how do the substitutions affect the S_1 PES and why is the fluorescent state stabilized when electron-donating groups are added ?

These questions, are currently being addressed by quantum chemistry calculations. Computational results on the PES, minimum energy path and population dynamics simulations on all molecules could bring new insights to better understand these observations. The relation between photo-induced charge translocation and excited-state lifetime has to be clarified.

An alternative interpretation of the different isomerization dynamics could also invoke the kinetic torsional energy carried by the wave packet. As we have worked at a fixed excitation wavelength, the NAIP switch, is expected to bear the least amount of kinetic energy. Nevertheless, the NAIP displays the fastest wave packet and isomerization dynamics, leading us to conclude that the kinetic energy brought to the molecule is not affecting the isomerization speed. To verify this point, measurements varying the excitation wavelength on one of the molecules could be performed.

Finally, and unlike what was observed for rhodopsin and its analogues (see Chapter 1), where a correlation between speed and efficiency could be highlighted, even the fastest photoswitches all show Z → E quantum yields in the range of 0.2-0.3, thus rejecting a Landau-Zener-type argument to explain the results. This rather suggests that the branching ratio is controlled at the conical intersection, in agreement with reference[54].

For an improvement of the isomerization quantum yield, one thus may have to act on the conical intersection, either by other molecular structural changes which would affect the topology of the CI but which remain unclear until now, or by using a strong optical field, as shown in reference[125].

2. Ultrafast coherent dynamics in NAIPs and rhodopsin

According to the above scenario, the coherent character of the photo-reaction bears a lot of similarities with that of retinal in rhodopsin. Blue-shifting ESA has been observed on sub-50 fs time scales in retinal proteins[27, 30, 31], most probably reflecting the initial high-frequency stretch relaxation of retinal. It is more clearly observed in the isorhodopsin measurements performed by Schoenlein and co-workers[42] where they could follow a clear ~100 fs ESA blue-shift (see fig. 4.27.B).

All NAIPs molecules show a clear ESA dynamic shift on a 160 fs (NAIP) to 230 fs (ZW-NAIP) time scale. Figure 4.27.A recalls the ESA shift from ZW-NAIP. This evolution represents the wave packet motion on the excited-state potential energy surface (PES) from the Franck-Condon (FC) region down to a region most probably close to the conical intersection (CI).

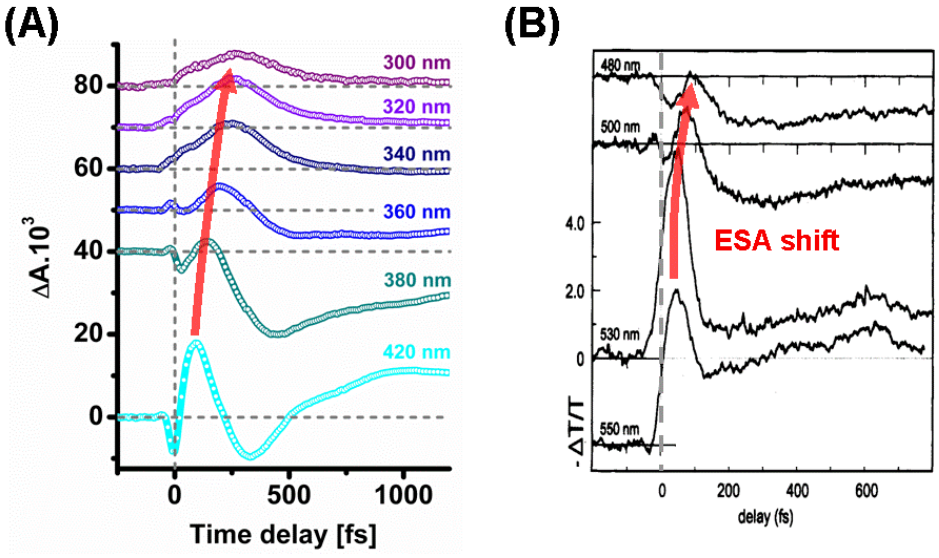

Figure 4.27. **A**. ZW-NAIP transient at 300, 320, 340, 360, 380 and 420 nm showing the dynamic shift of ESA. **B**. Isorhodopsin transients at 550, 530, 500 and 480 nm showing an ESA shift. Picture taken and adapted from Schoenlein et al[42].

The delayed ground-state recovery and subsequent impulsive photoproduct formation observed in the NAIPs data can be again put in perspective with what has been measured on the rhodopsin protein by Schoenlein, Peteanu, Wang and coworkers[27, 30, 31]. But a few years later Haran et al.[32] performed the same type of transient absorption experiment but further into the red and near-IR regions of the spectrum (600-900 nm). Thanks to their high signal-to-noise ratio, they could observe around 800 nm a small signal composed of a delayed and impulsive induced absorption following the stimulated emission that they could not assign at that time. In the case of the photoswitches, the advantage of broadband detection maybe makes the difference, as it allows a precise tracking of the spectral evolution of the different bands (see fig. 4.14 for example). We can claim here that in NAIPs this red impulsive PA merges into the PA and is the starting point of a series of oscillations. In both NAIPs and rhodopsin cases, the SE is similarly short and followed by a rapid red (NAIPs) or near-IR (rhodopsin) induced absorption, preceding the ground state wave packet dynamics. One may conjecture that the 800-nm induced absorption is by analogy the early-time signature of the population arrival in the photoproduct state of rhodopsin.

Figure 4.28.A and B present a comparison between the red-shifted quasi-impulsive induced absorption for the fastest photoswitch (NAIP) and for rhodopsin, respectively. The similarity of the signals is striking.

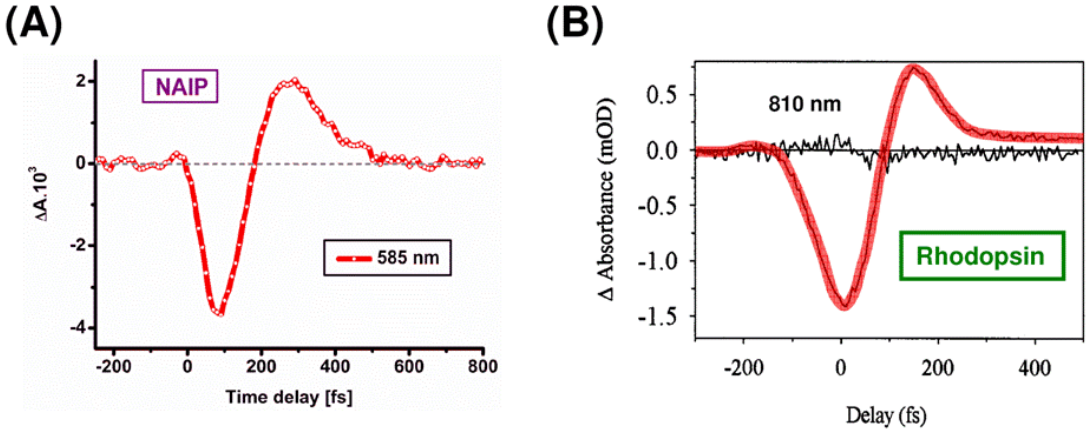

Figure 4.28. **A**. NAIP transient at 585 nm showing stimulated emission followed by a quasi-impulsive ground state absorption. **B**. Rhodopsin transient at 810 nm taken and adapted from Haran et al.[32].

We previously argued that the NAIPs photoswitch ground-state oscillations are the signature of a wave packet initially created in the excited state, which survives in the photoproduct after passing through the conical intersection.

Figure 4.29.A displays a panel of transients from the MeO-NAIP photoswitch, highlighting the appearance of the impulsive PA on the red-wavelength edge, which then merges into the PA band and becomes the first peak of a series of oscillations. Figure 4.29.B presents data taken from Haran et al.[32], where the same behavior is observed in rhodopsin.

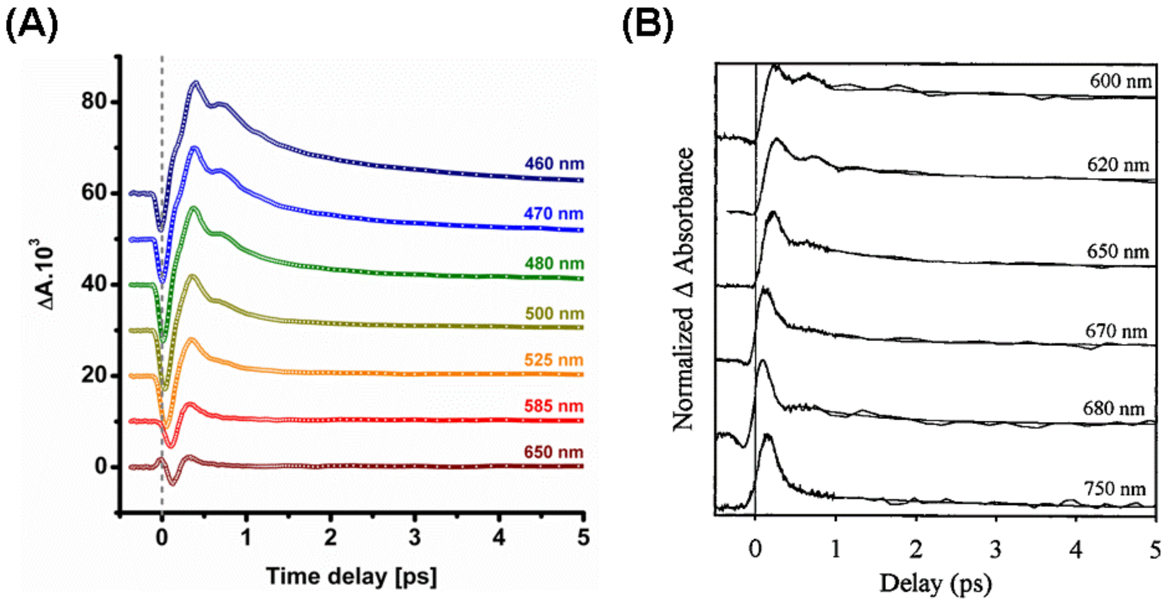

Figure 4.29. **A**. MeO-NAIP transients at 460, 470, 480, 500, 525, 585 and 650 nm. The impulsive ground state photoproduct absorption PA appears into the red and then time-shifts with decreasing wavelength, giving rise a series of rapidly damped low-frequency oscillations. **B**. Rhodopsin transients at selected wavelengths in the red absorption band of rhodopsin PA (picture taken from Haran et al.[32].

These data comparisons between NAIP switches and rhodopsin data are highlighting the fact that the goal of including, into a small photoswitch in solution, the rhodopsin's excited-state dynamics and isomerization scenario has been achieved and confirmed by this experimental work.

Chapter 5

Forward (Z → E) and backward (E → Z) reactions

This chapter is dedicated to the study of the photoswitching bi-directionality. The idea is to compare the Z → E and E → Z photoreactions, which are predicted by theory to be equally fast. Both reactions are tested for 3 switches (ZW-NAIP, MeO-NAIP and NAIP) where Z or E isomer majority can be obtained. In contrast to Chapter 4, they are all diluted in deuterated methanol-d4 solvent to be able to perform ^{1}H-NMR measurement prior to the TA experiments. The weak (~10^{-3}) solvent signals were not corrected in the data presented in this Chapter.

A. The zwitterionic switch ZW-NAIP

1. Isomer ratios determined by NMR and static difference spectra

A fresh ZW-NAIP (Z) pure sample was diluted to a concentration C = 3.10^{-2} M and then separated into two parts. The first one was carefully kept in the dark at room temperature so as to keep the highest possible concentration of Z isomers. The second part was irradiated at 454.5 nm (40 mW) for 24 hours using the spectral line from an Argon laser, in order to photoconvert Z isomers into E isomers. Indeed, the latter absorbs ~3 times more than the Z form at this wavelength (see fig. 4.1 in Chapter 4).

A great majority of Z isomer in the first sample solution is obtained (see fig.5.1 below) and is thus called “Z isomer sample” in the following. It is the one used to measure and characterize the Z → E photoreaction. The irradiated sample, in which E isomers are in majority (see fig.5.1), is named “E isomer sample” and is utilized on the contrary to investigate the E → Z reaction.

Before TA experiments (and before taking absorption spectra) the sample solutions were measured by ^{1}H-NMR spectroscopy[126](300 MHz). Figure 5.1 shows two specific proton signatures used to differentiate E and Z isomers and to characterize the Z/E isomer ratios of both solutions (see Chapter 3 for details).

Calculations of area ratios between E and Z isomers specific signatures are performed. This leads to a 98.5% concentration of Z isomers in the “Z isomer sample”. In the irradiated “E isomer sample“ solution, the concentration of E isomers reaches 88.5%, confirming that the continuous irradiation has been able to photoconvert a larger amount of Z isomers into E isomers. These E/Z isomer ratio are nearly constant for several hours[111, 119].

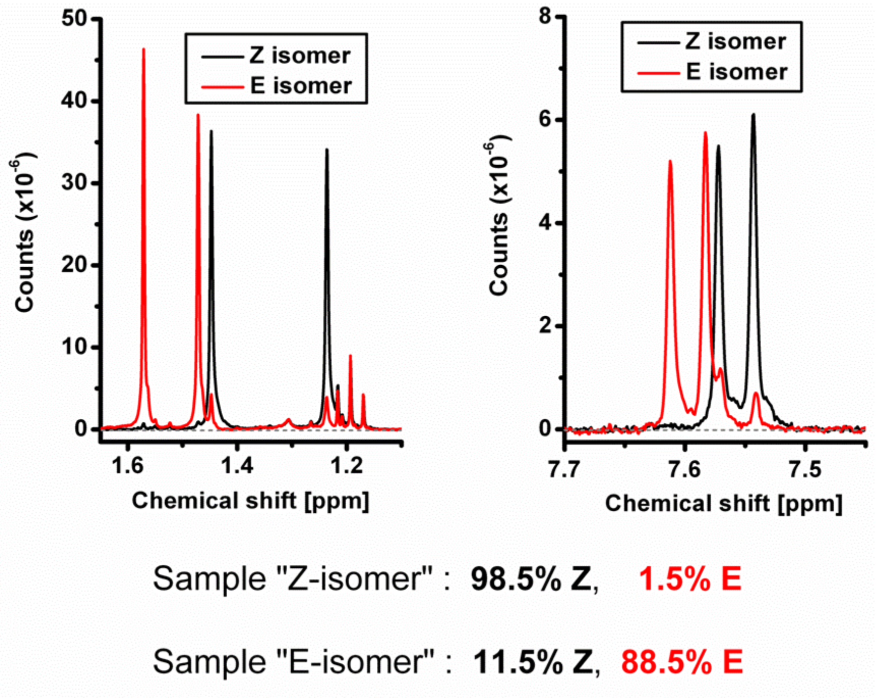

Figure 5.1. NMR spectra in the 1.1 to 1.65 ppm region and 7.4-7.7 ppm region. The respective areas of Z and E signals determine the Z/E ratios of the Z and E sample solutions, which are 98.5% // 1.5% and 11.5% // 88.5%, respectively.

Figure 5.2.A displays the absorption spectra of both diluted sample solutions. The concentrations of the samples diluted in CD_3OD were kept equal ($1.1*10^{-3}$ M in 10 mL reservoirs). The difference absorption spectra of the E sample spectrum and the Z sample spectrum, or vice versa (mirror image with respect to $\Delta A = 0$) are plotted in figure 5.2.B, together with the reference difference spectra obtained independently[111]. They almost perfectly match and further confirm that our solutions are in majority containing Z or E isomers. These two difference spectra will be used as references to characterize the Z → E (E-Z difference spectrum) and E → Z (Z-E difference spectrum) reactions when the photoconversions in the transient absorption experiments are achieved. They are seen in the data when relaxation is over, and were named quasi-static spectra in Chapter 4.

Figure 5.3.A shows the absorption spectra measured before and after TA experiments for Z and E isomer samples. In figure 5.3.B the differences between the spectra before and after experiments are plotted for both samples. They show the E-Z and Z-E difference spectra, respectively, as highlighted by the reference difference spectra which are overlaid. During the Z → E (E → Z) experiment, pump-induced photoconversion of Z (E) isomers into E (Z) isomers has occurred as expected, as shown by

the E-Z (Z-E) difference spectrum. Apart from these differences, no sign of sample degradation by laser light exposure during experiments is observed.

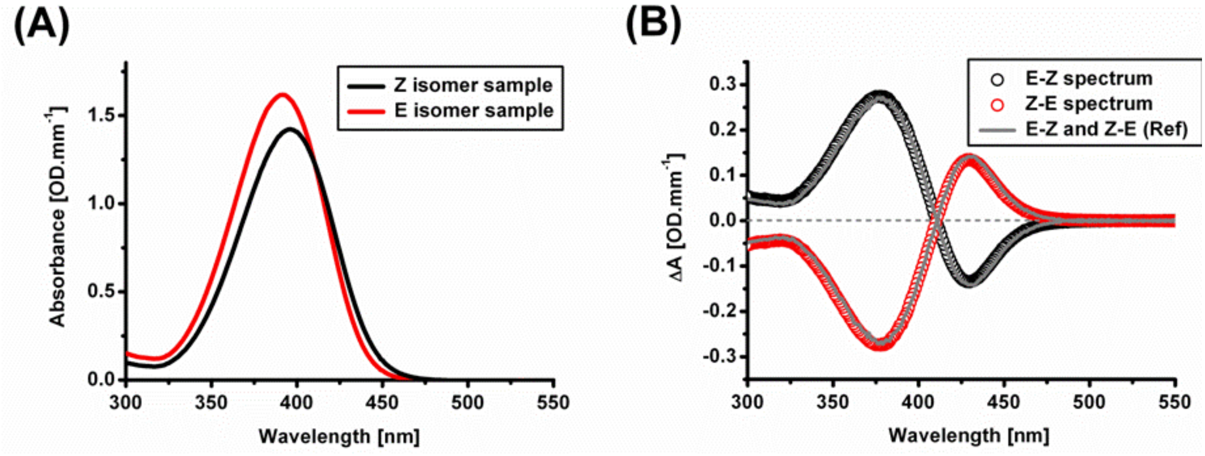

Figure 5.2. **A**. Absorption spectra of the Z and E ZW-NAIP sample solutions before experiments. One has been kept in the dark and has large Z-isomer majority, and the second has been irradiated at 454.5 nm and E-isomers are in majority. **B**. E-Z (black, will concern the Z→E photoconversion) and Z-E (red, will concern the E→Z experiment) difference spectra obtained subtracting the spectra described in A. They are compared to reference E-Z and Z-E scaled difference spectra (grey lines) obtained independently[111].

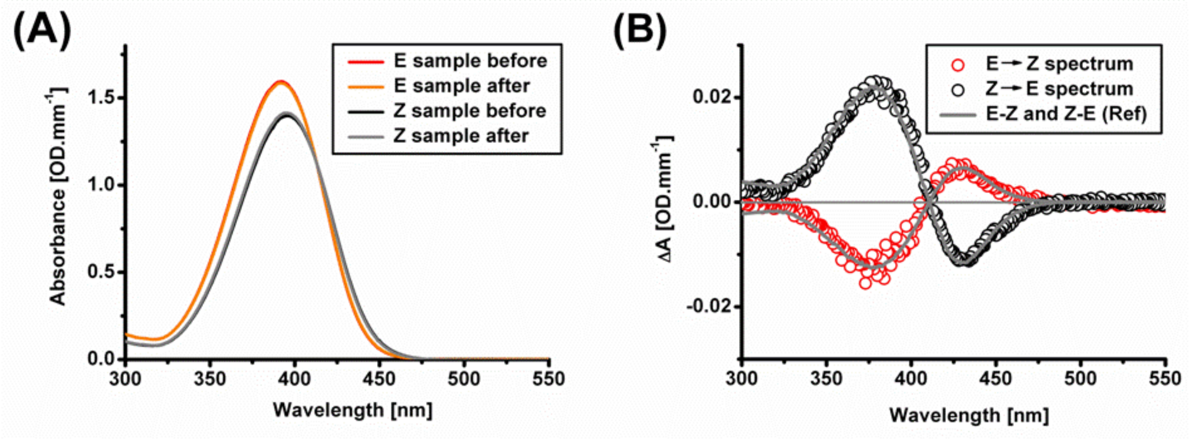

Figure 5.3. **A**. Absorption spectra of the E and Z ZW-NAIP sample solutions before and after experiments. One has been kept in the dark and has large Z-isomer majority (98.5%, named Z sample on the graph), and the second has been irradiated at 454.5 nm and has 88.5% E-isomer concentration (E sample). No sample degradation is observed after illumination with laser light during the TA experiments, but small differences can be seen and are plotted in B. **B**. E-Z (black, showing the Z→E photoconversion) and Z-E (red, showing the E→Z photoconversion) difference spectra (after – before) obtained subtracting the spectra for both sample solutions described in A. They are compared to reference E-Z and Z-E scaled difference spectra[111] (grey lines).

An important remark has to be mentioned at this stage. The experiment duration (and thus 400-nm excitation exposure time), computer-controlled, is exactly the same in both measurements. But as clearly seen in figure 5.3.B, the amplitude of the E-Z difference spectrum is almost twice as large as the Z-E difference spectrum. Despite the fact that the Z/E ratios are not exactly reversed (98.5/1.5 and

88.5/11.5) and that E has a slightly larger extinction coefficient at 400 nm ($\varepsilon_Z/\varepsilon_E$ at 400 nm is 0.9) we can already suggest that the E → Z and Z → E reaction quantum yields are different, the latter being higher by a factor of ~2. This observation will be further detailed below.

2. Results for forward (Z→E) and backward (E→Z) isomerization reactions

Figure 5.4.A displays the wavelength and time-resolved pump-induced absorption changes (ΔA) of the Z isomer sample of ZW-NAIP molecules in deuterated methanol. The ΔA 2D-map is presented in the range of 325 – 610 nm as a function of time-delay up to 100 ps. Figures 5.4.B and 5.4.C present selected spectra and kinetic traces from the same data set.

This measurement of the Z → E reaction of the ZW-NAIP molecule, performed again and presented here as a control and comparative experiment, features the same behavior as the one presented in details before (Note that the spectral range measured here is smaller than in figure 4.2 of Chapter 4). In particular the pronounced dynamic spectral shifts and coherent oscillations, showing the wave-packet-like population evolution both in ground and excited states, are reproduced as expected.

The panel composed of figures 5.5.A, B and C is similar to the one of figure 5.4, but now focuses on the E → Z experiment measured with the E isomer sample solution. Globally, spectro-temporal features and band assignments are similar in both experiments, but large differences can be observed when comparing both data sets.

Indeed, the first observation is that the impulsive photoproduct absorption PA (λ>500 nm), which was clearly observed in the Z → E experiment, seems to be less intense. It can be clearly observed when comparing figure 5.4.A to 5.5.A, and also by looking at the spectra (see 0.4 ps spectrum in fig. 5.4.B and 5.5.B) and kinetic traces (see PA curved arrow and corresponding transients in figure 5.4.C and 5.5.C). The broad 0.4-ps spectrum of the Z → E reaction significantly extends into the red part of the spectrum while the amplitude of the one from the E → Z reaction is weaker in that spectral region.

Moreover, the oscillations that are obvious in the 2D-map at 440-450 nm for the forward reaction have disappeared in the E → Z photoreaction experiment. Indeed, the large amplitude (~20% of the signal) oscillations which were extracted by a fit procedure in Chapter 4 have completely vanished, as it will be highlighted below (see fig. 5.9.B).

Finally the last qualitative difference is located into the 10-100-ps time sections of figure 5.4.A and 5.5.A. They show quasi-static spectra after ~30ps, which appears to be of opposite signs and have the spectral characteristics of E-Z and Z-E difference spectra, respectively. This is in agreement with the steady-state results (fig.5.3) showing that bi-directional isomerization has been achieved, and this is detailed in the next paragraph.

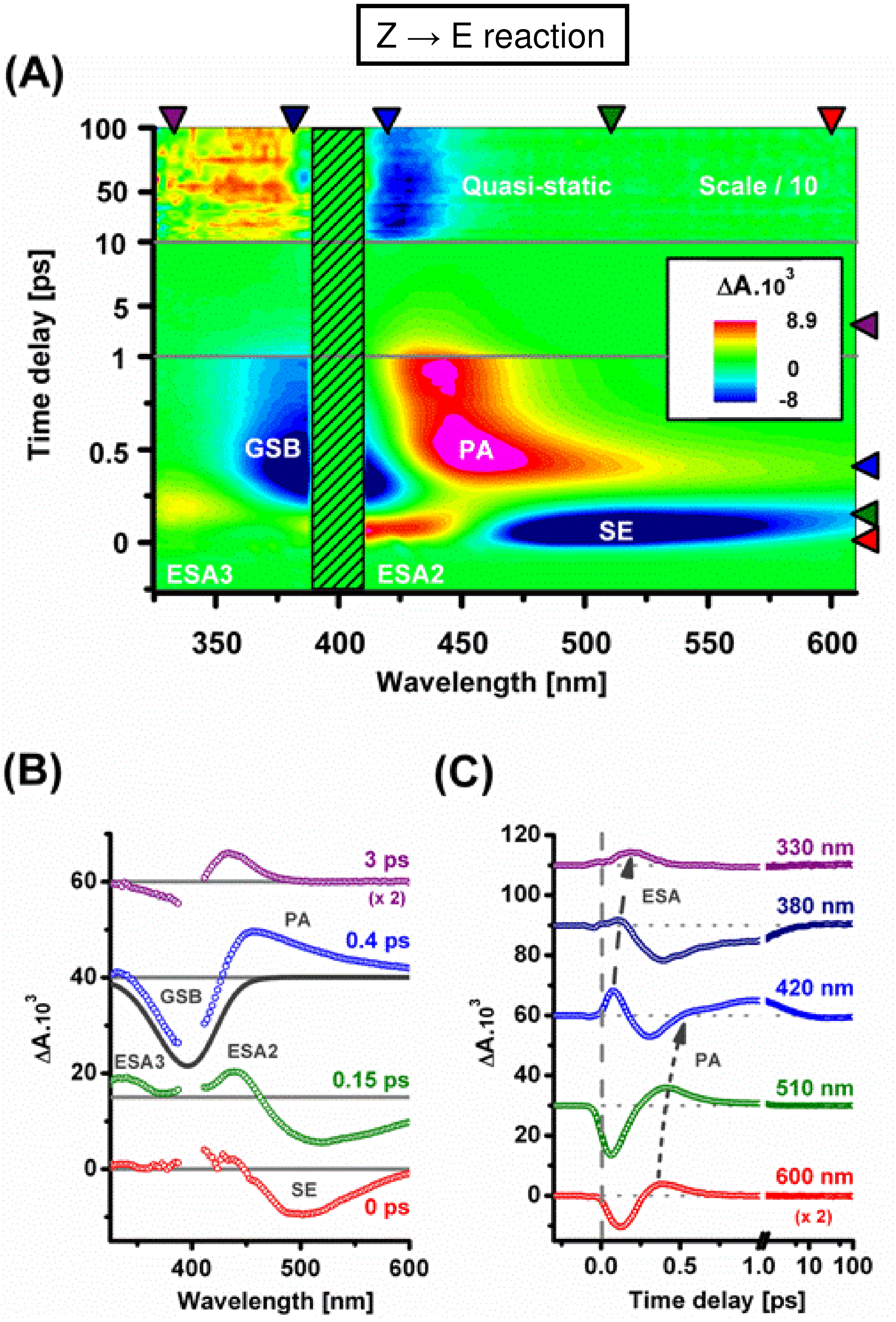

Figure 5.4. A. 2D-map of the UV–Vis transient absorption change ΔA of ZW-NAIP “Z sample” in CD_3OD as a function of wavelength and time delay. The ΔA color scale in the 10-100 ps time section has been divided by a factor of 10. The crossed-out portion around 400 nm is disregarded. **B.** Spectra (open circles) at delays indicated by the cursors on the right handside of figure A. Along with the 0.4-ps spectrum, the inverted Z isomer ground state absorbance is shown (solid line). **C**. Kinetic traces at wavelength indicated by the cursors on the top of panel A.

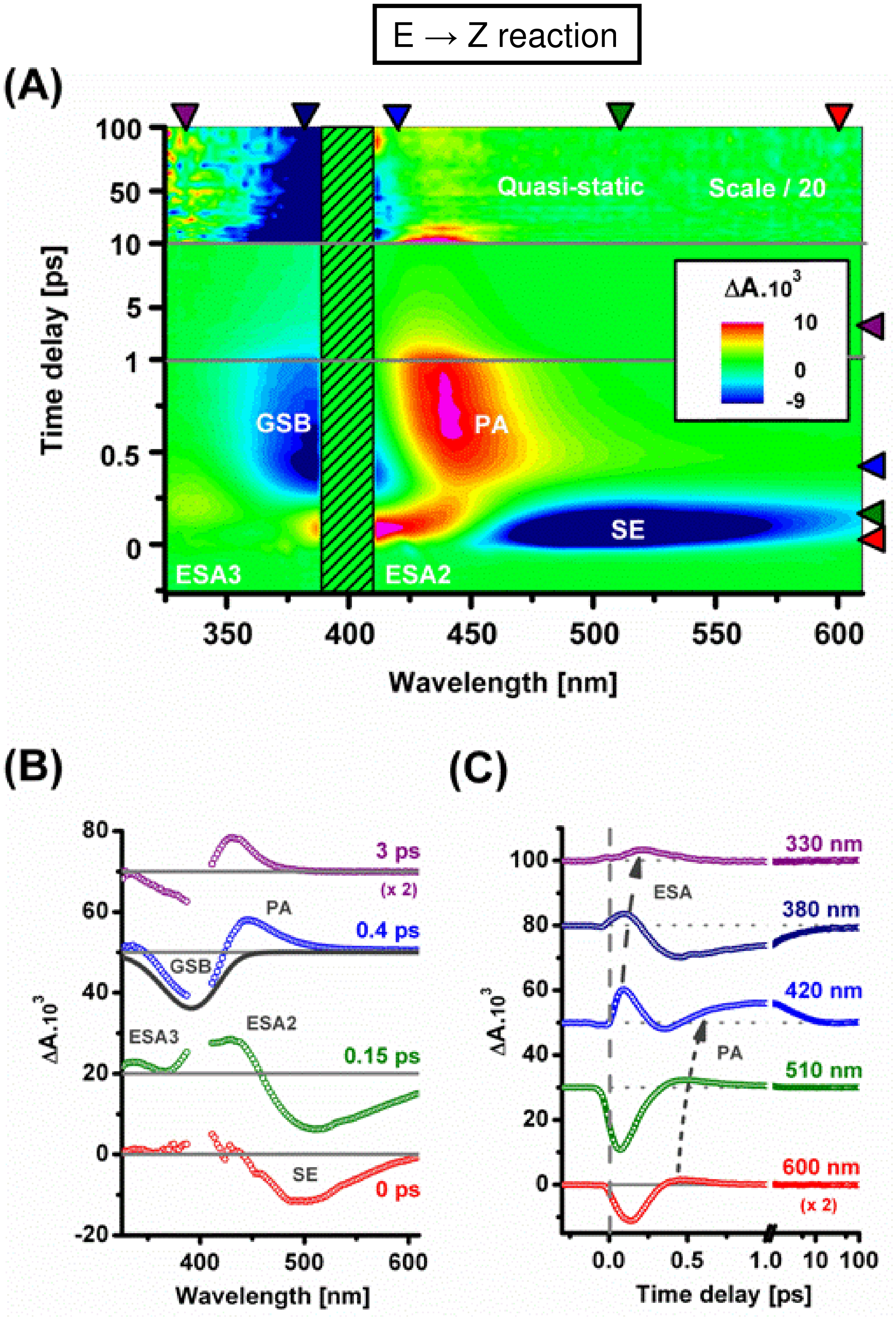

Figure 5.5. **A**, **B**, **C**. Same as fig. 5.4.A, B and C for ZW-NAIP "Z sample" in CD_3OD, respectively. In A the color scale in the 10-100 ps time section has been divided by a factor of 20, to be able show the weak-amplitude quasi-static spectra.

3. Analysis of the TA experiments

a. Quasi-static spectra

Both quasi-static difference spectra (>30 ps) from the Z → E and E → Z transient absorption experiments are plotted in figure 5.6, together with the scaled reference E-Z and Z-E difference spectra[111]. The spectra are only displayed in the visible range, where the noise level is low enough so that an accurate comparison with reference spectra can be made[*]. Both Z → E and E → Z reaction difference spectra are in very good agreement with the scaled references. This clearly indicates that, for both reactions, the isomerisation is accomplished before 30 ps.

In contrast to the E-Z difference spectra obtained in the measurement of Chapter 4, the positive band above 450 nm is not observed. The only difference between these two experiments is the sample age, the one presented in this Chapter being freshly-synthesized and measured. We suggest that these tentatively-assigned transient distorted forms or by-products of the photoswitches appear with aged samples (several months). The mechanistic reasons for this observation are unknown.

A last obvious observation from figure 5.6 is that, as suggested by the analysis of figure 5.3, the isomerization quantum yield is confirmed to be different in one isomerization direction or the other. Indeed, a factor of ~2 is needed to scale the E-Z and Z-E obtained quasi-static spectra. This scaling factor is found to be ~1.7 from the difference spectra presented in figure 5.3. These two observations unambiguously show that the reaction quantum yield of the Z → E reaction is larger than the E → Z reaction. The value of the almost pure Z isomer bleach value at time zero can be obtained by the fitting procedure of Chapter 4, yielding $\Delta A = -11.10^{-3}$ at 374 nm for example, and the leftover Z bleach value can be derived from the quasi-static difference spectrum ($\Delta A = -2.6.10^{-3}$ at 374 nm). It gives an approximate Z → E reaction quantum yield of 0.24 ± 0.03, in good agreement with Chapter 4. Thus the reaction quantum yield of the E → Z reaction is approximately this value divided by ~2, i.e. ~0.12. These values are in agreement with more accurate ones obtained by combined NMR and mid-IR spectroscopy (Réhault et al.[119]).

---

[*] As the UV range was acquired simultaneously with the Vis range (300-600nm), the noise is larger in the UV region due to the fact that the continuum amplitude is weaker, and thus the reference correction is not as good. As the quasi-static spectra amplitudes are in the order of a few 10^{-4} for the measured E-Z or Z-E difference spectrum, this is an issue.

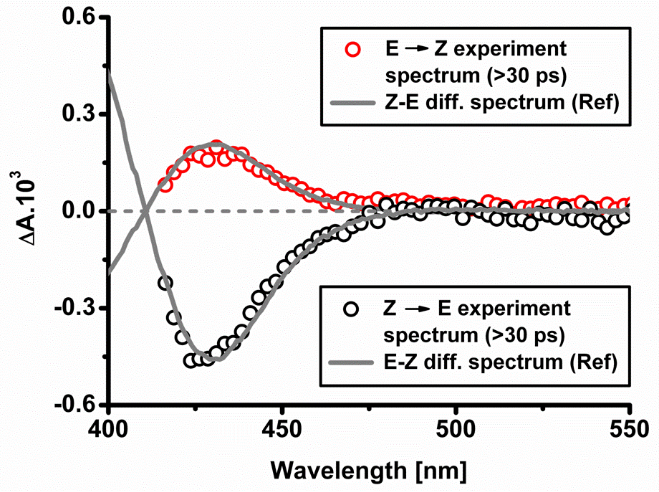

Figure 5.6. Quasi-static difference absorption spectra of Z → E (black circles) and E → Z (red circles) reactions in the visible range. Scaled reference E-Z and Z-E difference spectra (solid grey) are added for comparison.

b. Ground state relaxations

Figure 5.7 compares the transients at 370 and 440 nm for both Z → E and E → Z reactions. The time scale is specifically chosen to focus on the ground state relaxation dynamics, from 1 to 100 ps. This figure shows that, except a constant offset between the curves, both ground state thermalizations occur on the same time scale from 1 to ~30 ps. After that, the quasi-static regime is reached.

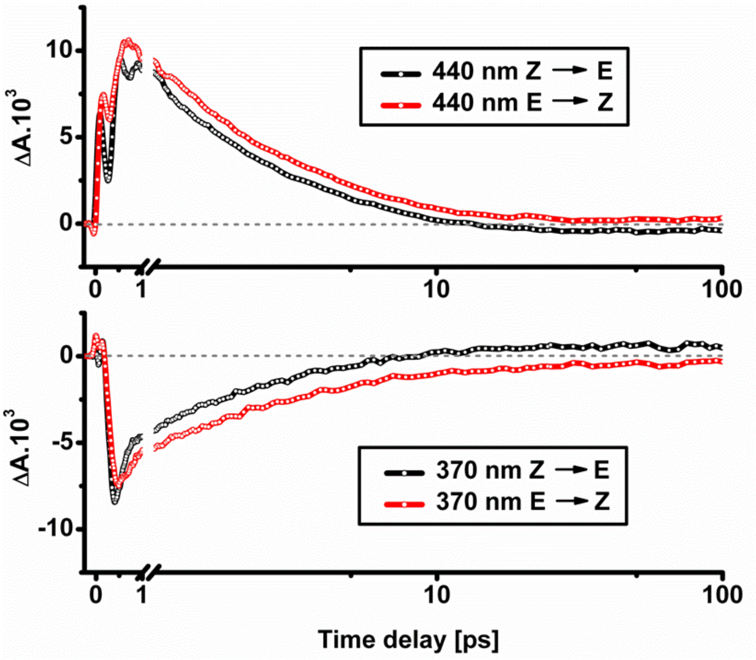

Figure 5.7. Transients at 440 nm and 370 nm for both Z → E (black) and E → Z (red) reactions. It shows ground state relaxation dynamics evolving on the same time scale.

To quantitatively compare both ground state dynamics, SVD is applied considering both Z → E and E → Z data for t ≥ 1.2 ps. Global fitting of the 3 dominant singular value kinetic traces obtained in each case is performed using the same procedure as in Chapter 4 (see Complementary Information).

Four time constants are sufficient to fit the singular transients and obtain flat residuals for both reaction measurements (see Complementary Information). An ultrafast component is needed to account for ultrafast leftover contributions (0.27 ps) and is neglected in the following discussion. Figure 5.8 presents the DADS of both datasets. Both infinite-time DADSs are in good agreement with their respective quasi-static spectra shown in figure 5.6. The other two time constant values are found to be 0.95 ± 0.1 ps and 4.6 ± 0.2 ps for the Z → E reaction, in very good agreement with Chapter 4, and 1.3 ± 0.1 ps and 5.1 ± 0.2 ps for the E → Z one. The values are quantitatively close and moreover, the spectral shapes and amplitudes are also very much alike. The same spectral shift of ~20 nm is observed between the shorter-lived (0.95 and 1.3 ps) and longer-lived (4.6 and 5.1 ps) DADSs, showing ground-state relaxation and cooling.

These observations and analysis show that in both the Z → E and E → Z reaction measurements, the ground-state relaxations proceed on the same time scale.

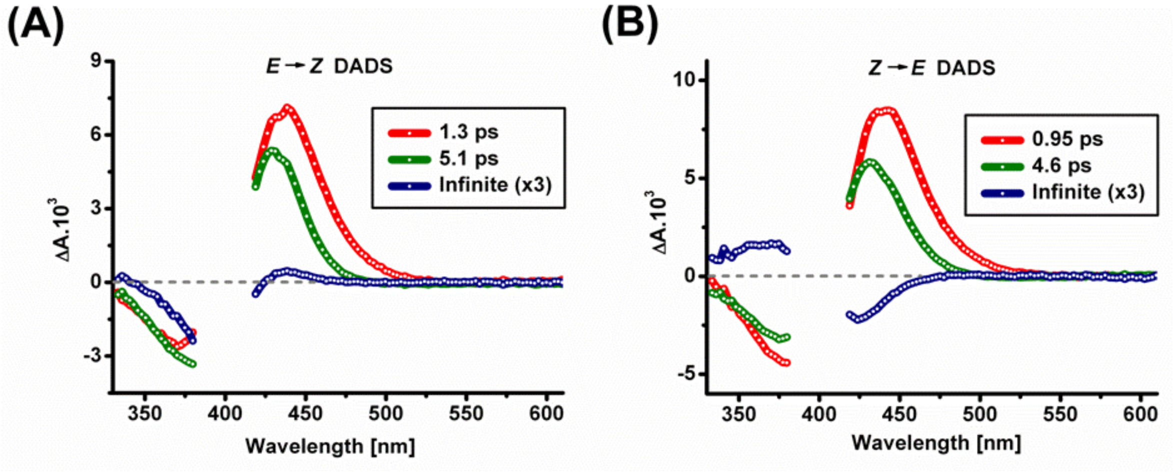

Figure 5.8. **A**. Decay Associated Difference Spectra (DADS) of the transient absorption data of ZW-NAIP E → Z reaction. The two major decay components of 1.3 ± 0.1 and 5.1 ±0.2 ps are related to solvation/IVR and cooling, while the infinite-time DADS represents the quasi-static spectrum and thus the Z-E difference spectrum. **B**. DADS derived from SVD and global analysis for the Z → E reaction. The obtained 0.95 ± 0.1 ps, 4.6 ± 0.2 ps and infinite-time components DADS are plotted.

c. Wave packet behaviour

As seen on figure 5.4 and 5.5, the ESA3 signal around 330 nm is observed in both datasets. The qualitative comparison of the kinetic traces in figure 5.4.C and 5.5.C indicates that the ESA dynamic shift appears in both datasets. Figure 5.9 shows the two kinetic traces of Z → E and E → Z reactions at 330 nm. The signal is weak but we can observe that the ESA3 from E → Z reaction is broader and shifted by ~20 to ~30 fs. The first weak positive peak at t=0 ps comes from solvent signal. The negative contribution at t > 0.7 ps is due to the GSB.

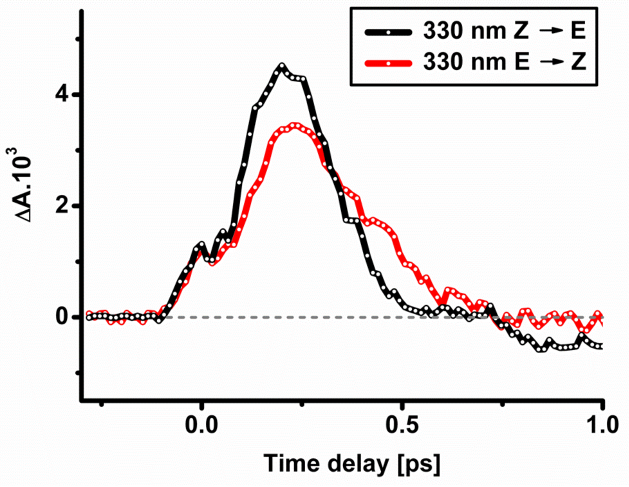

Figure 5.9. Transients at 330 nm (3 curves averaged at 328, 330 and 332 nm) of Z → E (black) and E → Z (red) reactions.

In the panels of figure 5.10 representative wavelengths for both Z → E and E → Z reactions are presented for comparison. Figure 5.10.A and B show both transients at 367 nm and 445 nm, in the blue part and red parts of both isomer absorption spectra, respectively, but this time with a focus on the early-times dynamics. Surprisingly, both E → Z transients do not show any oscillations unlike the Z → E ones, in which they are clearly observed (see Chapter 4 also).

Another interesting feature, obviously seen in fig. 5.7, is the offset between both curves, which represents the converted isomer absorption difference. It corresponds to a [E-Z] (-) [Z-E] difference, the difference of the respective difference spectra of both reactions. We can already note that this offset is constant after 1 or 1.5 ps, in agreement with the isomerization occurring on the before 1 ps. One may then attempt to obtain the isomer difference spectrum by conveniently subtracting these two datasets.

Indeed, when considering only one reaction as in Chapter 4, we had to wait ~10 ps so that the ground-state recovery had sufficiently progressed to be able to observe the first appearance of the positive band of the difference spectrum. With these forward and backward reaction data, as the relaxation times are almost equal (see above), a subtraction procedure will eliminate the signal due to the vibrationally-hot ground-state species, so as to reveal the isomer difference signal only. This will be developed in the next section.

Figures 5.10.C and D display the transients at 509 and 602 nm, respectively. Both figures yield the same conclusion, i.e. a lower amplitude of the impulsive photoproduct absorption in the E → Z reaction. Eventhough the transients presented here are not corrected for the static absorption difference at the excitation wavelength (400 nm), this difference cannot explain what is observed in the figures (the E → Z transients should be further reduced by a factor 0.91, the absorption ratio between Z and E samples at 400 nm). Despite the difference in the early times, after ~0.7 ps the transients overlay very well.

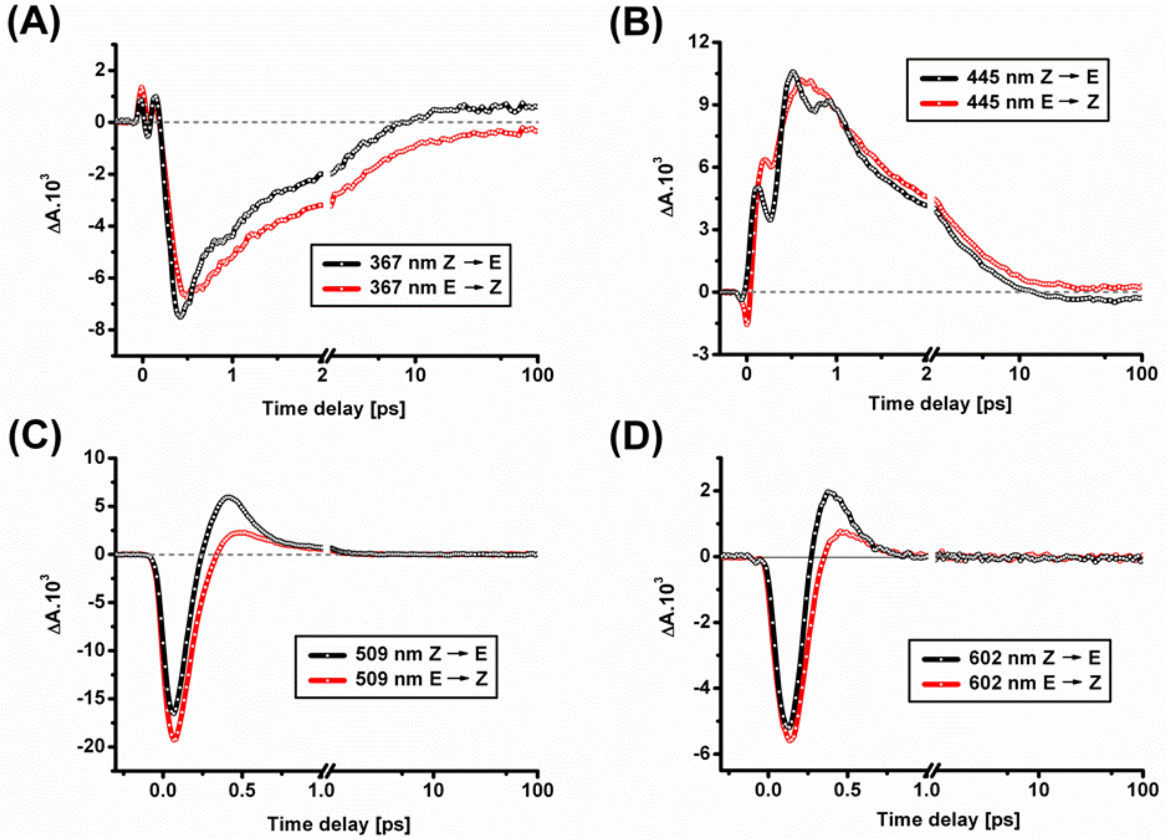

Figure 5.10. **A**. Transient at 367 nm for both measured reactions (Z → E in black and E → Z in red). Signal amplitudes are as measured. 3 curves are averaged at 365, 367 and 369 nm to obtain the ones presented in the figure. **B**, **C** and **D**. Transients at 445 nm, 509 and 602 nm, respectively, for both reactions (Z → E in black and E → Z in red).

Figure 5.11 shows the 602-nm transient together with simultaneous fits and performed using the functions described in Chapter 4 (see § 4.A.3.b). The SE time constant is fixed to 0.14 ps, assuming that the lifetime reported by fluorescence measurements is the same for both isomers, in order to better compare the PA amplitude, delay and time spreading. The onset time and the convolution standard deviation (σ) of the PA are left as local parameters, while the others are global. With that procedure we see that the E → Z PA contribution is two times lower in amplitude, broadened and shifted by 50 fs.

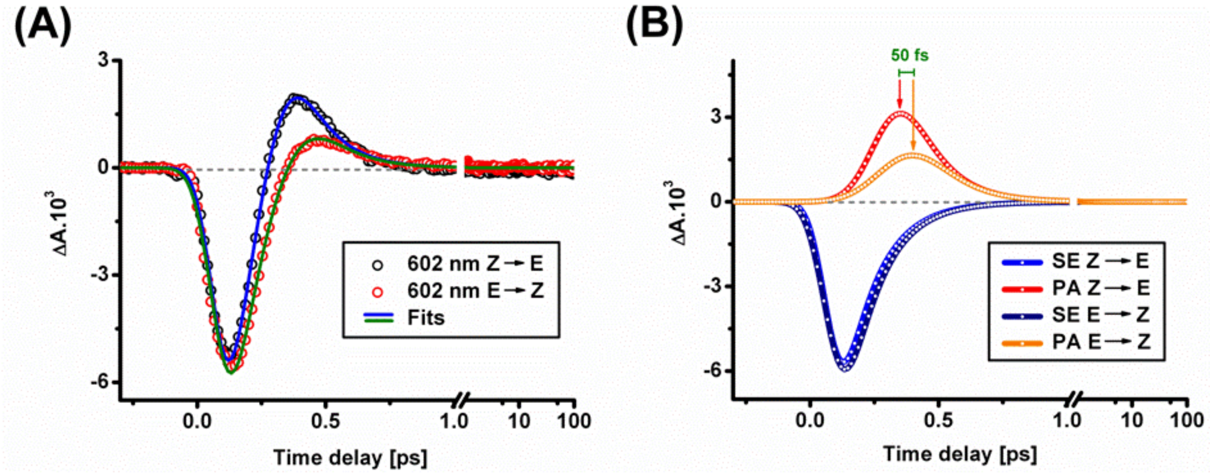

Figure 5.11. **A**. Transients at 602 nm for both Z → E (black circles) and E → Z (red circles) reactions together with their fits using the model described in the text. **B**. Fit decomposition of the 2 contributions of each fit (SE and PA). The fit results give a ~50-fs difference between the wavepacket arrival times in the ground state (350 and 400 fs at this wavelength, respectively).

As a short summary, we can say that the ESA coherent evolution on the PES surface is also observed for the E → Z reaction, but is arriving ~20-30 fs later and its wave packet-like temporal shape is broadened. The impulsive arrival in the ground state represented by the PA band in the red part of the spectrum shows a lower-amplitude and also temporally-broadened wave packet-like signal, arriving ~50 fs later than for the Z → E reaction. Finally, no oscillations are detected in the E → Z experiment.

Assuming that the wavelengths probed in both reactions correspond to the same torsion angles, we can suggest at this stage that the wave packet evolution is slightly slower on the excited state PES of the E isomer compared to Z.

d. Additional insights on isomerization timing

As highlighted above, a convenient subtraction of the Z → E and E → Z datasets may reveal, as both vibrationally-hot populations relax on the same time, the isomer difference only and thus provide a more precise timing of the isomerization reaction.

First, the difference in the sample absorptions at 400 nm has to be accounted for. We thus weight the E → Z data with a factor 0.91, derived from fig. 5.3.A. Figure 5.12 shows the spectra at 3 ps for both reactions. As pointed out in Chapter 4, no isomer difference signal is detectable in these spectra, because they are largely dominated at this time delay by ground-state relaxation processes.

But if our scenario developed in Chapter 4 is correct, the isomerization has already occurred. As presented above, it is almost equally fast in both directions. Hence, the E-Z (Z-E) isomer difference spectrum should be hidden in the Z → E (E → Z) data spectrum on a sub-ps time scale, and in particular in the spectrum at 3 ps. Subtracting E → Z from Z → E data will reveal an amplified E-Z difference spectrum. This is performed in figure 5.12 (blue curve), where it is indeed clearly observed.

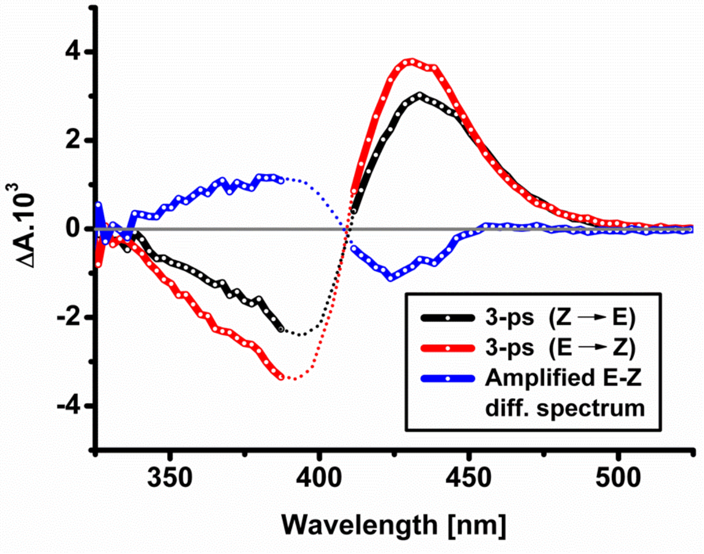

Figure 5.12. Principle of the data subtraction. Both the E-Z and Z-E difference spectrum are hidden in the 3-ps spectra (*Z* → *E* in black and *E* → *Z* in red) by the vibrationally hot ground state absorption and the bleach recovery. As ground-state relaxations occur on the same time scales, and are spectrally very similar for both reactions, the subtraction leads to an amplified E-Z spectrum.

Applying the same subtraction with the complete data sets, after isomerization has occurred (0.4 ps), yields the data plotted in figure 5.13. They reveal the E-Z isomerization spectrum which is already distinguishable on a sub-ps time scale, and is modulated at early times by the ground state coherent oscillations from the Z → E reaction.

Figure 5.14 plots two transients from figure 5.13 at 370 nm and 440 nm. They clearly indicate an isomer difference spectrum which is formed on a sub-ps time scale, showing that isomerization has occurred. Vibrational relaxation of the “hot” ground state species induces a slower rise within a few picoseconds, leading to a signal level that does not evolve after that. This isomer difference signal is modulated by anti-phased oscillations from the Z → E reaction on these blue- and red-shifted wavelengths compared to the absorption. These observations support the sub-picosecond isomerization scenario presented in Chapter 4.

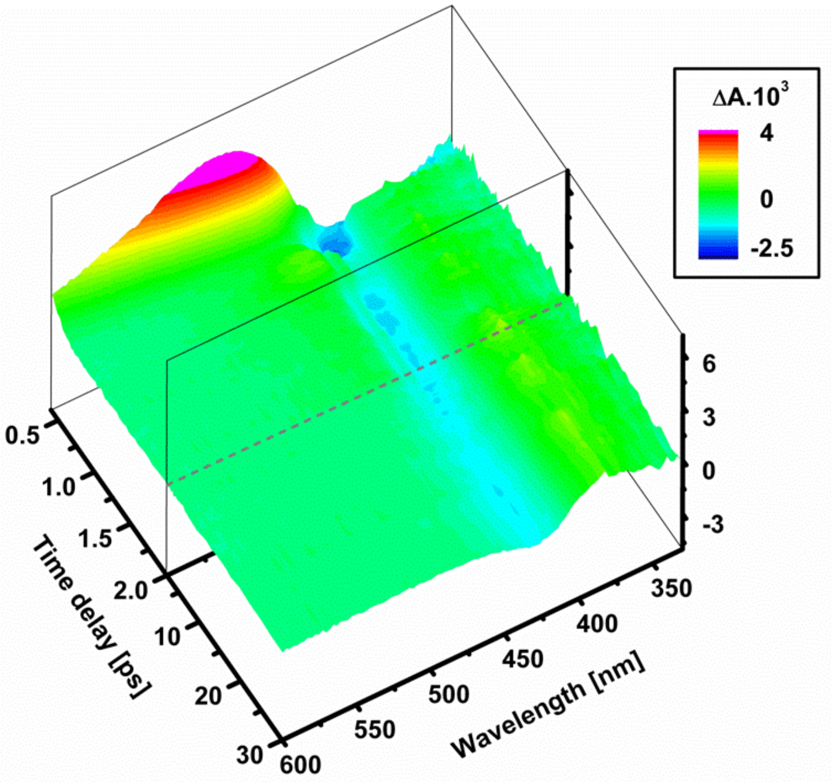

Figure 5.13. Result of the subtraction of $Z \rightarrow E$ and $E \rightarrow Z$ data explained in the text in the 0.4-30 ps time window and 325-600 nm wavelength range. ΔA changes are color-coded. The subtraction clearly shows a sub-picosecond formation of the amplified E-Z difference spectrum, modulated at early times by oscillations. Data were interpolated between 390 and 410 for the clarity of the figure.

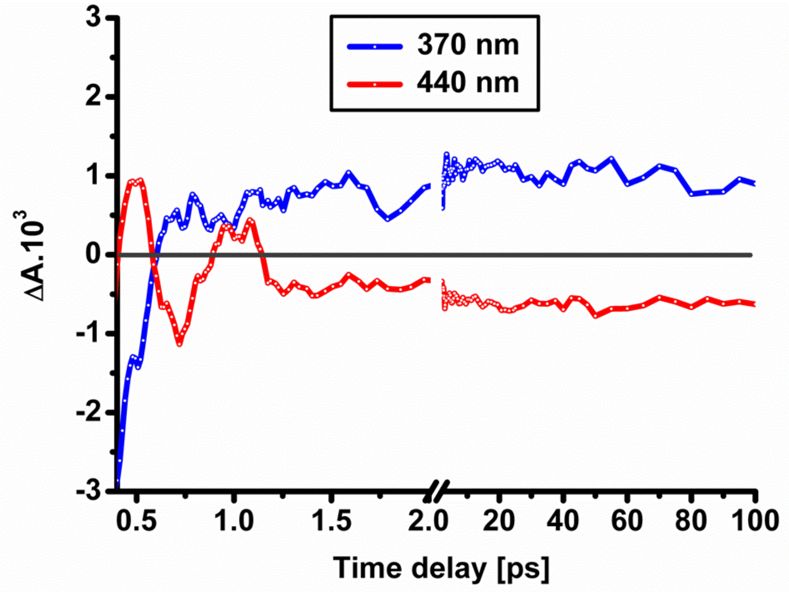

Figure 5.14. Subtraction of E → Z from Z → E data at 370 nm (blue line) and 440 nm (red line). Both traces are obtained by averaging data at three wavelengths (367, 370 and 372 nm and 438, 440 and 443 nm). It shows a sub-picosecond formation of the photoproduct highlighted by simultaneous positive (370 nm) and negative (440 nm) signals corresponding to the E-Z difference spectrum, which further relaxes on a few picoseconds time scale. It is fully relaxed after ~ 20 ps. Oscillations are modulating the signals at early times.

B. The MeO-NAIP switch

1. Isomer ratios and experimental conditions

Z and E isomer sample solutions of MeO-NAIP were obtained using the same procedure described for ZW-NAIP. ^{1}H-NMR spectra of both samples were acquired prior to TA experiments. The concentration of the Z and E isomer solutions were 9.3 10^{-3} and 7.2 10^{-3} M, respectively, in a volume of 0.5 mL of CD_3OD. Figure 5.15 shows NMR spectra in E and Z isomer sensitive regions. The analysis of the spectra yields a 95.5% concentration of Z isomers in the “Z isomer sample” and 88% E isomer in the “E isomer sample“ solution. Hence, with this photoswitch it was also possible to accumulate the metastable E isomer, and thus create relative concentration in E and Z isomers large enough for the investigation of forward and backward reaction. The two isomer ratios of the Z and E samples are in the same range to that of ZW-NAIP in the previous section. They are also stable for hours[1, 2] with this compound.

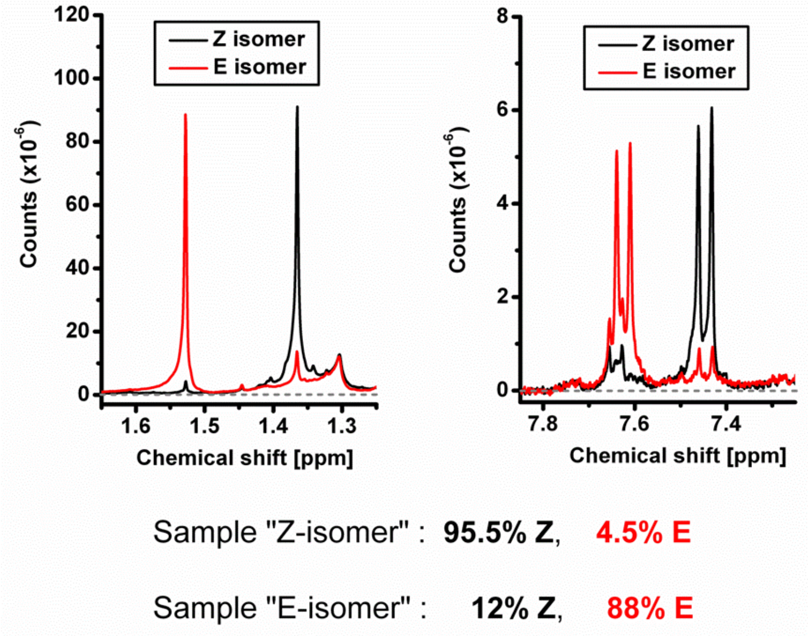

Figure 5.15. NMR spectra in the 1.2 to 1.7 ppm region and 7.25-7.85 ppm regions. Z/E ratios of 95% // 5% and 12% // 88% are obtained for the Z and E MeO-NAIP samples, respectively.

The absorption spectra measured before and after TA experiments for Z and E isomer samples are presented in figure 5.16.A. Both solutions were diluted 10 times after NMR. The differences between the spectra before and after experiments are plotted for both samples in figure 5.16.B. They show the

MeO-NAIP E-Z and Z-E difference spectrum, respectively, as highlighted by the reference difference spectra[53] which are overlaid. Despite these expected isomer absorption differences due to photoconversion, no sign of sample degradations by laser light exposure during experiments are observed.

We note that, unlike the different Z → E and E → Z reaction quantum yields found for ZW-NAIP, the amplitude of both difference spectra are similar here (identical 400-nm excitation exposure time), pointing to an approximately equal quantum yield for both reactions, taking into account the small difference in the solutions concentrations. This is in agreement with results obtained by other methods[1, 53] and the results of Chapter 4, yielding a ~0.27 reaction quantum yield.

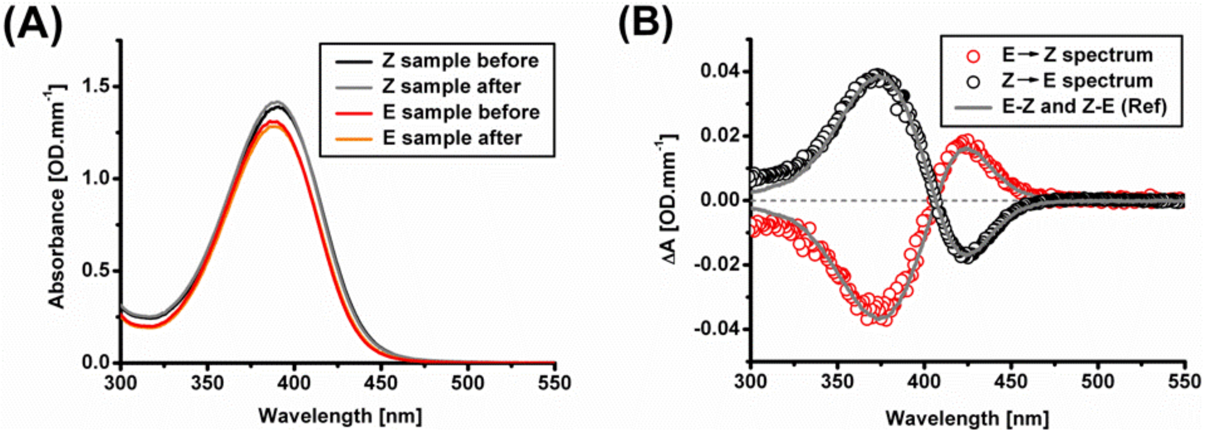

Figure 5.16. **A**. Absorption spectra of the E and Z MeO-NAIP sample solutions before and after experiments. **B**. E-Z (black, showing the Z→E photoconversion) and Z-E (red, showing the E→Z photoconversion) difference spectra (after – before) obtained by subtracting the spectra of A for both sample solutions. They are compared to reference E-Z and Z-E scaled difference spectra[53] (grey lines).

2. Results for MeO-NAIP's Z→E and E→Z isomerization reactions

As the MeO-NAIP sample used for this experiment was in low quantity (so a small sample solution reservoir of only 2 mL for each measurement), the photo-converted quantity of molecules in both solutions was evolving faster than in the previous experiments. This is why only the first scans were kept for each TA experiment, leading to a lower signal-to-noise ratio than usual. This is why these data will only be briefly and qualitatively compared.

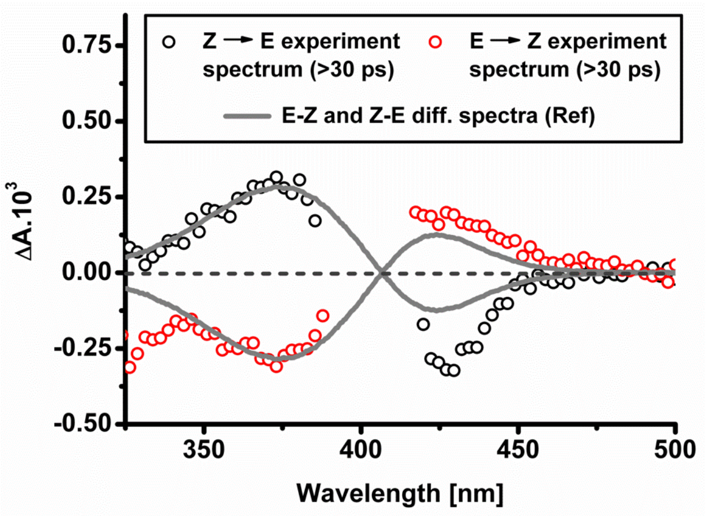

Figure 5.17. Quasi-static spectra for both Z E and E Z experiments. The E-Z and Z-E reference spectra[53] have been overlaid for comparison. Deviations from this reference spectrum are observed in the visible range.

Figure 5.17 shows the quasi-static spectra observed at long delays for both measurements. Opposite quasi-static spectra are observed, suggesting that isomerization has occurred in both reactions, but they do not match perfectly with the reference E-Z and Z-E spectra. The lower signal-to-noise ratio of these experiments may be responsible for this discrepancy, as it can be observed in figure 5.18.

Figure 5.18.A and B displays the absorption changes ΔA of the Z and E isomer samples of MeO-NAIP molecules diluted in deuterated methanol. It was measured in the range of 310 – 700 nm and up to a time delay of 100 ps.

The measurement of the *Z* → *E* reaction of the MeO-NAIP molecule, performed again and presented here as a control and comparative experiment, features the same behavior as the one presented in details before. The *E* → *Z* data presented in figure 5.18.B again features the qualitative characteristics as the *Z* → *E* experiment but also reveals that the PA is again weaker in the *E* → *Z* reaction and that the oscillations are significantly reduced.

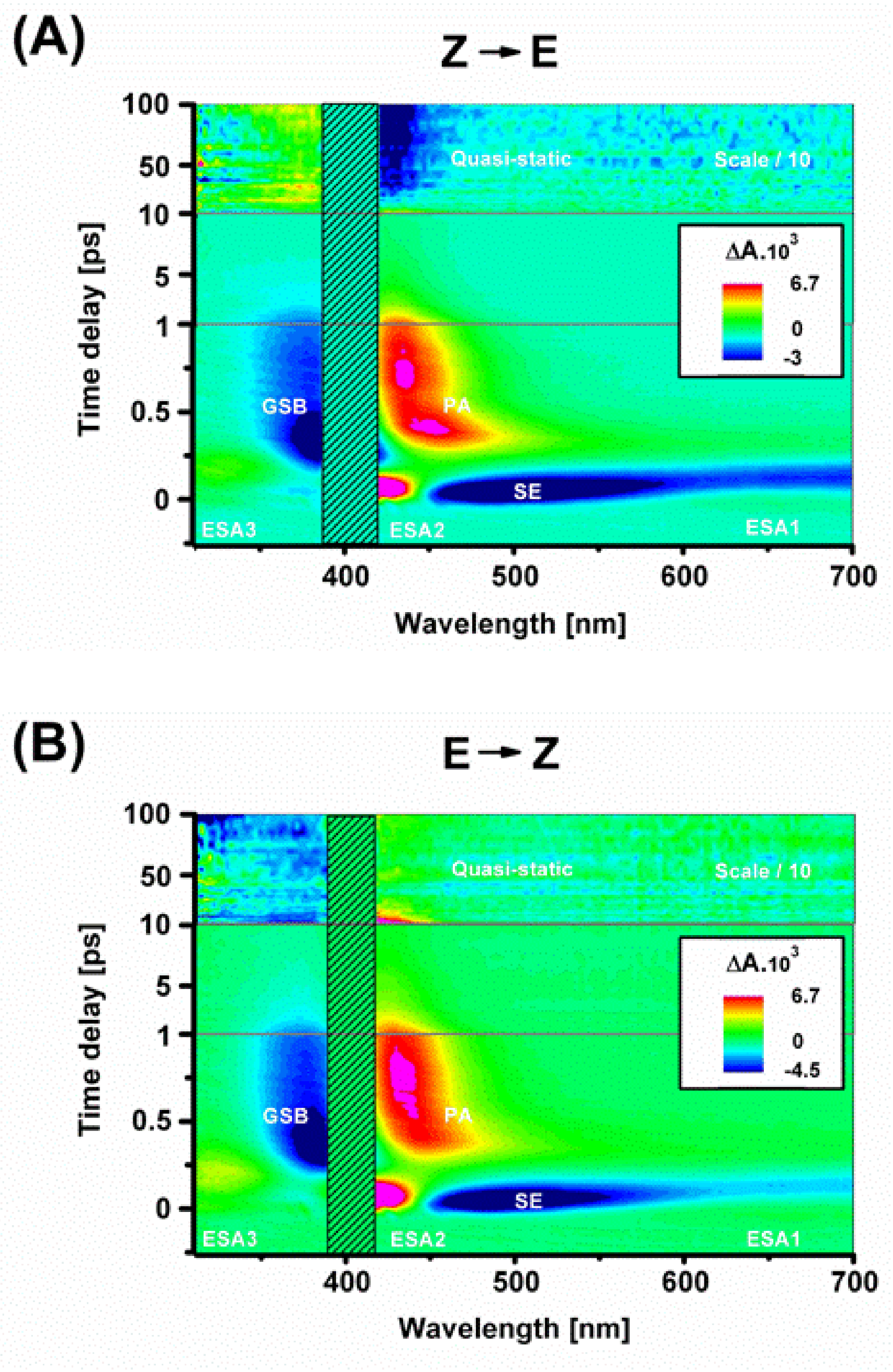

Figure 5.18. A. 2D-map of the UV–Vis transient absorption change ΔA of MeO-NAIP "Z sample" in CD_3OD as a function of wavelength and time delay. The color scale has been divided by a factor of 10 in the 10-100 ps time section. **B.** Same as A for MeO-NAIP "E sample".

Figure 5.19 displays three transients from both Z → E and E → Z reactions. The transients in the red part of the isomers absorption spectra (446 nm), plotted in figure 5.19.A, show that, unlike the ZW-NAIP sample where oscillations have completely vanished, they can still be distinguished for the E → Z reaction, but are reduced. Figures 5.19.B and 5.19.C show the transients at 509 and 602 nm, respectively. The data indicate that the PA in the E → Z reaction is weaker, but not significantly broader or delayed (both PA maxima are at 0.33 ps at 602 nm for example). Finally, and as for ZW-NAIP molecules, the ground-state relaxations again proceed on the same time scale.

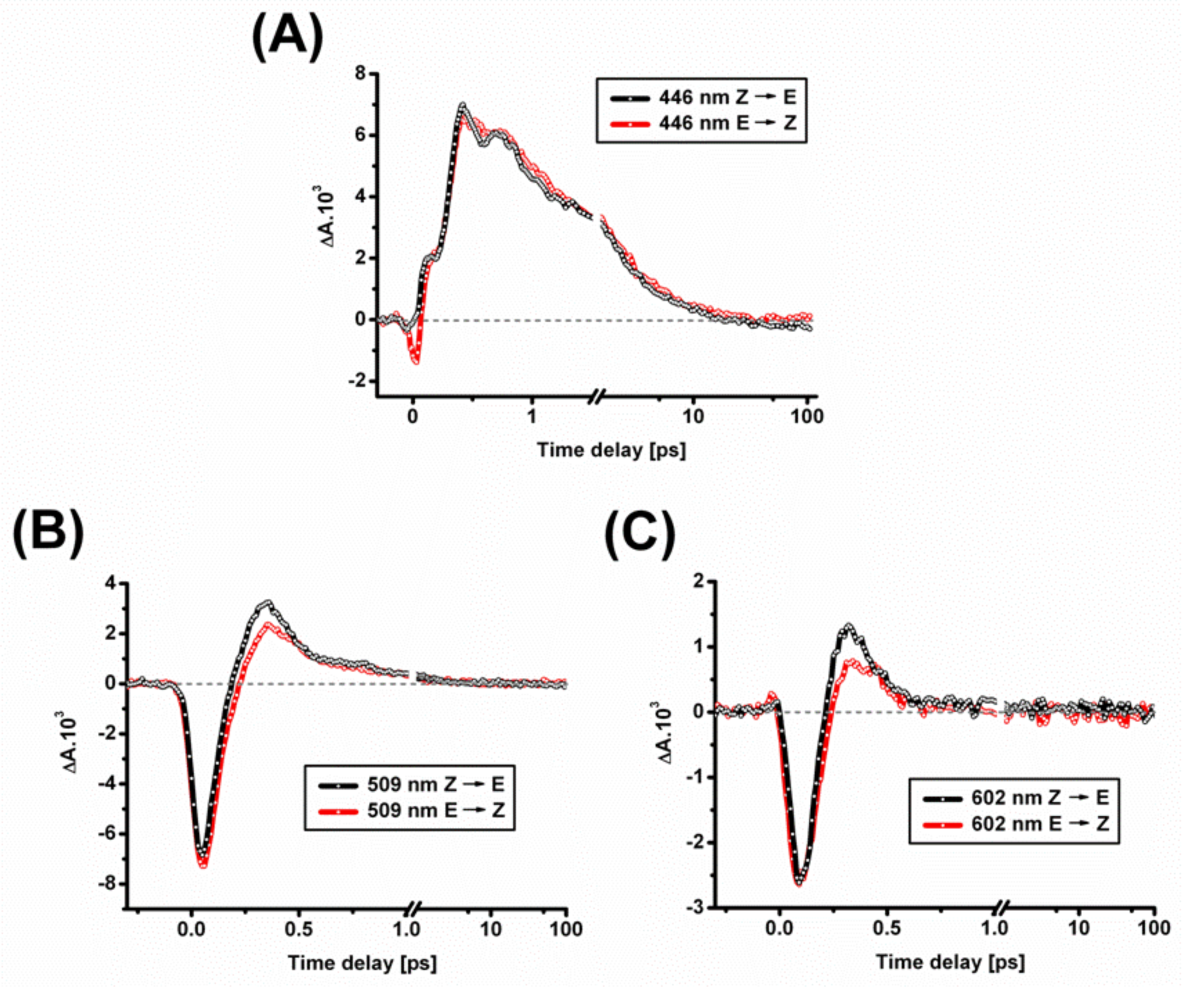

Figure 5.19. **A**. Transient at 446 nm for both measured reactions (Z → E in black and E → Z in red). **B** and **C**. Same as A for transients at 509 and 602 nm, respectively.

C. The NAIP switch

NAIP Z-sample solution was obtained by diluting the powder of synthesized molecules (90%-Z/10%-E), in deuterated methanol. The E isomer sample was obtained by a 24-hours illumination at 400 nm, a favorable wavelength for Z → E isomer conversion. ^{1}H-NMR spectra of both samples are presented in figure 5.20. The Z isomer sample shows a good isomer ratio of 90%-Z/10%-E, whereas the E isomer sample only has 63% of E isomer, showing that accumulation of the E form of the NAIP molecule is difficult.

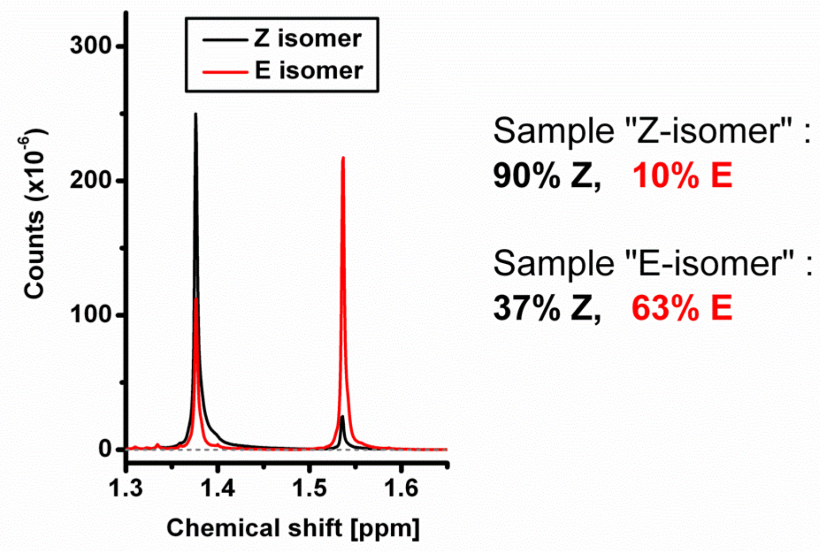

Figure 5.20. NMR spectra of both NAIP sample solutions between 1.2 and 1.7 ppm. It shows Z/E isomer ratios of 90% // 10% and 37% // 63% for the Z and E sample solutions, respectively.

Given the NMR results of figure 5.20, an accurate comparison between transient measurements of forward and backward reactions of NAIP could not be achieved. The transient absorption data of the Z → E isomerization reaction are shown in the Complementary Information section concerning Chapter 4. They show that Z → E isomerization has occurred, by comparing the quasi-static spectrum with the E-Z spectrum (see fig. 5.21). But for E → Z reaction no isomerization signature is obtained, probably because the isomer difference spectrum is too small to be accurately detected, due to the large presence of Z isomers in that sample.

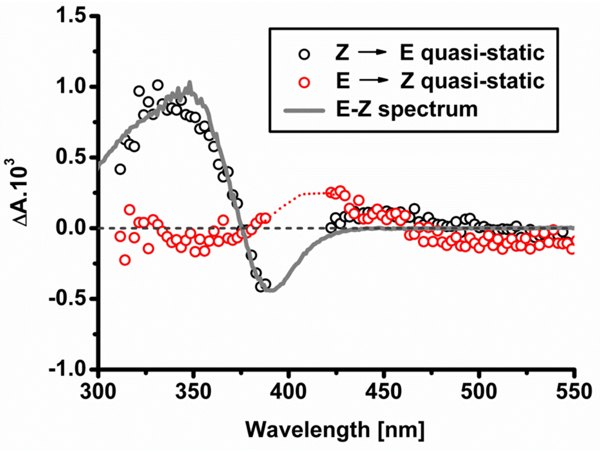

Figure 5.21. Quasi-static spectrum for delays >30ps for NAIP for Z → E (black circles) and E → Z (red circles) reactions. The E-Z difference spectrum is overlaid as a reference. The good agreement between the Z → E quasi-static and the E-Z spectrum shows that isomerization is achieved after 30 ps. On the contrary, the E sample does not show significant signature of isomer conversion.

D. Discussion on isomerization bi-directionality

As far as ground-state relaxation dynamics are concerned, the thermalization in both Z and E isomer ground states of the same molecule appear to be occurring on the same time scale. Moreover, throughout the different experiments on all these photoswitches, the ground-state relaxation dynamics of the different molecules can also be described and analyzed by a common bi-exponential thermalization process (~1-1.5 ps and ~4.6-9ps). This gives strong support to the assignment of these times in terms of inter-molecular processes with the solvent, namely vibrational relaxation and solvation, and heat dissipation to the surrounding.

The ES dynamic time shift and spreading, and the PA first appearance are very similar for both *Z* → *E* and *E* → *Z* reactions for the molecules studied in this Chapter, as no change is observed for MeO-NAIP and as only ~20-30 fs and ~50-fs time shifts are seen when comparing ESA and PA signals of ZW-NAIP . Assuming that the wavelengths probed in both reactions are the same, this experimentally reveals that the wave packet propagation time on the excited-state PES of Z and E isomers differs by less than ~15%, thus suggesting that these surfaces and respective reaction paths are very much alike. This confirms the QM/MM calculations that were made on the representative MeO-NAIP molecule (see fig. 3.5 in Chapter 3), where the PES of the S_1 state of Z and E isomer forms revealed similar curvatures along the reaction coordinate axis. Recent calculations[111] on ZW-NAIP also suggest that the E and Z excited-state PESs allow for the same interpretation.

Using the ZW-NAIP data, we are able to extract the isomer difference spectrum, due to the almost identical spectro-temporal properties of the ground state relaxation signals and to the sufficiently high signal-to-noise ratio, by subtracting the ground state thermalization contributions. This approach reveals the difference spectrum being formed at delays significantly shorter than 1 ps, thus confirming that isomerization is indeed achieved on a sub-picosecond time scale.

Moreover, the quantum yields are equal in both *Z* → *E* and *E* → *Z* reactions of MeO-NAIP, but it is twice as large for *Z* → *E* than for *E* → *Z* in ZW-NAIP (~0.24 and ~0.12, respectively). This difference is not reflected in the isomerization times, which do not change significantly. We thus suspect that, as the reaction branching occurs at the conical intersection, the topology of the CI and the direction of the wave packet propagation is more important than its speed.

The differences observed in the ground state oscillations in the *E* → *Z* reaction of ZW-NAIP (disappearance) and MeO-NAIP (significant amplitude decrease) compared to *Z* → *E* cannot be explained only by the shape of the PES along the torsional reaction coordinate. Two reasons could explain the absence or the significant decrease of ground-state oscillations in the E → Z experiments. First, a larger dephasing can occur already in the excited state, as suggested by fig. 5.9, and progressively induce the loss of coherence, that would be then undetectable in the ground state. The second possibility is that one of the isomer ground state PES has a reduced intra-molecular coupling of the torsional modes, leading to longer coherence times. With the present data and considering the reaction quantum yields, it would mean that the Z isomer ground state PES better sustain torsional coherences than that of the E isomer.

We have a direct experimental support thus backing the conclusion drawn in Chapter 4 of an isomerization occurring before 0.4 ps and most likely in the vicinity of the conical intersection. Further insight will come from wave packet dynamics simulations, based on a more accurate description of potential energy surfaces by including a third mode ("wagging" mode of the pyrroline ring). Our experimental results will be a key contribution to validate these computations. We are also thinking of novel experimental approaches, targeting the ultrafast dynamics close to the CI, as it will be discussed in the conclusions of this work.

Chapter 6

Investigation of solvent properties

In this Chapter, the investigation of isomerization properties in different solvents of the ZW-NAIP photoswitch, taken as a representative member of the coherently-isomerizing NAIP family, is achieved in view of addressing environmental issues and influence on the reaction. A comparison is made between ZW-NAIP dynamics in methanol and two other alcoholic solvents, butanol and decanol, differing from the first one on properties such as viscosity, dielectric constant or thermal conductivity. The aim is to see if such solvent properties influence the $Z \rightarrow E$ photo-reaction of ZW-NAIP, through possible temporal and/or spectral changes. First we want to compare the data and check if the scenario and/or the timing are modified. We are particularly interested to see how the dynamics of the excited state, the isomerization timing and the coherent oscillations, presented in details in Chapter 4, are possibly affected. Changes in the ground-state thermalization and in the isomerization quantum yields are also important questions to be investigated.

This could help to disentangle ZW-NAIP intra-molecular dynamics from the ZW-NAIP/solvent inter-molecular ones, and give further information on the system and its interplay with its environment.

A. Steady-state absorption and experimental conditions

The zwitterionic ZW-NAIP molecules were diluted to optical densities of 0.66, 0.63 and 0.54 mm^{-1} at 400 nm in methanol, butanol and decanol, respectively, and pumped at the same excitation density, in the linear regime of excitation. Data were acquired in the visible range (410-675 nm) for all solutions and for decanol also in the UV range (330-390 nm), in order to compare the results to what has been found for methanol in this region. All data were acquired between -0.5 and 100 ps. The solvent contributions were subtracted as described in Chapter 2. The responses in the different solvents are very similar except for the Raman lines at ~450 nm that are stronger in butanol (~x3) and decanol (~x5) than in methanol. Eventhough ~95% of the response is removed, small residuals from these Raman signals can be still distinguished around 450 nm (see fig. 6.4 and 6.5).

We assume here for ZW-NAIP in butanol and decanol that, like in methanol, the Z isomers are in great majority when the samples are kept at in the dark at room temperature[*]. Figure 6.1 show the normalized absorption spectra of ZW-NAIP in these 3 solvents. Almost no difference is observed, the spectral shapes being extremely similar, but a slight blue-shift (due to solvent polarity differences) of the absorption maximum of ZW-NAIP in decanol (395 nm) is observed, compared to methanol and butanol (397 nm). Here the solvents seem to have a very small effect on the absorptions, and thus a small effect on the $S_0 \rightarrow S_1$ transition.

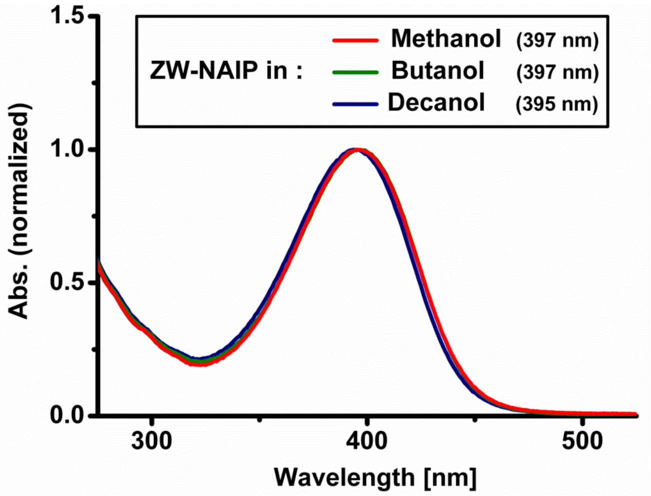

Figure 6.1. Normalized absorption spectra of ZW-NAIP Z-isomer sample solution in methanol (red line), butanol (green line) and decanol (blue line), with $S_0 \rightarrow S_1$ transition absorption maxima at 397, 397 and 395 nm, respectively.

Steady-state absorption spectra were taken before and immediately after the transient absorption experiments and are plotted in figures 6.2.A, C and E for methanol, butanol and decanol, respectively. Figures 6.2.B, D and F display the difference spectra of the static spectra (after experiment – before experiment). All spectra compare well with the reference E-Z spectrum (see figure 6.3 below), showing that the *Z* → *E* reaction observed in all three TA experiments. Noticing that the experimental time was the same in all experiments and taking into account the different absorptions at 400 nm of the 3 samples, we can make a more quantitative analysis of the difference spectra. Indeed, the formation of E isomers during the experiment with methanol and butanol is the same, thus suggesting that the quantum yields are similar (~0.25) in both solvents. The data in decanol show a reduced E isomer formation (-30%), suggesting that the quantum yield of ZW-NAIP of the *Z* → *E* reaction of ZW-NAIP is reduced to ~0.17 in decanol.

---

[*] NMR measurements were not performed on the ZW-NAIP/butanol and ZW-NAIP/decanol samples. See Chapter 5 for ZW-NAIP/CD_3OD NMR results.

The normalized difference spectra of methanol, butanol and decanol are overlaid in figure 6.3. They show very similar shapes above 350 nm where they compare very well with the E-Z reference difference spectrum.

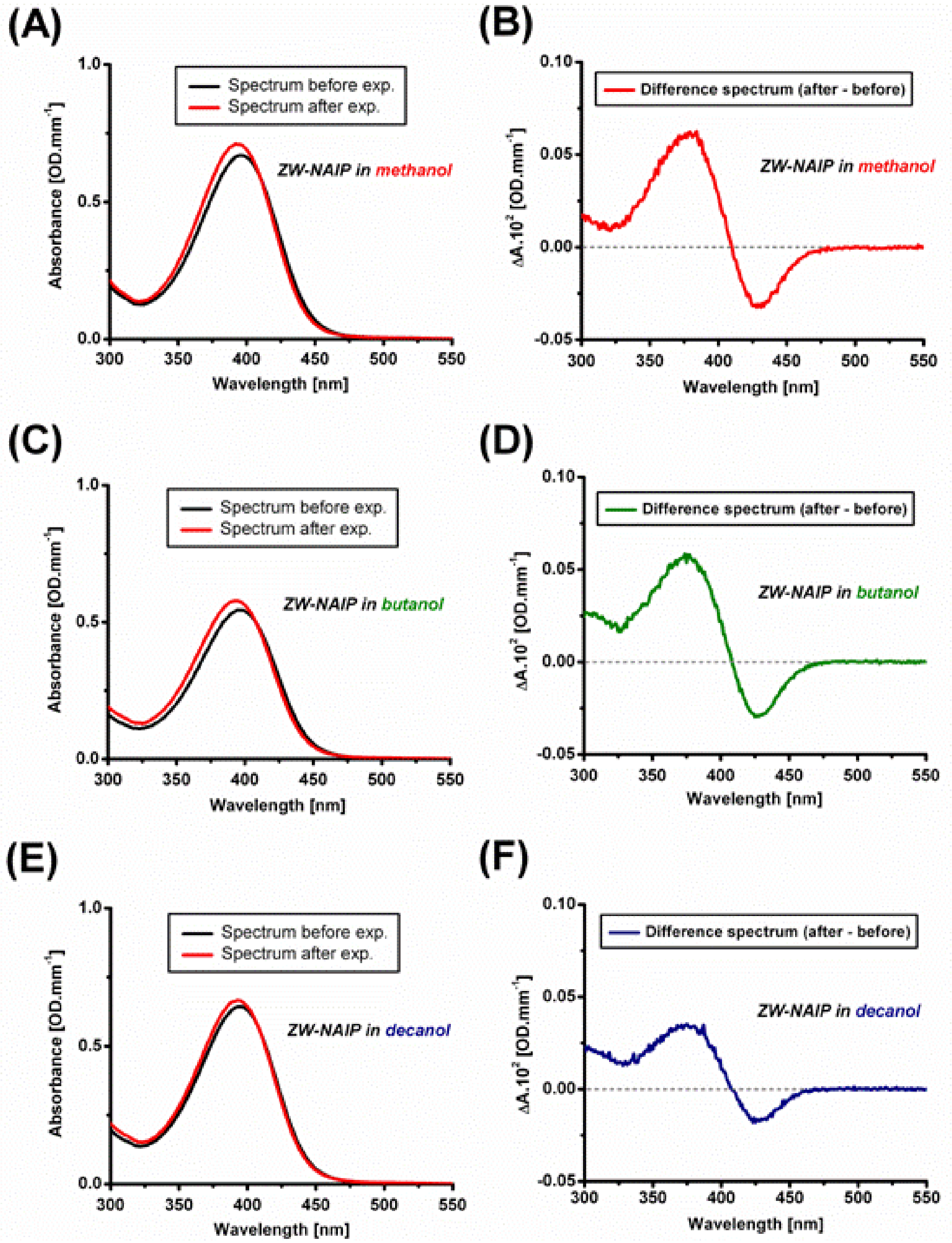

Figure 6.2. **A**. ZW-NAIP in methanol absorption spectra measured before (black line) and after (red line) transient absorption experiments. No sample degradation is observed, except a small difference plotted in B. **B**. Difference spectrum (after – before) of the latter absorption spectra, corresponding to the E-Z difference spectrum (see figure 3 below), therefore showing the Z → E photoconversion. (**C**,**D**) and (**E**,**F**). Same as (A,B) in butanol and decanol, respectively.

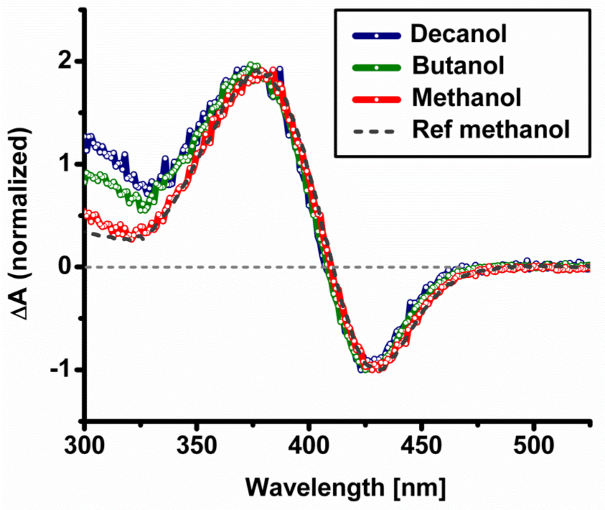

Figure 6.3. Normalized (to the negative value at 425 nm) absorption differences for ZW-NAIP in methanol (red line), butanol (green line) and decanol (blue line). The scaled reference E-Z difference spectrum[111] (grey dashed line) is added for comparison.

B. Isomerization of ZW-NAIP in different solvents followed by TA spectroscopy

1. Control experiment: ZW-NAIP in methanol

A control experiment was made for ZW-NAIP in methanol[*], and as it is the third Z → E experiment on ZW-NAIP in methanol discussed in this work, it is not presented in details. A panel showing the data is available in the Complementary Information. The results are the same as the ones presented before (see Complementary Information), but with a slightly lower signal-to-noise ratio than in Chapter 4.

2. ZW-NAIP photo-reaction in butanol and decanol

Figures 6.4.A and 6.5.B display the wavelength and time-resolved pump-induced absorption changes (ΔA) of ZW-NAIP molecules in butanol and decanol, respectively. The ΔA 2D-maps are presented in the range of 410 – 675 nm as a function of and up to 100-ps time-delay between pump and probe pulses. The full range measured for decanol (330-675 nm) can be found in the Complementary Information section. Figures 6.4.B (6.5.B) and 6.4.C (6.5.C) present selected spectra and kinetic traces from the data set of ZW-NAIP in butanol (decanol).

Both data can be similarly described as it was done in Chapter 4 and 5 for the Z → E reaction of ZW-NAIP in methanol. Again the delayed and impulsive PA arrival in the red part of the spectrum is present, and subsequent oscillations can be also clearly distinguished around 440-450 nm. Two noticeable differences appear though. The ESA (ESA2 band) amplitude appears stronger in decanol than in butanol. Also the quasi-static difference spectrum appear to be weaker in decanol, in agreement with what has been observed above, with the lower quantum yield in decanol suggested by the lower total E isomer formation during the experimental time. This point will be further developed in § 6.C.1.

---

[*] This experiment was performed again as a reference comparison data set, and also because the ZW-NAIP sample used for these experiments was recycled from a previous one (Chapter 4). As the results compares well (see Complementary Information) with the previous experiments, we are confident that the sample is not degraded.

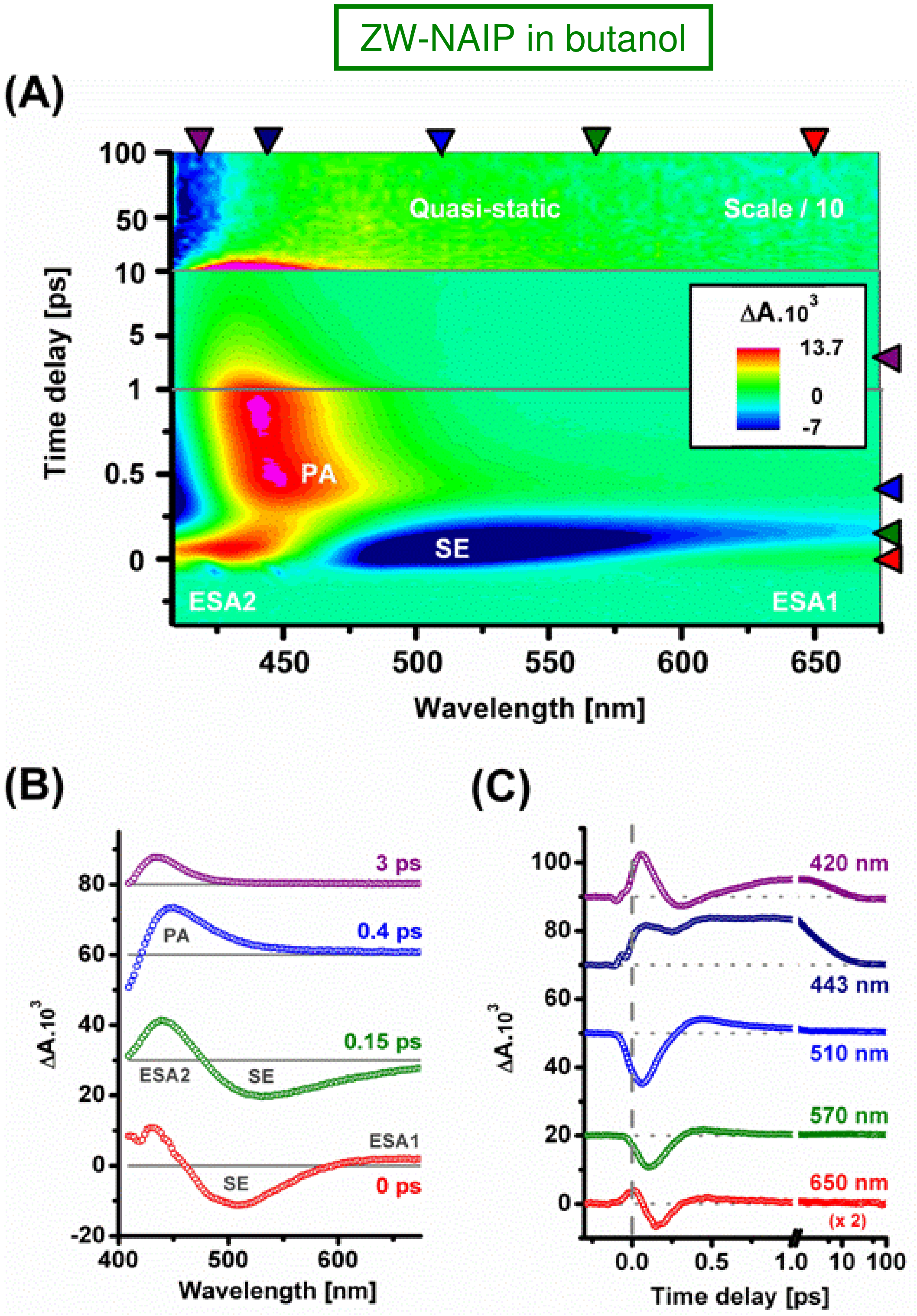

Figure 6.4. **A.** 2D-map of the Vis transient absorption change ΔA of ZW-NAIP in butanol. **B.** Spectra (open circles) at delays indicated by the cursors on the right of figure 6.4.A. **C**. Kinetic traces at wavelengths indicated by the cursors on the top of figure 6.4.A.

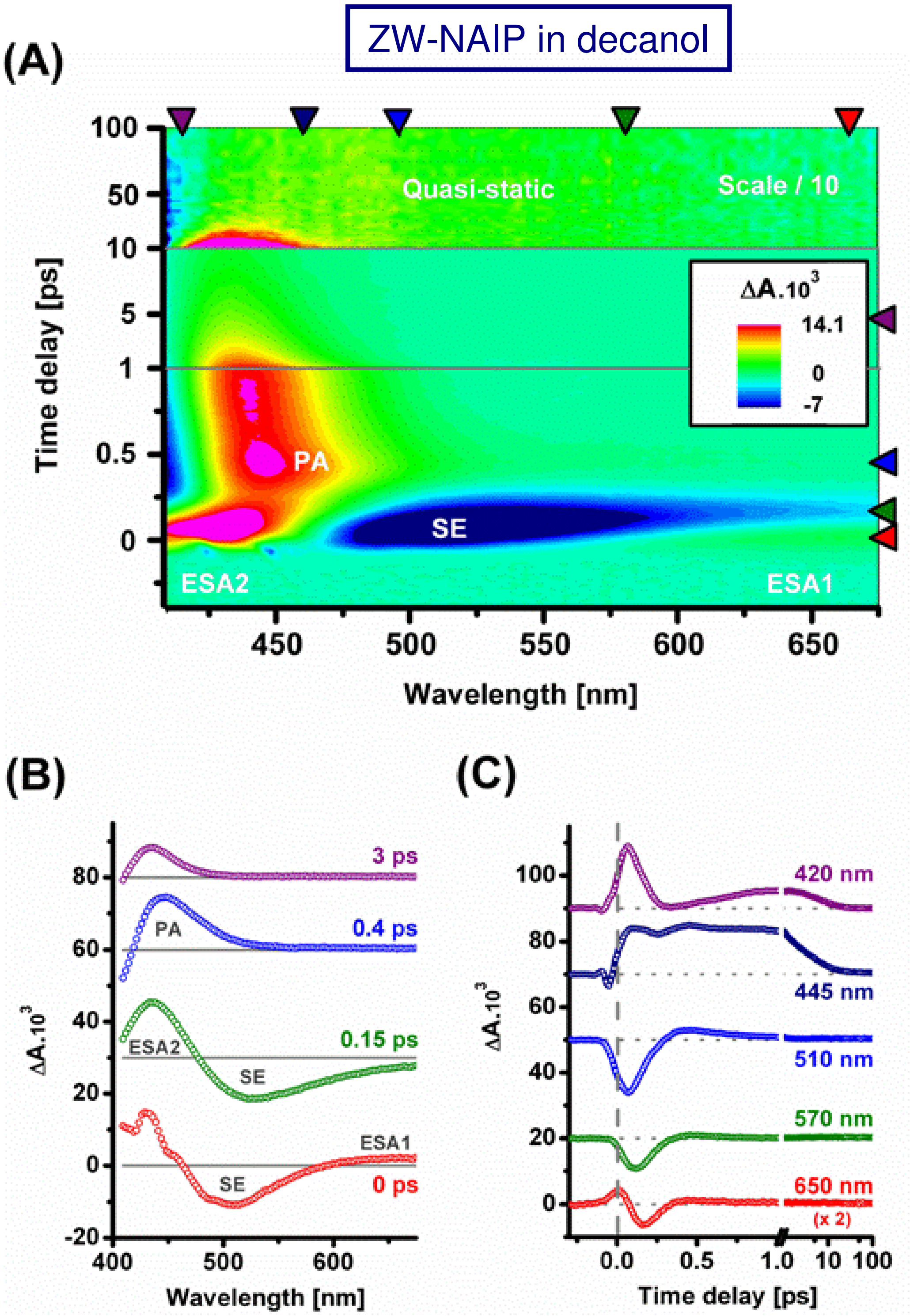

Figure 6.5. Same as figure 6.4 for ZW-NAIP in decanol.

C. Comparison and interpretation

1. Ground-state dynamics and quasi-static spectra

SVD and global analysis after 1.2 ps were performed on the 3 data sets using the same procedure as the one already detailed for ZW-NAIP in Chapter 4 (§ 4.A.4.b). The results (DADS) are shown in figures 6.6.A, B and C for methanol, butanol and decanol, respectively. The 3 data sets can be analyzed using 2 decay time constants (a fast and slower one) characterizing the thermalization, and an infinite time constant to account for the quasi-static difference spectrum observed at long time delays. A gradual increase is observed, the fastest time constants being 1.3, 1.6 and 1.95 ± 0.1 ps and the slower ones 4.8, 7.1 and 7.6 ± 0.2 ps for methanol, decanol and butanol, respectively. Figures 6.6.D, E and F compares for the different solvents their DADS (normalized) associated to each fastest, slower and infinite time constant.

The spectral shapes of the DADS reveal that, eventhough a small gradual blue-shift may be observed from methanol to decanol, the influence of the solvent properties are negligible on the spectral characteristics of the ground thermalization process. The only noticeable difference is on the time scales involved, where a ~30% increase from methanol to decanol of the ground state vibrational relaxation/solvation and heat dissipation to the solvent is reported. This can be explained by different dielectric solvations and thermal conductivity properties of the solvents (see discussion of § 6.C.3 below).

Concerning the presence of the positive band for $\lambda>425$ nm in the quasi-static spectra, we refer to Chapter 4 and the discussion about the use of freshly-synthesized samples (§ 4.A.2). Anyway the presence of this band does not allow a precise determination and comparison of quantum yields using data in the visible range. But an approximate value of the quantum yield can be determined, as described in Chapter 4 (§ 4.A.4.b), from the data at 375 nm that were measured for ZW-NAIP in decanol. We also find a reduced reaction quantum yield (~0.12[*]), slightly smaller, though, that what is found with the static spectra difference analysis.

---

[*] Leftover Z bleach at long delays is $-1.2.10^{-3}$ and bleach at time zero is -1.10^{-2}.

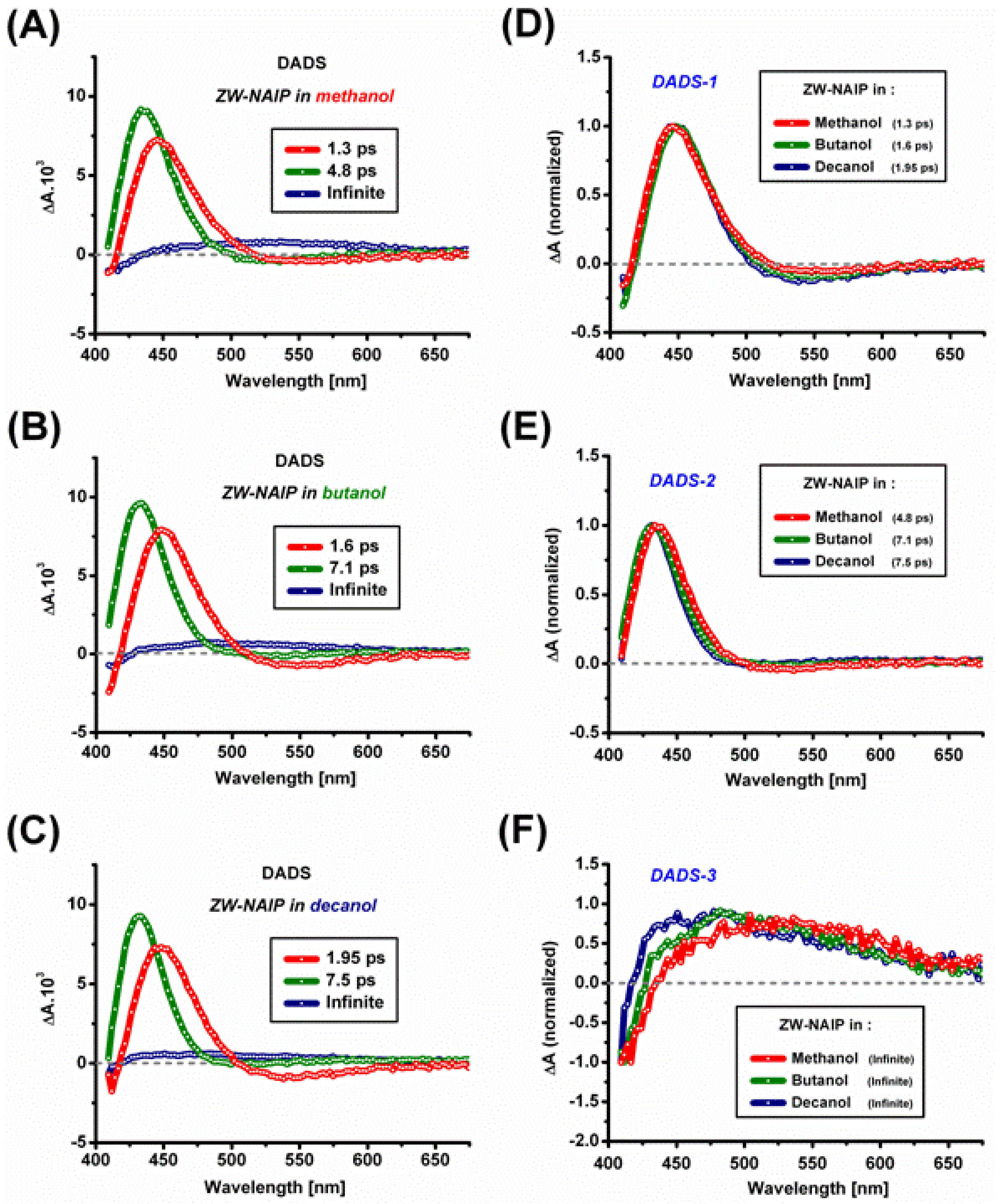

Figure 6.6. The DADS of ZW-NAIP in methanol, butanol and decanol in the visible range are presented in figures **A**, **B** and **C**, respectively. They were obtained by the same procedure as the one described in Chapter 4. All data can be described by two decays, a fast (1.3, 1.6 and 1.9 ps from methanol to decanol) and a slower one (4.8, 7.1 and 7.5 ps from methanol to decanol), reflecting ground state thermalization processes, and an infinite time constant, corresponding to the quasi-static spectrum observed at long-delays. In figures **B**, **D** and **F** each solvent DADSs are normalized and compared with the DADSs of the same time scale for the 3 solvents. They are almost perfectly overlapping, showing that, eventhough the time scales are slightly different, the thermalization processes are not significantly affected.

2. Comparison of coherent properties

a. Excited-state absorption shift

Figure 6.7 compares the ESA signals (previously referred to as ESA3) of ZW-NAIP in methanol and decanol. Both transients taken at 335 nm compare very well. Indeed, they both show a rise clearly larger than the instrument response function (80 fs), a delayed maximum pointing at ~220 fs, and similar decays.

This indicates that the ESA signal, and thus the excited-state potential energy surface, is not significantly affected by the solvent properties differences. We can suggest at this point that inter-molecular effects are thus small compared to intra-molecular ones concerning the excited-state PES and the time scale involved. No barrier is created or amplified by the solvent properties on the excited-state PES, which is in agreement with the calculated barrierless excited-state path that has been presented in Chapter 3.

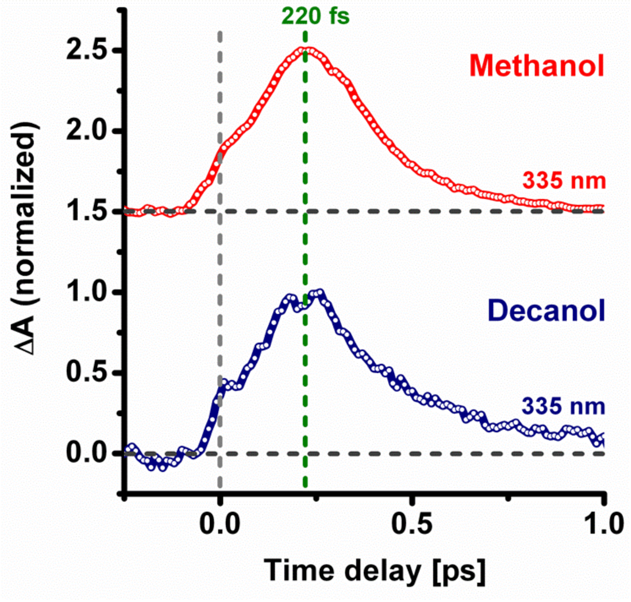

Figure 6.7. Normalized transients of ZW-NAIP molecules in methanol (red, data from Chapter 4) and decanol (blue) at 335 nm, where the ESA3 band time-shift is clearly seen. Both traces compares well, with an ESA3 maximum pointing at ~220 fs. 3 transients at 333, 335 and 337 nm were averaged to produce the kinetic trace presented for decanol.

b. Photoproduct arrival time

Figure 6.8.A and B present the kinetic traces of ZW-NAIP in methanol, butanol and decanol at 650 and 530 nm, respectively. These two figures highlight the similarity of the dynamics in the 3 solvents, and of the ground state delayed arrival time (referred to as the PA), which is found to be extremely similar at both wavelengths (0.38-0.4 ps at 650 nm and 0.44 ps at 530 nm).

Like what has been discussed above, no significant change is observed on these signals. A small decrease of the PA amplitude in decanol is observed though in both figures. As the time scales are not affected, no energy barrier creation or amplification on the PES that could slow down the reaction is observed. Nevertheless, the decrease in the PA amplitude of the measurement in decanol may correlate with the lower quantum yield of the reaction, most probably controlled in the region of the conical intersection which would be affected by the solvent properties.

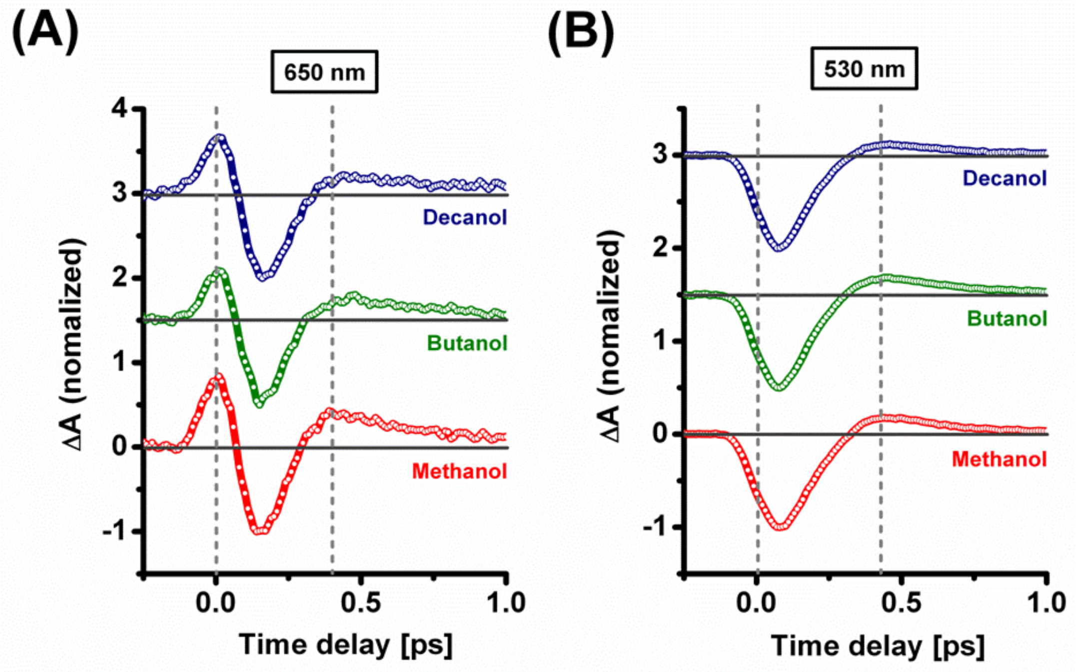

Figure 6.8. **A**. Normalized transients at 650 nm for ZW-NAIP in methanol (red), butanol (green) and decanol (blue), showing the delayed ground state signal (PA arrival times). The kinetic traces are very similar and the PA peaks are at ~0.38-0.4 ps, in very good agreement with the data from Chapter 4. **B**. Normalized transients at 530 nm for methanol (red), butanol (green) and decanol (blue). They show a common peaking time of the PA of ~ 0.44 ps at this wavelength, in agreement with Chapter 4 (0.43 ps).

c. Oscillations

Figure 6.9A presents the modulation observed in the signals and that were extracted at 445 nm for ZW-NAIP in methanol, butanol and decanol, using the fitting procedure described in detail for ZW-NAIP in Chapter 4 (see § 4.A.3.d). The fits yield periods of 590, 570 and 580 ± 10 fs (56, 58 and 57 cm^{-1}, respectively) and damping time constants of 330, 310 and 320 ± 20 fs for ZW-NAIP in methanol, butanol and decanol, respectively. These values are in excellent agreement with the ones found in Chapter 4 (period of 560 fs and damping time of 320 fs).

In figure 6.9.B the normalized extracted oscillations are compared to the one extracted at the same wavelength in Chapter 4, highlighting the invariance of the oscillations with respect to the solvents.

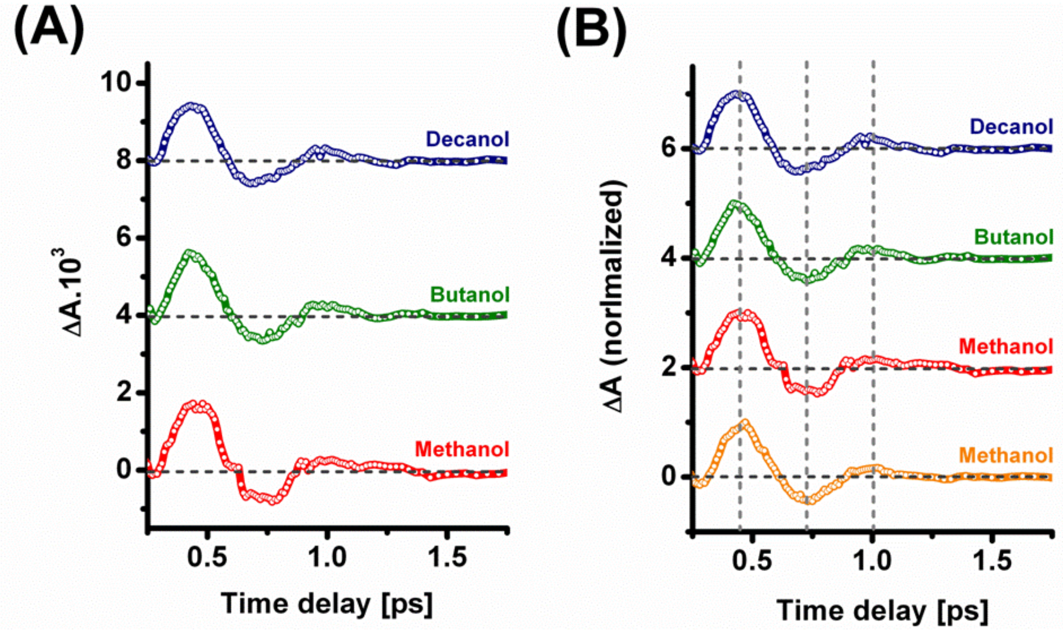

Figure 6.9. **A**. Extracted oscillations from traces at 445 nm (methanol, red line, and butanol, green line) and 443 nm (decanol, blue line). The fitted kinetic traces were averaged over 3 transients (443, 445 and 447 nm for methanol and butanol, and 440, 443 and 445 for decanol) to increase the signal-to-noise ratio. The procedure has been described in details in Chapter 4. **B**. The same oscillations have been normalized for methanol (red), butanol (green) and decanol (blue). They are compared to the extracted oscillations of ZW-NAIP in methanol from Chapter 4 (orange). In both figures the traces are vertically shifted for clarity.

3. Interpretation and conclusions

The results presented in this Chapter all point towards absent (ES dynamics and coherent properties) or weak (GS thermalization dynamics) solvent effect on the photo-reaction of ZW-NAIP.

First, the fact that the isomerization of the ZW-NAIP switch, characterized by a full rotation of the pyrroline ring, is not solvent-dependent is surprising. As a matter of fact, similarly weak viscosity dependencies observed for larger molecules like retinal or the GFP chromophore had been attributed to approximately volume-conserving isomerization mechanisms. These motions involve however the simultaneous rotation around two bonds (e.g. bicycle pedal or "hula twist"), and can thus not be invoked for the NAIP kind of switches wherein rotation is limited to the central double bond.

But in the case of the isomerization of ZW-NAIP in decanol, which has a viscosity ~20 times higher than methanol, the isomerization speed remains 0.4 ps. This strongly suggests that the organization of the solvent is such that weak inter-molecular interactions are occurring. This behaviour differs from other isomerizing systems where a strong dependence on solvent viscosity was reported (see e.g. reference[127]). Another possibility is that the excited-state energy barrier which may be created is too small compared to the kinetic energy (excess energy) brought to the molecule.

Moreover, the oscillations are not significantly affected. The amplitudes, frequencies (~60 cm^{-1}) and damping times (~300 fs) of the oscillations remain the same in each solvent, very much like what Zgrablic et al.[68] observed for retinal excited-state coherences in different solvents. Thus, the intra-molecular coupling of the torsion with other intra-molecular modes seems to be the only coherence-damping process involved, as suggested in the previous Chapters. No inter-molecular parameter is affecting these coherent process governed only by intra-molecular properties.

The only strong effect of the solvent in found in the case of ZW-NAIP in decanol. Indeed, and eventhough the isomerization speed is the same as in the other solvents (0.4 ps), the quantum yield of the isomerization reaction is significantly decreased (30 to 50 %). This experimental observation can be related to the theoretical work of reference[128] in which it was shown that solvent properties can influence the branching of a reaction by affecting the conical intersection topology.

Finally, the trend of a ground-state relaxation slow down, as one goes from methanol to decanol, is qualitatively in agreement with solvation[120] and reduced heat dissipation to the surrounding solvent.

The results presented in this Chapter show no strong effects of the solvent properties on the isomerization ultrafast dynamics and coherent properties, strongly supporting the idea that they are controlled by intra-molecular properties. Only the quantum yield was modified in the case of decanol, suggesting that the solvent environment can affect the region of the conical intersection where the reaction branching is controlled. Further experiments regarding the influence of solvent properties in a more systematic investigation could include water-glycerol mixtures so as to reach significantly higher viscosity values and the effect of hydrogen bonding, when protic and aprotic solvents are compared.

Conclusions

As introduced in Chapter 1, photo-isomerization is a key process triggering many biological functions, with fundamental questions to be further investigated, such as the parameters governing the reaction speed, the efficiency or the coherent properties sometimes observed.

In this context, a detailed study of the photo-reaction of a new synthetic photoswitch family has been achieved. For that purpose, and as it involved measuring spectro-temporal dynamics on ultra-short time scales, a femtosecond transient absorption (pump/probe) spectroscopy setup has been built. It was thus possible to measure, over a broadband spectral range (290-975 nm) and a large time window (up to 6 ns), pump-induced absorption changes with a time resolution of 80 fs and a high signal-to-noise ratio (Chapter 2).

Five differently-substituted members of this family (NAIP, MeO-NAIP, Prot-MeO-NAIP, ZW-NAIP and MeO-NABFP), showing great theoretical expectations for ultrafast isomerization and convenient steady-state properties, have been presented in Chapter 3.

They were all measured by transient absorption spectroscopy and the results were presented in Chapter 4. Two isomerization scenarios were observed. The first one concerns the MeO-NABFP molecule, which shows an ultrafast, mostly rate-equation-like, isomerization reaction (τ_{iso} = 600 fs). The other four molecules (NAIP, MeO-NAIP, Prot-MeO-NAIP and ZW-NAIP) show faster, sub-500-fs isomerization times, with indications of vibrational coherences. First, the wave packet-like evolution of the population can be followed through the spectro-temporal shift of the excited-state absorption, reflecting motion from the Franck-Condon region towards the conical intersection. This has been measured to occur on a 160 to 230 fs time scale, depending on the sample. A "spectroscopically-dark" time window, most probably related to the CI, has been identified after this excited-state evolution and was found to last 100 to 150 fs. The second specific signal is the delayed (250 to 380 fs) and quasi-impulsive repopulation of the ground state observed with a ground-state induced absorption signal, best observed in the red part of the spectrum and after the dark time window. Finally, this impulsive signal leads to quickly-damped ($\tau_{damping}$ = 300 fs), low-frequency (60-110 cm^{-1}) oscillations, reflecting the wave packet motion and coherence loss in the ground state potentials. For the quantitative analysis of the dynamics, a hybrid fitting model has been suggested, able to describe the data in a quantitative way and to account for the duality of the dynamics, showing both coherent and stochastic behaviour. All these experimental observations and analysis lead to a scenario which can be described by involving two modes, a stretching one acting in the first ~50 fs, as suggested by experimental time resolution-limited Raman activity in the 1600 cm^{-1} range, followed by torsional motion, which can be almost completely traced during the isomerization reaction. It gives precisely-clocked isomerization timings of the molecules with values from 260 to 380 fs, occurring after the passage through the conical intersection and its associated dark time window. These results suggest a barrierless reaction path from the excited to the photoproduct state and isomerizations at the maximum speed limit, experimentally corroborating what has been found by theoretical modelling and population dynamics simulations of these compounds. Moreover, comparison of the dynamics with the reference isomerization of retinal in rhodopsin highlights the targeted biomimetic aspect of the NAIP family, reproducing spectro-temporal features and, thus, most of the potential energy surface topology properties of retinal in rhodopsin. Finally, substitution effects on the structure could be identified. The ones affecting the rotating pyrroline moiety mainly influence the intrinsic value of the torsional mode, as seen with the different oscillations frequencies reported. More important are the substitutions on the other part of the molecule, the indanone moiety. Adding an oxygen atom, placed like in MeO-NABFP in between the pyrroline and the phenyl rings, leads to a less favorable excited-state potential energy surface, and to a slower, and non-coherent isomerization process.

The study of the bi-directionality (Z → E and E → Z) of the reaction of two molecules (ZW-NAIP, MeO-NAIP) has been presented in Chapter 5. The first and important conclusion is that isomerization is occurring on the same time scale in both directions, indicating excited-state potential energy surfaces and reaction paths that are probably very similar for both isomers, as predicted by theoretical calculations. Moreover, in the case of the ZW-NAIP, thanks to a subtraction procedure of both reaction directions data, the signature of isomer formation is found on a sub-picosecond time scale, giving strong support to the isomerization reaction scenario proposed in Chapter 4.

The environment influence has been investigated in Chapter 6, where measurements on one photoswitch (ZW-NAIP) in three different solvents (methanol, butanol and decanol), showing different properties, were performed. The measurements reveal very similar dynamics for the three solvents. Neither viscosity nor dielectric constant changes influence the isomerization speed. Only the thermalization through energy dissipation to the solvent is weakly affected, and suggested to be related to /governed by thermal conductivity solvent parameters. Likewise, the observed ground-state relaxation slow down is also consistent with a slower dielectric relaxation in less polar solvents. The quantum yield of the reaction in decanol is found to be as fast, but smaller though, showing that the solvent may influence the branching of the reaction in that case. This investigation shows that the isomerization temporal dynamics of the photoswitches are mainly governed by intra-molecular parameters, and that inter-molecular ones may have a role in influencing the branching of the reaction and thus the quantum yield, as suggested by in the theoretical work of reference[128].

This photoswitch family based on the NAIP structure appears to be a very good model system to study the precise clocking of coherent isomerization reaction dynamics, and thus molecular structural changes, combining theoretical and experimental investigations. As they are synthetically flexible, substitutions governing the isomerization speed or torsional frequency could be experimentally identified. Nevertheless, the maximum reaction quantum yield is 0.25-0.3, significantly lower than that of rhodopsin (0.67). Intra-molecular parameters, controlling isomerization speed, seem to be "locked" into the NAIP structure and almost insensitive to the environment, which could be a good point towards future applications of these compounds. But other environmental parameters seem to be able to influence the reaction quantum yield, and are still lacking in the NAIP structure. The introduction of a chiral center may improve the efficiency of the molecule, as suggested in reference[2]. If speed is most probably a pre-requisite for high quantum efficiency, it does not appear though to be sufficient.

Deeper investigations come into our minds to continue this work and to further understand the photo-physics of the NAIP family. Based on the same transient absorption spectroscopy configuration, coherent control experiments, using pulse-shaping techniques on the pump pulse, can be an interesting direction, aiming at controlling the coherent properties[129] and/or improving the quantum yield of the reaction. When pure enantiomeric solutions of the chiral forms of the photoswitches will be available, time-resolved circular dichroism (CD) measurements may also be performed[*], to investigate a unidirectional direction of rotation. Moreover, the collaboration with R. Huber and A. Leitenstorfer (Konstanz University) may lead to a 3-pulse experiment, consisting of an excitation pulse at 400 nm, a UV-Vis continuum probe and a strong IR pulse, non-resonant with a transition, that would be sent during the "spectroscopically-dark" time windows (e.g. between 230 and 380 fs for ZW-NAIP) identified in this work. It is the time range during which the branching of the reaction, i.e the quantum yield, is determined in the potential energy surface region referred to as the conical intersection. The short, strong and non-resonant IR field could, as it has been recently shown[125], locally modify the PES during its duration and influence the outcome of the reaction. Finally, a collaboration with F. Lépine (Lyon) has already started to study the photoelectron spectroscopy of the photoswitches in the gas phase.

The tight collaboration between theory (Pisa), synthesis (Ferrara, Perrugia) and experimental spectroscopy (Strasbourg, Lausanne, Zurich) has been succesful and opens new research directions and applications. Indeed, chemists are currently incorporating NAIP switches into peptides, trying to create a molecule which auto-assembles, and they are also synthesizing a chiral version of the structure. Theoreticians are currently calculating the reaction paths of the remaining switches (NAIP and MeO-NABFP), trying to develop a simplified model of the NAIP structure in order to save computational time, and they are thinking about incorporating a third "wagging" mode for a more accurate description of the PES. Moreover, the results brought by this work and other spectroscopy techniques (Fluorescence up-conversion and mid-IR spectroscopy) are strongly supporting the idea that this molecules can become a reference model for both theoretical and experimental investigation

---

[*] A femtosecond broadband circular dichroism setup has been recently built in the Institute by L. Mangot in the team of H. Dorkenoo and A. Fort.

of isomerization reactions. It could give new insights in the comprehension of the parameters governing them and about coherence effects. Furthermore, applications are also currently under development. Not only these switches can be used as “steric” photoswitches, involving the molecular torsion for light-controlled modulation of peptide functions, but a molecule such as ZW-NAIP, featuring a permanent dipole moment of ~15D on the rotating part, can also be used as a dipole moment photoswitch, thus able to control and modulate functions by polar electrostatic interactions, or even to be used as a local electrostatic photosensor.

Complementary information

Chapter 4

SVD and global analysis (see fig. CI.1.A and B) of the two prominent singular transients were performed on the 300-330 nm range of ZW-NAIP data (see § 4.A.4.b), where the ESA is observed almost pure, considering time delays larger than 0.35 ps. Excited-state time constants in line with fluorescence up-conversion measurements are found (0.15ps (90%) and 0.85 ps (10%)). A longer 8.8-ps and weak amplitude decay accounts for ground state dynamics.

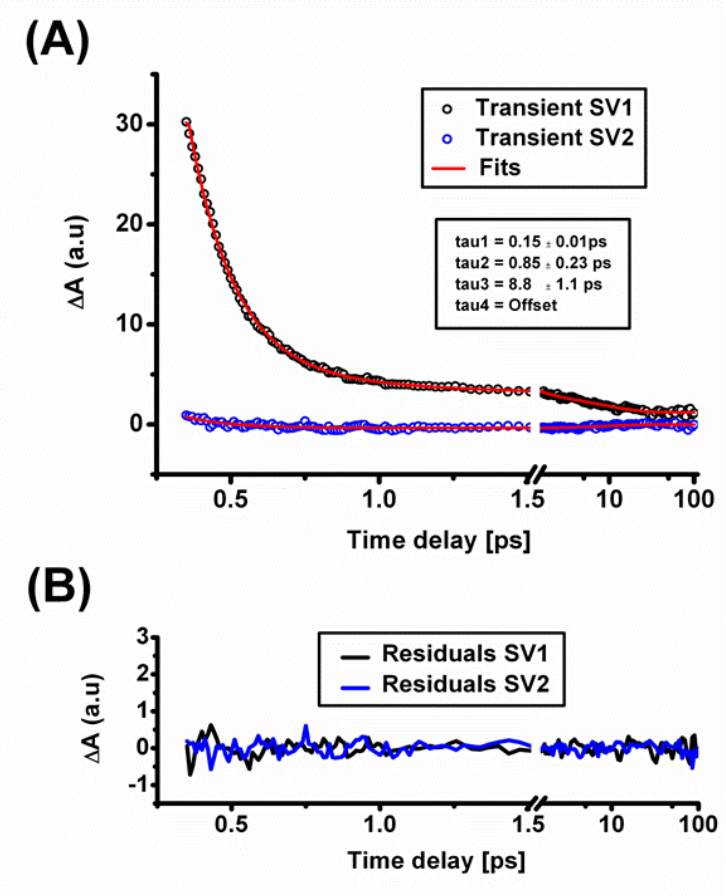

Figure CI.1. **A**. Fits of the two singular transients obtained by SVD. The decay times are indicated on the figure. **B**. Residuals from both fits.

The Prot-MeO-NAIP steady-state spectra measured before and after experiments are presented in figure CI.2.A, and the difference is plotted in figure CI.2.B, showing that Z → E isomer conversion has occurred during the experiment presented in § 4.B.

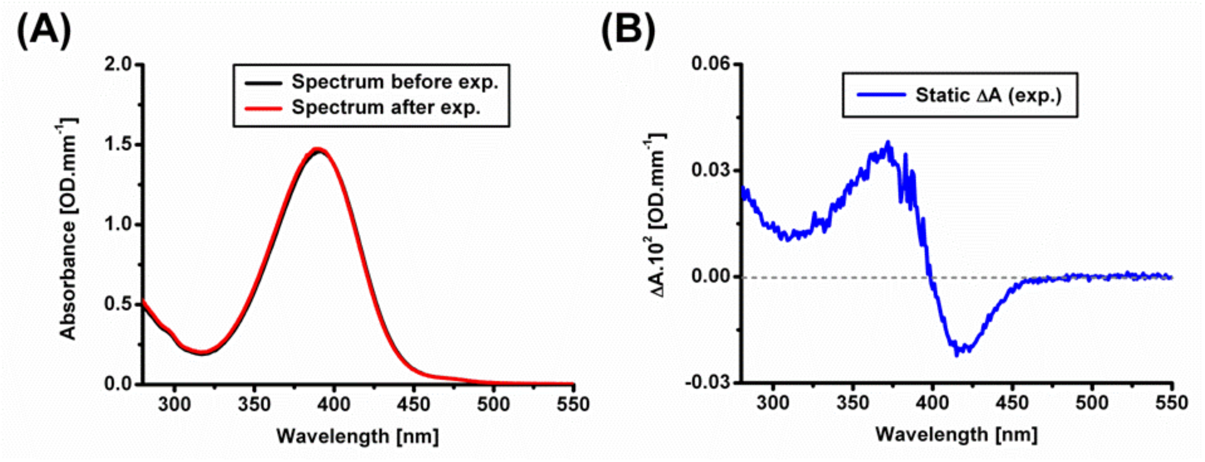

Figure CI.2. **A**. Steady-state spectra measured before and immediately after the pump/probe experiments. The difference is plotted in **B**, showing Z → E isomer conversion during the experiment.

Figures CI.3, 4 and 5 display the wavelength and time-resolved absorption changes (ΔA) of MeO-NAIP, Prot-MeO-NAIP and NAIP molecules in methanol, respectively (see § 4.B). They are presented in the range of 300 to 700 nm (300-650 nm for NAIP) and up to time delays of 100 ps[*]. The quasi-static spectra of figgures CI.3A, 4.A and 5.A show that isomerization has occurred.

Figures CI.3B (CI.4.B, CI.5.B) and CI.3.C (CI.4.C, CI.4.C) present selected spectra and kinetic traces from the MeO-NAIP (Prot-MeO-NAIP, NAIP, respectively) data set. As it has been highlighted for ZW-NAIP, dynamic spectral shifts and coherent oscillations pointing to a wave packet-like population in both excited and ground states are observed.

---

[*] For MeO-NAIP, time delays for wavelengths above 460 nm were acquired only up to 15 ps.

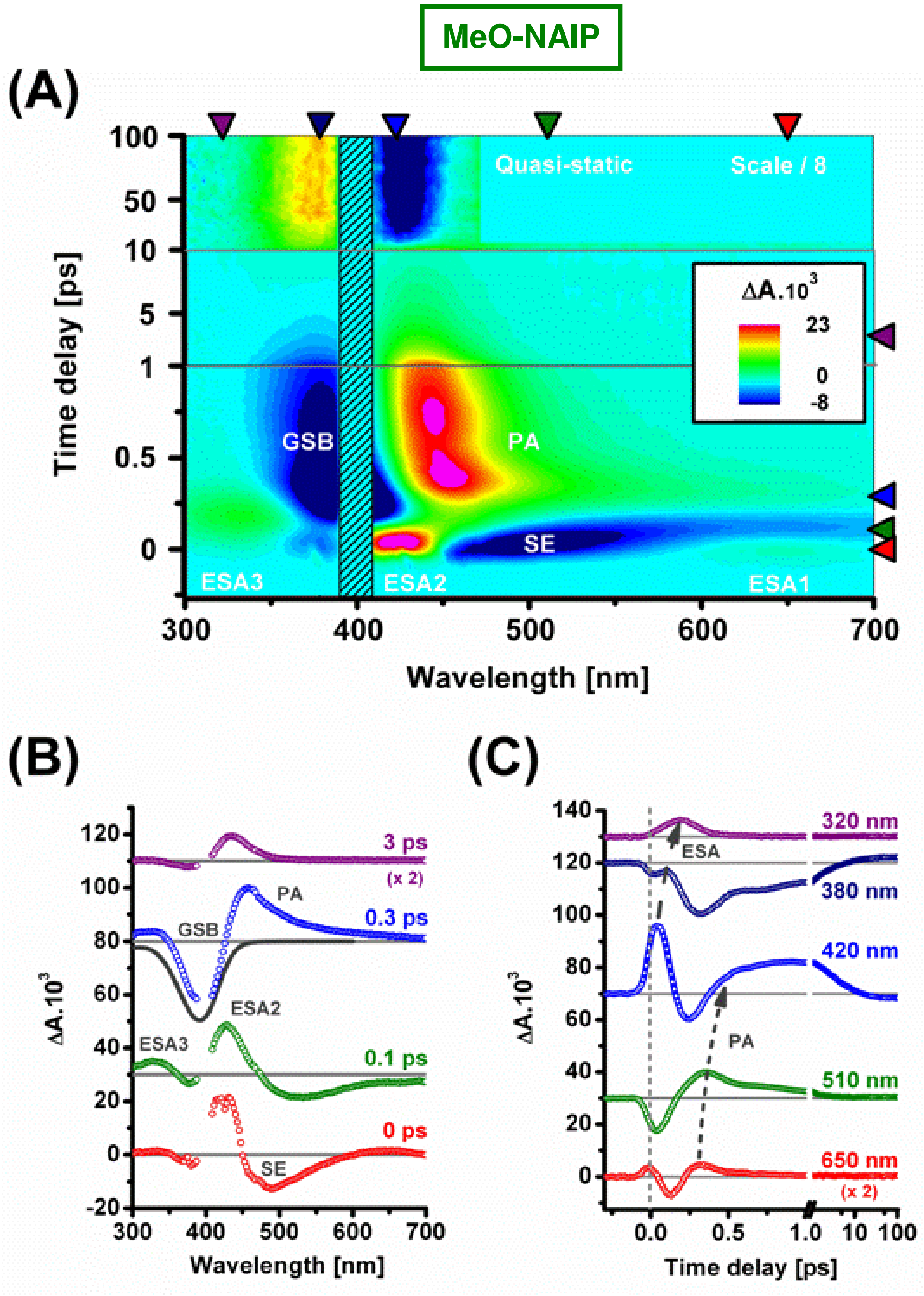

Figure CI.3. **A.** 2D-map of the UV–Vis transient absorption change ΔA of MeO-NAIP in methanol as a function of wavelength and time delay. The time scale is separated into 3 linear sections, from -0.25 to 1 ps, 1 to 10 ps and 10 to 100 ps. Because of enhanced noise due to pump scattering around 400 nm, the crossed-out portion is disregarded. **B**. Spectra (open circles) at delays indicated by the cursors on the right of figure CI.3.A. Along with the 0.3-ps spectrum, the inverted scaled ground state absorbance is shown (solid line). **C.** Selected kinetic traces at wavelength indicated by the cursors on the top of figure CI.3.A. Curved arrows highlight the spectral shift of excited-state absorption (ESA) and photoproduct absorption (PA).

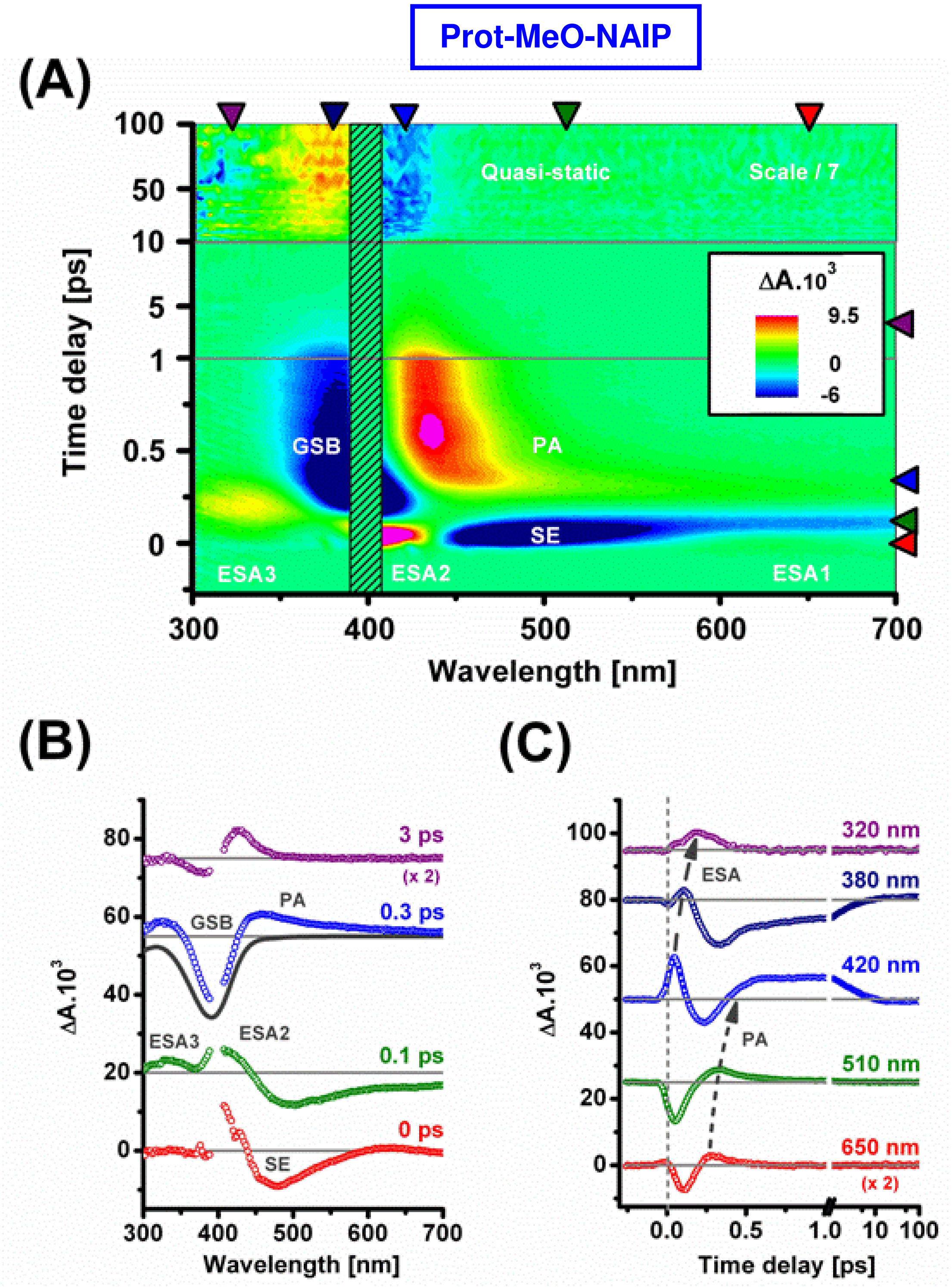

Figure CI.4. Same as fig. CI.3 for Prot-MeO-NAIP in methanol.

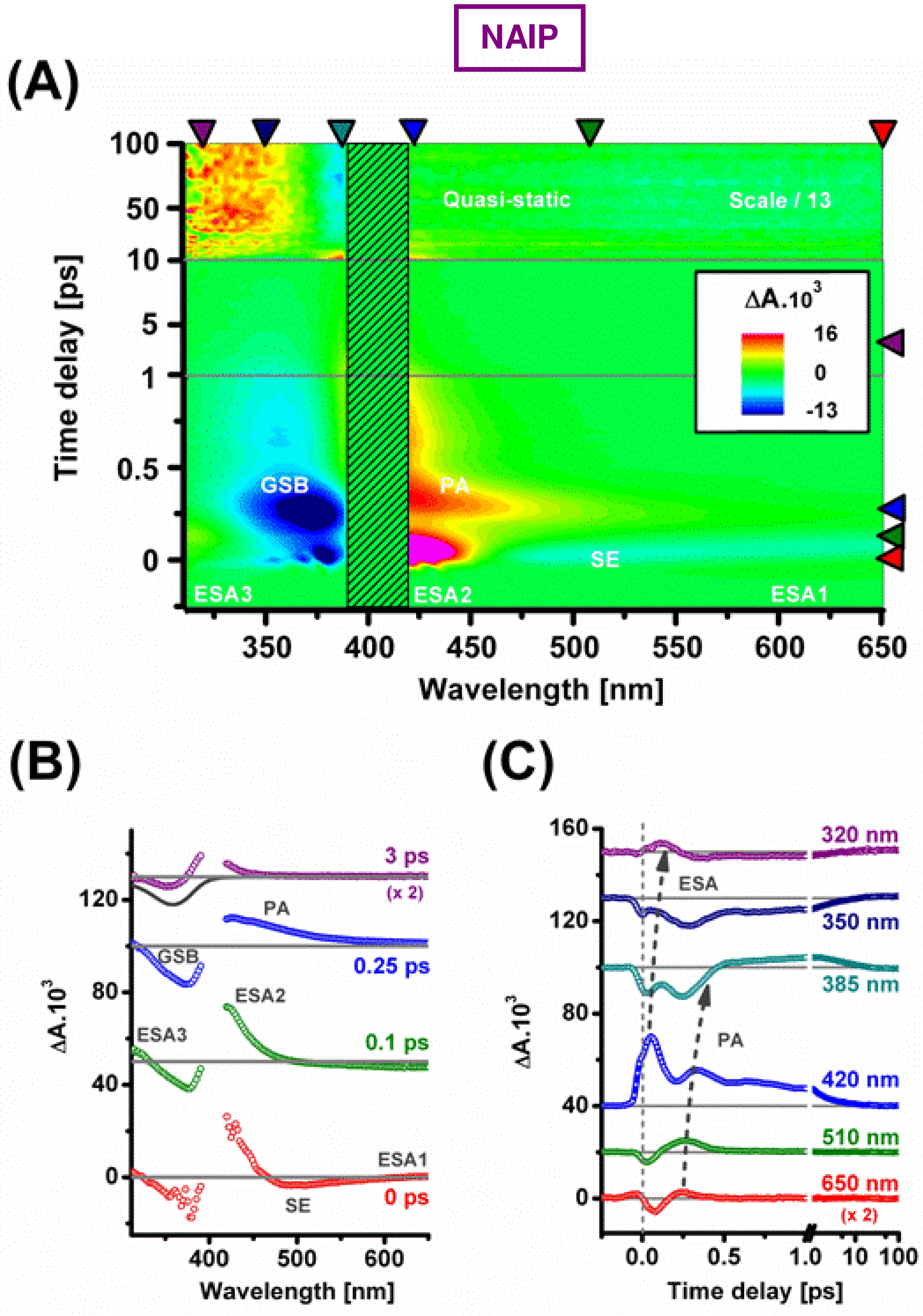

Figure CI.5. Same as fig. CI.3 for NAIP in methanol.

The simultaneous fits of blue- and red-shifted wavelengths for MeO-NAIP, Prot-MeO-NAIP and NAIP are plotted in figures CI.6A, 7A and 8A, respectively (see § 4.B). The residuals are indicated in figures CI.6B, 7B and 8B.

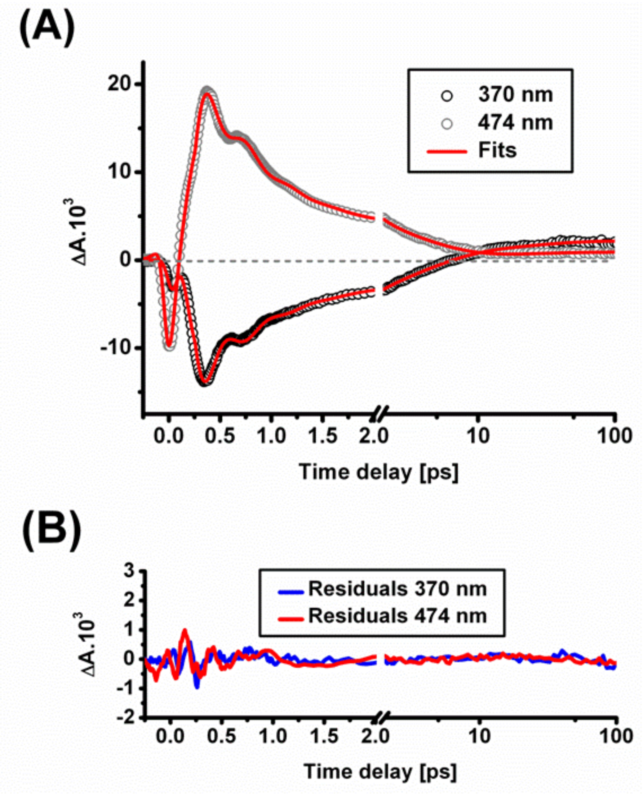

Figure CI.6. **A**. Transients at 370 and 474 nm together with their fits using the fitting function described in Chapter 4. **B**. Residuals of the fits.

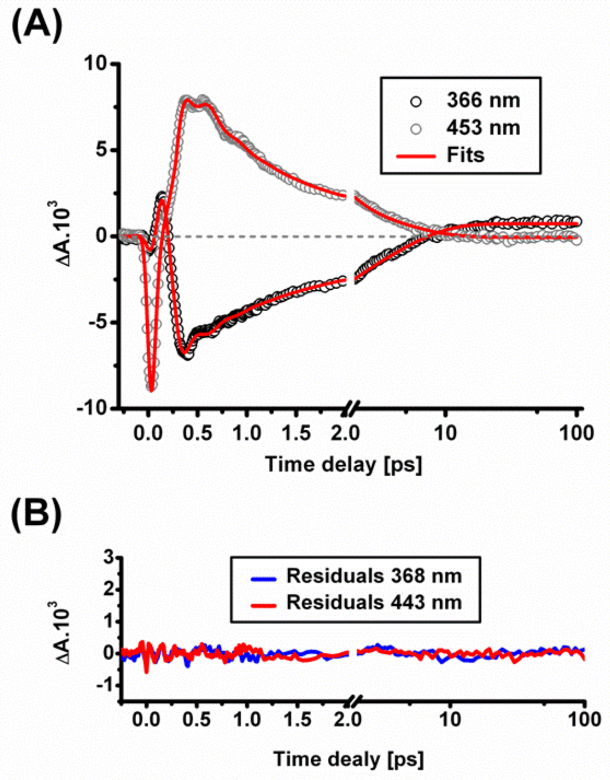

Figure CI.7. Same as CI.6 for Prot-MeO-NAIP.

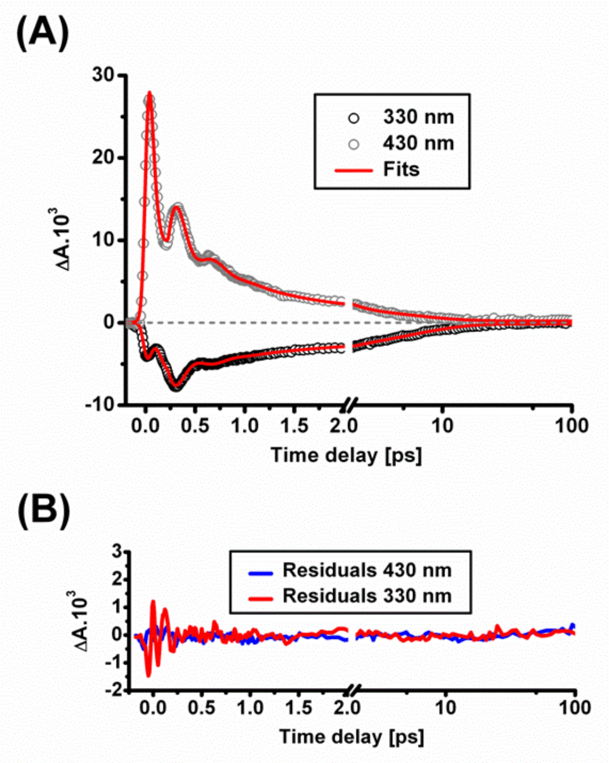

Figure CI.8. Same as CI.6 for NAIP.

The fits and residuals of the singular transients obtained by SVD for MeO-NAIP, Prot-MeO-NAIP and NAIP are plotted in figures, CI.9, 10 and 11, respectively (see § 4.B for discussion). The DADS obtained by the procedure described in Chapter 2 are plotted in figure CI.12.A, B and C, respectively.

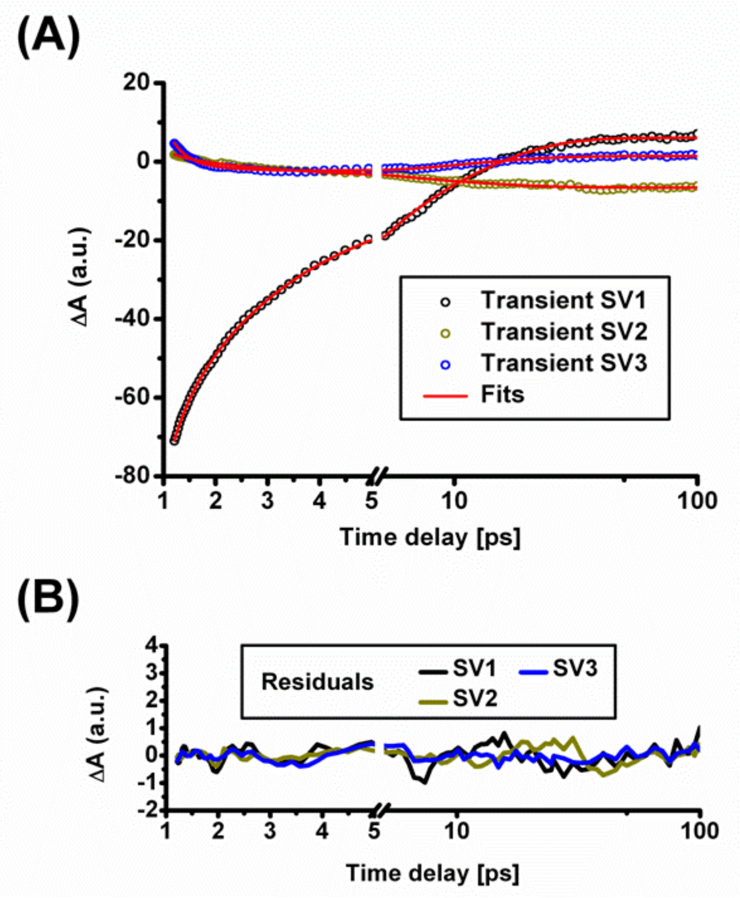

Figure CI.9. **A.** Fits of the three singular transients obtained by SVD on MeO-NAIP molecules. The decay times are indicated in § 4.B and the procedure is described in § 4.A.4.b. **B.** Residuals from the fits.

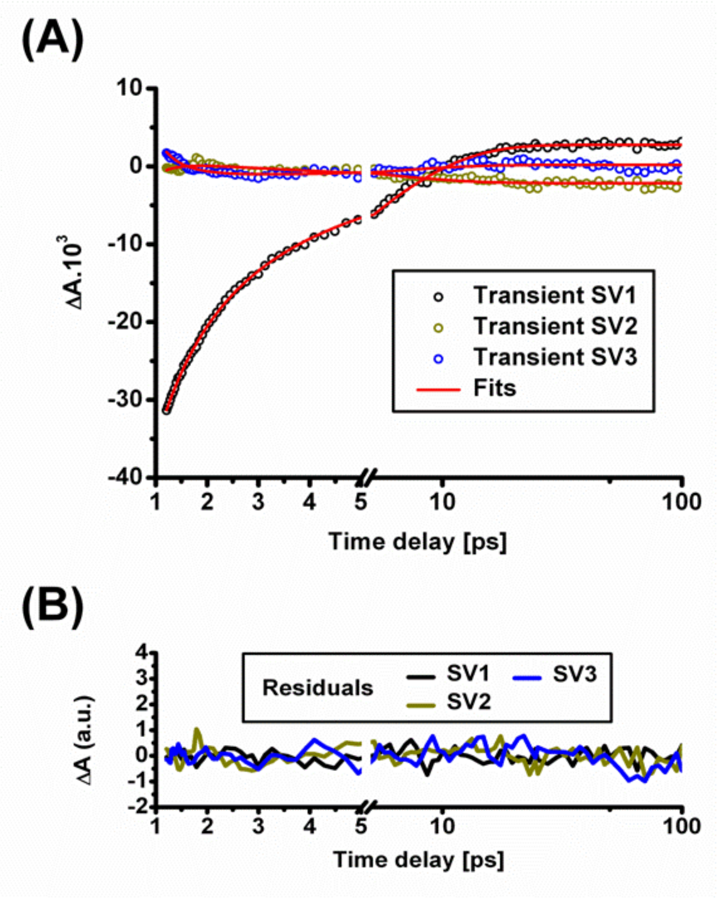

Figure CI.10. Same as CI.9 for Prot-MeO-NAIP.

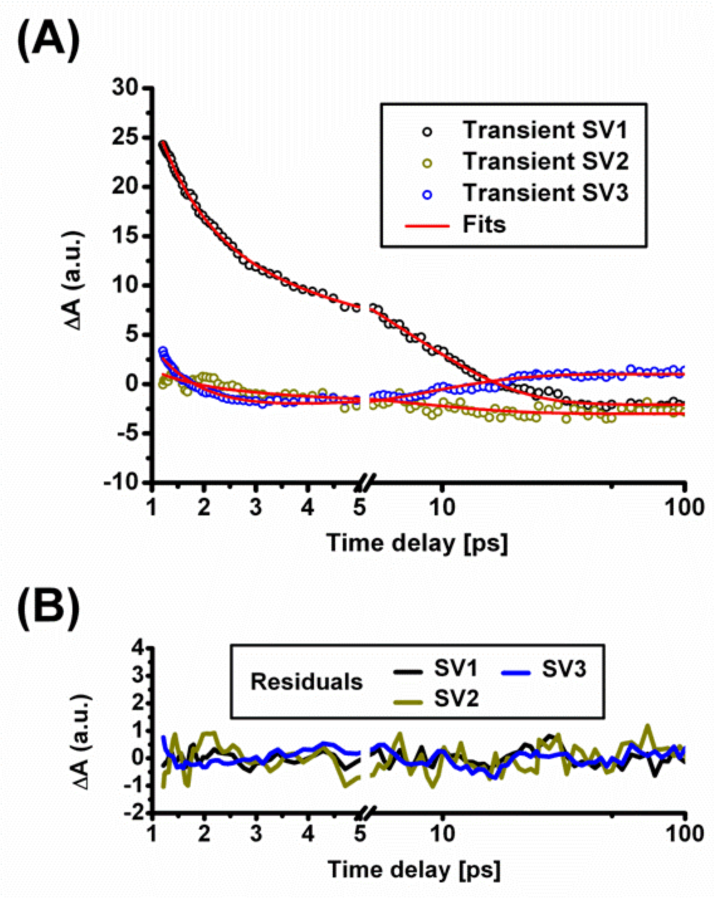

Figure CI.11. Same as CI.9 for NAIP.

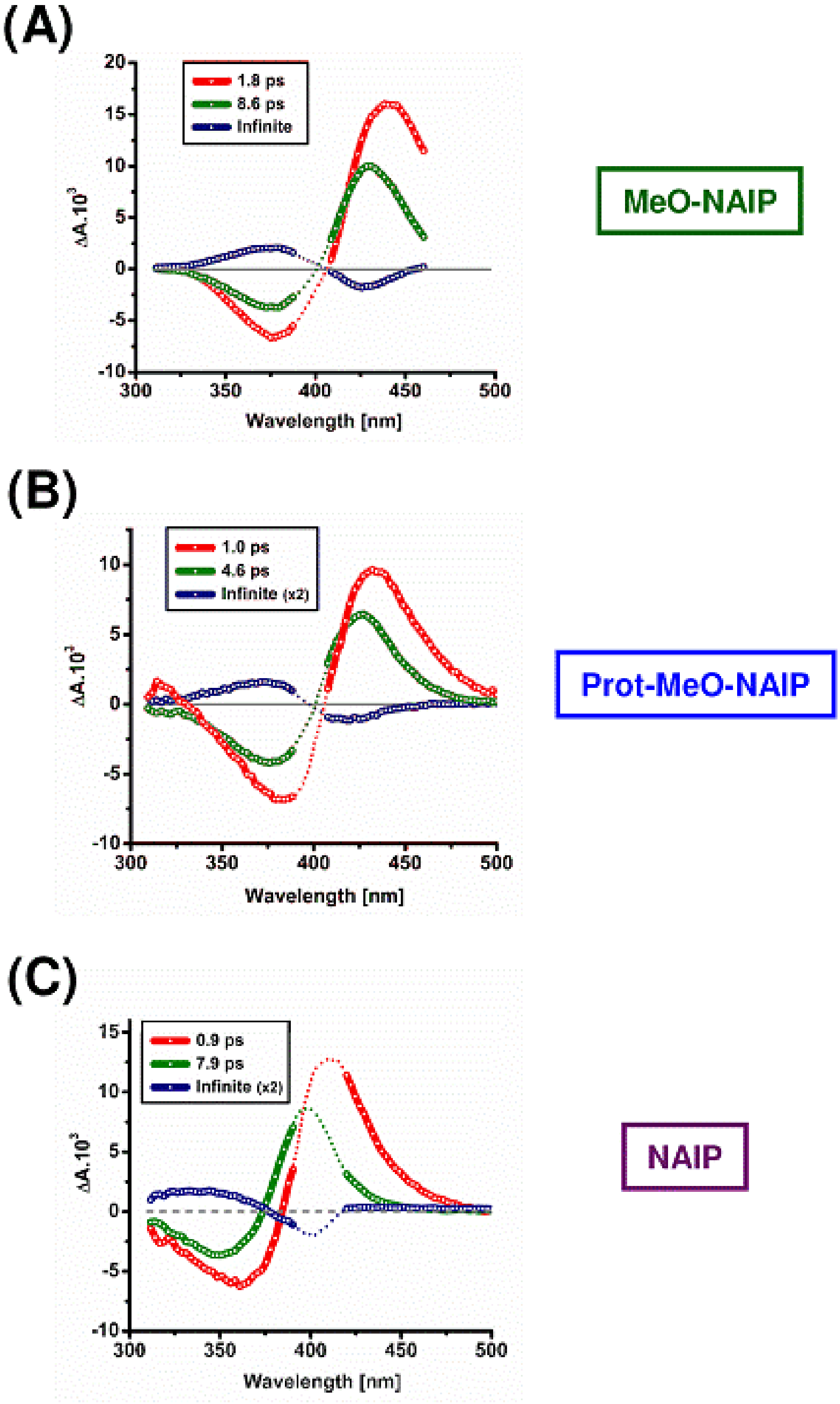

Figure CI.12. **A**. Decay Associated Difference Spectra (DADS) of the ground state thermalization decays of the transient absorption data of MeO-NAIP. They are related to solvation/IVR and cooling. **B**. Same as A for Prot-MeO-NAIP. **C**. Same as A for NAIP.

Figure CI.13 shows the quasi-static spectrum observed at delay times > 30 ps in the Prot-MeO-NAIP measurement. It shows by comparison with the static difference spectrum (see fig. CI.2 also) that isomerization is achieved before 30 ps (see § 4.B).

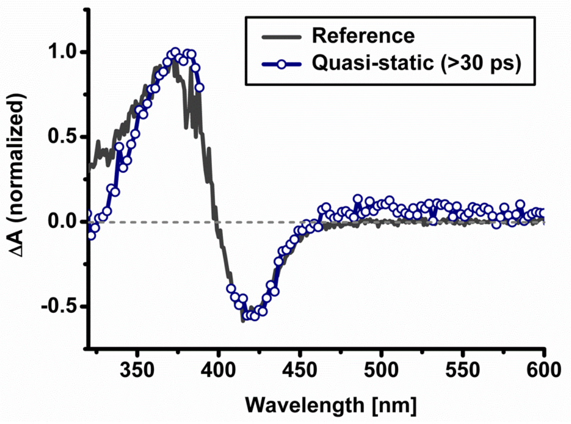

Figure CI.13. Quasi-static spectrum for delays >30ps for Prot-MeO-NAIP (blue circles). The difference of the static spectra is overlaid as a reference. The good agreement between both difference spectra shows that isomerization is achieved in less than 30 ps.

Figure CI.14.A and B plots the singular transients fits and residuals related to the MeO-NABFP DADS shown in fig. 4.26 of § 4.D.

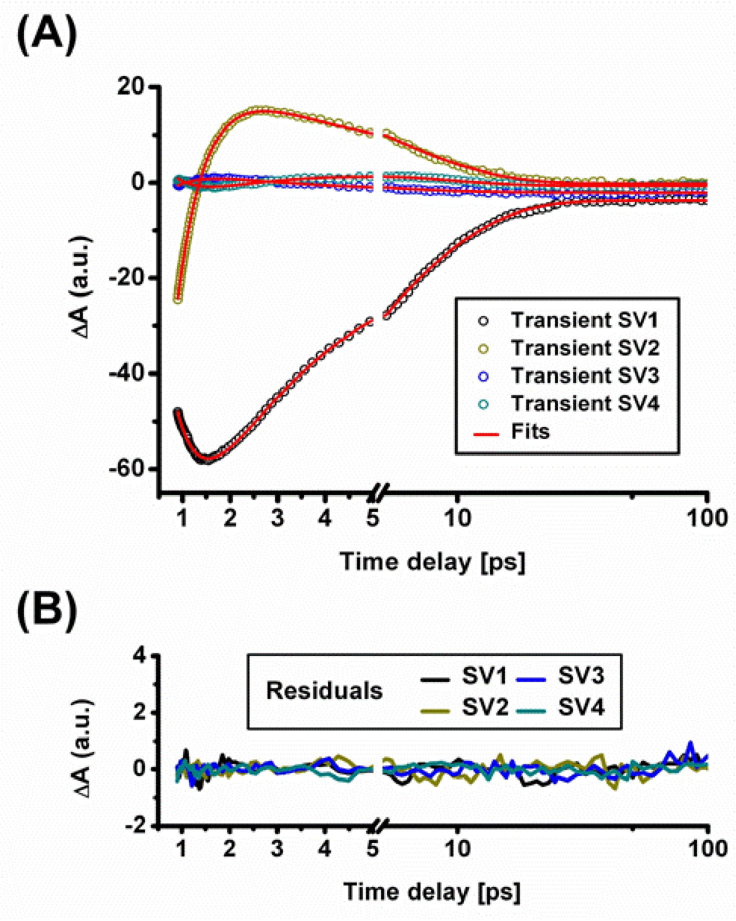

Figure CI.14. **A.** Fits of the four singular transients obtained by SVD on MeO-NABFP molecules. The decay times are indicated in § 4.D and the procedure is described in § 4.A.4.b. **B.** Residuals from the fits.

Chapter 5

The fits of the singular transients obtained by SVD on the ZW-NAIP Z and E solution data sets are presented figure CI.15 and CI.16, respectively. They yield DADS plotted in figure 5.8 of § 5.A.3.b in Chapter 5.

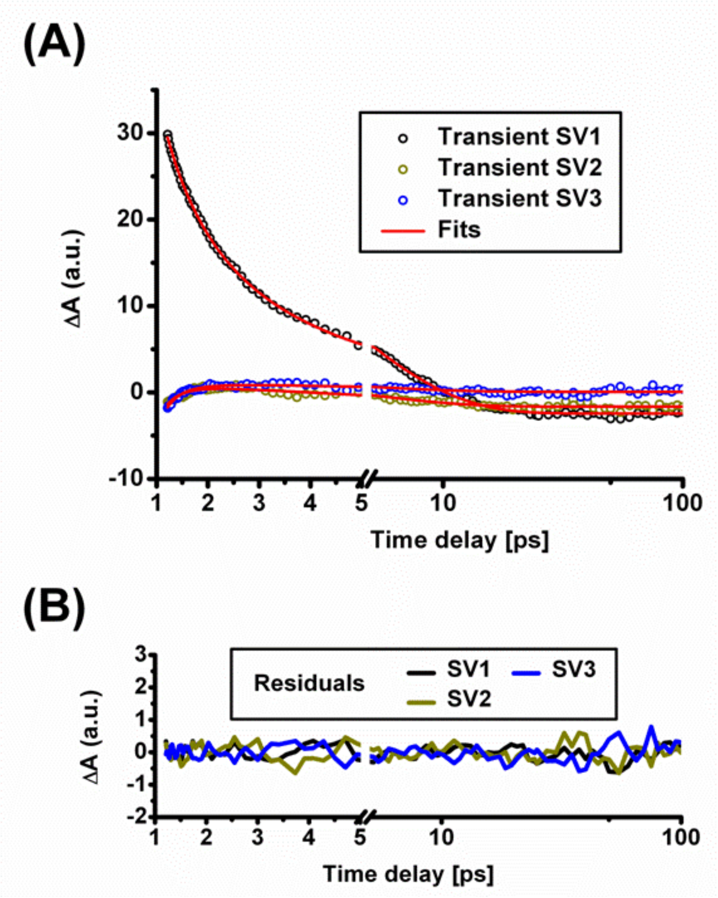

Figure CI.15. **A.** Fits of the three singular transients obtained by SVD on ZW-NAIP "Z sample" solution. The decay times are indicated in § 5.A.3.b and the procedure is described in § 4.A.4.b. **B.** Residuals from the fits.

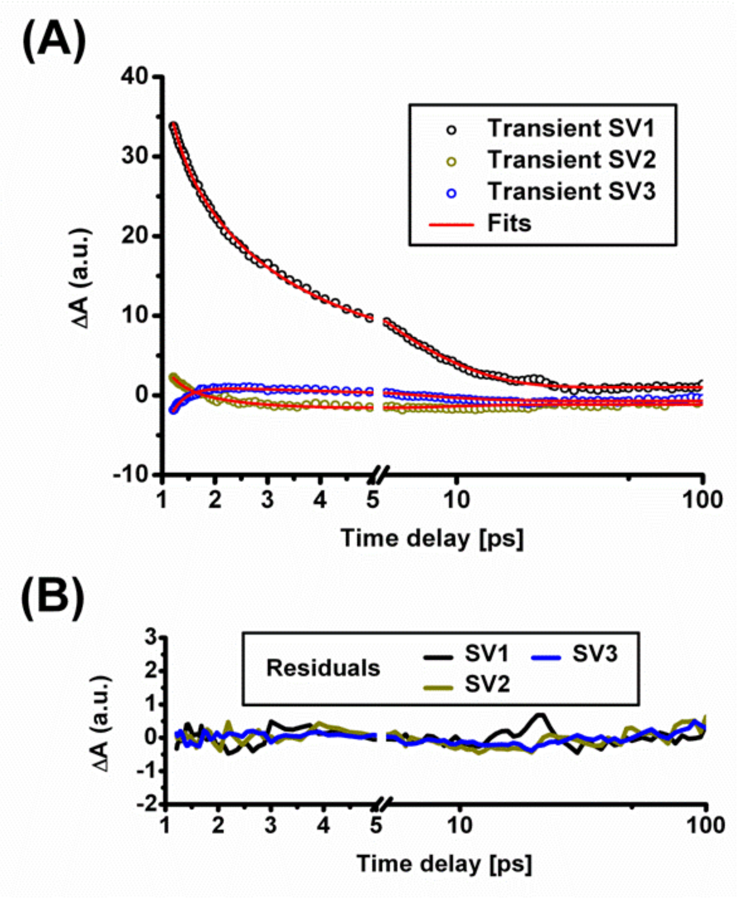

Figure CI.16. Same as figure CI.15 for the ZW-NAIP “E sample” solution.

Figure CI.17 shows the results of the control experiment performed on ZW-NAIP in methanol.

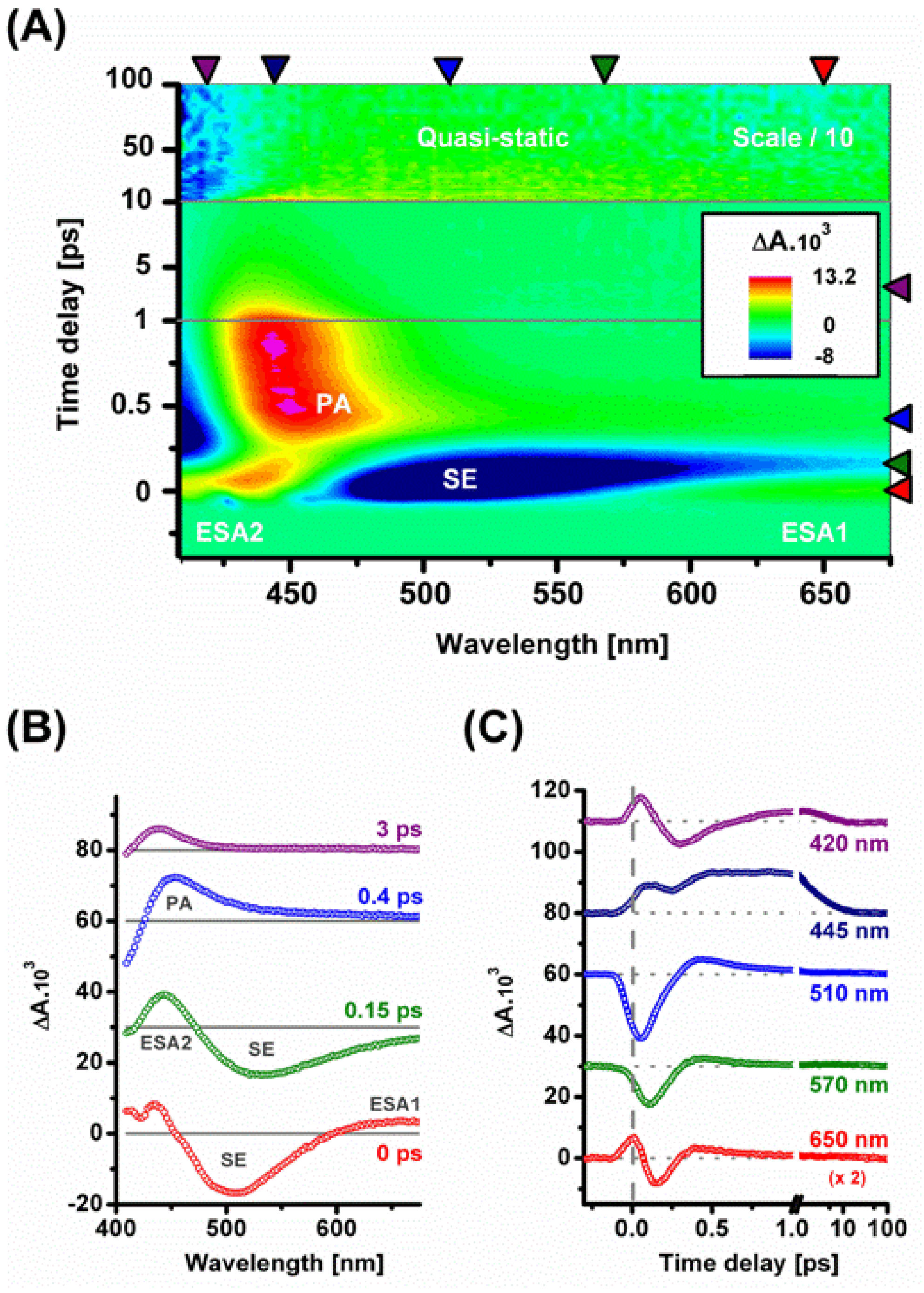

Figure CI.17. **A**. 2D-map of the transient absorption change ΔA of ZW-NAIP in methanol measured in the visible range as a function of wavelength and time delay. **B**. Spectra (open circles) at delays indicated by the cursors on the right of figure A. **C.** Selected kinetic traces at wavelength indicated by the cursors on the top of figure A. Curved arrows highlight the spectral shift of excited-state absorption (ESA) and photoproduct absorption (PA).

Figure CI.18 presents an example of transient at 440 nm for both ZW-NAIP experiments in methanol from Chapter 4 and 6.

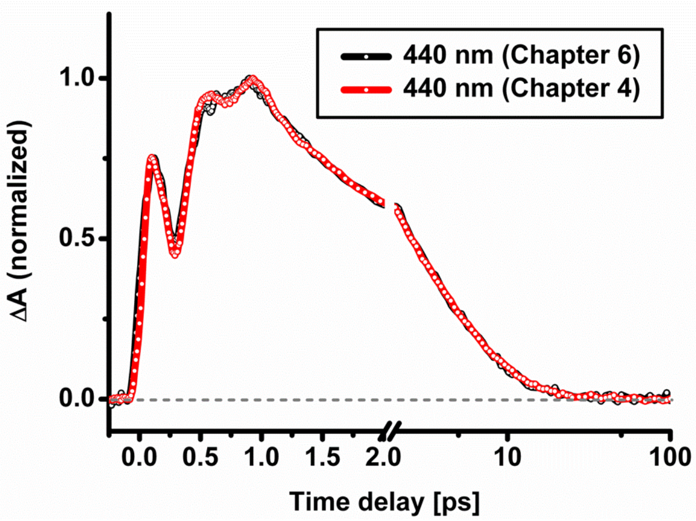

Figure CI.18. Comparison of the normalized 440-nm transients of ZW-NAIP in methanol from Chapter 4 and 6. The results compares well, eventhough the signal-to-noise ratio is higher in the measurement of Chapter 4.

Figure CI.19 presents the results for ZW-NAIP in decanol in the full range measured (330-675 nm).

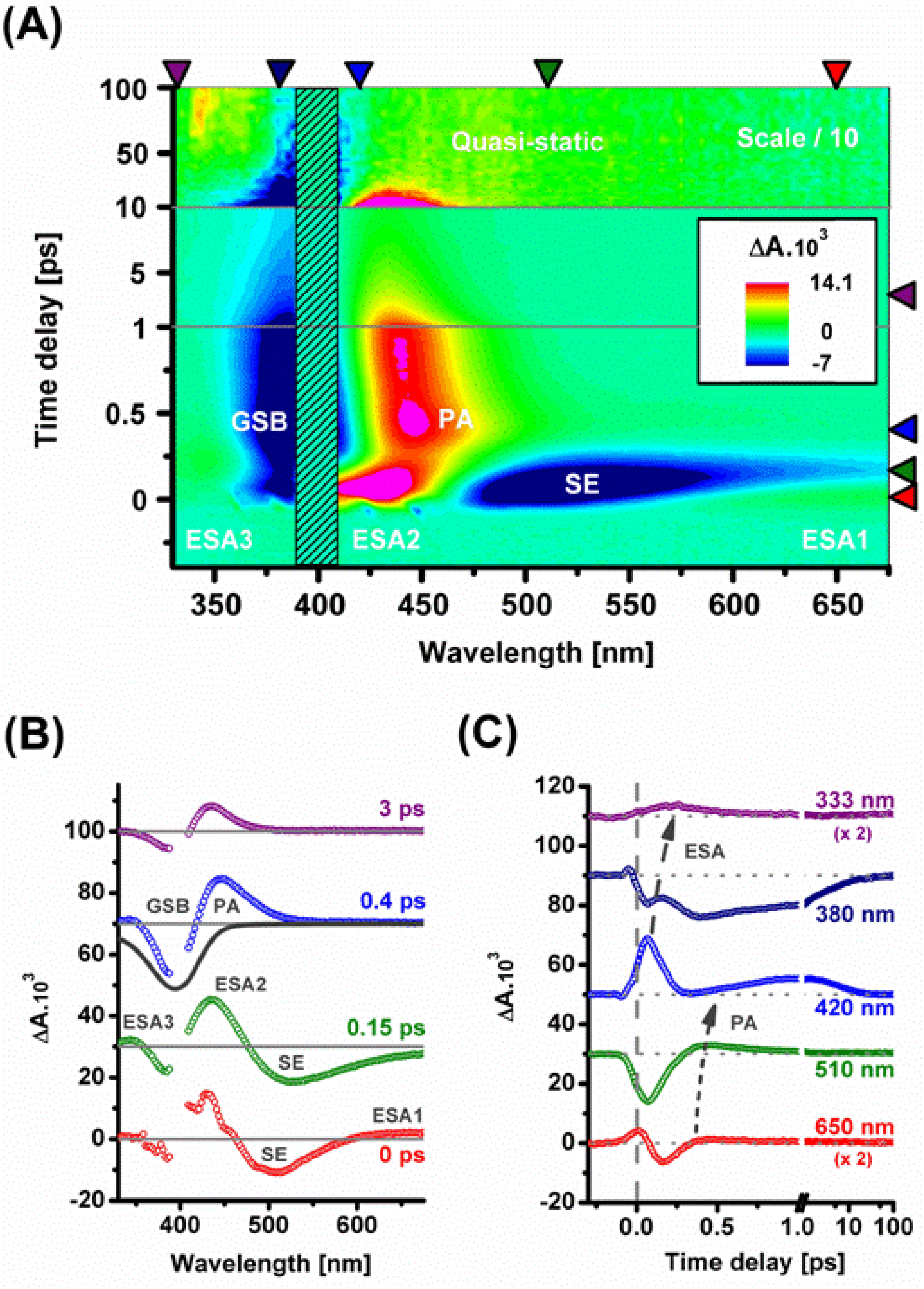

Figure CI.19. Same as figure CI.17 for ZW-NAIP in decanol in the UV-Vis range.

References

1. Lumento, F.; Zanirato, V.; Fusi, S.; Busi, E.; Latterini, L.; Elisei, F.; Sinicropi, A.; Andruniów, T.; Ferré, N.; Basosi, R.; Olivucci, M., Quantum Chemical Modeling and Preparation of a Biomimetic Photochemical Switch. *Angew. Chem. Int. Ed.* **2007,** 46, (3), 414-420.

2. Sinicropi, A.; Martin, E.; Ryazantsev, M.; Helbing, J.; Briand, J.; Sharma, D.; Léonard, J.; Haacke, S.; Cannizzo, A.; Chergui, M.; Zanirato, V.; Fusi, S.; Santoro, F.; Basosi, R.; Ferré, N.; Olivucci, M., An artificial molecular switch that mimics the visual pigment and completes its photocycle in picoseconds. *Proc. Nat. Acad. Sc. USA* **2008,** 105, (46), 17642-17647.

3. Wald, G., Molecular Basis of Visual Excitation. *Science* **1968,** 162, (3850), 230-239.

4. Vos, M. H.; Martin, J.-L., Femtosecond processes in proteins. *Biochimica et Biophysica Acta (BBA) - Bioenergetics* **1999,** 1411, (1), 1.

5. Kochendoerfer, G. G.; Mathies, R. A., Ultrafast Spectroscopy of Rhodopsins: Photochemistry at its best! *Israel journal of chemistry* **1995,** 35, (3-4), 211-226.

6. Pebay-Peyroula, E.; Rummel, G.; Rosenbusch, J. P.; Landau, E. M., X-ray Structure of Bacteriorhodopsin at 2.5 Angstroms from Microcrystals Grown in Lipidic Cubic Phases. *Science* **1997,** 277, (5332), 1676-1681.

7. Edman, K.; Nollert, P.; Royant, A.; Belrhali, H.; Pebay-Peyroula, E.; Hajdu, J.; Neutze, R.; Landau, E. M., High-resolution X-ray structure of an early intermediate in the bacteriorhodopsin photocycle. *Nature* **1999,** 401, (6755), 822.

8. Luecke, H.; Schobert, B.; Richter, H.-T.; Cartailler, J.-P.; Lanyi, J. K., Structure of bacteriorhodopsin at 1.55 Å resolution. *Journal of Molecular Biology* **1999,** 291, (4), 899.

9. Varo, G.; Lanyi, J. K., Kinetic and spectroscopic evidence for an irreversible step between deprotonation and reprotonation of the Schiff base in the bacteriorhodopsin photocycle. *Biochemistry* **1991**, (30), 5008-5015.

10. Tittor, J.; Oesterhelt, D., The quantum yield of bacteriorhodopsin. *FEBS Lett.* **1990,** 263, 296-273.

11. Dobler, J.; Zinth, W.; Kaiser, W.; Oesterhelt, D., Excited-state reaction dynamics of bacteriorhodopsin studied by femtosecond spectroscopy. *Chem. Phys. Lett.* **1988,** 144, (2), 215-220.

12. Mathies, R. A.; Brito Cruz, C. H.; Pollard, W. T.; Shank, C. V., Direct Observation of the Femtosecond Excited State *cis-trans* isomerization in bacteriorhodopsin. *Science* **1988,** 240, 777-779.

13. Petrich, J. W.; Breton, J.; Martin, J. L.; Antonetti, A., Femtosecond absorption spectroscopy of light-adapted and dark-adapted bacteriorhodopsin. *Chemical Physics Letters* **1987,** 137, (4), 369.

14. Haran, G.; Wynne, K.; Xie, A.; He, Q.; Chance, M.; Hochstrasser, R. M., Excited state dynamics of bacteriorhodopsin revealed by transient stimulated emission spectra. *Chemical Physics Letters* **1996,** 261, (4-5), 389.

15. Hasson, K. C.; Gai, F.; Anfinrud, P. A., The photoisomerization of retinal in bacteriorhodopsin: Experimental evidence for a three-state model. *Proceedings of the National Academy of Sciences of the United States of America* **1996,** 93, (26), 15124-15129.

16. Du, M.; Fleming, G. R., Femtosecond time-resolved fluorescence spectroscopy of bacteriorhodopsin: Direct observation of excited state dynamics in the primary step of the proton pump cycle. *Biophysical Chemistry* **1993,** 48, 101-111.

17. Gai, F.; Hasson, K. C.; McDonald, J. C.; Anfinrud, P. A., Chemical Dynamics in Proteins: The Photoisomerization of Retinal in Bacteriorhodopsin. *Science* **1998,** 279, (5358), 1886-1891.

18. Ye, T.; Friedman, N.; Gat, Y.; Atkinson, G. H.; Sheves, M.; Ottolenghi, M.; Ruhman, S., On the Nature of the Primary Light-Induced Events in Bacteriorhodopsin: Ultrafast Spectroscopy of Native and C13=C14 Locked Pigments. *The Journal of Physical Chemistry B* **1999,** 103, (24), 5122.

19. Haacke, S.; Schenkl, S.; Vinzani, S.; Chergui, M., Femtosecond and picosecond fluorescence of native bacteriorhodopsin and a nonisomerizing analog. *Biopolymers* **2002,** 67, (4-5), 306-309.

20. Schmidt, B.; Sobotta, C.; Heinz, B.; Laimgruber, S.; Braun, M.; Gilch, P., Excited-state dynamics of bacteriorhodopsin probed by broadband femtosecond fluorescence spectroscopy. *Biochimica et Biophysica Acta (BBA) - Bioenergetics* **2005,** 1706, (1-2), 165.

21. Warshel, A., Bicycle-pedal model for the first step in the vision process. *Nature* **1976,** 260, (5553), 679.

22. Birge, R. R., Nature of the Primary Photochemical Events in Rhodopsin and Bacteriorhodopsin. *Biochim. Biophys. Acta* **1990,** 1016, (3), 293-327.

23. Palczewski, K.; Kumasaka, T.; Hori, T.; Behnke, C. A.; Motoshima, H.; Fox, B. A.; Trong, I. L.; Teller, D. C.; Okada, T.; Stenkamp, R. E.; Yamamoto, M.; Miyano, M., Crystal Structure of Rhodopsin: A G Protein-Coupled Receptor. *Science* **2000,** 289, (5480), 739-745.

24. Nathans, J., Rhodopsin: structure, function, and genetics. *Biochemistry* **1992,** 31, (21), 4923.

25. Shichida, Y., Ultra-fast Laser Spectroscopy of Visual Pigments. *Photochemistry and Photobiology* **1990,** 52, (6), 1179-1185.

26. Kandori, H.; Shichida, Y.; Yoshizawa, T., Photoisomerization in Rhodopsin. *Biochemistry (Moscow)* **2001,** 66, (11), 1197.

27. Schoenlein, R. W.; Peteanu, L. A.; Mathies, R. A.; Shank, C. V., The first step in vision: femtosecond isomerization of rhodopsin. *Science* **1991,** 254, (5030), 412-415.

28. Dartnall, H. J. A., *Vision Res.* **1967,** 8, 339-358.

29. Filipek, S.; Teller, D. C.; Palczewski, K.; Stenkamp, R., The Crystallographic Model of Rhodopsin and its Use in Studies of Other G Protein-Coupled Receptors. *Annual Review of Biophysics and Biomolecular Structure* **2003,** 32, (1), 375-397.

30. Peteanu, L. A.; Schoenlein, R. W.; Wang, Q.; Mathies, R. A.; Shank, C. V., The first step in vision occurs in femtoseconds: complete blue and red spectral studies. *Proc. Nat. Acad. Sc. USA* **1993,** 90, (24), 11762-11766.

31. Wang, Q.; Schoenlein, R. W.; Peteanu, L. A.; Mathies, R. A.; Shank, C. V., Vibrationally coherent photochemistry in the femtosecond primary event of vision. *Science* **1994,** 266, (5184), 422-424.

32. Haran, G.; Morlino, E. A.; Matthes, J.; Callender, R. H.; Hochstrasser, R. M., Femtosecond Polarized Pump-Probe and Stimulated Emission Spectroscopy of the Isomerization Reaction of Rhodopsin. *J. Chem. Phys. A* **1999,** 103, (14), 2202-2207.

33. Chosrowjan, H.; Mataga, N.; Shibata, Y.; Tachibanaki, S.; Kandori, H.; Shichida, Y.; Okada, T.; Kouyama, T., Rhodopsin Emission in Real Time: A New Aspect of the Primary Event in Vision. *Journal of the American Chemical Society* **1998,** 120, (37), 9706.

34. Kandori, H.; Furutani, Y.; Nishimura, S.; Shichida, Y.; Chosrowjan, H.; Shibata, Y.; Mataga, N., Excited-state dynamics of rhodopsin probed by femtosecond fluorescence spectroscopy. *Chem. Phys. Lett.* **2001,** 334, 271-276.

35. González-Luque, R.; Garavelli, M.; Bernardi, F.; Merchán, M.; Robb, M. A.; Olivucci, M., Computational evidence in favor of a two-state, two-mode model of the retinal chromophore isomerization. *Proc. Nat. Acad. Sci. USA* **2000,** 97, (17), 9379-9384.

36. Kandori, H.; Yoshihara, K.; Tomioka, H.; Sasabe, H., Primary photochemical events in halorhodopsin studied by subpicosecond time-resolved spectroscopy. *The Journal of Physical Chemistry* **2002,** 96, (14), 6066.

37. Kobayashi, T.; Kim, M.; Taiji, M.; Iwasa, T.; Nakagawa, M.; Tsuda, M., Femtosecond Spectroscopy of Halorhodopsin and Rhodopsin in a Broad Spectral Range of 400-1000 nm. *The Journal of Physical Chemistry B* **1998,** 102, (1), 272.

38. Lenz, M. O.; Huber, R.; Schmidt, B.; Gilch, P.; Kalmbach, R.; Engelhard, M.; Wachtveitl, J., First Steps of Retinal Photoisomerization in Proteorhodopsin. *Biophys J.* **2006,** 91, (v), v.

39. Huber, R.; Kohler, T.; Lenz, M. O.; Bamberg, E.; Kalmbach, R.; Engelhard, M.; Wachtveitl, J., pH-Dependent Photoisomerization of Retinal in Proteorhodopsin. *Biochemistry* **2005,** 44, (6), 1800.

40. Rupenyan, A.; van Stokkum, I. H. M.; Arents, J. C.; van Grondelle, R.; Hellingwerf, K.; Groot, M. L., Characterization of the Primary Photochemistry of Proteorhodopsin with Femtosecond Spectroscopy. *Biophysical Journal* **2008,** 94, (10), 4020.

41. Lutz, I.; Sieg, A.; Wegener, A. A.; Engelhard, M.; Boche, I.; Otsuka, M.; Oesterhelt, D.; Wachtveitl, J.; Zinth, W., Primary reactions of sensory rhodopsins. *Proceedings of the National Academy of Sciences of the United States of America* **2001,** 98, (3), 962-967.

42. Schoenlein, R. W.; Peteanu, L. A.; Wang, Q.; Mathies, R. A.; Shank, C. V., Femtosecond dynamics of cis-trans isomerization in a visual pigment analog: isorhodopsin. *J. Chem. Phys.* **1993,** 97, (46), 12087-12092.

43. Wang, Q.; Kochendoerfer, G. G.; Schoenlein, R. W.; Verdegem, P. J. E.; Lugtenburg, J.; Mathies, R. A.; Shank, C. V., Femtosecond Spectroscopy of a 13-Demethylrhodopsin Visual Pigment Analogue: The Role of Nonbonded Interactions in the Isomerization Process. *J. Chem. Phys.* **1996,** 100, (43), 17388-17394.

44. Freedman, K. A.; Becker, R. S., Comparative investigation of the photoisomerization of the protonated and unprotonated n-butylamine Schiff bases of 9-cis-, 11-cis-, 13-cis-, and all-trans-retinals. *Journal of the American Chemical Society* **1986,** 108, (6), 1245.

45. Hou, B.; Friedman, N.; Ruhman, S.; Sheves, M.; Ottolenghi, M., Ultrafast Spectroscopy of the Protonated Schiff Bases of Free and C13C14 Locked Retinals. *The Journal of Physical Chemistry B* **2001,** 105, (29), 7042.

46. Herbst, J.; Heyne, K.; Diller, R., Femtosecond Infrared Spectroscopy of Bacteriorhodopsin Chromophore Isomerization. *Science* **2002,** 297, (5582), 822-825.

47. Kobayashi, T.; Saito, T.; Ohtani, H., Real-time spectroscopy of transition states in bacteriorhodopsin during retinal isomerization. *Nature* **2001,** 414, (6862), 531-534.

48. Takayoshi, K.; Atsushi, Y.; Takashi, S.; Hiroyuki, O.; Motoyuki, T., Sub-5-fs Real-time Spectroscopy of Transition States in Bacteriorhodopsin During Retinal Isomerization. *Photochemistry and Photobiology* **2007,** 83, (2), 363-369.

49. Ferré, N.; Olivucci, M., Probing the Rhodopsin Cavity with Reduced Retinal Models at the CASPT2//CASSCF/AMBER Level of Theory. *Journal of the American Chemical Society* **2003,** 125, (23), 6868.

50. Andruniów, T.; Ferré, N.; Olivucci, M., Structure, initial excited-state relaxation, and energy storage of rhodopsin resolved at the multiconfigurational perturbation theory level. *Proc. Nat. Acad. Sci. USA* **2004,** 101, (52), 17908-17913.

51. Migani, A.; Sinicropi, A.; Ferré, N.; Cembran, A.; Garavelli, M.; Olivucci, M., Structure of the intersection space associated with Z/E photoisomerization of retinal in rhodopsin proteins. *Faraday Discussions* **2004,** 127, 179-191.

52. Cembran, A.; Bernardi, F.; Olivucci, M.; Garavelli, M., Excited-State Singlet Manifold and Oscillatory Features of a Nonatetraeniminium Retinal Chromophore Model. *Journal of the American Chemical Society* **2003,** 125, (41), 12509.

53. Sinicropi, A.; Basosi, R.; Olivucci, M., Recent applications of a QM/MM scheme at the CASPT2//CASSCF/AMBER (or CHARMM) level of theory in photochemistry and photobiology. *Journal of Physics: Conference Series* **2008**, 012001.

54. Levine, B. G.; Martinez, T. J., Isomerization Through Conical Intersections. *Ann. Rev. Phys. Chem.* **2007,** 58, (1), 613-634.

55. Coto, P. B.; Sinicropi, A.; De Vico, L.; Ferr; N.; Olivucci, M., Characterization of the conical intersection of the visual pigment rhodopsin at the CASPT2//CASSCF/AMBER level of theory. *Molecular Physics* **2006,** 104, 983.

56. Frutos, L. M.; Andruniów, T.; Santoro, F.; Ferré, N.; Olivucci, M., Tracking the excited-state time evolution of the visual pigment with multiconfigurational quantum chemistry. *Proceedings of the National Academy of Sciences* **2007,** 104, (19), 7764-7769.

57. Atkins, P. W.; Friedman, R. S., *Molecular Quantum Mechanics*. 3rd ed.; Oxford University Press: 1997.

58. Ohmori, K., Wave-Packet and Coherent Control Dynamics. *Annu. Rev. Phys. Chem.* **2008,** 60, 487-511.

59. Zewail, A. H., Femtochemistry: Atomic-Scale Dynamics of the Chemical Bond Using Ultrafast Lasers (Nobel Lecture)13. *Angewandte Chemie International Edition* **2000,** 39, (15), 2586-2631.

60. Dantus, M.; Rosker, M. J.; Zewail, A. H., Real-time femtosecond probing of ``transition states'' in chemical reactions. *The Journal of Chemical Physics* **1987,** 87, (4), 2395.

61. Pollard, W. T.; Dexheimer, S. L.; Wang, Q.; Peteanu, L. A.; Shank, C. V.; Mathies, R. A., Theory of dynamic absorption spectroscopy of nonstationary states. 4. Application to 12-fs resonant impulsive Raman spectroscopy of bacteriorhodopsin. *The Journal of Physical Chemistry* **1992,** 96, (15), 6147.

62. Szarka, A. Z.; Pugliano, N.; Palit, D. K.; Hochstrasser, R. M., Vibrational coherence in the solution phase photoisomerization reaction of cis-stilbene. *Chem. Phys. Lett.* **1995,** 240, (1-3), 25.

63. Hou, B.; Friedman, N.; Ottolenghi, M.; Sheves, M.; Ruhman, S., Comparing photoinduced vibrational coherences in bacteriorhodopsin and in native and locked retinal protonated Schiff bases. *Chem. Phys. Lett.* **2003,** 381, (5-6), 549-555.

64. Kahan, A.; Nahmias, O.; Friedman, N.; Sheves, M.; Ruhman, S., Following Photoinduced Dynamics in Bacteriorhodopsin with 7-fs Impulsive Vibrational Spectroscopy. *J. Am. Chem. Soc.* **2007,** 129, 537-546.

65. Chosrowjan, H.; Taniguchi, S.; Mataga, N.; Unno, M.; Yamauchi, S.; Hamada, N.; Kumauchi, M.; Tokunaga, F., Low-Frequency Vibrations and Their Role in Ultrafast Photoisomerization Reaction Dynamics of Photoactive Yellow Protein. *J. Chem. Phys. B* **2004,** 108, (8), 2686.

66. Vos, M. H.; Lambry, J. C.; Robles, S. J.; Youvan, D. C.; Breton, J.; Martin, J. L., Direct observation of vibrational coherence in bacterial reaction centers using femtosecond absorption spectroscopy. *Proceedings of the National Academy of Sciences of the United States of America* **1991,** 88, (20), 8885-8889.

67. Vos, M. H.; Jones, M. R.; Hunter, C. N.; Breton, J.; Martin, J. L., Coherent nuclear dynamics at room temperature in bacterial reaction centers. *Proceedings of the National Academy of Sciences of the United States of America* **1994,** 91, (26), 12701-12705.

68. Zgrablić, G.; Haacke, S.; Chergui, M., Vibrational coherences of the protonated Schiff base of all-trans retinal in solution. *Chem. Phys.* **2007,** 338, (2-3), 168.

69. Dexheimer, S. L.; Wang, Q.; Peteanu, L. A.; Pollard, W. T.; Mathies, R. A.; Shank, C. V., Femtosecond impulsive excitation of nonstationary vibrational states in bacteriorhodopsin. *Chem. Phys. Lett.* **1992,** 188, (1), 61-66.

70. Sporlein, S.; Zinth, W.; Wachtveitl, J., Vibrational Coherence in Photosynthetic Reaction Centers Observed in the Bacteriochlorophyll Anion Band. *The Journal of Physical Chemistry B* **1998,** 102, (38), 7492.

71. Pollard, W. T.; Fragnito, H. L.; Bigot, J. Y.; Shank, C. V.; Mathies, R. A., Quantum-mechanical theory for 6 fs dynamic absorption spectroscopy and its application to nile blue. *Chem. Phys. Lett.* **1990,** 168, (3-4), 239.

72. Dhar, L.; Rogers, J. A.; Nelson, K. A., Time-resolved vibrational spectroscopy in the impulsive limit. *Chemical Reviews* **1994,** 94, (1), 157.

73. Moulton, P. F., Spectroscopic and laser characteristics of Ti:Al2O3. *J. Opt. Soc. Am. B* **1986,** 3, (1), 125.

74. Reid, G. D.; Wynne, K., Ultrafast Laser Technology and Spectroscopy. *Encyclopedia of Analytical Chemistry: Instrumentation and Applications* **2000**, 13644-13670.

75. Asaki, M. T.; Huang, C.-P.; Garvey, D.; Zhou, J.; Kapteyn, H. C.; Murnane, M. M., Generation of 11-fs pulses from a self-mode-locked Ti:sapphire laser. *Opt. Lett.* **1993,** 18, (12), 977.

76. Jung, I. D.; Kärtner, F. X.; Matuschek, N.; Sutter, D. H.; Morier-Genoud, F.; Zhang, G.; Keller, U.; Scheuer, V.; Tilsch, M.; Tschudi, T., Self-starting 6.5-fs pulses from a Ti:sapphire laser. *Opt. Lett.* **1997,** 22, (13), 1009.

77. Spence, D. E.; Kean, P. N.; Sibbett, W., 60-fsec pulse generation from a self-mode-locked Ti:sapphire laser. *Opt. Lett.* **1991,** 16, (1), 42.

78. Morgner, U.; Kärtner, F. X.; Cho, S. H.; Chen, Y.; Haus, H. A.; Fujimoto, J. G.; Ippen, E. P.; Scheuer, V.; Angelow, G.; Tschudi, T., Sub-two-cycle pulses from a Kerr-lens mode-locked Ti:sapphire laser. *Opt. Lett.* **1999,** 24, (6), 411.

79. Strickland, D.; Mourou, G., Compression of amplified chirped optical pulses. *Optics Communications* **1985,** 55, (6), 447.

80. Wynne, K.; Reid, G. D.; Hochstrasser, R. M., Regenerative amplification of 30-fs pulses in Ti:sapphire at 5 kHz. *Opt. Lett.* **1994,** 19, (12), 895.

81. Barty, C. P. J.; Gordon Iii, C. L.; Lemoff, B. E., Multiterawatt 30-fs Ti:sapphire laser system. *Opt. Lett.* **1994,** 19, (18), 1442.

82. Backus, S.; Peatross, J.; Huang, C. P.; Murnane, M. M.; Kapteyn, H. C., Ti:sapphire amplifier producing millijoule-level, 21-fs pulses at 1 kHz. *Opt. Lett.* **1995,** 20, (19), 2000.

83. Treacy, E., Optical pulse compression with diffraction gratings. *Quantum Electronics, IEEE Journal of* **1969,** 5, (9), 454.

84. Fork, R. L.; Martinez, O. E.; Gordon, J. P., Negative dispersion using pairs of prisms. *Opt. Lett.* **1984,** 9, (5), 150.

85. Martinez, O., 3000 times grating compressor with positive group velocity dispersion: Application to fiber compensation in 1.3-1.6 µm region. *Quantum Electronics, IEEE Journal of* **1987,** 23, (1), 59.

86. Cheriaux, G.; Rousseau, P.; Salin, F.; Chambaret, J. P.; Walker, B.; Dimauro, L. F., Aberration-free stretcher design for ultrashort-pulse amplification. *Opt. Lett.* **1996,** 21, (6), 414.

87. Amplitude, T., Pulsar Manual. **2005**.

88. Couairon, A.; Mysyrowicz, A., Femtosecond filamentation in transparent media. *Physics Reports* **2007,** 441, (2-4), 47.

89. Franken, P. A.; Hill, A. E.; Peters, C. W.; Weinreich, G., Generation of Optical Harmonics. *Physical Review Letters* **1961,** 7, (4), 118.

90. Shen, Y. R., The Principles of Nonlinear Optics. *John Wiley & Sons, New York* **1986**.

91. Petra, B., Borate Materials in Nonlinear Optics. *Advanced Materials* **1998,** 10, (13), 979-992.

92. Adhav, R. S.; Adhav, S. R.; Pelaprat, J. M., BBO's nonlinear optical phase-matching properties. *Laser Focus* **1987,** 23, (88).

93. Bloembergen, N.; Lallemand, P., Complex Intensity-Dependent Index of Refraction, Frequency Broadening of Stimulated Raman Lines, and Stimulated Rayleigh Scattering. *Physical Review Letters* **1966,** 16, (3), 81.

94. Alfano, R. R.; Shapiro, S. L., Observation of Self-Phase Modulation and Small-Scale Filaments in Crystals and Glasses. *Physical Review Letters* **1970,** 24, (11), 592.

95. Fork, R. L.; Shank, C. V.; Hirlimann, C.; Yen, R.; Tomlinson, W. J., Femtosecond white-light continuum pulses. *Opt. Lett.* **1983,** 8, (1), 1.

96. Yang, G.; Shen, Y. R., Spectral broadening of ultrashort pulses in a nonlinear medium. *Opt. Lett.* **1984,** 9, (11), 510.

97. Nagura, C.; Suda, A.; Kawano, H.; Obara, M.; Midorikawa, K., Generation and Characterization of Ultrafast White-Light Continuum in Condensed Media. *Appl. Opt.* **2002,** 41, (18), 3735.

98. Tzankov, P.; Buchvarov, I.; Fiebig, T., Broadband optical parametric amplification in the near UV-VIS. *Optics Communications* **2002,** 203, (1-2), 107.

99. Gaeta, A. L., Catastrophic Collapse of Ultrashort Pulses. *Physical Review Letters* **2000,** 84, (16), 3582.

100. Dharmadhikari, A. K.; Rajgara, F. A.; Mathur, D., Systematic study of highly efficient white light generation in transparent materials using intense femtosecond laser pulses. *Applied Physics B: Lasers and Optics* **2005,** 80, (1), 61.

101. Adair, R.; Chase, L. L.; Payne, S. A., Nonlinear refractive index of optical crystals. *Physical Review B* **1989,** 39, (5), 3337.

102. Kovalenko, S. A.; Ruthmann, J.; Ernsting, N. P., Femtosecond hole-burning spectroscopy with stimulated emission pumping and supercontinuum probing. *The Journal of Chemical Physics* **1998,** 109, (5), 1894.

103. Kovalenko, S. A.; Dobryakov, A. L.; Ruthmann, J.; Ernsting, N. P., Femtosecond spectroscopy of condensed phases with chirped supercontinuum probing. *Physical Review A* **1999,** 59, (3), 2369.

104. Lorenc, M.; Ziolek, M.; Naskrecki, R.; Karolczak, J.; Kubicki, J.; Maciejewski, A., Artifacts in femtosecond transient absorption spectroscopy. *Applied Physics B: Lasers and Optics* **2002,** 74, (1), 19.

105. Briand, J.; Bräm, O.; Léonard, J.; Cannizo, A.; Zanirato, V.; Chergui, M.; Olivucci, M.; Haacke, S., Coherent Ultrafast Torsional Motion and Isomerisation of a Biomimetic Dipolar Photoswitch. *Submitted* **2009**.

106. Zizak, G.; Bradshaw, J. D.; Winefordner, J. D., Rate equation solution for the temporal behavior of a three-level system. *Appl. Opt.* **1980,** 19, (21), 3631.

107. van Stokkum, I. H. M.; Larsen, D. S.; van Grondelle, R., Global and target analysis of time-resolved spectra. *Biochimica et Biophysica Acta (BBA) - Bioenergetics* **2004,** 1657, (2-3), 82.

108. Helbing, J.; Bonacina, L.; Pietri, R.; Bredenbeck, J.; Hamm, P.; van Mourik, F.; Chaussard, F.; Gonzalez-Gonzalez, A.; Chergui, M.; Ramos-Alvarez, C.; Ruiz, C.; López-Garriga, J., Time-Resolved Visible and Infrared Study of the Cyano Complexes of Myoglobin and of Hemoglobin I from Lucina pectinata. **2004,** 87, (3), 1881.

109. Bonacina, L., Ultrafast structural dynamics in electronically excited many-body systems. *Ph.D. Thesis, EPFL Lausanne* **2004**.

110. Bonacic-Koutecký, V.; Koutecký, J.; Michl, J., Neutral and Charged Biradicals, Zwitterions, Funnels in S1, and Proton Translocation: Their Role in Photochemistry, Photophysics, and Vision. *Angewandte Chemie International Edition in English* **1987,** 26, (3), 170-189.

111. Melloni, A.; Paccani, R. R.; Donati, D.; Zanirato, V.; Sinicropi, A.; Parisi, M. L.; Martin, E.; Basosi, R.; Fusi, S.; Latterini, L.; Ferré, N.; Olivucci, M., Modeling, Preparation and Characterization of a Dipole Moment Switch Driven by Z/E Photoisomerization. *submitted* **2009**.

112. Zanirato, V.; Pollini, G. P.; De Risi, C.; Valente, F.; Melloni, A.; Fusi, S.; Barbetti, J.; Olivucci, M., Synthesis of biomimetic light-driven molecular switches via a cyclopropyl ring-opening/nitrilium ion ring-closing tandem reaction. *Tetrahedron* **2007,** 63, (23), 4975.

113. Roos, B. O., The Complete Active Space Self-Consistent Field Method and its Applications in Electronic Structure Calculations. In *Advances in Chemical Physics*, Lawley, K. P., Ed. Wiley: 1987; Vol. 69, pp 399-445.

114. Andersson, K.; Malmqvist, P. A.; Roos, B. O.; Sadlej, A. J.; Wolinski, K., Second-order perturbation theory with a CASSCF reference function. *The Journal of Physical Chemistry A* **1990,** 94, (14), 5483.

115. Karlström, G.; Lindh, R.; Malmqvist, P.-Å.; Roos, B. O.; Ryde, U.; Veryazov, V.; Widmark, P.-O.; Cossi, M.; Schimmelpfennig, B.; Neogrady, P.; Seijo, L., MOLCAS: a program package for computational chemistry. *Computational Materials Science* **2003,** 28, (2), 222.

116. Ferré, N.; Olivucci, M., The amide bond: pitfalls and drawbacks of the link atom scheme. *Journal of Molecular Structure: THEOCHEM* **2003,** 632, (1-3), 71.

117. Ferré, N.; Cembran, A.; Garavelli, M.; Olivucci, M., Complete-active-space self-consistent-field/Amber parameterization of the Lys296–retinal–Glu113 rhodopsin chromophore-counterion system. *Theoretical Chemistry Accounts: Theory, Computation, and Modeling (Theoretica Chimica Acta)* **2004,** 112, (4), 335.

118. Sinicropi, A.; Andruniow, T.; Ferre, N.; Basosi, R.; Olivucci, M., Properties of the Emitting State of the Green Fluorescent Protein Resolved at the CASPT2//CASSCF/CHARMM Level. *Journal of the American Chemical Society* **2005,** 127, (33), 11534.

119. Réhault, J.; Zanirato, V.; Helbing, J.; Olivucci, M., Ultrafast Bi-Directional Isomerization of a Dipolar Biomimetic Photoswitch. *Submitted* **2009**.

120. Horng, M. L.; Gardecki, J. A.; Papazyan, A.; Maroncelli, M., Subpicosecond Measurements of Polar Solvation Dynamics: Coumarin 153 Revisited. *J. Chem. Phys.* **1995,** 99, (48), 17311-17337.

121. Bräm, O.; Cannizo, A.; Chergui, M., unpublished results.

122. Briand, J.; Helbing, J.; Cannizzo, A.; Chergui, M.; Zanirato, V.; Haacke, S.; Olivucci, M., Ultrafast Isomerization Dynamics of Biomimetic Photoswitches. *Proceedings of the XVIth international conference on Ultrafast Phenomena (UP), Springer Series in Chemical Physics* **2009**.

123. Réhault, J.; Helbing, J., unpublished results.

124. Latterini, L., unpublished results.

125. Sussman, B. J.; Townsend, D.; Ivanov, M. Y.; Stolow, A., Dynamic Stark Control of Photochemical Processes. *Science* **2006,** 314, (5797), 278-281.

126. Technical assistance by Emilie Couzigné with NMR measurements is highly acknowledged

127. Dietzek, B.; Tarnovsky, A. N.; Yartsev, A., Visualizing overdamped wavepacket motion: Excited-state isomerization of pseudocyanine in viscous solvents. *Chemical Physics* **2009,** 357, (1-3), 54.

128. Burghardt, I.; Hynes, J. T.; Gindensperger, E.; Cederbaum, L. S., Ultrafast excited-state dynamics at a conical intersection: the role of environmental effects. *Physica Scripta* **2006**, (1), C42.

129. Branderhorst, M. P. A.; Londero, P.; Wasylczyk, P.; Brif, C.; Kosut, R. L.; Rabitz, H.; Walmsley, I. A., Coherent Control of Decoherence. *Science* **2008,** 320, (5876), 638-643.